NORTHWESTERN UNIVERSITY

# Mechanical Design and Analysis of Three-dimensional (3D) Assembly, with Applications on Wearable Electronics,Thermo-electric Energy Harvester and Microflyer

A DISSERTATION

SUBMITTED TO THE GRADUATE SCHOOL
IN PARTIAL FULFILLMENT OF THE REQUIREMENTS

for the degree

DOCTOR OF PHILOSOPHY

Field of Theoretical and Applied Mechanics

By

Kan Li

EVANSTON, ILLINOIS

March 2019

# ABSTRACT

Mechanical Design and Analysis of Three-dimensional (3D) Assembly, with Applications on Wearable Electronics,Thermo-electric Energy Harvester and Microflyer

Kan Li

The rapid development of flexible electronics enables a huge amount of bio-integrated applications with advantages of the mechanical compliance, stretchability and comformability of the devices. My dissertation further advances this area by a series of projects, which include designing and optimizing novel compliant structures, proposing novel elastomer encapsulation process for the robust protection for stretchable devices, applying novel 3D structures to enable fully integrated health-monitoring system and compliant thermoelectric energy harvesting system, designing novel 3D self-assembled structures, and exploring the applications of 3D mesostructures.

## Acknowledgements

Although I have no idea how I chose to become a PhD student, it worth the time thinking about who to be, what I like, and whom I love. Thanks to this 4-year journey, providing me enough time to think about both science and life.

Thanks to Prof. Yonggang Huang, Prof. John A. Rogers and Prof. Yihui Zhang, for supervising me and teaching me how to do research. Thanks to my colleagues and collaborators, always, for the friendship and diligence in work. Thanks to Feng Zhu, Lin Chen, Ao Wang and Ce Yang, for helping with the projects.

Thanks to my parents, with my deepest gratitude, for their warm love, continued patience and endless support, despite they have no idea what I was doing.

Thanks to my friend Siyi Liu, for standing on my side always.

Thanks to someone, buried but rooted in deep heart, for being the one, and making me firm on every step.

Thanks to a respected elder who lends a hand when I felt drown.

Thanks to me, for never giving up hope.

*"The hell I step on is the shadow of heaven."*

# Preface

This dissertation is submitted for the degree of Doctor of Philosophy at Northwestern University. The research described herein was conducted under the supervision of Professor Yonggang Huang in the Department of Civil and Environmental Engineering, Department of Mechanical Engineering and by courtesy Department of Materials Science and Engineering, Northwestern University, between October 2014 and November 2018.

This work is to the best of my knowledge original, except where acknowledgements and references are made to previous work. Neither this, nor any substantially similar dissertation has been or is being submitted for any other degree, diploma or other qualification at any other university.

Part of this work has been presented in the following publications:

K. Jang, K. Li, H. Chung, S. Xu, H. Jung, Y. Yang, J. Kwak, H. Jung, J. Song, C. Yang, A. Wang, Z. Liu, J. Lee, B. Kim, J. Kim, J. Lee, Y. Yu, B. Kim, H. Jang, K. Yu, J. Kim, J. Lee, J. Jeong, Y. Song, Y. Huang, Y. Zhang, J. Rogers, “Self-Assembled, Three Dimensional Network Designs for Soft Electronics”, *Nature Communications* , 2017.

K. Nan, S. Kang, K. Li, K. Yu, F. Zhu, J. Wang, A. Dunn, C. Zhou, Z. Xie, M. Agne, H. Wang, H. Luan, Y. Zhang, Y. Huang, J. Rogers, “Compliant and stretchable thermoelectric coils for energy harvesting in miniature flexible devices”, *Science advances* , 2018.

K. Li, X. Cheng, F. Zhu, L. Li, Z. Xie, H. Luan, Z. Wang, Z. Ji, H. Wang, F. Liu, Y. Xue, C. Jiang, X. Feng, L. Li, J.A. Rogers, Y. Huang and Y. Zhang, "A Generic Soft Encapsulation Strategy for Stretchable Electronics", submitted.

H. Zhao, K. Li, M. Han, F. Zhu, A. V. Guaradado, P. Guo, Z. Xie, Y. Park, L. Chen, X. Wang, Y. Yang, H. Luan, C. Liang, H. Wang, Y. Xue, R. D. Schaller, D. Chanda, Y. Huang, Y. Zhang and J. A. Rogers, "Mechanically Guided 3D Self-Assembled Mesostructures on Kirigami Elastomer Substrate", to be submitted.

B.H. Kim, K. Li, et al., "3D Microflyer", to be submitted.

# Table of Contents

# List of Tables

# List of Figures

CHAPTER 1

# Introduction

The purpose of the chapter is to present the motivation for the research activities on 3D assembly, and to provide a general background about flexible and stretchable electronics.

## 1.1. Methods for forming 3D mesostructures

The methods for forming 3D micro- and nanostructures in advanced materials is developing rapidly, because of their potential for creating material systems with fundamentally new characteristics and functionalities. These "metamaterials" can have some novel properties that do not occur naturally such as negative refractive index [**153**] and artificial magnetism [**131**]. Some latest progress in methods for fabricating 3D mesostructures are introduced.

### 1.1.1. Nozzle-based 3D printing

3D printing techniques represent some of the most broadly recognized developments in the field of formation of 3D mesostructures. The most widely used method relies on the robotic control of scanning deposition nozzles that print the 3D structures layer-by-layer [**124, 102, 18, 163, 180**]. The printing materials are typically formulated from particulate or polymeric species. These techniques can be further divided in to two groups depending on the properties of the inks and the nature of the delivery process: inkject printing and microextrusion printing. Inkject printing, which uses liquid links as printing materials, is also known as the drop-on-demand printing, that uses thermal or acoustic process to exploits nozzles and deliver liquid droplets to desired locations [**124, 102, 29, 147, 200**]. Microextrusion printing uses viscoelastic inks and offers great possibilities in 3D structuring. Recent research interests in this area are in conductive and biomaterial inks because of their promising foreseen in key applications such as solid-state lighting, wearable devices, tissue scafolds and regenerative medicine.

### 1.1.2. Light-based 3D writing

3D writing techniques reply on patterned exposure of materials to light, that usually involve locally induced two- or multiphoton polymerization [**27, 30, 119, 118, 173**], UV photocuring [**227, 60, 172**] or selective melting [**93**].

The two-photon lithography approach uses specially formulated photopolymers that absorb two photons, typically in the infrared region of the spectrum. As the focused laser beam scans laterally in the photopolymer and the stage scans vertically, the point of focus moves in a 3D trajectory under computer control, thereby enabling the fabrication of a desired 3D micro-structure with ultrahigh resolution.

The projection micro-stereolithography (P$\mu$SL) forms complex 3D mesostructures in a layer-by-layer manner based on photopolymerization reactions in resin materials [**237, 172, 236**]. Each layer corresponds to a 2D image of a sectional slice of the desired 3D shape, formed by projection through a spatial light modulator using a demagnifying lens system. Exposure to UV light solidifies the liquid resin to form a thin, solid 2D layer in the geometry of the image. This scheme provides excellent structural diversity and high resolution in micrometer range over areas of several centimeters [**237**].

The continuous liquid interface production method improves the process of P$\mu$SL by eliminating the need to coat the resin after each exposure [**66, 181**].

### 1.1.3. Stress-controlled folding technologies for 3D systems

The stress-controlled folding techniques forms 3D structures from 2D precursor structures, that fully leverage the sophisticated technologies that exist for micro- and nanofabrication, and for materials deposition in the semi-conductor and integrated photonic industries. These approaches include two classes of advanced techniques based on 4D printing and micro- and nano- scale origami.

The 4D printing scheme is based on 3D printing techniques but forms structures that have a bilayer or multilayer heterogeneous design with mismatched strains that follow from external stimulation, for example to water or heat, thereby inducing self-folding or self-rolling into 3D shapes responsively.

The micro- and nano- scale origami scheme utilizes folding deformations that can serve as the basis for origami-inspired assembly at micro- or nanoscales. The origami schemes based on thin-film residual stresses typically rely on strain mismatch between different materials in different layers to induce self-folding. Another strategy involves active materials such as hydrogels [**43, 179, 136**], shape memory polymers [**42, 41, 202**] or shape memory alloys [**51, 110, 34**], liquid crystal elastomers [**196, 198**] or photoactive polmers [**62, 144**] to create spatially non-uniform strains, thereby deforming 2D structures into 3D shapes.

### 1.1.4. Mechanically guided assembly

The mechanically guided 3D assembly approach involves precisely controlled, deterministic 2D-3D transformations [**206**] that expand the range of accessible 3D geometries, while maintaining compatibility with 2D microsystem technologies mentioned above. The process begins with the formation of a thin film 2D precursor on a source wafer or other planar substrate, followed by the release and then precise patterning of regions that establish strong sites of adhesion to a prestretched elastomer substrate upon contact [**206, 211, 229, 212**]. The release of the prestrain induces compressive forces at the bonding sites. The result causes the 2D precursor to geometrically transform into an engineered 3D configuration through spatially dependent deformations and in- and out-of-plane translational and rotational motions. Further advances of this technology will follow from the development of routes such as free-standing, isolated 3D mesostructures after separation from the elastomer substrates, apply active materials such as shape memory polymers for morphable 4D assembled structures, extensively use engineered substrates to further extend the variance, etc. Opportunities also exist in extending these concepts in mechanical assembly from structures with lateral sizes in the nano-scale regime to graphene and other 2D materials.

## 1.2. Flexible electronics

Biology is soft, elastic and curved, but silicon wafers are not. This fundamental mismatch in mechanics and form stimulates the development of flexible electronics which overcome this problem and enable applications that are impossible to achieve with hard, planar integrated circuits that exist today. Creating the next generation of implantable or wearable electronics will require the mechanical flexibility, which is is particularly important for device components that are in direct contact of the skin or soft tissue to minimize the discomfort of worn or attached electronics.

### 1.2.1. Development in structures

Based on the fundamental application of mechanics of thin film materials, some typical structures include wrinkled "wavy" shapes [**25, 78, 69**], the "bridge-island" design [**82, 207, 84, 91, 112**], 2D planar serpentine designs [**82, 207, 104, 59, 199, 231, 235, 215, 32**], and 2D fractal inspired designs [**207, 32**].

### 1.2.2. Development in materials

The biological interface of organic electronics is a relatively recent development, although organic electronics have been intensively studied and developed over the past half-century, as widely used in commercial applications such as photoconductors in photocopying and laser printing, electrochromic films, anticorrosion and antistatic coatings, organic light-emitting diode (OLED) displays and lighting, organic photovoltaic cells (OPVs) and organic thin-film transistors (OTFTs). The process made towards soft implantable and wearable devices relies not only on these advances in conducting and semiconducting polymers, but also on additional biomimetic properties, such as stretchability, self healing and biodegradability.

### 1.2.3. Applications

The increasing attention of flexible and stretchable electronics partly owe to their outstanding mechanical performances that fit well with the purposes of bio-integration [**139, 83, 177, 189, 233, 114**], thereby holding great promise for applications in a wide range of and/or portable electronic devices, such as soft surgical instruments [**26, 80, 187, 221**], "epidermal" health/wellness monitors [**75, 82, 71, 86, 208, 24, 63, 214**], drug delivery and/or therapy systems [**160, 67, 107**], and stretchable power supplies [**207, 223, 165**].

### 1.2.4. Challenge and prospects

Despite the rapid development of flexible electronics, several scientific and engineering challenges need to be overcome before the fully exploration of the benefits of stretchable and flexible electronics in practical bio-integrated devices. First, the current understanding of electronics-biological interfaces are still limited, and further explorations of the theoretical model of this complex system is required. From an engineering viewpoint, one of the biggest challenges is the data analysis, which requires the signal processing and handling of huge amounts of data. Further improvement of long-term environmental stability and mechanical durability of the flexible devices is essential, and the devices should be well protected under the potential damage from outer environment.

The ultimate goal of the bio-integrated flexible electronics is the development of seamless, bidirectional interfaces between humans and machines, overcoming the huge number of challenges from practical applications.

CHAPTER 2

# Mechanical Studies on Three-dimensional (3D) Helical Microstructures Bonded to Elastomers for Stretchable Electronics

## 2.1. Introduction

Stretchable electronics and optoelectronics have been receiving increasing attention, owing to the outstanding mechanical performances that fit well with the purposes of bio-integration [**139, 83, 177, 189, 233, 114**], thereby holding great promise for applications in a wide range of and/or portable electronic devices, such as soft surgical instruments [**26, 80, 187, 221**], "epidermal" health/wellness monitors [**75, 82, 71, 86, 208, 24, 63, 214**], drug delivery and/or therapy systems [**160, 67, 107**], and stretchable power supplies [**207, 223, 165**]. Several classes of materials and mechanics design schemes [**139, 114, 82, 207, 78, 84, 104, 203, 217, 157, 222**] have been proposed to offer high flexibility and stretchability in high-performance, inorganic electronic materials (e.g., single-crystal silicon) that are intrinsically brittle and stiff. Of these schemes, the "island-bridge" design [**82, 207, 84, 91, 112**], in which the functional components reside on non-deformable platforms (i.e. islands) electrically connected by deformable interconnects (i.e. bridges), represents an effective strategy that has been widely adopted in various device systems. Upon stretching, the bridges deform substantially to provide stretchability, while the islands undergo negligible deformation (usually $< 1\%$ strain) to ensure mechanical integrity of the active devices [**207, 84, 162**]. Generally, the stretchability ($\varepsilon^{system}_{stretchability}$) of a system in the square island-bridge configuration with a filling ratio ($f$) can be related to the stretchability of interconnect by $\varepsilon^{system}_{stretchability} = (1 - \sqrt{f})\varepsilon^{interconnect}_{stretchability}$ [**232**]. Hence, the electrical interconnects need to offer an ultra-high level of stretchability (e.g. $\sim 100\%$), so as to insure sufficient stretchability (e.g., $\sim 20\%$) of the island-bridge system, especially for those designs with high fill factors (e.g., $\sim 64\%$) of active devices [**232, 228**]. Lithographically defined interconnects in planar configurations of serpentine, self-similar serpentine, Peano, and other space-filling curves have been devised, and explored both theoretically and experimentally [**82, 207, 104, 59, 199, 231, 235, 215, 32**]. These planar interconnects, when partially bonded or non-bonded to the elastomeric substrate, could offer an extreme level (e.g. $> 300\%$) of stretchability for optimized configurations, because of relatively free deformations via bending and/or twisting to reduce the strain energy. However, exposure of these interconnects to the outside environment can lead to damage of these structures or of adjacent materials by physical contact [**82, 235**]. Encapsulation provides a solution, but the motions of the interconnects will be highly constrained if solid encapsulants (e.g., Ecoflex, PDMS) are used [**81**]. As such, the resulting stretchability of these encapsulated interconnects are generally not sufficient for many practical applications that demand large filling ratios for device miniaturization. For example, a representative class of planar interconnects, even with optimized, designs, could offer elastic stretchability just up to $\sim 60\%$ when encapsulated by an ultra-soft silicone elastomer (e.g., $\sim 3$ kPa), as to be shown in present study. This yields elastic stretchability below $\sim 12\%$ for the system with $\sim 64\%$ filling ratio, which might fall short for some of the most demanding biomedical applications, where the strains (e.g. skin, heart, or elbo) may exceed 20%.

This chapter proposes to exploit a class of three-dimensional (3D) helical interconnects that can offer the elastic stretchability up to > 130% in the encapsulated conditions, thereby fitting well with the biomedical applications mentioned above. This type of 3D interconnects can be assembled from ultra-thin 2D serpentine ribbons, by using a controlled buckling approach [**206, 229**], that relies on a prestretched elastomeric substrate to transfer compressive forces to the ribbons at well-defined sites. A powerful aspect of this assembly approach is the versatility in the applicable materials, ranging from brittle inorganic semiconductors to plastic metals and polymers, and length scales, ranging from sub-microns to several decimeters. In addition, this assembly approach is fully compatible with the state-of-art semi-conductor technologies [**206**], as well as most of the techniques exploited in achieving stretchable electronic systems [**139**], thereby holding great potential in applications in forming 3D stretchable electronics. Here, a systematic study on the elastic stretchability of the helical interconnects formed with the above approach was carried out, via combined finite element analysis (FEA) and experiments (done by Prof. Rogers group), for both the encapsulated and partially bonded conditions. The results show quantitatively the advantage of helical interconnects over the conventional 2D serpentine interconnects, in terms of the elastic stretchability, over a broad range of conditions. Furthermore, this study elucidates the effects of various fabrication parameters on the elastic stretchability, revealing both monotonous dependences (e.g., on the moduli of substrate and encapsulation) and non-monotonous dependences (e.g., on the prestrain of substrate and the thickness of metal layer). These results could serve as guidelines for design optimization of this new class of 3D helical interconnects for applications in functional stretchable devices.

## 2.2. Results and Discussion

### 2.2.1. High Elastic Stretchability of 3D Helical Interconnects in the Encapsulated Conditions

A schematic illustration of the fabrication process of encapsualted helical interconnects appears in Figure 2.1a in the page 35.The 2D precursor with a filamentary serpentine configuration that consists of two identical arcs (with central arc angle $\theta_0$) in a unit cell was trasfer printed onto a pre-stretched elastomeric substrate (Dragon skin, Smooth-on, Inc, 166 kPa), in a matter that certain desired sites (red in Figure 2.1a) have strong covalent bonding while the other regions have weak van der Waals interactions. Release of prestrains ($\varepsilon_{prestrain}$) in the substrate triggers compressive buckling in the 2D precursor, transforming it into 3D helical configurations that results from energy minimization of spatially varying deformation. The helical mesostructure remains tethered to the elastomeric substrate after the assembly process, which can be utilized directly as a freely-deforming interconnect to offer an ultra-high stretchability ($> \varepsilon_{prestrain}$). To provide a mechanical protection from surrounding environment, a class of ultra-soft silicone [**63, 64**], with the modulus in the range of 1 kPa $-$ 20 kPa, can be adopted to encapsulate the helical interconnects. The interconnects usually exploits metal and polyimide (PI) in a multi-layer configuration of PI/metal/PI, which maintains the metal layer at the neutral mechanical plane to reduce the strain, as shown in Figure 2.1b. Optical microscope images of three traces of helical interconnects appear in Figure 2.1c, and the geometric details are highlighted in Figure 2.1d with scanning electron microscope (SEM) images and corresponding FEA predictions from two different view angles. Here, the interconnect is 50 $\mu$m wide, and uses a sandwich construction of 4.0 $\mu$m PI/0.4 $\mu$m Nickel (Ni)/4.0 $\mu$m PI.The other geometric parameters of the 2D serpentine precursor include central arc angle $\theta_0 = 180°$ and arc radius $R = 425$ $\mu$m, yielding a total wire length of $l_{total} = 10.68$ mm, as shown in Figure 2.2.

To analyze the mechanical performances of encapsulated helical interconnects, we employed 3D FEA to analyze the deformation and strain distribution of the system under uniaxial stretching. The elastic stretchability is determined based on the criterion when the Mises stress of metal layer exceeds the yield strength ($\sim$ 600 MPa for Ni, correspond to $\sim$ 0.3% yield strain) at 1/4 width of any certain section of the wire shaped interconnect. The PI has yield and fracture strain ($> 8\%$) that are much larger than those for the metal ($\sim$ 0.3%) [**113**], such that the elastic stretchability is limited by the metal layer. Similar criterion has been validated by previous experimental studies [**228, 32**] using both cyclic mechanical testing and four-probe electrical measurement. A representative set of helical interconnects formed with the same 2D precursor as that in Figure 2.1d, and the prestrain ranging from 0% to 350%, was analyzed, and the corresponding configurations are shown in Figure 2.2.

For the purpose of comparison, we studied a set of 2D serpentine interconnects with the same material composition (PI/Ni/PI), and the same key geometric parameters, including the width ($w$), the thickness ($t_{metal}$ and $t_{PI}$), the span ($S$), and the amplitude

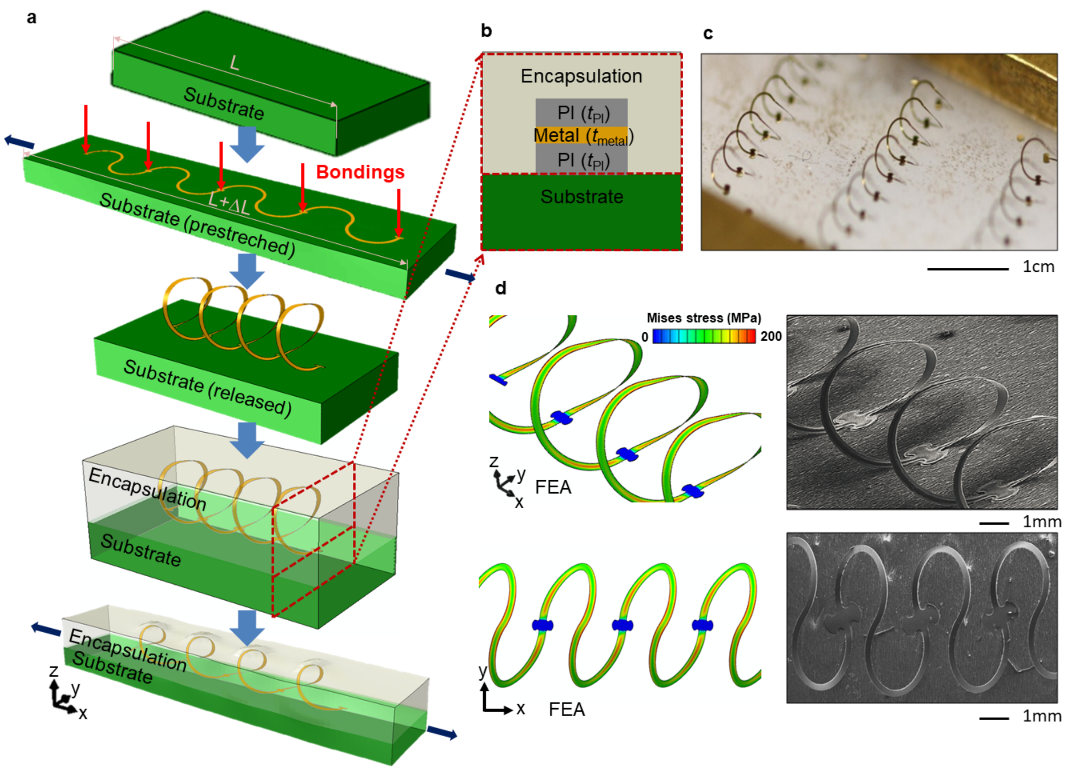


Figure 2.1. Device construction and mechanics under deformation. (a) Schematic illustration of the prestrain strategy for fabricating 3D helical interconnects; (b) Cross-sectional view of encapsulated 3D helical interconnects; (c) SEM image of the 3D helical interconnect arrays and FEM result; (d) FEM and SEM image of 3D helical interconnect, with perspective and top views.

($A = 0.9$ mm). The number of unit cells is fixed as 5 for these 2D serpentine interconnects, so as to yield a range [9.36 mm, 11.09 mm] of total length ($l_{total}$) that is close to the counterpart (10.68 mm) of 3D helical interconnects. Previous studies [**228, 32**], demonstrated that the 2D serpentine interconnects, when fully bonded to the substrate, exhibit different deformation modes, such as local winkling and global buckling. For 2D serpentine interconnects with sufficiently large thicknesses (e.g. comparable to the width),

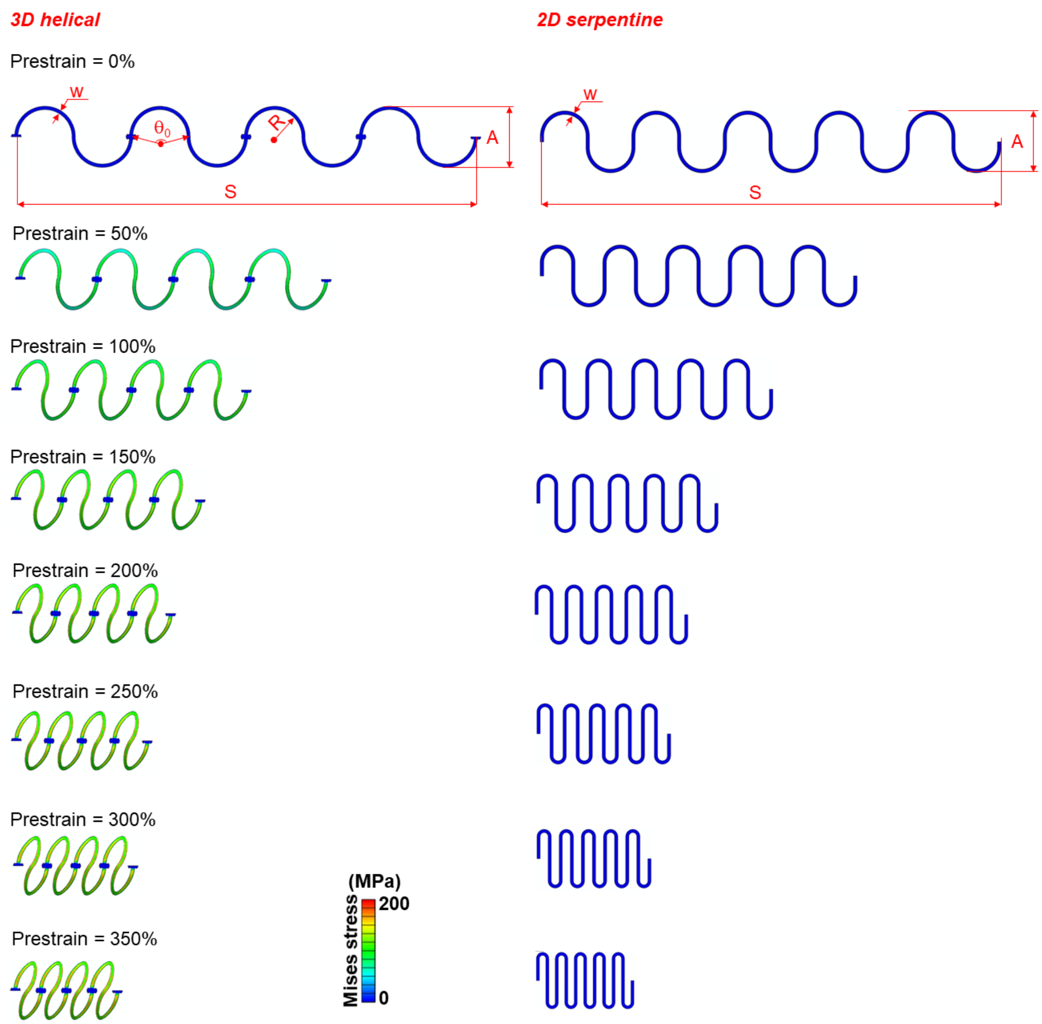


Figure 2.2. Schematic illustration of configuration for 3D helical and 2D serpentine interconnects. Configuration and Mises stress distribution of buckled-up 3D helical interconnect and 2D serpentine interconnect, with prestrain 0% (precursor), 50%, 100%, 150%, 200%, 250%, 300%, 350% respectively. Illustration of geometric parameters are shown in 2D precursor (prestrain=0%).

they undergo non-buckling deformations mainly in terms of bending. This offers another effective means to enhancement of elastic stretchability, via a mechanism that weakens the effect of mechanical constraint from the substrate by stiffening the interconnects with larger thicknesses. To provide a thorough comparison between 3D helical and 2D serpentine interconnects, we took into account an additional set of serpentine interconnects with the same in-plane dimensions and a much larger thickness ($t_{Ni}$ = 50 $\mu$m) to yield the non-buckling mode.

Figure 2.3a shows the elastic stretchability of 3D helical interconnects formed with different levels of prestrain, in comparison to those 2D serpentine interconnects under two different deformation modes (local winkling and non-buckling). The elastic stretchability of helical interconnects increase from 13% at $\varepsilon_{prestrain} = 0\%$ to $\sim$ 131% (corresponding to a peak) at $\varepsilon_{prestrain} = 200\%$, and then decreases slightly with a further increase of prestrain. This slight decrease of elastic stretchability can be mainly attributed to the increased shear deformation at a higher prestrain that leads to the formation of a knot-like structure at the top part of the helical interconnect in the front view of the deformed configurations (Figure 2.4a). Such knot-like structure can be hardly unraveled to provide stretchability due to the constraint of surrounding elastomer, as evidenced by the deformed configurations of helical interconnect with 250% prestrain configurations (Figure 2.4a). In contrast, the interconnect formed with 100% prestrain in which such knot-like structure does not appear, can be unraveled more uniformly (Figure 2.4a). Over the entire range of prestrain, the helical interconnects outperforms the thin serpentine interconnects (with local wrinkling mode), typically by a factor $> 2.3$ for representative prestrains ($> 100\%$). As compared to the thick serpentine interconnects (with non-buckling mode) that results in better mechanics than the thin counterparts, the 3D helical interconnects with a sufficient prestrain (e.g. $> 100\%$) still exhibit a considerable enhancement (e.g. $> 1.8$ times) in the elastic stretchability.

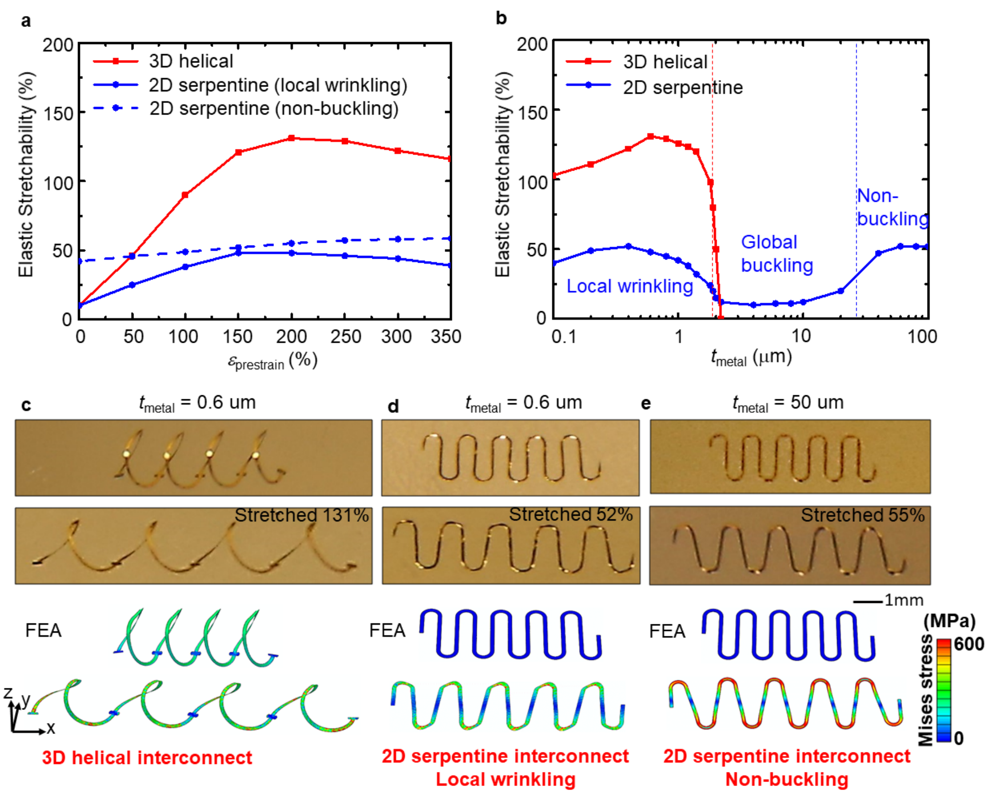


Figure 2.3. Numerical analyses and experimental verification. (a) Influence of prestrain ($t_{Ni} = 0.4$ $\mu$m for 3D helix and 2D serpentine buckling mode 1, and $t_{Ni} = 50$ $\mu$m for 2D serpentine non-buckling mode); (b) Influence of Metal thickness ($\varepsilon_{prestrain} = 200\%$); SEM and FEM perspective view image of (c) 3D helical coil, (d) 2D planar serpentine buckling mode 1 and (e) 2D planar serpentine non-buckling mode, with unstretched and stretched configuration.

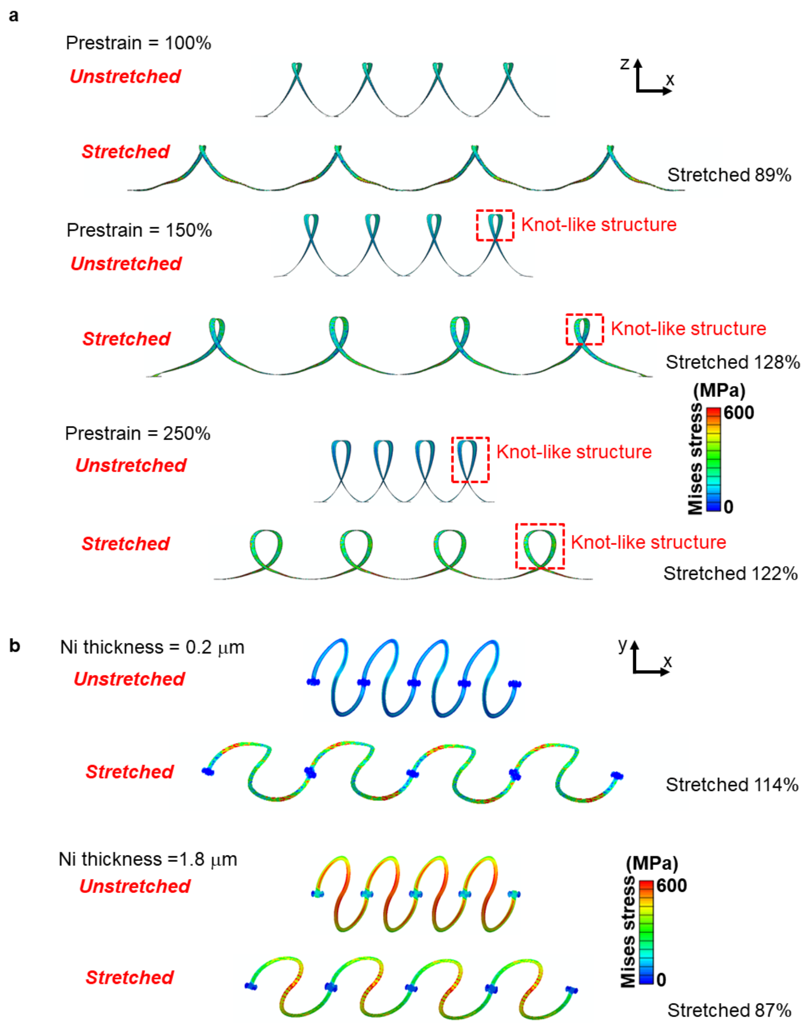


Figure 2.4. Numerical analysis of prestrain effect and metal thickness effect. Influence of (a) prestrain ($t_{metal}$=0.6 $\mu$m, $t_{PI}$=6.0 $\mu$m, $E_{encapsulation}$=3 kPa, $E_{substrate}$=20 kPa), (b) metal thickness ($\varepsilon_{prestrain}$=200%, $E_{encapsulation}$ = 3 kPa, $E_{substrate}$=20 kPa) on stretchability and stretched configuration with Mises stress distribution.

Since the metal thickness of the interconnects plays a significant role in the elastic stertchability, we then fix the overall geometries of 3D helical and 2D serpentine interconnects, and compare their stretching limits over a wide range of metal thicknesses ($t_{Ni}$). A represent set of FEA results appears in Figure 2.3b for the interconnects formed with $\varepsilon_{prestrain} = 200\%$, and $t_{Ni}$ varying in the range of 0.1 $\mu$m to 100 $\mu$m. With the increase of metal thickness, the elastic stretchability of helical interconnect increases initially to reach its maximum ($\sim$ 131%) at $t_{Ni}$=0.6 $\mu$m, and then decrases as $t_{Ni}$ keeps increasing. Such decrease can be attributed to the shift of failure point before and after the peak point, as shown in Figure 2.4b. As the metal thickness increases to a critical value ($t_{Ni,critical}$), the plastic yield occurs associated with the buckling deformation during the assembly process of the helical interconnect, thereby indicating no capability of accomodating any additional stretching in a reversible manner (corresponding to zero elastic stretchabiilty). Differently, with the change of metal thickness, the serpentine interconnect exhibit three types of deformation modes, namely, local wrinkling, global buckling and non-buckling modes [**228, 32**]. The transition between different modes leads to a non-monotonous variation of elastic stretchability, as shown in Figure 2.3b. For the mode of local wrinkling, a local maximum ($\sim$ 52% stretchability) appears at $t_{Ni}$=0.4 $\mu$m. For the mode of non-buckling, the elastic stretchability increases slightly with increasing the thickness, and approaches an ideal limit ($\sim$ 52% stretchability) without any out-of-plane deformations. Thereby, with the corresponding optimized metal thicknesses, the 3D helical interconnect still offer a much larger elastic stretchability ($\sim$ 131%) than that ($\sim$ 52%) of 2D serpentine interconnects.

The configurations of a representative 3D helical interconnect (with $\varepsilon_{prestrain}$=200% and $t_{Ni}$=0.6 $\mu$m) before and after stretching ($\sim$ 131%) are shown in Figure 2.3c. Similar results appear in Figure 2.3d,e for the 2D serpentine interconnects with $t_{Ni}$=0.6 $\mu$m and 50 $\mu$m, which exhibit the mode of local wrinkling and non-buckling, respectively. For all of the three different designs, good agreements of the deformed configurations can be observed between FEA predictions and optical images. After this set of validation, the numerical methods are used in the subsequent section to study the stretchability enhancement of helical interconnects over the serpentine interconnects under various fabrication parameters.

### 2.2.2. Effect of Fabrication Parameters on the Elastic Stretchabiity of Encapsulated 3D Helical Interconnects

This section summarizes the effects of key fabrication parameters on the performances of encapsulated 3D helical interconnect. In general, the elastic stretchabiilty of encapsulated 3D helical configurations is mainly affected by three groups of fabrication parameters: 1) material parameters ($E_{encapsulation}$, $E_{subsgtrate}$ and $E_{metal}$, for the materials of encapsulation, substrate and metal); 2) loading parameter ($\varepsilon_{prestrain}$); 3) geometric parameters ($w/R$, $t_{metal}/R$, $t_{PI}/R$ and $\theta_0$). To simplify the analyses, the arc radius of helical interconnects is kept unchanged as 425 $\mu$m in the following calculations. To demonstrate quantitatively the advantage of helical interconnects, the corresponding serpentine interconnects selected based on the consideration illustrated in Section 2 are analyzed as well for comparison.

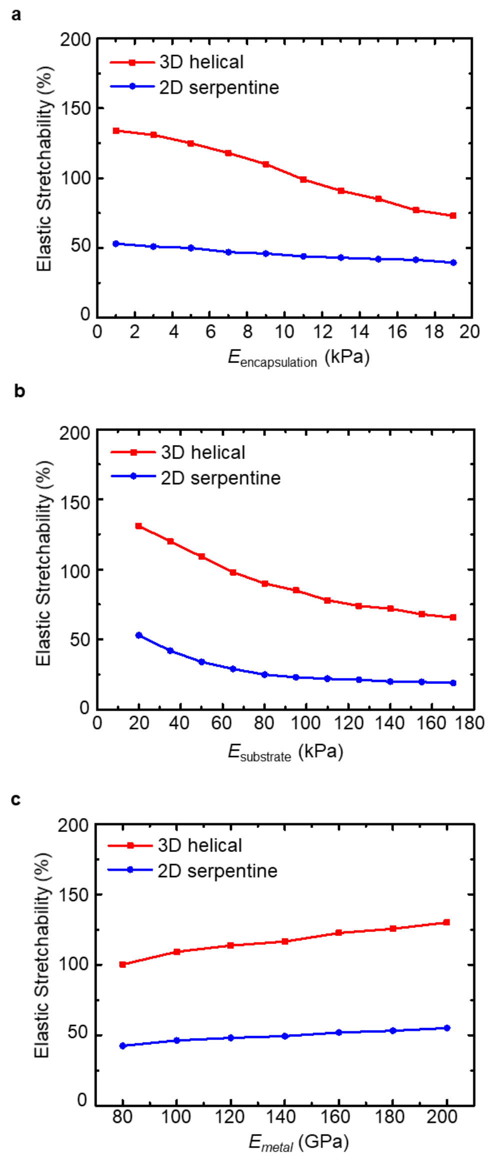


Figure 2.5. Numerical analyses of modulus effect. Influence of (a) encapsulation modulus, (b) substrate modulus and (c) metal modulus on stretchability, with 3D helix and 2D serpentine comparison ($\varepsilon_{prestrain} = 200\%$, $t_{Ni} = 0.6$ $\mu$m).

Figure 2.5 illustrates the effects of Young's moduli ($E$) of the encapsulation, substrate and metal layer on the elastic stretchability. Here, the prestrain and geometric parameters are fixed as $\varepsilon_{prestrain}$=200%, $\theta_0 = 180°$, $w = 50$ $\mu$m, $t_{metal} = 0.4$ $\mu$m, and $t_{PI} = 4.0$ $\mu$m. For both the helical and serpentine interconnects, the elastic stretchability increases as the Young's moduli of encapsulation or substrate decreases, or as that of metal layer increases. In comparison to serpentine interconnects, the elastic stretchability of helical interconnects are more sensitive to the change of encapsulation, partially because of the 3D configuration. For all of the designs considered here, the helical interconnects always outperform the serpentine ones in the elastic stretchability, typically by a factor between 1.8 and 3.7. The results highlight a considerable enhancement (¿3.2 times) in the case of relatively stiff substrate (e.g. $E_{substrate} > 50$ kPa), which results from a comparatively lower constraint of substrate on the helical interconnects than the serpentine ones.

As mentioned in Section 2.2.1, the elastic stretchability of 3D helical interconnects shows a non-monotonous dependence on the prestrain, and thereby an optimal prestrain that maximizes the elastic stretchability might exist. The decrease of elastic stretchability at the high-prestrain regime can be mainly attributed to the appearance of a knot-like strucutre (at the top part of the helical interconnect) that is difficult to unravel. This effect is essentially dependent on the stiffness of encapsulation as shown by the results of FIgure 2.6a. Except for the case of $E_{encapsulation}$=0 kPa (corresponding to a micro-fluid encapsulation), an optimal prestrain always exist, which shifts from $\sim 150\%$ to $\sim 250\%$, as $E_{encapsulation}$ decreases from 19 kPa to 1 kPa. Similar to the effect of prestrain, the helical configuration formed with a higher central arc angle ($\theta_0$) also exhibits a larger knot-like structure at the top part of the interconnect from the front view (Figure 2.7). Thereby, the dependence of elastic stretchability on the central arc angle shows a similar trend to that of prestrain, as shown in Figure 2.6b, suggesting the existence of an optimal arc angle that offers the highest stretchability. Such optimal arc angle also shifts from 165° to 195° with $E_{encapsulation}$ decreasing from 19 kPa to 1 kPa, for 200% prestrain used in the assembly.

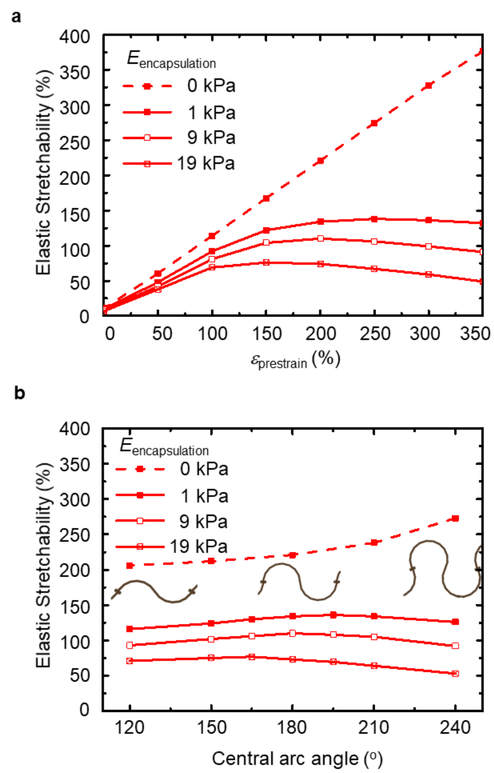


Figure 2.6. Numerical analyses of optimal stretchability. Influence of encapsulation modulus on optimal stretchability of (a) different prestrains and (b) different central arc angles.

The interconnect thickness, include both $t_{metal}$ and $t_{PI}$ are taken into account to provide a deeper insight into such effect, for both helical and serpentine interconnects (with $E_{encapsulation} = 3$ kPa, $E_{substrate} = 20$ kPa, $\varepsilon_{prestrain} = 200\%$, $w = 50$ $\mu$m and $\theta_0 = 180°$). Relative thin interconnct configurations are adopted for the serpentine interconnect to illustrate the design optimization under local wrinkling mode. The contours of elastic

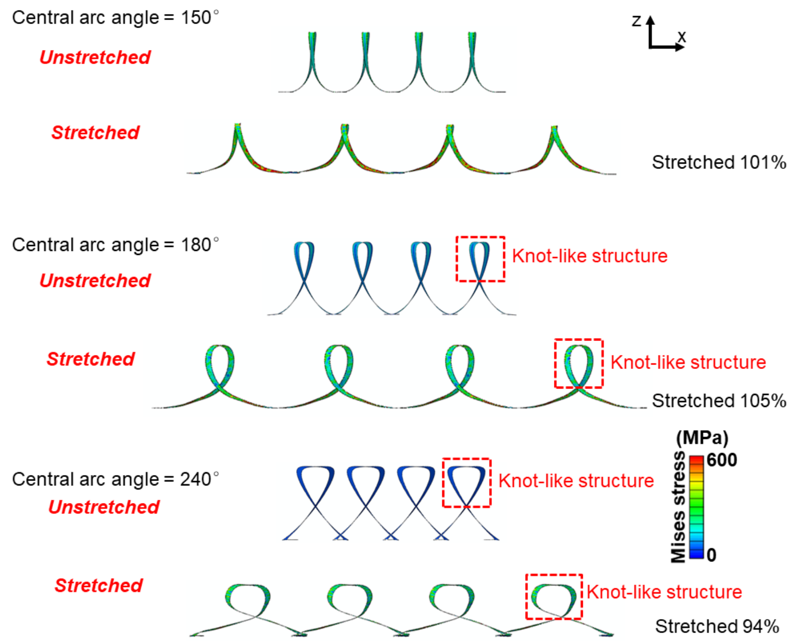


Figure 2.7. Numerical analysis of central arc angle effect ($\varepsilon_{prestrain}$=200%, $t_{metal}$=0.6 $\mu$m, $t_{PI}$=6.0 $\mu$m, $E_{encapsulation}$=3 kPa, $E_{substrate}$=20 kPa).

stretchability among various thicknesses of metal ad PI layers appear in Figure 2.8 for two different types of interconnects. The elastic stretchability reaches its maximum ($\sim$ 131%) at the design point ($t_{Ni}$ = 0.4 $\mu$m and $t_{PI}$ = 4.0 $\mu$m) for the helical interconnects. In comparison, the maximum ($\sim$ 53%) of serpentine interconnects is much lower, which occurs at the design point ($t_{Ni}$ = 0.6 $\mu$m and $t_{PI}$ = 2.5 $\mu$m). Figure 2.9 shows that the elastic stretchability of helical interconnect is not so sensitive to the width ($w$) as compared to the thickness.

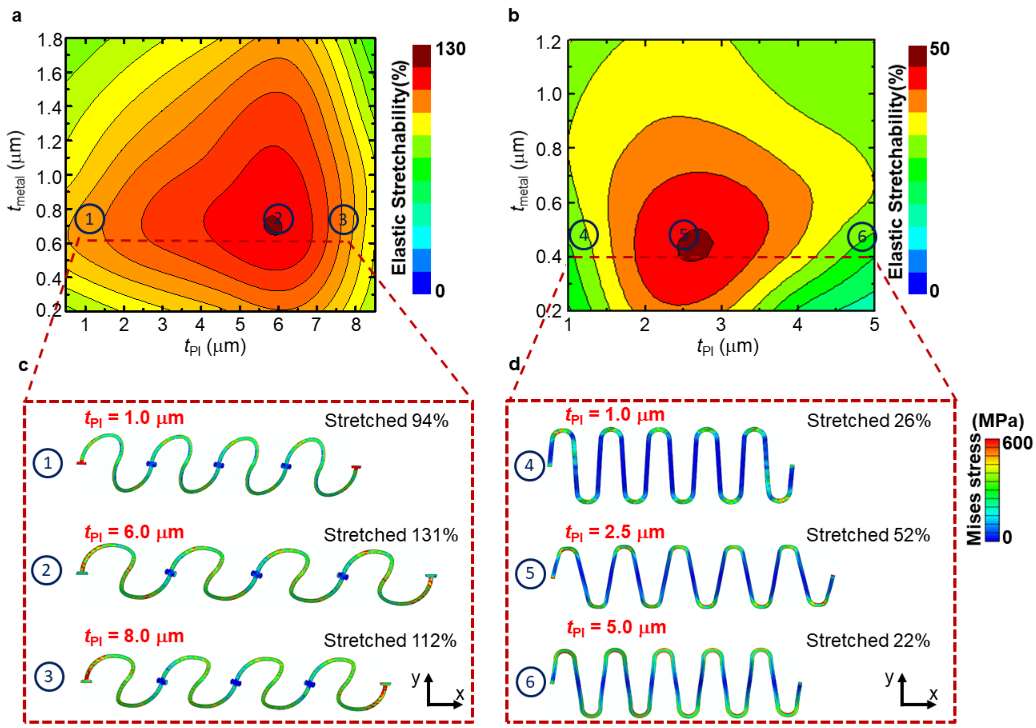


Figure 2.8. Numerical analyses of metal and PI layer thickness effect. Stretchability contour of $t_{Ni}$ and $t_{PI}$ for (a) 3D helical interconnect and (b) 2D serpentine interconnect ($\varepsilon_{prestrain} = 200\%$); (c) FEA results for the Mises stress distribution in 3D helical interconnect when stretched to the predicted total stretchability, with same $t_{Ni}$ (0.4 $\mu$m) but different $t_{PI}$ (1.0 $\mu$m, 6.0 $\mu$m and 8.0 $\mu$m seperately); (d) FEA results for the Mises stress distribution in 2D planar serpentine interconnect when stretched to the predicted total stretchability, with same $t_{Ni}$ (0.4 $\mu$m) but different $t_{PI}$ (1.0 $\mu$m, 2.5 $\mu$m and 5.0 $\mu$m separately).

### 2.2.3. Elastic Stretchability of 3D Helical Interconnects Encapsulated by Microfluid

Section 2.2.2 demonstrates that the 3D helical interconnects, even when encapsulated with elastomer with modulus low to 1 kPa, still offer an elastic stretchability much lower

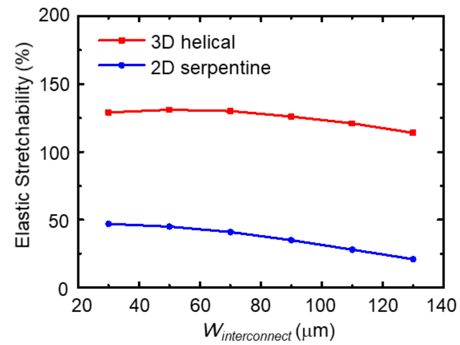


Figure 2.9. Numerical analysis of interconnect width effect ($\varepsilon_{prestrain}$=200%, $t_{metal}$=0.6 $\mu$m, $t_{PI}$=6.0 $\mu$m, $E_{encapsulation}$=3 kPa, $E_{substrate}$=20 kPa).

than the ideal limit (with $E_{encapsulation}$=0 kPa). In order to achieve a better mechanical performance under the encapsulated condition, the micro-fluids, such as uncured PDMS prepolymer (viscous liquid) [**81**] and the gels electrolyte [**207**], can be used. In this condition, the 3D helical interconnects can be always stretched to the initial 2D configuration, with causing any mechanical failure. The resulting elastic stretchability is essentially the same as that of unencapsulated interconnects. Here, we still analyze the corresponding serpentine interconnects selected based on the consideration illustrated in Section 2.2.1 for comparison.

A schematic illustration of unencapsulated interconnects appears in Figure 2.10a, in which both the helical and serpentine interconnects are bonded onto the substrate (20 kPa) at the istes highlighted red. Figure 2.10b,c shows the optical images and FEA predictions of two representative interconnects before and after stretching by corresponding elastic stretchabilities (226% for the helical interconnect and 117% for the serpentine

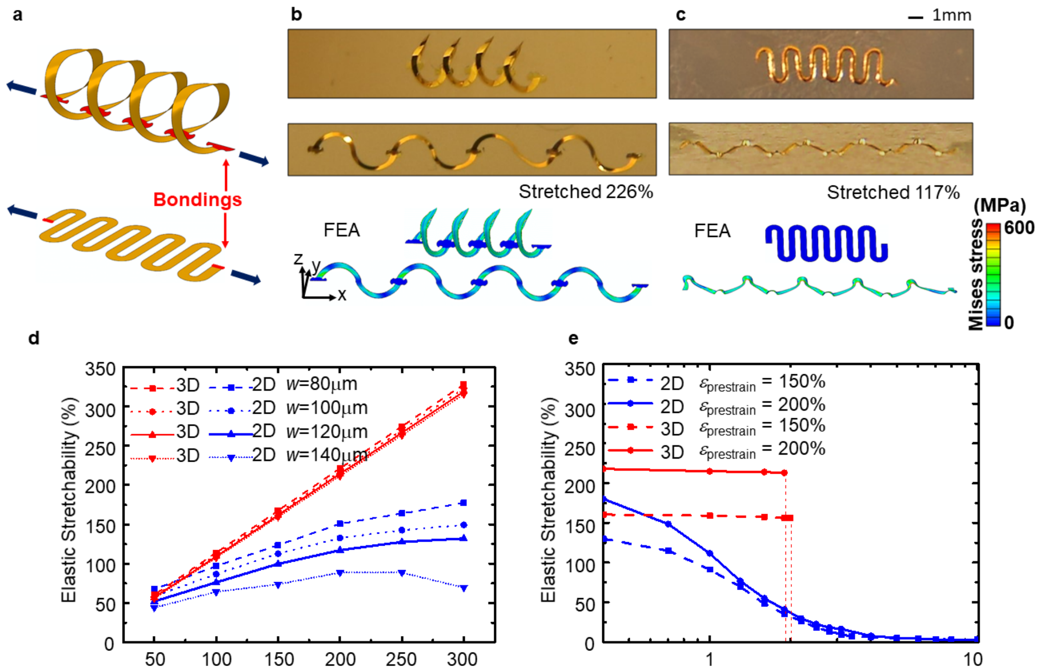


Figure 2.10. Numerical analyses of micro-fluid encapsulated devices and experimental verification. (a) Schematic illusion of micro-fluid encapsulated 3D helical interconnect and 2D serpentine interconnect; SEM and FEM image of micro-fluid encapsulated (b) 3D helical and (c) 2D serpentine interconnect, with unstretched and stretched configuration; (d) Influence of prestrain on stretchability for micro-fluid encapsulated 3D helical and 2D serpentine interconnect, with different width (80 $\mu$m, 100 $\mu$m, 120 $\mu$m, and 140 $\mu$m). (e) Influence of $t_{Ni}$ on stretchability for micro-fluid encapsulated 3D helical and 2D serpentine interconnect, with different prestrains (150% and 200%).

interconnect). The geometric parameters include the width ($w$ = 120 $\mu$m), the thickness ($t_{metal}$=0.6 $\mu$m and $t_{PI}$=2.5 $\mu$m), the span ($S$ = 2.27 $\mu$m), and the amplitude ($A$ = 0.97 mm). With a similar total wire length, the maximum curvature of the helical interconnect is obviously small than that of serpentine interconnect, because of the 3D geometry. As such, the helical interconnect offers a better performance in the elastic stretchability. Figure 2.10d illustrates the effect of prestrain on the elastic stretchabilities of both unencapsulated helical and serpentine interconnects, with four different widths (80 $\mu$m, 100 $\mu$m, 120 $\mu$m and 140 $\mu$m). For the 3D helical interconnect, the elastic stretchability increases almost in a linear manner with the prestrain ($\varepsilon_{prestrain}$) increasing, which is very insensitive to the change of interconnect width ($w$). For the 2D serpentine interconnect, the elastic stretchability decreases considerably with the increase of interconnect width. This suggests an advantage of using relatively wide helical interconnects for better electrical performances (i.e., conductivity). This is evidenced by the huge difference (e.g., 3.53 times for $\varepsilon_{prestrain}$=250% and 5.65 times for $\varepsilon_{prestrain}$=300%) of elastic stretchability for $w$=140 $\mu$m.

Similar to the interconnects encapsulated by solids, the thickness of interconnct also plays a significant role in the elastic stretchabiity of interconnects encapsulated by microfluids. Figure 2.10e elucidates such effect for the helical interconnects formed with prestrains of 150% and 200% (with $w$=120 $\mu$m). For the 3D helical interconnects, the stretchability decreases slightly with $t_{metal}$ increases, but as $t_{metal}$ reaches a critical value, the stretchability drops suddenly to zero, because the plastic yield will occur in the helical interconnects during the 3D assembly process. Below this critical thickness, the elastic stretchability of helical interconnects is much higher than the counterpart of serpentine interconnects, typically with a factor of 1.3 to 5.5.

## 2.3. Conclusion

This chapter exploits the mechanical properties for a class of three-dimensional (3D) helical interconnects that can be assembled from ultra-thin 2D serpentine ribbons by using the compressive buckling process induced by the released strain of a prestretched elastomeric substrate, on which the 2D precursor is selectively bonded. The 3D helical interconnect can offer a stretchability up tp $\sim 131\%$ in the solid encapsulated conditions, that can provides outstanding mechanical compliance to fit well with the biomedical applications as mentioned in the beginning of this chapter. The results present promising advantage in stretchability of 3D helical interconnects over the conventional 2D serpentine interconnects, over a broad range of fabrication parameters such as moduli of substrate and encapsulation, prestrain of substrate and thickness of metal and PI layer. These results could serve as guidelines for the future design and optimization of this new class of 3D helical interconnects applied in the functional stretchable devices.

CHAPTER 3

# A Generic Two-stage Encapsulation Strategy for Soft Electronics

Recent progress in stretchable forms of inorganic electronic systems has established a route to new classes of devices, with particularly unique capabilities in functional bio-interfaces, because of their mechanical and geometrical compatability with human tissues and organs. A reliable approach to physically and chemically protect the electronic components and interconnects is indispensable for practical applications, since a direct exposure to the environment could lead to failure or damage of fragile elements. Although recent reports describe various options in soft, solid encapsulation, the development of approaches that do not significantly reduce the stretchability remains an area of continued focus. Here, we reported a generic, soft encapsulation strategy that is applicable to a wide range of stretchable interconnect designs, including those based on two-dimensional (2D) serpentine configurations, 2D fractal-inspired patterns, and 3D helical configurations. This strategy forms the encapsulation while the system is in a pre-strained state, in contrast to the traditional approach that involves the strain-free configuration, followed by release of the pre-strain to complete the process. Combined theoretical modeling and experimental measurements highlight the deformation mechanisms of the interconnects encapsulated using both the proposed and the traditional strategy. A systematic comparison reveals that substantial enhancements (e.g., $\sim$ 6.0 times for 2D serpentine, $\sim$ 4.0 times for 2D fractal and $\sim$ 2.6 times for 3D helical) in the stretchability can be achieved through use of the proposed strategy. Demonstrated applications in highly-stretchable light-emitting diodes (LEDs) systems that can be mounted onto complex curvilinear surfaces illustrate the general capabilities in functional device systems.

### 3.1. Introduction

Rapid development of the technologies of stretchable electronics has enabled a diversity of mechanically-compliant bio-interfaces between rigid inorganic electronic components and soft biological tissues [**75, 77, 78, 82, 99, 123, 126, 127, 150, 149, 160, 165, 166, 174, 191, 204, 239, 57, 105, 161, 11**], as a means to monitor health conditions and to execute certain therapies [**94, 137, 139, 159, 58, 115, 74, 39, 7, 31, 36**]. A majority of previous studies in this area focused on the development of materials designs and mechanics concepts to achieve a high degree of deformability, while maintaining high-performance functionality [**22, 72, 108, 129, 151, 164, 193, 195, 216, 218, 69, 176, 228, 214, 109, 40, 192**]. A reliable scheme for encapsulating stretchable electronics platforms is essential for practical applications, since a direct physical contact with the outside environment could result in failure of fragile device components and/or interconnects [**82, 188**]. Despite the importance, relatively few studies focus on the development of encapsulation strategies with enhanced performance or robustness. Most approaches simply involve the application of soft elastomer encapsulants as a final step in the fabrication process [**70, 167, 169, 205, 63**]. For example, Vanfleteren's group [**13, 44, 53, 145**] studied extensively the deformation behaviors and failure mechanisms of planar serpentine-shaped conductors encapsulated with polymers. For stretchable metallic interconnects with different bonding conditions (e.g., fully or partially bonded to the substrates), the solid encapsulant typically leads to a pronounced reduction in the elastic stretchability, due to constraints on the out-of-plane motions of the interconnects. Liquid encapsulation schemes [**207, 208**] avoid this limitation, but they introduce leakage as a possible failure mode. Development of a generic solid encapsulation strategy that does not sacrifice stretchability remains a challenge.

Here, we report a two-stage sequence for introducing solid encapsulation materials on stretchable electronic systems, with wide applicability across the most advanced interconnect configurations, including three-dimensional (3D) helical coils [**38, 65, 79, 112, 206**], two-dimensional (2D) serpentine [**52, 54, 84, 95, 97, 104, 19, 73**] and 2D fractal-inspired shapes [**207, 32**]. This strategy forms the solid encapsulation while the electronic system is in a pre-stretched state, instead of the load-free state adopted in conventional strategies. Release of the pre-stretch after application of the encapsulation completes the process. In this manner, the constraints of the solid encapsulant on the interconnect deformations that occur under external loading can be relieved substantially, as demonstrated by both experiments and mechanics modeling. Quantitative studies based on finite element analysis (FEA) illustrate methods to optimize this two-stage encapsulating process to maximum the stretchability. By comparison to the conventional one-stage encapsulation strategy, this two-stage process increases the elastic stretchability, e.g., by factors of ∼2.6 for 3D helical interconnects, ∼6.0 for 2D serpentine interconnects, and ∼4.0 for 2D fractal interconnects. Highly stretchable collections of light-emitting diodes (LEDs) that be mounted onto complex curvilinear surfaces serve application examples.

## 3.2. Results and Discussion

### 3.2.1. A two-stage soft encapsulation strategy

Figure 3.1&3.2 presents a schematic illustration of a generic two-stage encapsulating process for stretchable electronics constructed with either 3D helical interconnects or 2D serpentine interconnects. Here, the coil interconnects with 3D helical configurations form via mechanically-guided assembly techniques, as reported in recent years [**65, 206, 229, 230**]. The example in Figure 3.1 used a uniaxial pre-strain ($\varepsilon_{prestrain}$=150%) in the elastomeric substrate (E=20 kPa; Ecoflex 00-30A/B, Smooth-on, USA), which drives the transformation of ultra-thin 2D precursors into 3D helical interconnects. During the first stage of the 2-stage encapsulating process, the substrate is pre-stretched to an encapsulating strain ($\varepsilon_{encap}$), at which the soft encapsulation layer (E = 3 kPa; Silbione 4717A/B, Bluestar Silicones, France) is added. In the second stage, the substrate is fully released to complete the encapsulation. In contrast, the conventional 1-stage encapsulating process form the solid encapsulation when the system is in a load-free state, without applying any pre-stretch (Figure 3.3). Note that the 2D serpentine interconnects are selectively bonded to the substrate at the two ends before the encapsulation, such that the pre-stretch leads to a buckled 3D configuration through controlled bending and twisting deformations.

Figure 3.4a and Figure 3.5a show the deformed configurations with Mises stress distributions for 3D helical and 2D serpentine interconnects stretched to the corresponding elastic limits, in which both the 1-stage and 2-stage encapsulating processes are taken into account. In both cases, the interconnects consist of polyimide (PI) / metal / polyimide (PI) multilayers, where PI layers (1.4 $\mu$m) serve as supports to mechanically protect the

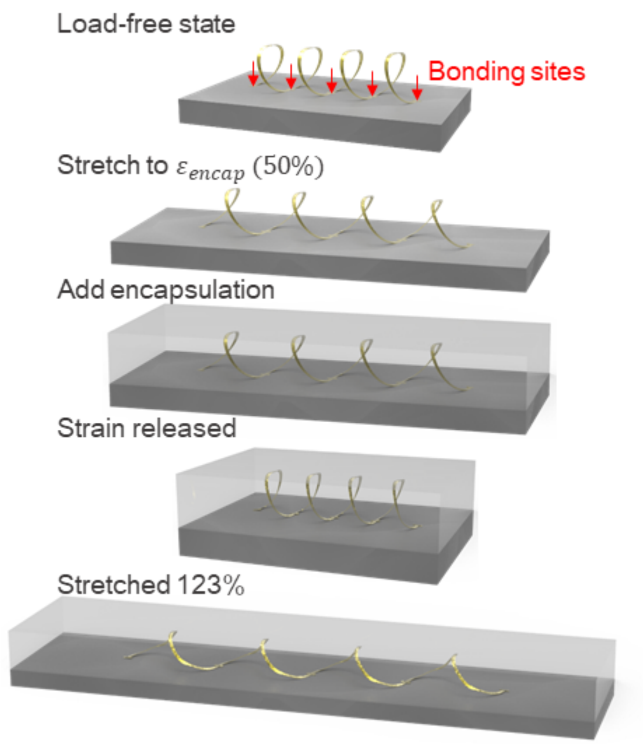


Figure 3.1. Process of the 2-stage soft encapsulation strategy for 3D helical interconnects. The soft elastomer encapsulation is added while the substrate, on which the 3D helical or 2D serpentine interconnects are selectively bonded, is stretched to an encapsulating strain ($\varepsilon_{encap}$).

ultra-thin metal layer (0.2 $\mu$m) from failure. Positioning the metal layer at the neutral mechanical plane of the sandwich design reduces the maximum strain in the metal during stretching, thereby increasing the overall stretchability. In the FEA (see Methods section 3.3.2 for details), the elastic stretchability is defined as the overall dimensional change below which the structural deformations can recover completely. Considering that the elastic strain limit of PI ($> 8\%$) [**234**] is much larger than that of metal (e.g. Au, $\sim 0.25\%$), the elastic stretchability is typically limited by the metal layer. According to quantitative calculations (Figure 3.4a & Figure 3.5a), the 3D helical interconnect can be

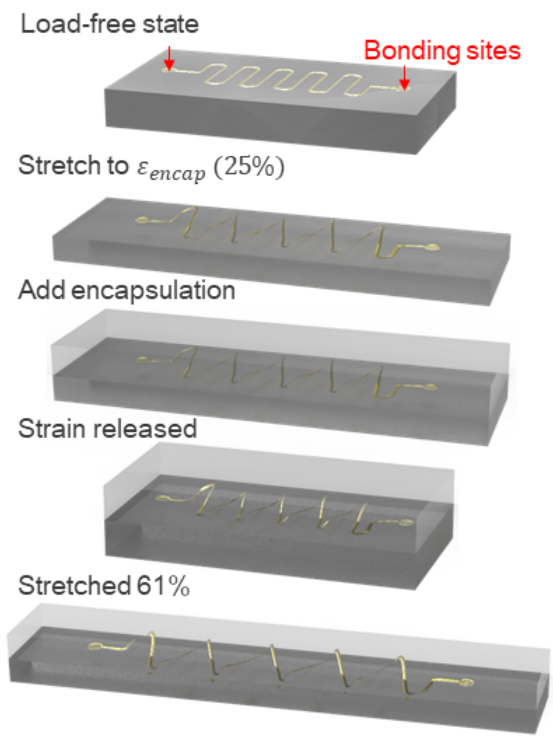


Figure 3.2. Process of the 2-stage soft encapsulation strategy for 2D serpentine interconnects. The soft elastomer encapsulation is added while the substrate, on which the 3D helical or 2D serpentine interconnects are selectively bonded, is stretched to an encapsulating strain ($\varepsilon_{encap}$).

elastically stretched to 123% using the 2-stage encapsulation approach ($\varepsilon_{encap} = 50\%$), which is ~2.6 times higher than that (46%) of the 1-stage scheme. The elastic stretchability (61%) of 2D serpentine interconnects with the 2-stage encapsulation is more than 6 times higher than that (9%) with 1-stage encapsulation.

The substantial improvements of elastic stretchability follow from the distinct mechanisms of stress accumulation. For interconnects with 1-stage encapsulation, the maximum Mises stresses in the metal layer increase rapidly and monotonically (Figure 3.4b & Figure 3.5b), as the stretching proceeds, which limits the elastic stretchability. By comparison,

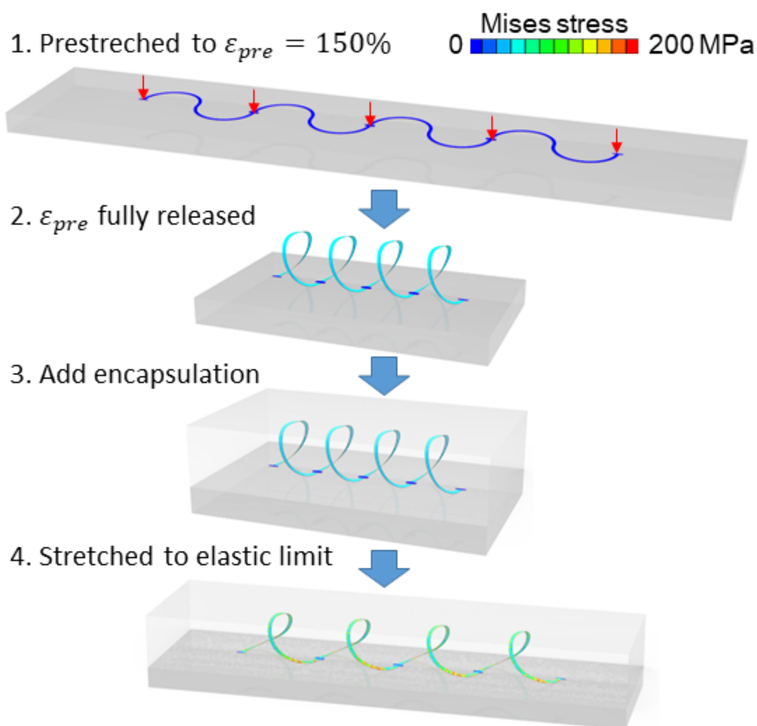


Figure 3.3. Process of the 1-stage encapsulation strategy for 3D helical intreconnects. 1. The 2D precursor was selectively bonded onto the prestretched ($\varepsilon_{prestrain}$=150%) substrate. 2. By releasing the prestretched substrate, the 2D precursor pops-up into 3D helical architecture as a result of compressive buckling. 3. Add encapsulation when the prestrain of substrate is fully released. 4. Stretch the device to elastic limit.

the maximum Mises stresses in the interconnects with 2-stage encapsulation decrease first to reach a local minimum as the applied strain reaches $\varepsilon_{encap}$, and then increases beyond $\varepsilon_{encap}$. This behavior is mainly attributed to pre-deformed interconnects that can accommodate an applied strain at least larger than $\varepsilon_{encap}$. The selection of a proper encapsulating strain ($\varepsilon_{encap}$) is essential in the design optimization, as elaborated in the next two sections.

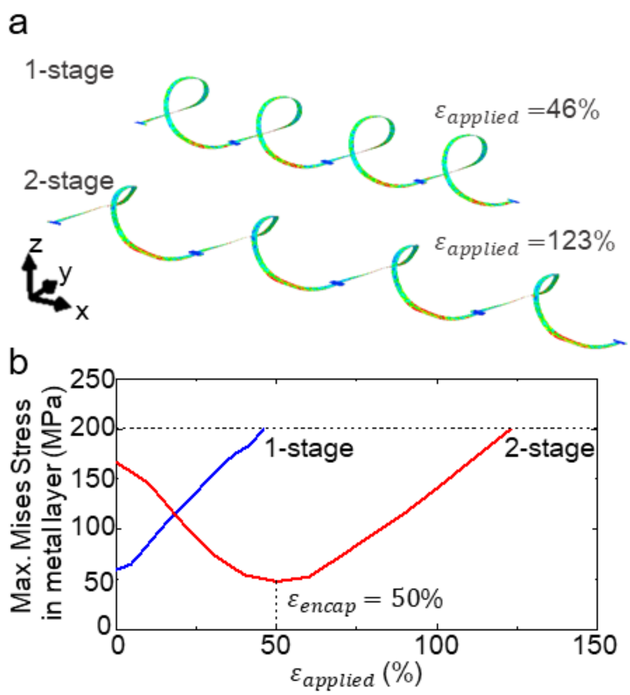


Figure 3.4. Deformed configuration and the maximum Mises stress distribution for 3D helical interconnects. (a) Deformed configurations of a 3D helical interconnect with the distribution of Mises stress in the metal layer of the sandwich (PI/metal/PI) structure in the conditions of 1-stage (top) and 2-stage (bottom) encapsulation. The applied strain corresponds to the elastic stretchability. (b) Maximum Mises stress in the metal layer of the 3D helical interconnect (a) as a function of the applied strain ($\varepsilon_{applied}$).

It is noteworthy that even the use of ultralow modulus elastomers (E = 3 kPa) in the 1-stage encapsulation scheme leads to significant reductions in the elastic stretchability of the interconnects, via consequent limits in their freedom of motion as a result of their low bending stiffnesses (Figure 3.6). In the condition of the same key geometric parameters (e.g., thickness, width, span, amplitude and total interconnect length), the 3D helical

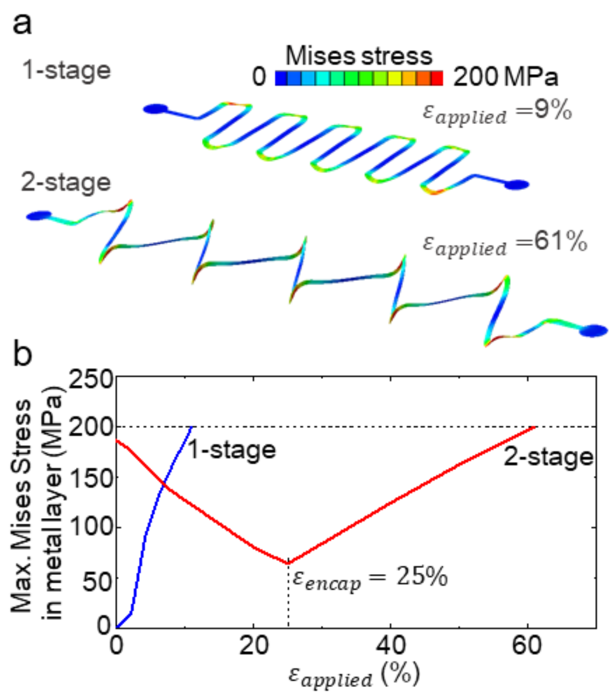


Figure 3.5. Deformed configuration and the maximum Mises stress distribution for 2D serpentine interconnects. (a) Deformed configurations of a 2D serpentine interconnect with the distribution of Mises stress in the metal layer of the sandwich (PI/metal/PI) structure in the conditions of 1-stage (top) and 2-stage (bottom) encapsulation. The applied strain corresponds to the elastic stretchability. (b) Maximum Mises stress in the metal layer of the 2D serpentine interconnect (a) as a function of the applied strain ($\varepsilon_{applied}$).

interconnects typically offer a higher elastic stretchability than the 2D serpentine interconnects (Figure 3.4a and Figure 3.5a), due to the more uniform stress distribution. But the thickness (e.g., $< 0.18$ mm) of elastomer encapsulation for 2D serpentine interconnects is thinner than that ($\sim 0.6$ mm) for 3D helical interconnects, thereby with a potential to provide a higher flexibility of the entire device (Figure 3.7).

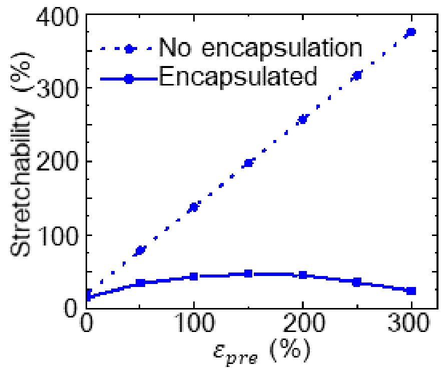


Figure 3.6. Elastic stretchability of a 3D helical interconnects with and without encapsulation. The parameters adopted in the simulations include $w = 50$ $\mu$m, $t_{PI} = 1.4$ $\mu$m, $t_{metal} = 0.4$ $\mu$m, $E_{metal} = 79$ GPa, $E_{encap} =$ 3 kPa.

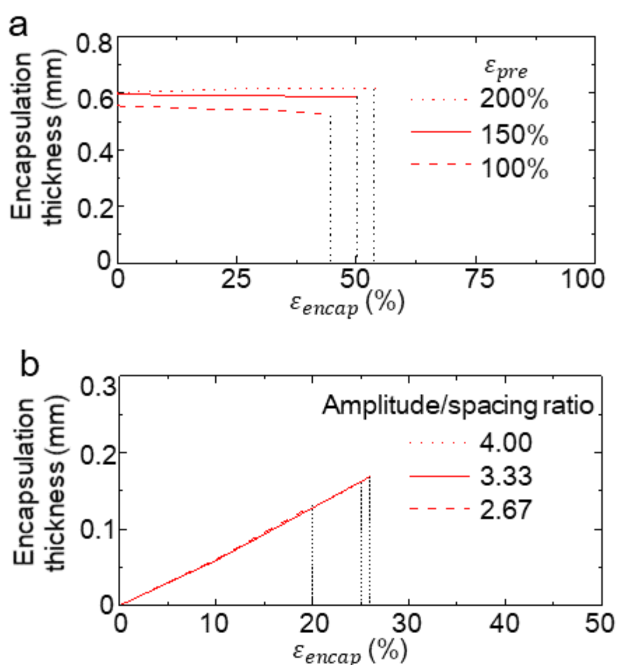


Figure 3.7. Encapsulation thickness for different encapsulating strain. (a) The encapsulation thickness versus the encapsulating strain for 3D helical interconnects (with $\varepsilon_{prestrain}$ 100%, 150% and 200%) and (b) 2D serpentine interconnects (with amplitude/spacing ratio 2.67, 3.33 and 4.00).

### 3.2.2. 3D helical interconnects

Quantitative mechanics modelling can serve as an important tool to optimize the processing parameters in the 2-stage encapsulation process for 3D helical interconnects. In the following analyses, the key geometric parameters of the 2D precursor for the formation of 3D helical interconnects include the width ($w = 50$ $\mu$m), central arc angle ($\theta_0 = 180°$) and arc radius (0.425 mm) (Figure 3.8). Figure 3.9 shows that the use of $\varepsilon_{encap}$ above a certain threshold (50% and 54% for $\varepsilon_{prestrain}$=150% and 200%, respectively) can lead to plastic yielding of the 3D helical interconnects before full release of the pre-stretch in the substrate. Below such a threshold, the elastic stretchability increases monotonically with increasing $\varepsilon_{encap}$, indicating an enhancement in stretchability by a factor of $> 2$ for $\varepsilon_{encap} > 39\%$. The threshold encapsulating strain ($\varepsilon_{encap-th}$) can be regarded as an optimal value to maximize the elastic stretchability during the 2-stage encapsulation.

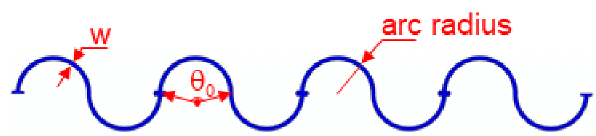


Figure 3.8. Geometric characterization of the 2D precursor of 3D helical interconnect. Key geometric parameters include width ($w = 50$ $\mu$m), central arc angle ($\theta_0 = 180°$) and arc radius (0.425 $\mu$m).

The encapsulation effect on the elastic stretchability also depends highly on the 3D helical configuration that is determined by the prestrain ($\varepsilon_{prestrain}$) and the geometric parameters of the 2D precursor adopted in the 3D assembly. Figure 3.10 shows that the elastic stretchability increases with increasing $\varepsilon_{prestrain}$ at the initial stage in both conditions of 1-stage and 2-stage encapsulation, because the 3D helical interconnects becomes denser. Beyond a critical prestrain, the elastic stretchability decreases with the further

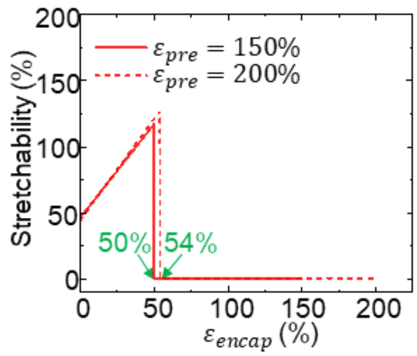


Figure 3.9. Elastic stretchability of an encapsulated 3D helical interconnect with use of different levels of encapsulating strains in the 2-stage encapsulation strategy.

increase of $\varepsilon_{prestrain}$. Such a non-monotonous dependence results from distinct reasons for the 1-stage and 2-stage encapsulating processes. During the 1-stage encapsulation, a knot-like structure forms when a sufficiently large $\varepsilon_{prestrain}$ is adopted (as mentioned in Section 2.2), which cannot be effectively unravelled during stretching, thereby limiting the further increase of elastic stretchability. During the 2-stage encapsulation, the threshold encapsulating strain ($\varepsilon_{encap-th}$) dramatically decreases at a large $\varepsilon_{prestrain}$ (Table 3.1), which results in a reduction in the elastic stretchability beyond $\varepsilon_{prestrain} \approx 200\%$. Despite these limits, the 2-stage encapsulation strategy enables a significant improvement in the elastic stretchability over the 1-stage strategy for all prestrains (up to $\sim$4 times for $\varepsilon_{prestrain}$=250%). The metal thickness also plays a crucial role, as evidenced by the FEA results in Figure 3.11. When the metal thickness is larger than a critical value, the elastic stretchability is totally suppressed, because plastic yielding occurs in the metal layer during the mechanically-guided 3D assembly, and any further external loading induces irreversible deformations in the interconnects.

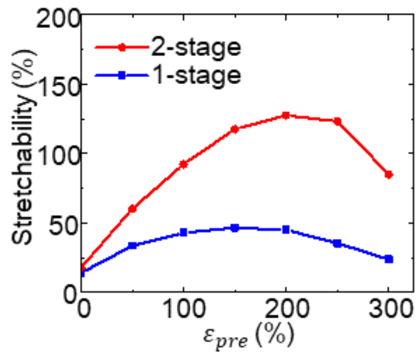


Figure 3.10. Elastic stretchability of 3D helical interconnects formed with different prestrains, in both the conditions of 1-stage and 2-stage encapsulation.

Table 3.1. Threshold encapsulating strain for encapsulated 3D helical interconnects induced by 2-stage process for different prestrains.

| $\varepsilon_{prestrain}(\%)$ | $\varepsilon_{encap-th}(\%)$ |
|---:|---|
| 0 | - |
| 50 | 40 |
| 100 | 45 |
| 150 | 50 |
| 200 | 54 |
| 250 | 43 |
| 300 | 40 |

As mentioned above, the knot-like structures formed in the conventional 1-stage encapsulation severely limits the elastic stretchability, since such structures cannot be unraveled to contribute to the stretchability, due to the constraints of the surrounding solid. Such knot-like structures mainly result from in-plane rotational motions at the peaks of the helices (Figure 3.12) and become evident when using high levels of prestrain ($\varepsilon_{prestrain}$) in the 3D assembly. The 2-stage encapsulation strategy avoids the formation of such knot-like structures by pre-stretching the substrate prior to adding the encapsulation.

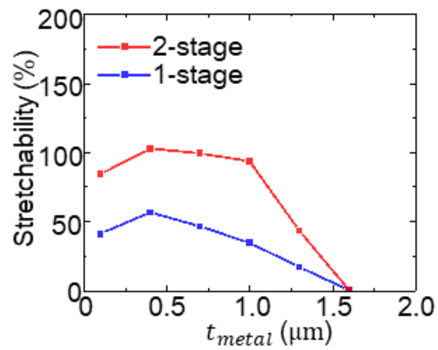


Figure 3.11. Elastic stretchability of 3D helical interconnects formed with different metal thicknesses, in both the conditions of 1-stage and 2-stage encapsulation.

This mechanism is highlighted by the optical images of deformed configurations based on experiments (Figure 3.12), which also agree reasonably well with FEA.

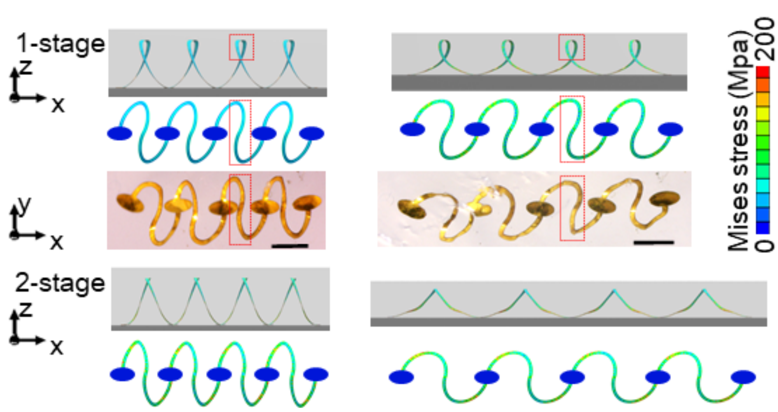


Figure 3.12. Optical images and FEA results on the un-deformed and deformed configurations of a 3D helical interconnect with Mises stress distributions in the conditions of 1-stage (top, $\varepsilon_{prestrain}$=0%) (left, load-free state; right, $\varepsilon_{applied}$=46%) and 2-stage encapsulating processes (bottom, $\varepsilon_{encap}$=50%) (left, load-free state; right, $\varepsilon_{applied}$=123%) (scale bars, 1 mm). The key geometric parameters of the 2D precursor used in the 3D assembly include $\varepsilon_{prestrain}$=150%, $t_{metal}$=0.4 $\mu$m, $t_{PI}$=3.0 $\mu$m, width ($w$=100 $\mu$m), central arc angle ($\theta_0 = 180°$) and arc radius (0.85 mm).

The 2-stage encapsulation strategy is scalable across a large range of dimensions. As shown in Figure 3.13, when the in-plane sizes are increased from 2.4 mm to 19.2 mm for fixed thicknesses of PI and metal layers, no obvious change in the elastic stretchability can be observed. Fatigue tests (Figure 3.14 and Figure 3.15) demonstrate the robustness of the electrical interconnects. In particular, the resistances of the 3D helical interconnects change very slightly, after repetitively stretching the structures to 46% and 123% for 1-stage and 2-stage encapsulating conditions, respectively, at a strain rate of 111%/min for a thousand cycles.

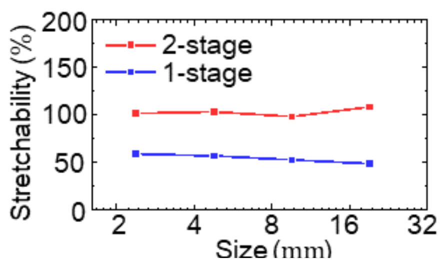


Figure 3.13. Scale effect on the elastic stretchability, where the size refers to the distance between the left-most and right-most bonding sites.

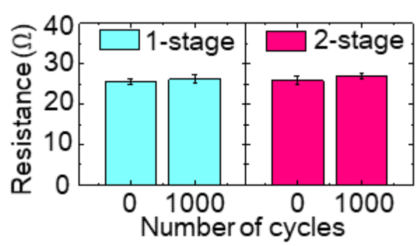


Figure 3.14. Resistance of a four-unit 3D helical interconnect presented in Figure 3.12 before and after cyclic stretching test.

To take full advantage of the sandwich (PI/metal/PI) design, the thicknesses of the metal layer and PI layer are changed simultaneously to study the variation of the elastic

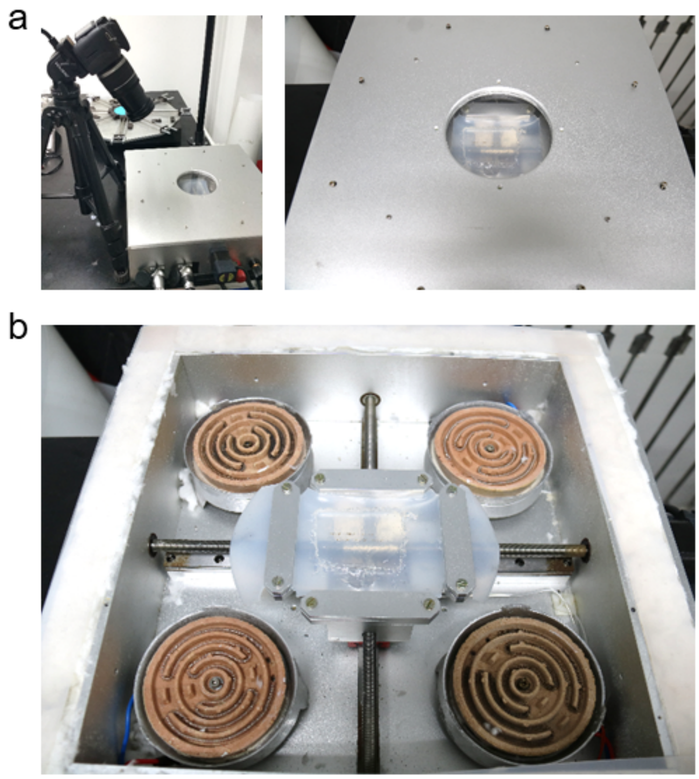


Figure 3.15. Optical images of the fatigue test facilities.

stretchability. The contour plots of elastic stretchability for the 2-stage (Figure 3.16a) and 1-stage (Figure 3.16b) encapsulating conditions both suggest an optimum set of thicknesses as $t_{PI}^{optimum}$=1.4 $\mu$m and $t_{metal}^{optimum}$=0.4 $\mu$m. When alternative encapsulating materials, substrate materials and metal materials (e.g. Au, Ni and Cr) are adopted, both the optimal encapsulating strain and the elastic stretchability vary, as shown in Figure 3.17 and Table 3.2, 3.3 and 3.4. In general, the elastic stretchability increases as the elastic modulus increases in the interconnect material, or decreases in the encapsulation and substrate materials. In all of the cases considered herein, the 2-stage encapsulation strategy can always enable an obvious improvement of the stretchability.

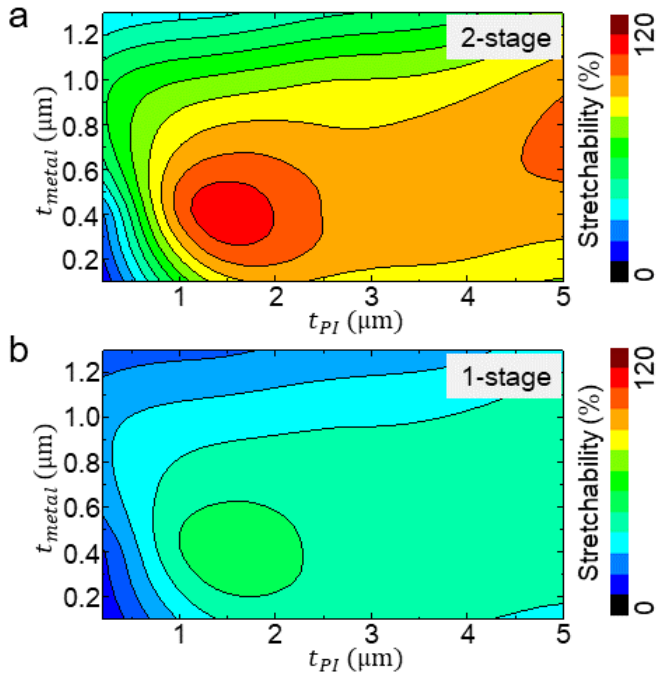


Figure 3.16. Contour plots of elastic stretchability in terms of the metal thickness and PI thickness in the conditions of (a) 2-stage and (b) 1-stage encapsulating processes.

Table 3.2. Threshold encapsulating strain for 2-stage encapsulated 3D helical interconnects with use of different levels of encapsulation modulus.

| $E_{encapsulation}$(kPa) | $\varepsilon_{encap-th}$(%) |
|---:|:---|
| 3 | 50 |
| 4 | 40 |
| 8 | 36 |
| 12 | 29 |
| 16 | 21 |
| 20 | 18 |

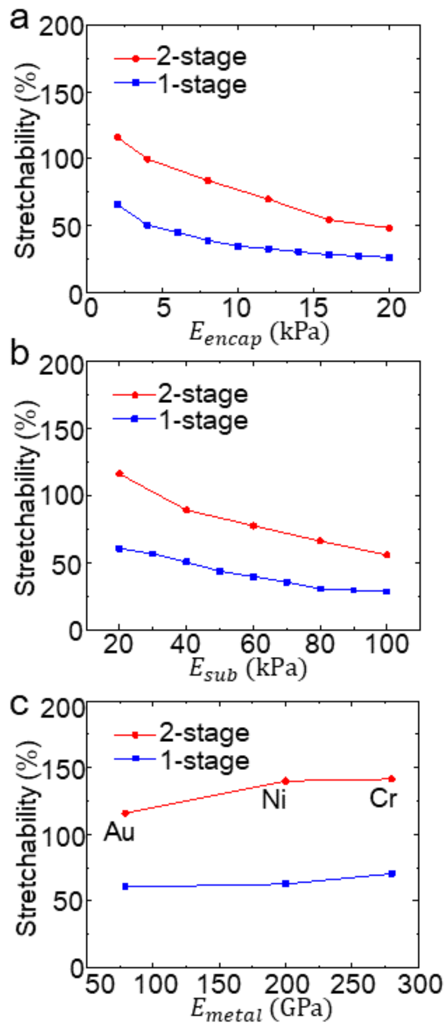


Figure 3.17. Elastic stretchability of 3D helical interconnects using different (a) encapsulation materials, (b) substrate materials and (c) metal materials.

### 3.2.3. 2D interconnects with serpentine and fractal-inspired designs

The use of conventional 1-stage encapsulations strategies and/or fully bonded 2D interconnects strongly limit the elastic stretchability, to values that are typically in the range of 10% or less. The 2-stage encapsulation strategy can improve the elastic stretchability

Table 3.3. Threshold encapsulating strain for 2-stage encapsulated 3D helical interconnects with use of different levels of substrate modulus.

| $E_{substrate}$(kPa) | $\varepsilon_{encap-th}$(%) |
|---:|---|
| 20 | 50 |
| 40 | 30 |
| 80 | 29 |
| 60 | 28 |
| 100 | 25 |

Table 3.4. Threshold encapsulating strain for 2-stage encapsulated 3D helical interconnects with use of different levels of metal modulus.

| $E_{metal}$(GPa) | $\varepsilon_{encap-th}$(%) |
|---:|---|
| 79 | 50 |
| 200 | 62 |
| 280 | 62 |

dramatically (e.g., $> 6$ times) by adopting a proper encapsulating strain, as compared to the 1-stage encapsulation (Figure 3.18). The improvement in stretchability increases with increasing $\varepsilon_{encap}$ up to a threshold, beyond which plastic yielding occurs in the metal layer after full release of the pre-stretch. The amplitude/spacing ratio of the 2D serpentine interconnects represents a key design parameter that affects the elastic stretchability (Figure 3.19). As compared to the 1-stage encapsulation, in which the elastic stretchability changes relative slightly, the elastic stretchability in the 2-stage encapsulation condition increases significantly with increasing the amplitude/spacing ratio (Figure 3.20). The threshold encapsulating strains ($\varepsilon_{encap-th}$) for different amplitude/spacing ratios are in Table 3.5. Similar to the 3D helical interconnects, the metal thickness and PI thickness also play important roles in the resulting elastic stretchability of 2D serpentine interconnects (Figure 3.21 and Figure 3.22). In this set of calculations, some key geometric parameters of 2D serpentine interconnects include the width ($w$=50 $\mu$m), amplitude (0.9 mm) and spacing (0.675 mm).

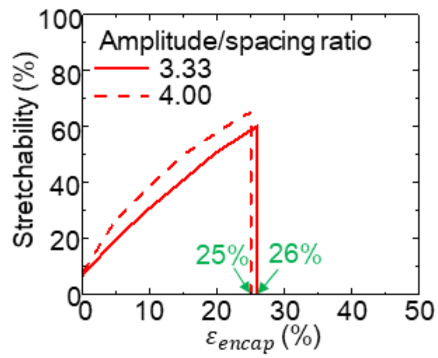


Figure 3.18. Elastic stretchability of an encapsulated 2D serpentine interconnect with use of different levels of encapsulating strains in the 2-stage encapsulation strategy.

Table 3.5. Threshold encapsulating strain for 2D serpentine interconnects for different amplitude/spacing ratios.

| Amplitude/spacing ratio | $\varepsilon_{encap-th}$(%) |
|---|---|
| 1.33 | 20 |
| 2.00 | 22 |
| 2.67 | 20 |
| 3.33 | 26 |
| 4.00 | 25 |
| 4.67 | 25 |
| 5.33 | 24 |

For the 2D serpentine interconnects, the improvement in stretchability enabled by the 2-stage encapsulation strategy results mainly from lateral buckling during the pre-stretching stage that leads to buckled 3D configurations. With solid encapsulation, such buckled 3D configurations can be unraveled more easily than for 2D configurations that are entirely restricted to the substrate surface. Good agreement between experiment

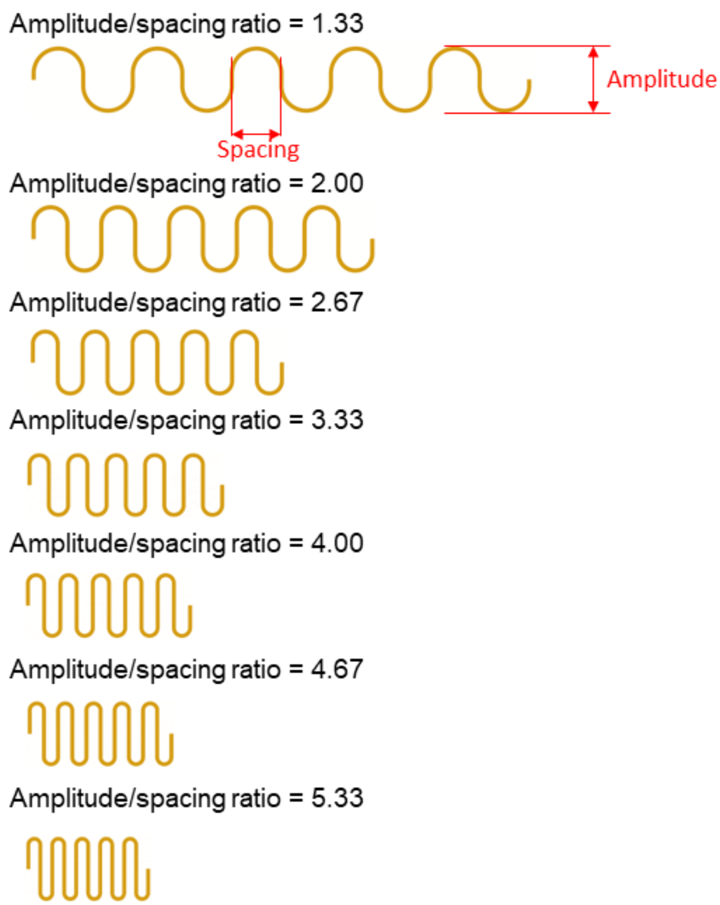


Figure 3.19. Geometric characterization of 2D serpentine with amplitude/spacing ratios. Key geometric parameters include width (50 $\mu$m), amplitude (0.9 mm) and spacing (0.675 mm).

and FEA verifies this deformation mechanism (Figure 3.23). The 2-stage encapsulation strategy applies to a range of different length scales (e.g., from 2.4 mm to 19.2 mm), with a negligible difference in the elastic stretchability (Figure 3.24). Results of cyclic stretching test under a similar condition to that in Figure 3.13 illustrate the robustness of encapsulated interconnects (Figure 3.25).

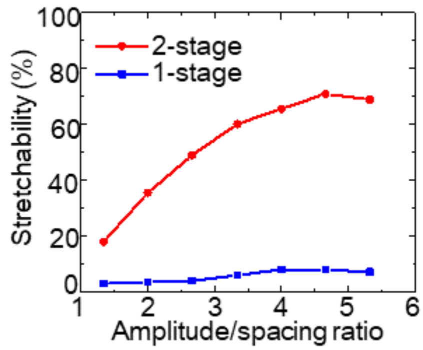


Figure 3.20. Elastic stretchability of 2D serpentine interconnects formed with different amplitude/spacing ratios, in both conditions of 1-stage and 2-stage encapsulation.

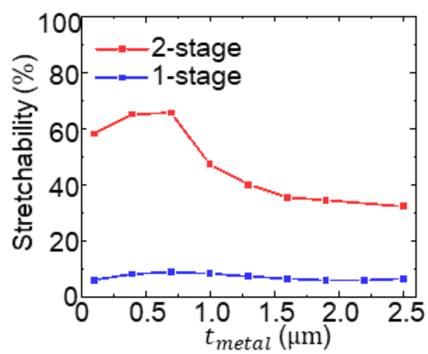


Figure 3.21. Elastic stretchability of 2D serpentine interconnects formed with different metal thicknesses, in both conditions of 1-stage and 2-stage encapsulation.

For the 2-stage encapsulation of 2D serpentine interconnects, the elastic stretchability depends highly on the encapsulation modulus, rather than the substrate modulus, because the buckled architectures mainly interface with the encapsulation material. Unlike the case for 1-stage encapsulation, the elastic stretchability is more sensitive to the substrate modulus in the range considered herein. This sensitivity can be attributed to the planar

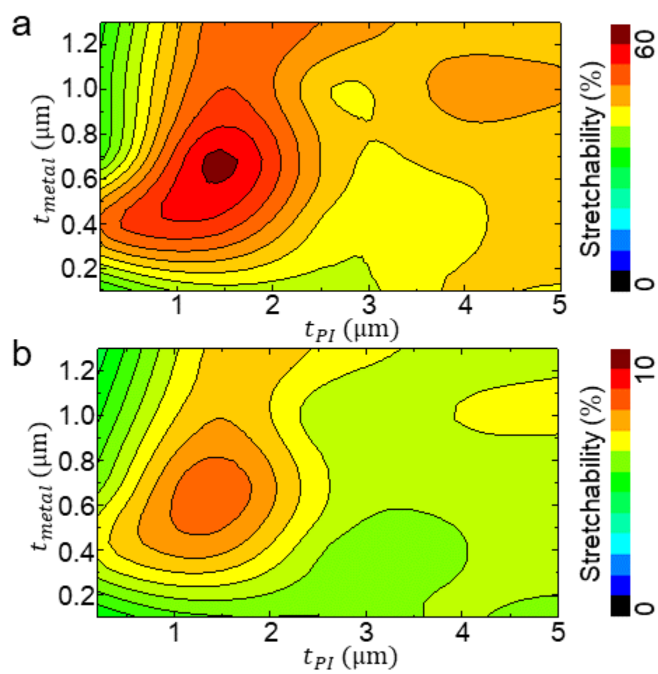


Figure 3.22. Stretchability contour for different various metal thickness and PI thickness with (a) 2-stage encapsulation strategy and (b) 1-stage encapsulation strategy.

configuration of the interconnects and their tight attachment to the substrate and the encapsulation materials and the fact that the substrate is more rigid than the encapsulant for these studies (Figure 3.26a&b). Figure 3.26c shows that the 2-stage encapsulation strategy can improve the elastic stretchability substantially for other choices of metals as well. Effects of the encapsulation modulus, substrate modulus and metal modulus on the threshold encapsulating strain of 2D serpentine interconnects are presented in Table 3.6, 3.7 and 3.8.

Existing studies demonstrated that free-standing interconnects with fractal-inspired 2D patterns can offer a larger elastic stretchability than 2D serpentine patterns, for a

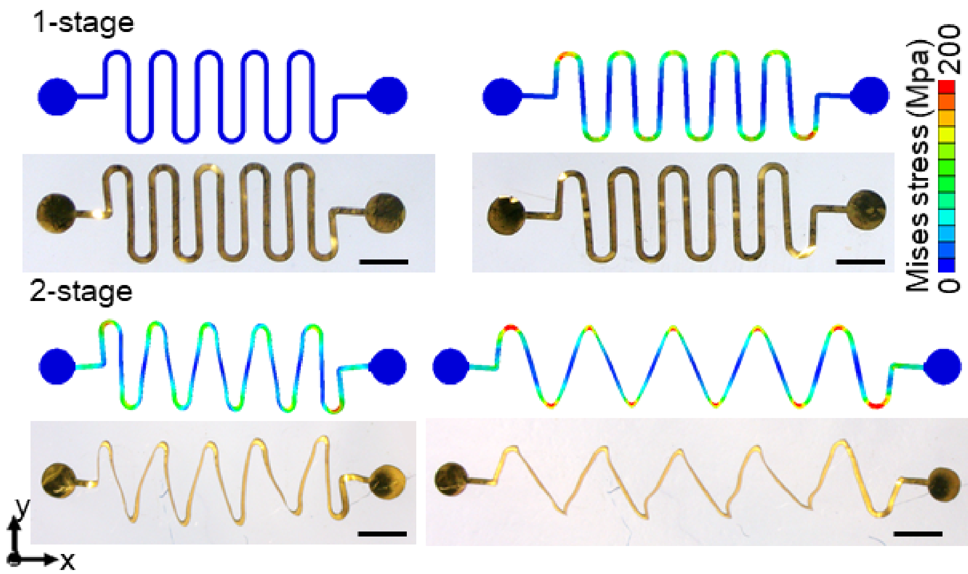


Figure 3.23. Optical images and FEA results on the un-deformed and deformed configurations of a 2D serpentine interconnect with Mises stress distributions in the conditions of 1-stage (top) (left, load-free state; right, $\varepsilon_{applied}$=7.0%) and 2-stage encapsulating processes (bottom, $\varepsilon_{encap}$=26%) (left, load-free state; right, $\varepsilon_{applied}$=61%) (scale bars, 1 mm). The key geometric parameters include $t_{metal}$=0.4 $\mu$m, $t_{PI}$=3.0 $\mu$m, width ($w$=100 $\mu$m), amplitude (1.8 mm) and spacing (1.35 mm).

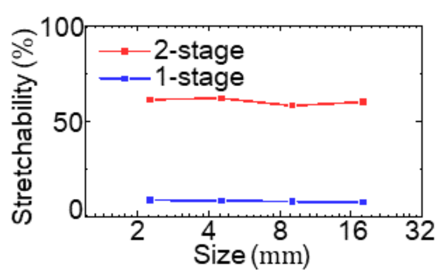


Figure 3.24. Scale effect on the elastic stretchability of 2D serpentine interconnects, where the size refers to the distance between the left-most and right-most bonding sites.

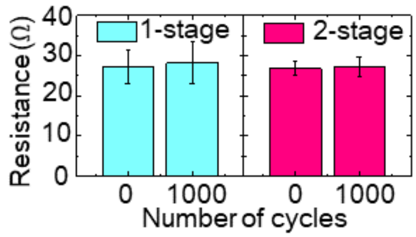


Figure 3.25. Resistance of a 2D serpentine interconnect before and after cyclic stretching test. Elastic stretchability of 2D serpentine interconnects using different

Table 3.6. Threshold encapsulating strain for 2-stage encapsulated 3D helical interconnects with use of different levels of encapsulation modulus.

| $E_{encapsulation}$(kPa) | $\varepsilon_{encap-th}$(%) |
|---:|---|
| 3 | 25 |
| 4 | 21 |
| 8 | 20 |
| 12 | 21 |
| 16 | 16 |
| 20 | 16 |

Table 3.7. Threshold encapsulating strain for 2-stage encapsulated 3D helical interconnects with use of different levels of substrate modulus.

| $E_{substrate}$(kPa) | $\varepsilon_{encap-th}$(%) |
|---:|---|
| 20 | 25 |
| 40 | 25 |
| 80 | 25 |
| 60 | 25 |
| 100 | 25 |

prescribed areal coverage of functional components in island-bridge designs [**207, 32**]. Similar to 2D serpentine interconnects, the conventional 1-stage solid encapsulation reduces the elastic stretchability of the 2D fractal interconnects to a relatively low level (e.g., ∼11%). By implementing the 2-stage encapsulation strategy, the elastic stretchability can

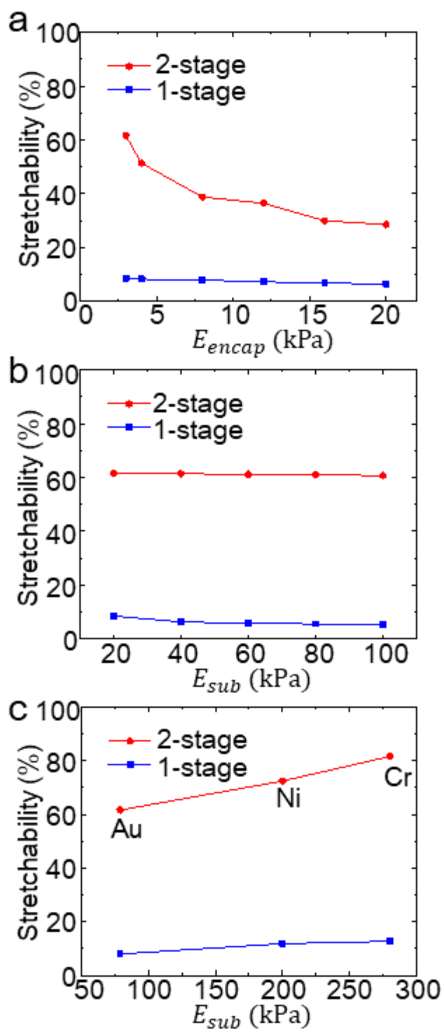


Figure 3.26. Elastic stretchability of 2D serpentine interconnects using different (a) encapsulation materials, (b) substrate materials and (c) metal materials.

be increased by more than 4 times, in comparison to the 1-stage encapsulation, through a mechanism (i.e., formation of buckled 3D configurations during the pre-stretch) similar to that of the 2D serpentine interconnects. Figure 3.27 presents the FEA results of deformed configurations with Mises stress distribution, when the 2D fractal interconnect is

Table 3.8. Threshold encapsulating strain for 2-stage encapsulated 3D helical interconnects with use of different levels of metal modulus.

| $E_{metal}$(GPa) | $\varepsilon_{encap-th}$(%) |
|---|---|
| 79 | 25 |
| 200 | 32 |
| 280 | 32 |

stretched to the elastic limit, for both 1-stage and 2-stage encapsulation. Optical images collected at the same applied strains show good agreement with FEA.

### 3.2.4. Highly stretchable LED systems with solid encapsulation

The reported 2-stage encapsulation strategy has general utility across a broad range of stretchable electronic devices. As an example, we demonstrated a 3D electromagnetic (EM) energy harvester that can power commercial LEDs, as presented in Figure 3.28a&b. This system exploits a spring-like 3D helical architecture to serve both as the antenna and as the interconnects. The entire system was formed through the mechanically-guided 3D assembly, in which an equal biaxial prestrain of $\varepsilon_{prestrain}$=150% was adopted. Optical images of the 3D device system appear in Figure 3.28b and Figure 3.29.

With a solid encapsulation, the elastic stretchability of the 3D device system is smaller than that of the individual unit cell of the 3D coil, in part due to the complicated interactions between elastomer encapsulation and closely distributed 3D coils, as presented in Figure 3.30a. In comparison to the 1-stage encapsulation, the elastic stretchabilities under both uniaxial and biaxial loadings are improved by a factor of around 4, through use of the 2-stage encapsulation with $\varepsilon_{encap}$=30% (Figure 3.30b). With the 2-stage encapsulation strategy, this device system offers ultra-high elastic stretchabilities (102% and

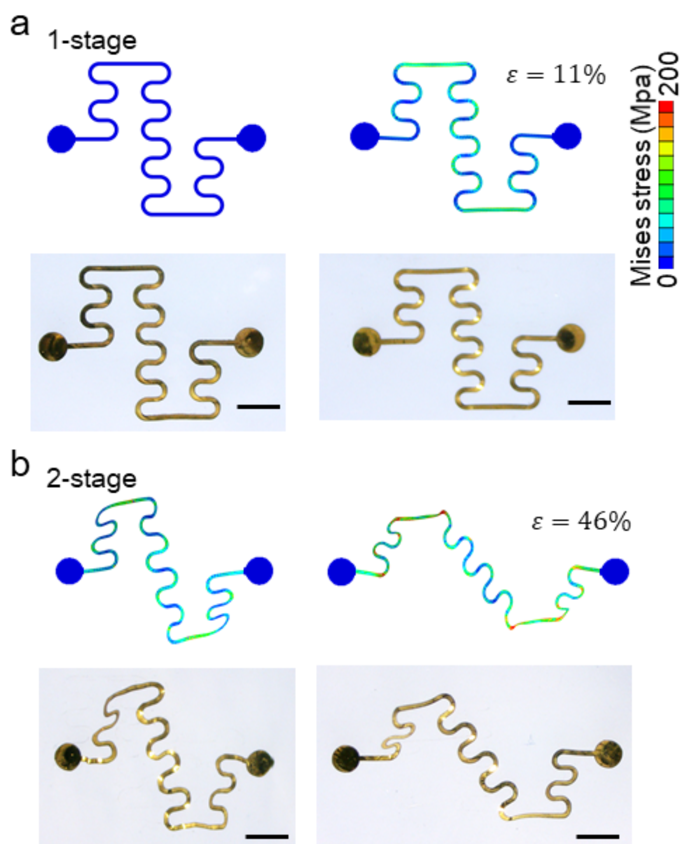


Figure 3.27. Optical images and FEA results on the un-deformed and deformed configurations of a 2D fractal interconnect with Mises stress distributions in the conditions of (a) 1-stage and (b) 2-stage encapsulating processes ($\varepsilon_{encap}$=28%) (scale bars, 1 mm).

94% for uniaxial and biaxial stretching, respectively). For such complex 3D constructions, the FEA can capture well the detailed deformations at different locations of the device, as evidenced by the agreement with the experimental results.

We characterized the electromagnetic (EM) property of the antenna by experimental measurement and EM simulations using the commercial software HFSS as presented in Figure 3.31. The difference of return loss parameter (S11) between the load-free state and

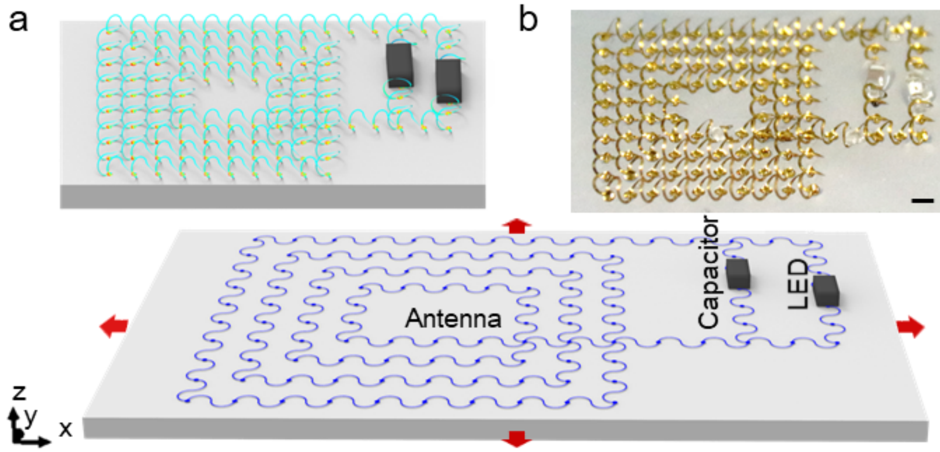


Figure 3.28. A 3D soft antenna consisting of helical mesostructures, illustrated by results of finite element analysis (FEA). (b) Angled optical image of an experimentally realized device (scale bar, 1 mm).

stretched (50%) state is relatively small, as shown by both the simulation and experiment results. Optical images of working device presented in Figure 3.32 prove the functionality under a large uniaxial stretch.

Figure 3.33,3.34 and 3.35 presents another encapsulated device demonstration, in the form of highly stretchable LED systems that use networks of 2D fractal interconnects (Figure 3.33a&b). For conventional 1-stage encapsulation, the elastic stretchability of the device system is only ∼10% for uniaxial or biaxial stretching (Figure 3.34a). This elastic stretchability is significantly increased, by a factor of ∼4, with the 2-stage encapsulation strategy, as illustrated in Figure 3.34b. The experimental results in Figure 3.34b present encapsulated working devices under such levels of stretching. Practical demonstrations with coupled bending and folding deformations show that the encapsulated device can be

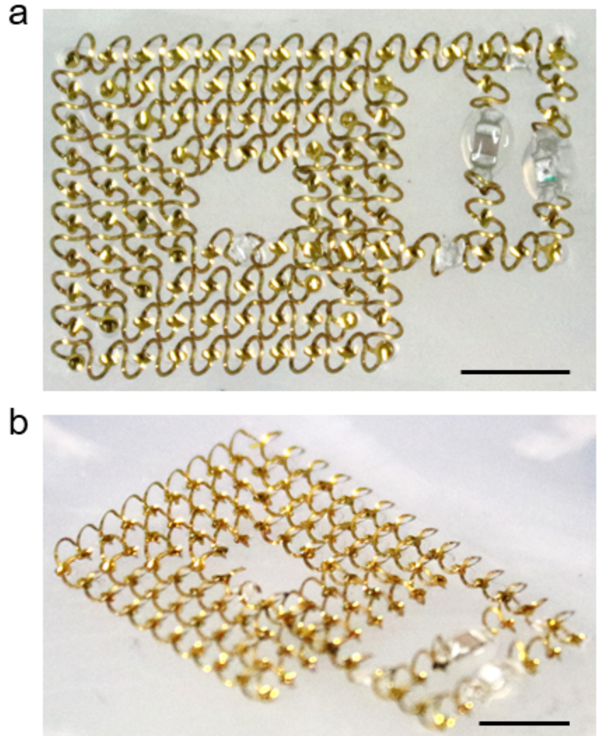


Figure 3.29. Optical images of the soft antenna network with 3D helical mesostructured (Scale bar, 5 mm).

mounted onto complex curvilinear surfaces (Figure 3.35), as an additional indication of excellent mechanical properties.

## 3.3. Methods

### 3.3.1. experimental

**3.3.1.1. Fabrication of the encapsulated 3D helical interconnects.** Spin-casting poly(methyl methacrylate) (PMMA; ∼100 nm in thickness, Microchem, USA) formed a thin sacrificial layer on a silicon wafer. Spin-casting polyimide (PI; ∼3 $\mu$m in thickness, Sigma-Aldrich, USA), depositing thin layers of metal by electron beam evaporation

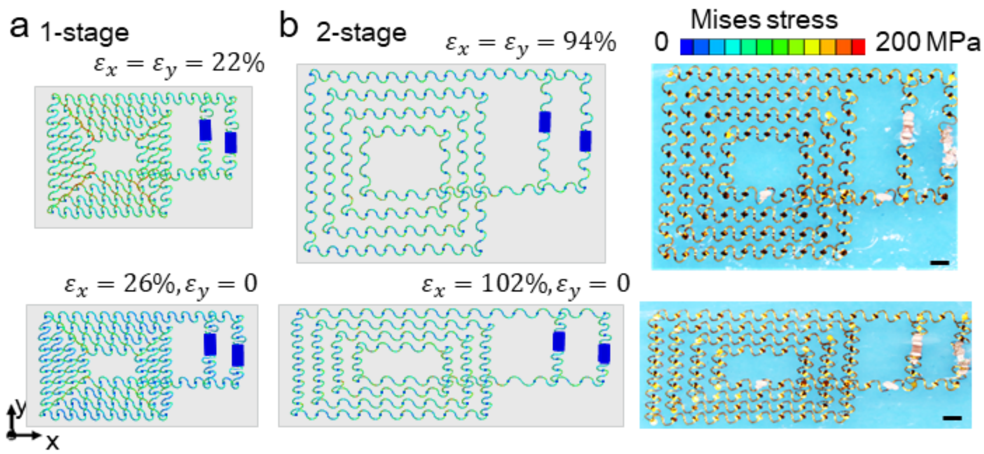


Figure 3.30. System-level deformations under uniaxial and biaxial stretching and Mises stress distribution determined by FEA in the conditions of (a) 1-stage and (b) 2-stage encapsulating processes. Optical images are shown in d for the 2-stage encapsulation (scale bars, 1 mm).

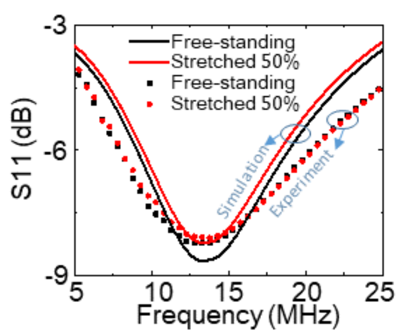


Figure 3.31. Electromagnetic (EM) characterization of the 3D helical antenna, showing the return loss parameter (S11) versus frequency based on EM simulation and experiment measurements.

(Cr/Au , thickness 10/400 nm), and spin-casting another layer of polyimide followed by femtosecond laser cutting (Rofin, Deutsch) defined a network of 2D serpentine structures, referred to here as the 2D precursor. Dissolving the PMMA by immersion in acetone

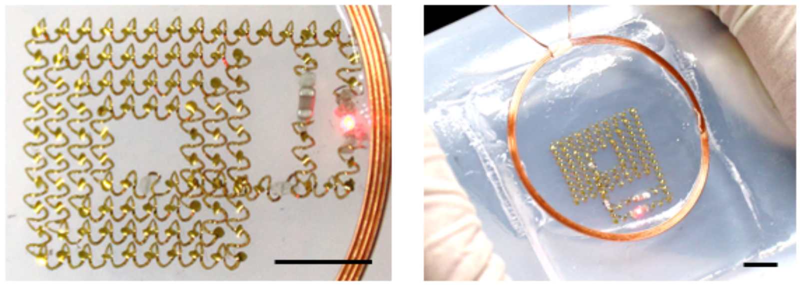

Figure 3.32. Optical images of the working device, in the un-deformed and uniaxially stretched (50%) states, respectively (scale bars, 5 mm).

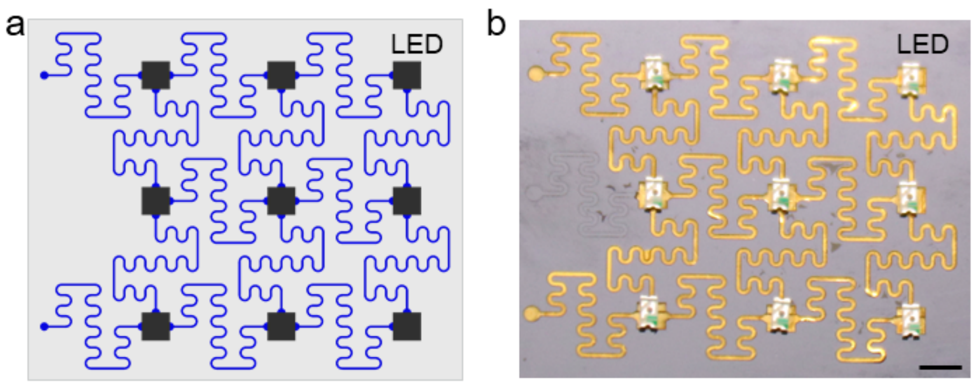


Figure 3.33. (a) Illustration of the device with a 3 by 3 array consisting of 2D fractal interconnects. (b) Optical image of an experimentally realized device (scale bar, 1 mm).

for 10 mins allowed retrieval of the 2D precursor onto the surface of a PDMS stamp (Sylgard 184, Dow Corning Corporation, USA). Selective gummimg of silicone rubber (705, RTV, NanDa, China) through a shadow mask (i.e., a thin (0.1 mm) sheet of PET film patterned with laser cutting) defined sites for strong bonding to a silicone elastomer substrate (thickness 1 mm; Ecoflex 00-30A/B, Smooth-on, USA). A custom mechanical stage allowed application of precisely controlled levels of biaxial strain to this elastomer.

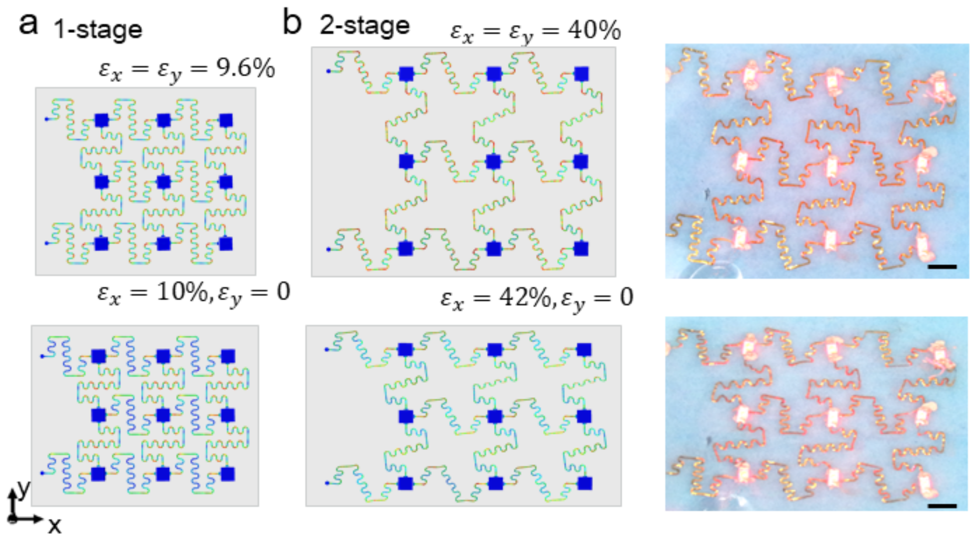


Figure 3.34. System-level deformations under uniaxial and biaxial stretching and Mises stress distribution determined by FEA in the conditions of (a) 1-stage and (b) 2-stage encapsulating processes. Optical images are shown in d for the 2-stage encapsulation (scale bars, 1 mm).

Transfer printing the 2D precursor onto a prestrained substrate and stewing (12 hours, $23°C$) the system activated the formation of strong bonds between the patterned 2D precursor and the surface of the silicone substrate. Partially releasing this prestrain (two stage encapsulation) or fully releasing this prestrain (one stage encapsulation) followed by casting a uniform layer of an ultra-low-modulus elastomer (Silbione 4717A/B, Bluestar Silicones, France) encapsulated the entire system while preserving freedom of motion of the helical coils upon application of strain.

**3.3.1.2. Fabrication of the encapsulated 2D serpentine and 2D fractal inspired interconnects.** Most of the processes are similar to those described in the previous section. In the preparation of 2D serpentine (and 2D fractal-inspired) structures, transfer

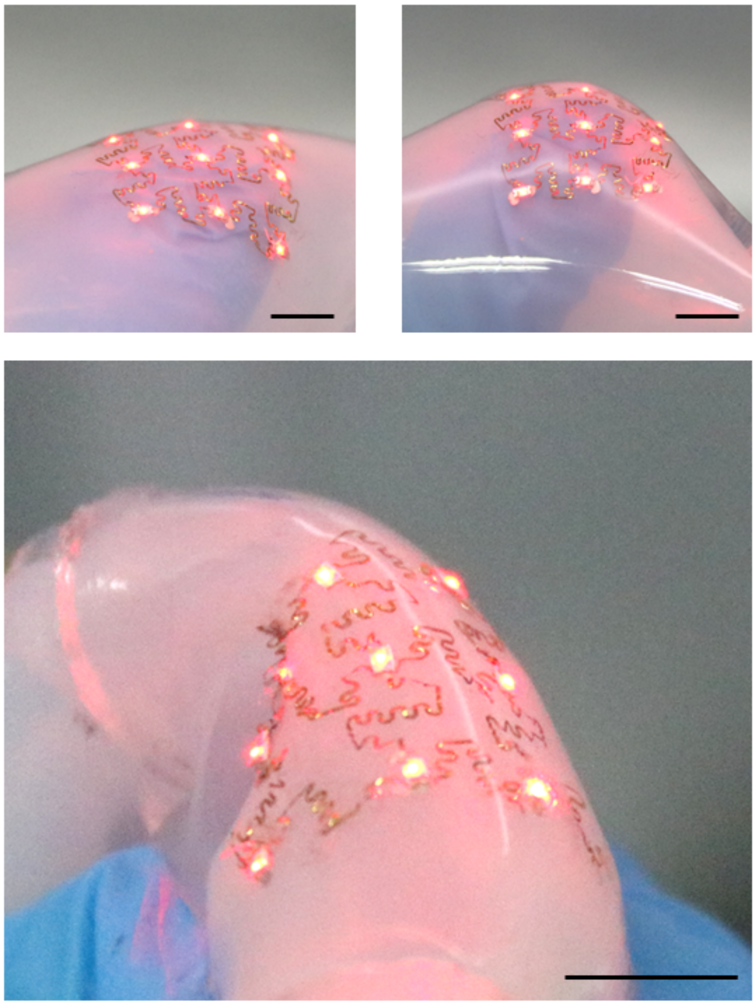

Figure 3.35. Optical images of the working device under different forms of complex mechanical loadings. This device is formed using the 2-stage encapsulation strategy with encapsulating strain $\varepsilon_{encap}$=25% (scale bars, 5 mm).

printing the 2D precursor onto a load-free substrate formed the interconnects for encapsulation. Prestretching the substrate (two stage encapsulation) or keeping the zero strain state (one stage encapsulation) followed by casting a uniform layer of an ultra-low-modulus elastomer (Silbione 4717A/B) completed the encapsulation.

**3.3.1.3. Circuit design and test of the soft LED system.** In the circuit consisting of 3D helical coils, resonant inductive coupling using a network of unshielded 3D helical coil served as the basis for a wireless power receiver. A parallel capacitor (180 pF) defined a resonance at 13.56 MHz, as measured using an RF Impedance Analyzer (4291A, Hewlett Packard). The transmitter consisted of a circular wire wound coil with a radius of 43 mm, matched at 13.56 MHz, powered with an amplifier module (WSPAS-11000, Wattsine, China). With this system, the circuit is capable of operating the system to light the LED. In the circuit constructed with an array of 2D fractal interconnects, the DC power (15V, 610E, TREK, USA) supply is directly exploited.

**3.3.1.4. Cyclic stretching test of the 3D helical and 2D serpentine interconnects.** A customized biaxial mechanical stretcher allowed precise control of strain applied to the substrate. A low strain rate (1000 cycles, 50 mm/min) was used in the cyclic stretching tests. Four sets of experiments were performed for the 3D helical interconnects and 2D serpentine interconnects formed with the 1-stage and 2-stage encapsulating processes, respectively. The resistances in these interconnects were measured before and after the cyclic stretching test.

### 3.3.2. Finite Element Analysis

Three-dimensional finite element analysis allowed prediction of the mechanical deformations and the Mises stress distributions of the individual 3D coils, 2D serpentine and 2D fractal interconnects as well as the network designs. Four-node shell elements with a three-layer (PI/metal/PI) composite modelled the 3D and 2D interconnects, and eight-node solid elements modelled the encapsulation and substrate. Refined meshes ensured the computational accuracy using commercial software (Abaqus). To evaluate the stretchability in the encapsulated condition, the 3D and 2D interconnects are embedded in the encapsulation material and tied onto the substrate by predefined constraints. The elastic stretchability corresponds to the point at which the metal layer exceed the yield strength (~200 MPa for Au) across one quarter of the width of any section of the interconnect, and this criterion is supported by previous experimental studies [**32, 228**]. A hyperelastic constitutive relation, i.e., the Mooney-Rivlin law, captured the properties of the elastomeric encapsulation ($E_{encapsulation}$=3 kPa and $\nu_{encapsulation}$=0.49) and substrate material ($E_{substrate}$=20 kPa and $\nu_{substrate}$=0.49). The relevant material parameters are ($C_{10}$=0.40 kPa, $C_{01}$=0.10 kPa, $D_1$=0.04 kPa$^{-1}$) for the encapsulation and ($C_{10}$=2.68 kPa, $C_{01}$=0.67 kPa, $D_1$=0.006 kPa$^{-1}$) for the substrate in Abaqus. The other material parameters used are: $E_{PI}$=2.5 GPa, $\nu_{PI} = 0.27$ for polyimide; and $E_{Au}$=79 GPa, $\nu_{Au}$=0.27 for gold. Here, $E$ is elastic modulus and $\nu$ is Poisson's ratio.

### 3.3.3. Electromagnetic Simulation

The finite element method was used in the electromagnetic simulations to get the return loss parameter (S11) of the 3D soft antenna. The simulations were performed using the commercial software Ansys HFSS (Ansys HFSS 13 User's guide, Ansys Inc. 2011), where the lumped port was used, and the port impedance was set according to the matched capacitor (180 pF). The adaptive mesh (tetrahedron elements) together with a spherical surface (2000 mm in radius) as the radiation boundary, was adopted to ensure computational accuracy. The material parameters include the relative permittivity ($\varepsilon_r$), relative permeability ($\mu_r$) and conductivity ($\sigma$) of Au, PI, Ecoflex and Silbione, i.e., $\varepsilon_r$(Au) = 1,

$\mu_r$(Au) = 0.99996 and $\sigma$(Au) = $4.1 \times 10^7$ S/m; $\varepsilon_r$(PI) = 3.5, $\mu_r$(PI) = 1 and $\sigma$(PI) = 0 S/m; $\varepsilon_r$(Ecoflex) = 2.8, $\mu_r$(Ecoflex) = 1 and $\sigma$(Ecoflex) = 0 S/m; and $\varepsilon_r$(Silbione) = 4.4, $\mu_r$(Silbione) = 1 and $\sigma$(Silbione) = 0 S/m.

## 3.4. Conclusion

We developed a generic solid encapsulation method, capable of offering unprecedented elastic stretchabilities for a broad range of interconnect configurations. In comparison to the conventional 1-stage encapsulation, the proposed 2-stage encapsulation can enable an increase of stretchability by factors of $\sim$6 for 2D serpentine interconnects, $\sim$4 for 2D fractal interconnects, and $\sim$2.6 for 3D helical interconnects. Combined theoretical and experimental studies elucidated the underlying mechanisms of such stretchability enhancement and the effects of various design parameters. Device demonstrations in encapsulated soft LED systems constructed with 3D helical interconnects and 2D fractal interconnects show the ultra-high stretchability can be well maintained at the device level. The presented soft encapsulation strategy has general utility in various stretchable interconnect technologies, and therefore, has promising applications in the design of stretchable devices with different targeted applications.

# CHAPTER 4

# Self-assembled Three-dimensional Network Designs for Soft Electronics

Low modulus, compliant systems of sensors, circuits and radios designed to intimately interface with the soft tissues of the human body are of growing interest, due to their emerging applications in continuous, clinical-quality health monitors and advanced, bioelectronic therapeutics. Although recent research establishes various materials and mechanics concepts for such technologies, all existing approaches involve simple, two-dimensional (2D) layouts in the constituent micro-components and interconnects. Here we introduce concepts in three-dimensional (3D) architectures that bypass important engineering constraints and performance limitations set by traditional, 2D designs. Specifically, open-mesh, 3D interconnect networks of helical microcoils formed by deterministic compressive buckling establish the basis for systems that can offer exceptional low modulus, elastic mechanics, in compact geometries, with active components and sophisticated levels of functionality. Coupled mechanical and electrical design approaches enable layout optimization, assembly processes and encapsulation schemes to yield 3D configurations that satisfy requirements in demanding, complex systems, such as wireless, skin-compatible electronic sensors.

## 4.1. Introduction

Rapid advances in the development of precision chem/ biosensors, low-power radio communication systems, efficient energy harvesting/storage devices, high-capacity memory technologies and miniaturized electronic/optoelectronic components create opportunities for qualitatively expanding the ways that microsystem technologies can be integrated with the human body for treating disease states and monitoring health status [**139, 185, 137, 94, 159**]. Realizing this potential requires not only advances in the components but also in the strategies for their collective integration into systems that offer stable, long-term operation at intimate biotic/abiotic interfaces [**139, 137, 94**]. Promising research in this direction focuses on development of materials and mechanics concepts to enable system-level properties that are mechanically and geometrically matched to those of the soft tissues of the human body [**150, 149, 75, 99, 126, 78, 82, 160, 208, 123, 39, 204, 203, 239, 127, 191, 77, 174, 165, 166**]. Although previously reported approaches provide significant utility in this context [**82, 208, 95, 104, 84, 52, 54, 207, 32, 97, 92, 64, 86, 98, 214, 130, 68, 219, 238**], they all rely on planar, two-dimensional (2D) layouts of the functional elements and electrical interconnects, where the 2D geometries and/or materials define the essential physical characteristics. The work reported here pursues a different strategy, in which system architectures adopt engineered, three-dimensional (3D) designs to provide properties that circumvent intrinsic limitations associated with traditional, 2D counterparts. Specifically, combined experimental and theoretical results demonstrate that open networks of 3D microscale helical interconnects offer nearly ideal mechanics for soft electronic systems that embed chip-scale components, by virtue of model, spring-like behaviors similar to those in man-made

[**141, 152, 213**] (for example, coil spring) and biological [**50, 20, 37, 155, 194**] (for example, tendrils) analogues. Furthermore, scalable methods for forming the required 3D mesostructures together with systematic approaches for defining mechanically and electrically optimized layouts allow immediate application to complex systems. Wireless sensor platforms capable of physiological status monitoring in soft, skin-mounted formats provide demonstration examples. These findings could find broad utility in many classes of soft microsystems technologies.

## 4.2. Results and Discussion

### 4.2.1. Mechanics of 3D helical coils

The assembly approach builds on recently introduced concepts in deterministically controlled buckling processes [**238, 141**], in which initial 2D structures spontaneously transform into desired 3D shapes [**206, 229**]. Figure 4.1a presents finite element analyses (FEA, see Methods section for details) for the formation of an extended, spiral network of 3D helical microstructures from a corresponding 2D precursor that takes the form of a collection of filamentary serpentine ribbons (widths: 50 mm; multilayer construction: 2.5 $\mu$m PI/1.0 $\mu$m Au/5 nm Cr/2.5 $\mu$m PI). Each unit cell consists of two identical arcs with central angle $\theta_0$ and radius $r_0$. The two ends include small discs that form strong covalent siloxane bonds to an underlying elastomeric silicone substrate in a state of biaxial prestrain; other regions adhere only through weak van der Waals interactions. Compressive forces induced by releasing the prestrain cause the 2D precursor to geometrically transform, through a coordinated collection of in-plane and out-of-plane translational and rotational motions, into an engineered 3D configuration via controlled buckling deformations [**206, 229**]. Specifically, each unit cell transforms into a single turn of a corresponding 3D helical microcoil whose pitch ($p$) depends on the serpentine geometry and the magnitude of the prestrain, $\varepsilon_{pre}$, according to $p = 4r_0 \sin(\theta_0/2)/(1+\varepsilon_{pre})$. The overall shape of coil follows mainly from $\varepsilon_{pre}$ and $\theta_0$ (Figure 4.2). Optical images of a representative structure appear in Figure 4.1b. The key dimensions match those from FEA. For example, the experimental and FEA results for the pitch, height of the microcoils are $1150 \pm 40$ $\mu$m, $530 \pm 50$ $\mu$m and 1170 $\mu$m, 520 $\mu$m, respectively.

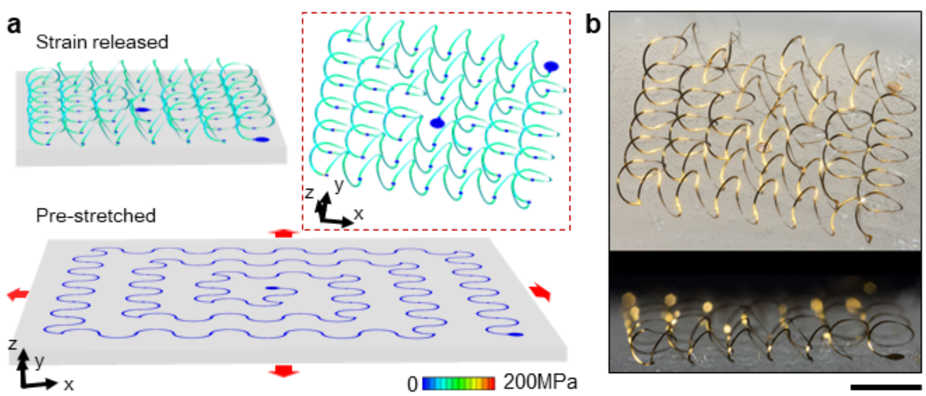


Figure 4.1. Assembly of conductive 3D helical coils. (a) Process for assembly illustrated by finite element analysis (FEA). A 2D filamentary serpentine structure bonded at selected locations to an underling, bi-axially stretched ($\varepsilon_{pre}$) soft elastomeric substrate (pre-streched). Corresponding 3D helical coils formed by relaxation of the substrate to its initial, unstretched state (strain released). The color represents the magnitude of Mises stress in the metal layer. (b) Angled and cross-sectional optical images of an experimentally realized structure. The traces consist of lithographically defined multilayer ribbons of polyimide/Au or Cu/polyimide bonded to a silicone substrate. Scale bar, 1 mm.

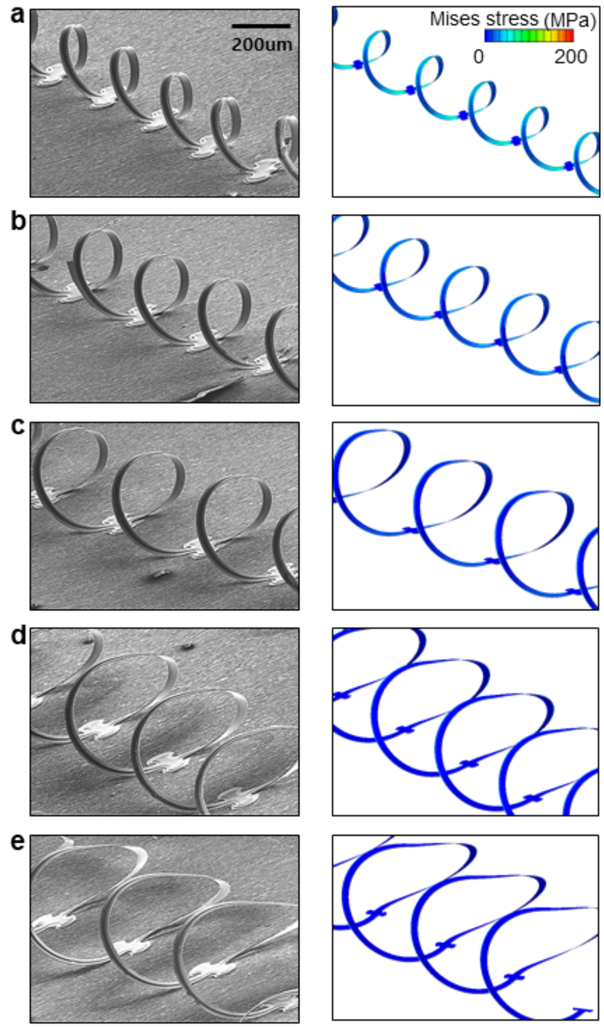


Figure 4.2. SEM images and corresponding FEA results for 3D helical interconnects formed from 2D serpentine microstructures with different arc angles: (a) 120°, (b) 150°, (c) 180°, (d) 210° and (e) 240°.

Although previous studies establish the utility of planar serpentine interconnects in soft electronics, the existence of sharp, localized stress concentrations that follow from their 2D formats and their physical coupling to the substrate limit performance for systems that require low modulus, elastic mechanics in compact designs. By comparison, 3D helical microstructures avoid this unfavorable mechanics due to smoothly varying, uniform distributions of deformation-induced stresses that follow directly from their 3D layouts. The result enables exceptionally high levels of stretchability and mechanical robustness, without the propensity for localized crack formation or fracture, as supported by results in Figure 4.3a,b. For purposes of quantitative comparison, consider a 2D serpentine interconnect with the same material composition (PI/Au/PI) and key geometric parameters (as presented in the previous Chapter 2 and Figure 2.2), including the width ($w$), the thickness ($t_{metal}$ and $t_{PI}$), the span ($S$) and the amplitude ($A$), as a corresponding 3D helix. Here the number of unit cells in the 2D serpentine is selected such that its total trace length ($l_{total}$) is approximately the same as that of the 3D counterpart (10.68 mm, $\theta_0 = 180°$ and $r_0 = 425$ mm). The limit of elastic stretchability, defined as the maximum overall dimensional change below which structural deformations can recover completely, corresponds to the point at which the constituent materials undergo plastic deformation at the locations of highest Mises stress. Results for analogous 2D and 3D systems appear in Figure 4.4. Due to the absence of stress concentrations, the elastic stretchability of the 3D helices significantly exceeds that of the 2D serpentines. The enhancement corresponds to a factor of ~3 for $\varepsilon_{pre} = 50\%$, and this factor increases continuously with $\varepsilon_{pre}$ until it reaches ~9.5 for $\varepsilon_{pre} = 300\%$ (Figure 4.4).

These improvements follow from qualitatively distinct deformation mechanisms in 3D compared to 2D layouts. Figure 4.3a illustrates the nearly ideal, spring-like mechanics that characterize responses in 3D helices. Here, deformations are almost completely decoupled from those of elastomeric substrate and the cross-sectional maximum Mises stress ($\sigma_{Mises}^{cross-section}$) are spatially uniform, except for small regions near the bonding

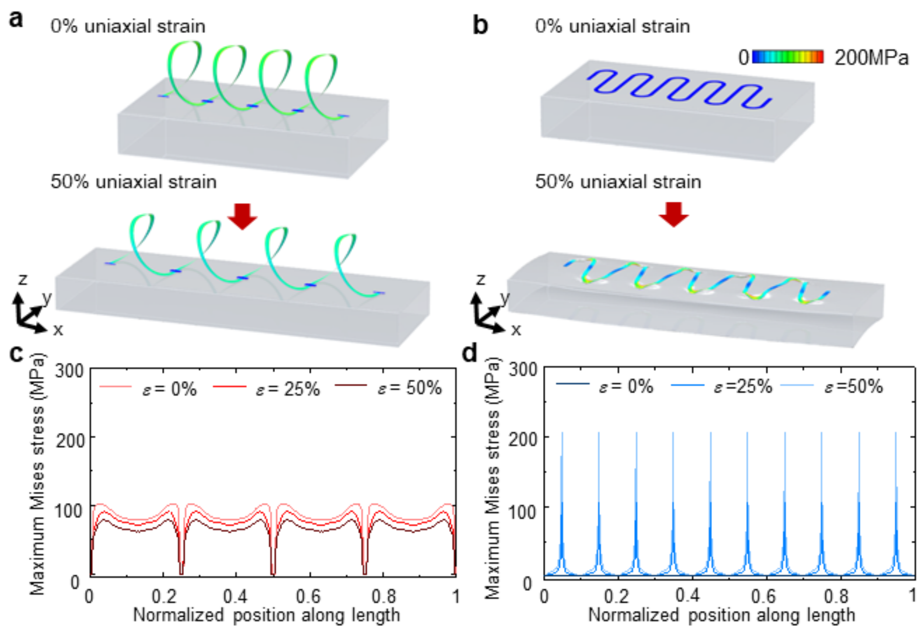


Figure 4.3. FEA results for the deformations and distributions of Mises stress in a 3D coil (a) and a 2D serpentine (b) with similar geometries at 0% and 50% uniaxial strain.(c) Distribution of maximum Mises stress for each cross section along the natural coordinate normalized by the arc length, for the 3D helical coil in a, for three different levels of applied strain (0%, 25%, 50%). (d) Similar results for the case of the 2D serpentine in b.

sites. Quantitative results from FEA appear in Figure 4.3c, which shows the maximum Mises stress for each cross section along the natural coordinate normalized by the arc length. Deformations of the 2D serpentine lead to sharp, unavoidable stress concentrations at the arc regions, as illustrated by the results in Figure 4.3d. The ratio of the peak stress [Peak($\sigma_{Mises}^{cross-section}$)] to its mean value [Mean($\sigma_{Mises}^{cross-section}$)] serves as a metric for the magnitude of this concentration. This ratio is only ∼1.2 for the 3D helices under both applied strains of 25% and 50%, which is nearly an order of magnitude smaller than the ratio (∼9.8) for the 2D serpentines. The non-uniformity in the stress distribution can be

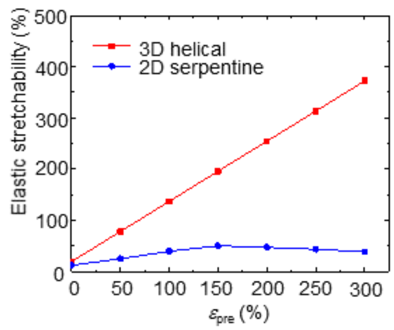


Figure 4.4. Elastic stretchability of the 3D helical coils and 2D serpentine with similar geometric parameters presented in Figure 2.2 as a function of prestrain used in the assembly.

characterized by the average absolute deviation relative to the mean value, as given by $F_{non-uniformity} = \frac{\int_0^1 \sigma_{Mises}^{cross-section} d\overline{S}}{Mean(\sigma_{Mises}^{cross-section})}$, where $\overline{S}$ denotes the natural arc coordinate normalized by the total trace length of entire interconnect. This dimensionless factor also highlights the qualitative differences (for example, 0.15 versus 1.06 for 50% stretch) between behaviors of the 3D helical and 2D serpentine microstructures. Even when compared to fractal 2D designs, in which microfluidic enclosures afford mechanical decoupling from the substrate [**208**] or to bar-type 2D serpentines, in which planar, scissor-like mechanics dominates [**169**], the 3D helical geometry is superior due to the spring-like responses and associated uniformity in the stress distribution (see Figure 4.5, 4.6 and Figure 2.3, 2.4&2.7 in the previous Chapter 2 for details). In particular, 3D helical interconnects outperform 2D serpentine designs that undergo buckling deformations in the form of local wrinkling, typically by a factor >2.3 for representative prestrains (>100%). As compared to thick serpentine interconnects that are dominated by planar, scissor-like mechanics, 3D helical interconnects with a sufficient prestrain (for example, >100%) exhibit a considerable enhancement (for example, >1.8 times) in the elastic stretchability. Similar improvements, at an even greater factor, apply relative to 2D interconnects with fractal-inspired layouts (Figure 4.6).

### 4.2.2. Design of 3D interconnect network of helical coils

The versatility in layouts that can be realized by the assembly approach outlined in Figure 4.1 and 4.3, the scalability of this process to large areas, and the excellent mechanical behaviors of the 3D helical designs facilitate straightforward implementation even in complex systems (see Figure 4.7, 4.8, 4.9, 4.10, 4.11, 4.12, 4.13 and 4.14). The optical image of Figure 4.15a presents an example that consists of ~50 separate chip-scale electrical components, ~250 distinct 3D helical interconnects (PI 2.5 $\mu$m/Au 1 $\mu$m/Cr 5 nm/PI 2.5 $\mu$m multilayers with 50 $\mu$m in width for each line; PI 2.5 $\mu$m/Au 1 $\mu$m/Cr 5 nm/PI 2.5 $\mu$m/Au 1 $\mu$m/Cr 5 nm/PI 2.5 $\mu$m multilayers with 50 $\mu$m in width for each crossing point) adhered at ~500 bonding sites to an elastomeric substrate (E=20 kPa; Ecoflex 00–50, Smooth-on, USA; ~4 cm diameter at rest), all encapsulated with an ultra-low-modulus elastomer (E=3 kPa; Silbione 4717A/B, Bluestar Silicones, France). As described subsequently, this platform provides wireless, battery-free capabilities in continuous monitoring of physiological health from mounting locations on the skin. The inset shows the device in a complex state of deformation to illustrate the soft, skin-like physical properties. The overall layout employs a spider-web-like geometry (Figure 4.16, 4.17 and 4.18), selected to avoid failure at any point in the system, to ensure uniform and extreme levels of stretchability and bendability in any direction and to minimize the overall system size. This unusual

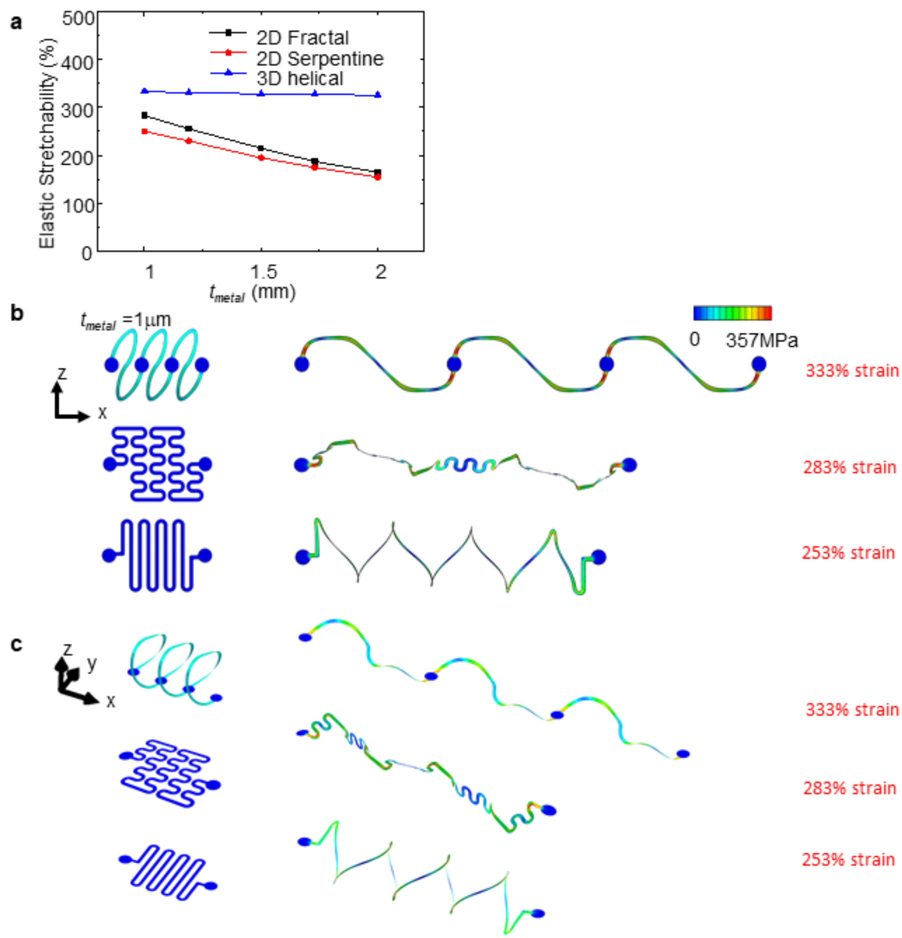


Figure 4.5. Mechanics of 3D helical interconnects in comparison to end-bonded 2D serpentine and fractal interconnects in the unencapsulated condition. (a) Elastic stretchability versus metal (Cu) thickness ($t_{metal}$) in the unencapsulated condition, for 2D serpentine, 2D fractal and 3D helical interconnects. For the purpose of comparison, the key geometric parameters (width, thickness, span, and amplitude) are approximately the same for the three interconnects. The interconnects are all made of single-layer copper. (b) FEA results on the configurations of 3D helical, 2D fractal and serpentine interconnects before and after stretched to the corresponding elastic limit, from a top-view perspective. (c) Similar results from a 3D-view perspective. The color represents the magnitude of Mises stress.

layout follows from a rigorous, systematic design approach that leverages FEA modeling. Specifically, for any given design, FEA allows rapid identification of locations of high Mises

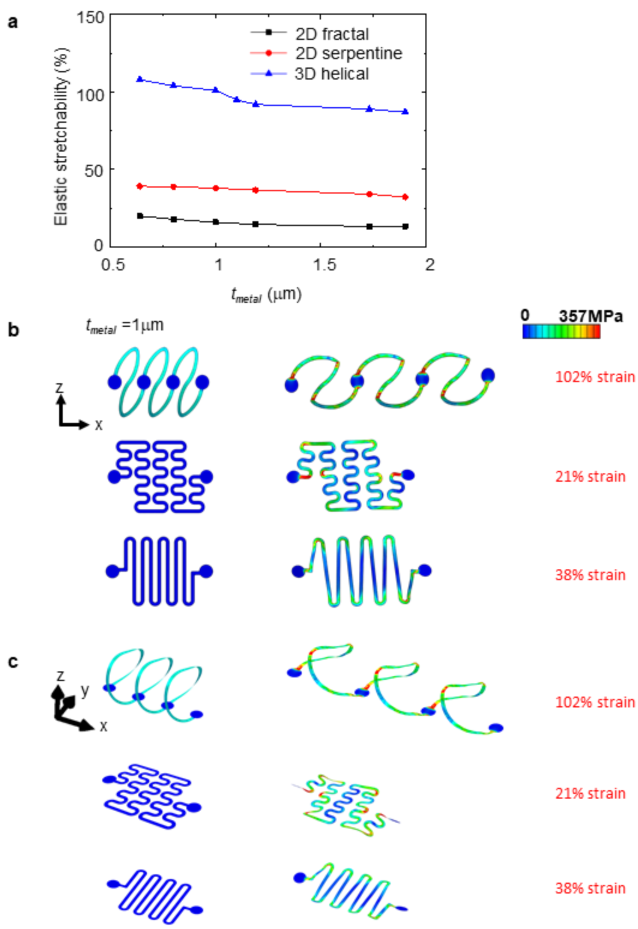


Figure 4.6. Mechanics of 3D helical interconnects in comparison to end-bonded 2D serpentine and fractal interconnects in the encapsulated condition. (a) Elastic stretchability versus metal (Cu) thickness ($t_{metal}$) in the encapsulated condition, for 2D serpentine, 2D fractal and 3D helical interconnects. For the purpose of comparison, the key geometric parameters (width, thickness, span, and amplitude) are approximately the same for the three interconnects. (b) FEA results on the configurations of 3D helical, 2D fractal and serpentine interconnects before and after stretched to the corresponding elastic limit, from a top-view perspective. (c) Similar results from a 3D-view perspective. The color represents the magnitude of Mises stress in the metal layer.

stresses and physical collisions between the different regions of the interconnect network and/or individual components, under various states of deformation within a desired range of strains. Under constraints of interconnect length and connectivity set by considerations in electrical performance (details described below), an iterative process guided by FEA allows optimization of all relevant parameters, including the magnitude of the prestrain in the assembly process, the spatial layouts of the components, the configurations of the bonding sites and the geometries of the 2D serpentine precursors. The use of serpentine unit cells with fixed dimensions across the entire circuit simplifies the design process and yields uniform distributions of Mises stresses.

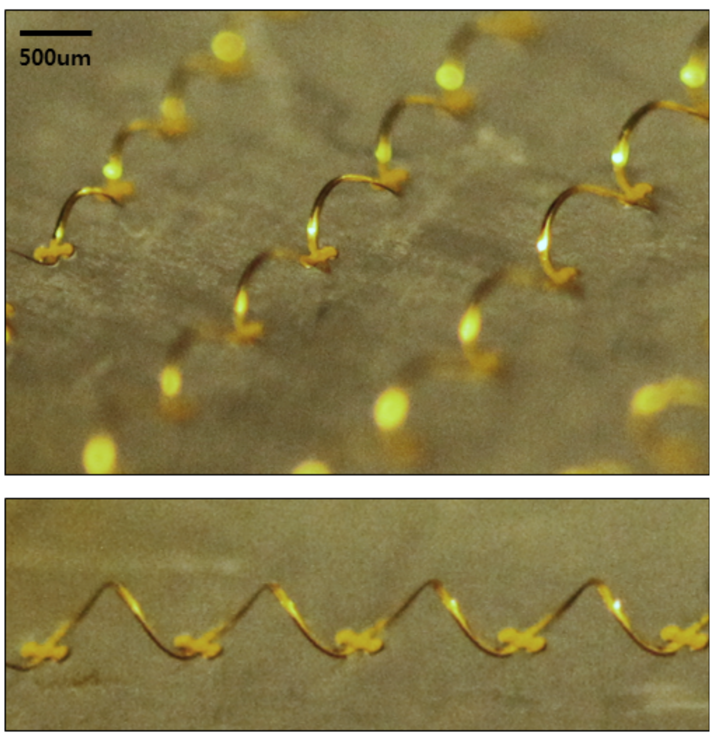


Figure 4.7. Fabricated 3D coil array.

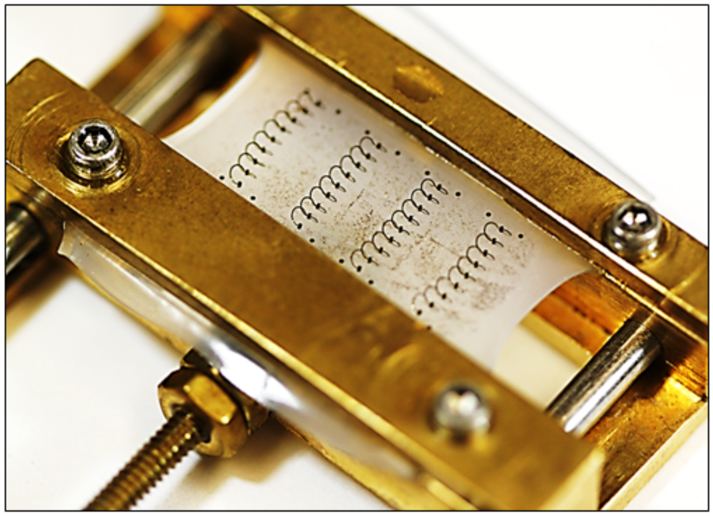

Figure 4.8. Fabricated 3D coil array.

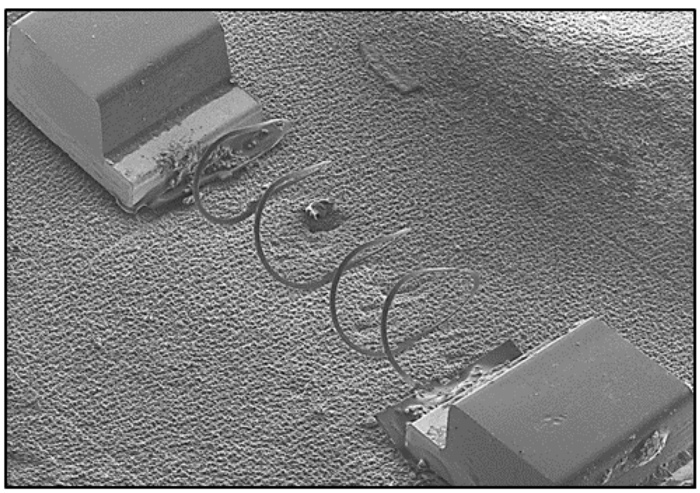

Figure 4.9. Commercial LED chips connected by 3D conductive coils.

Overlaid on these mechanical considerations is a set of electrical requirements. For example, the length of the line that supplies power must be minimized to reduce resistive dissipation and electromagnetic noise associated with radio frequency power delivery. A

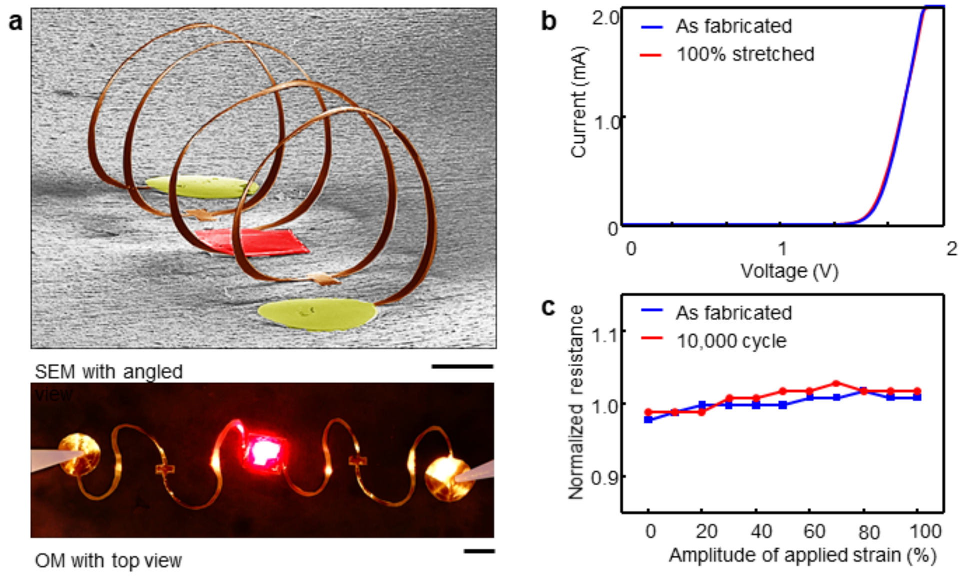


Figure 4.10. Thin film InGaAs LED components connected by 3D conductive coils: (a) SEM and OM images of the fabricated stretchable LED system with coil, (b) I-V curve of the LED system, (c) Mechanical fatigue test up to 10,000 cycles.

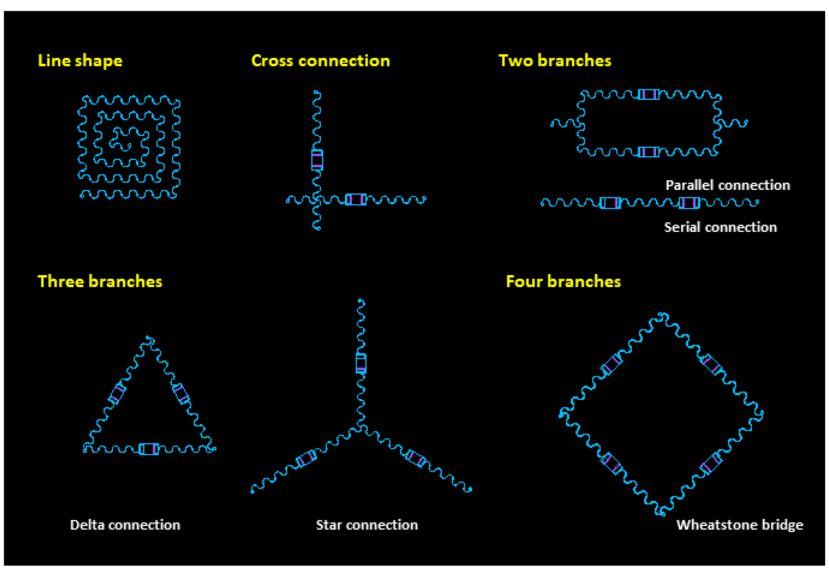


Figure 4.11. Mask design of 3D coil fabrication for basic element of electrical topology.

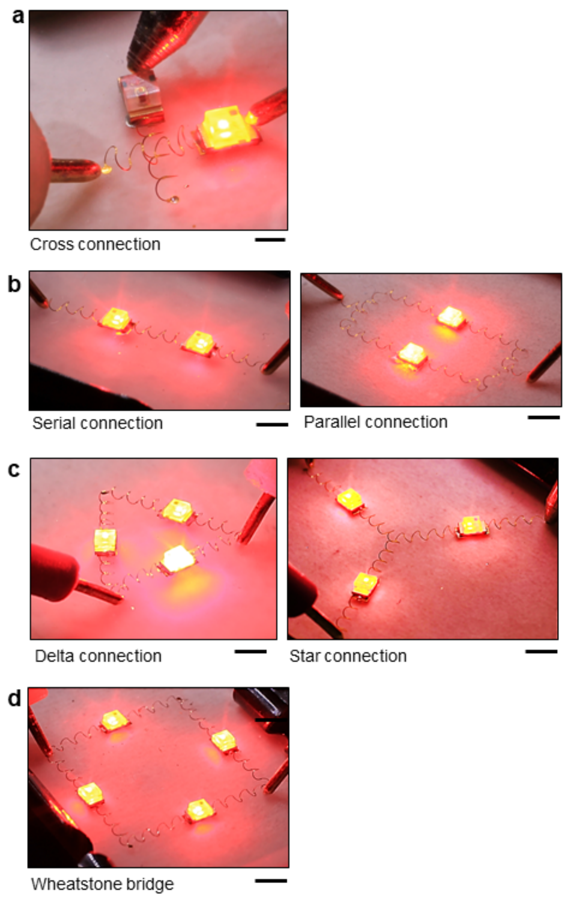


Figure 4.12. 3D coil fabrication for basic element of electrical topology. Scale bar is 3 mm.

large decoupling capacitor (22 mF) at the power source and smaller bypass capacitors at each branch of the supply route, all of which have low equivalent series resistance, help to suppress this noise. The antenna and the electrodes for sensing electrophysiological signals must be spatially separated from the power line to minimize electromagnetic interference, but they must also enable impedance matching (50 Ω). These and other coupled considerations in mechanics and electronics underpin the optimized design shown in Figure 4.15a.

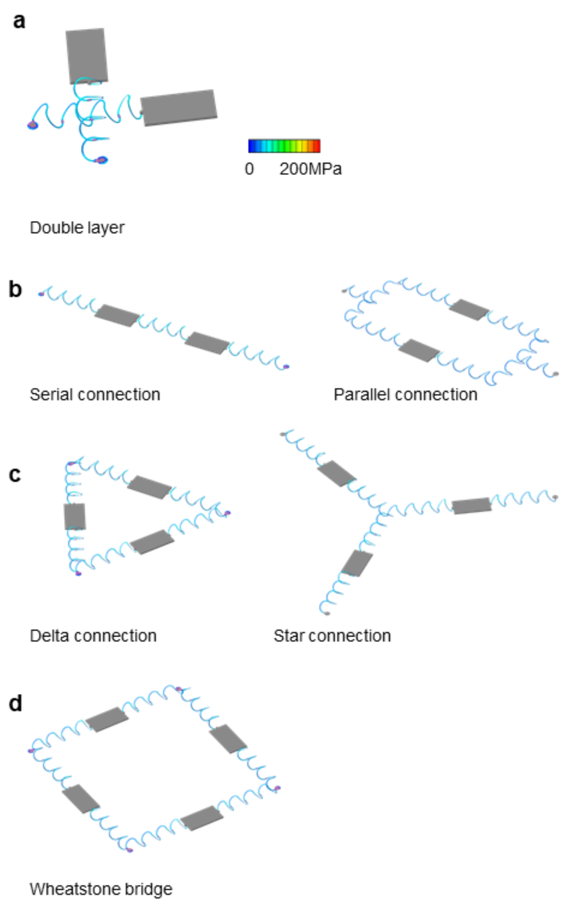


Figure 4.13. FEA predictions on the 3D configurations of basic elements of electrical topology shown in Figure 4.12.

The scanning electron microscope (SEM) images in Figure 4.15b,c&d highlight some key representative regions of this system, including heterogeneously integrated structures of 3D microcoils, chip-scale components and the supporting elastomeric substrate. In terms of the mechanics, these frames highlight the level of agreement between experiment and FEA predictions across the entire structure. Figure 4.15b illustrates electrical crossovers enabled by the multilayer construction of the traces. As shown in Figure 4.15b-d, the bonding sites retain an undeformed shape due to the low modulus of the underlying

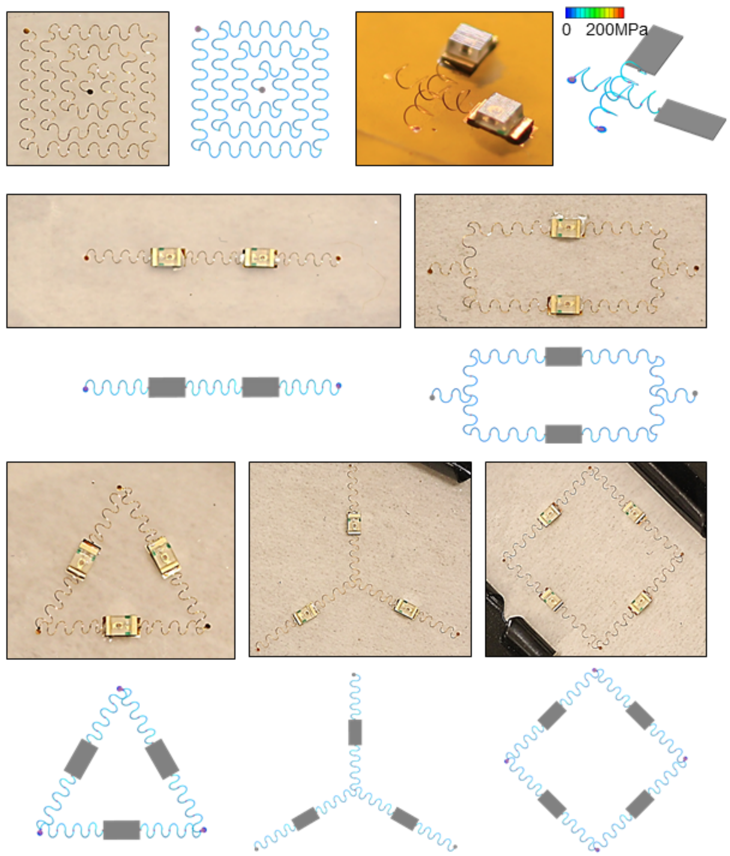


Figure 4.14. FEA results for basic circuits.

elastomer and the relatively large thickness (~6 $\mu$m) of the interconnect structure. The result leads to low levels of Mises stresses at these locations. The chip-scale components prevent corresponding near-surface regions of the elastomer from relaxing after release of the prestrain, thereby inducing a certain level of strain concentration. As such, the portions of the helical interconnects that join directly to the chips undergo a slightly enhanced compression, consistent with the increased Mises stresses in Figure 4.15d. The FEA results in the lower images show the stress field associated with the 3D microcoil.

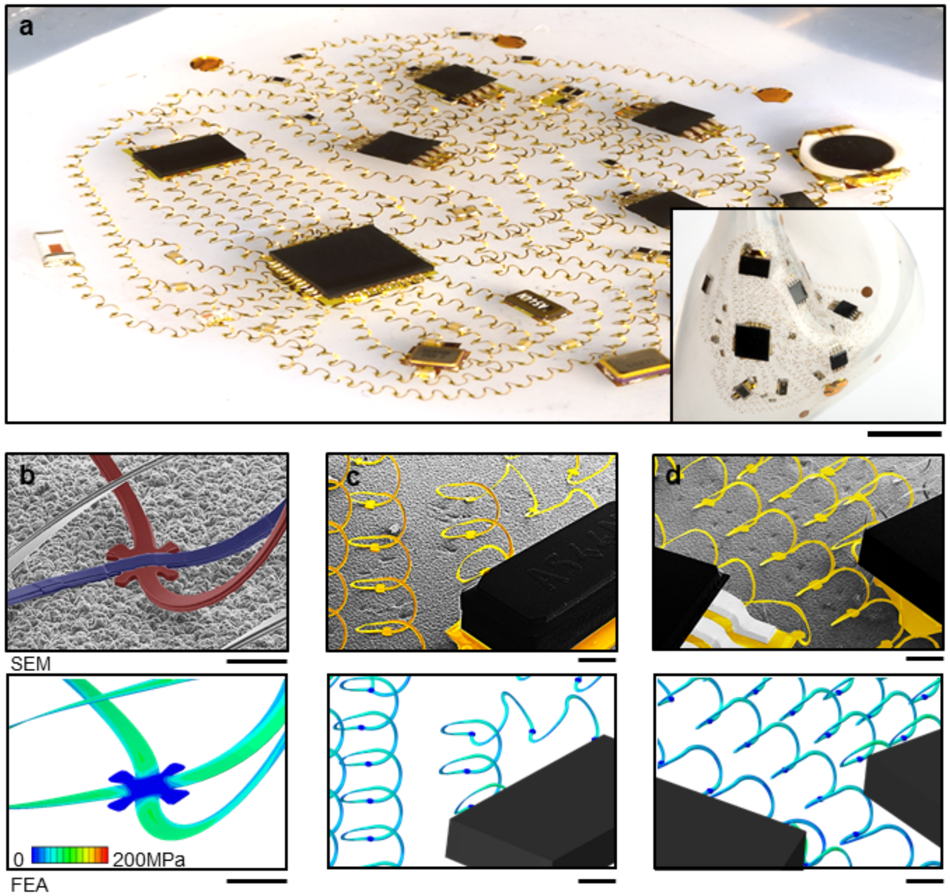


Figure 4.15. Optical image of the system at a bi-axially stretched state of 50%, showing ∼250 3D helices, ∼500 bonding sites, ∼50 component chips and elastomers for full encapsulation (Encapsulation material: Silbione 4717A/B, Bluestar Silicones, France; E=3 kPa; bottom substrate: Ecoflex 00-50A/B, Smooth-on, USA; E=20 kPa) Inset: optical image of the device under a complex state of deformation. Scale bar, 5 mm. Scanning electron micrographs and corresponding FEA results of representative regions of the 3D network, including (b) electrically isolated crossing points and (c,d) interfaces with chip components. Scale bars, 100 $\mu$m(b), 1 mm (c) and 1 mm (d). The widths and thicknesses of all coils throughout this system are 50 $\mu$m and 1 $\mu$m, respectively.

The maximum computed stress in the metal layer across the entire 3D interconnect structure is ∼130 MPa. This value corresponds to ∼0.19% strain, which is below the yielding point (∼0.3%).

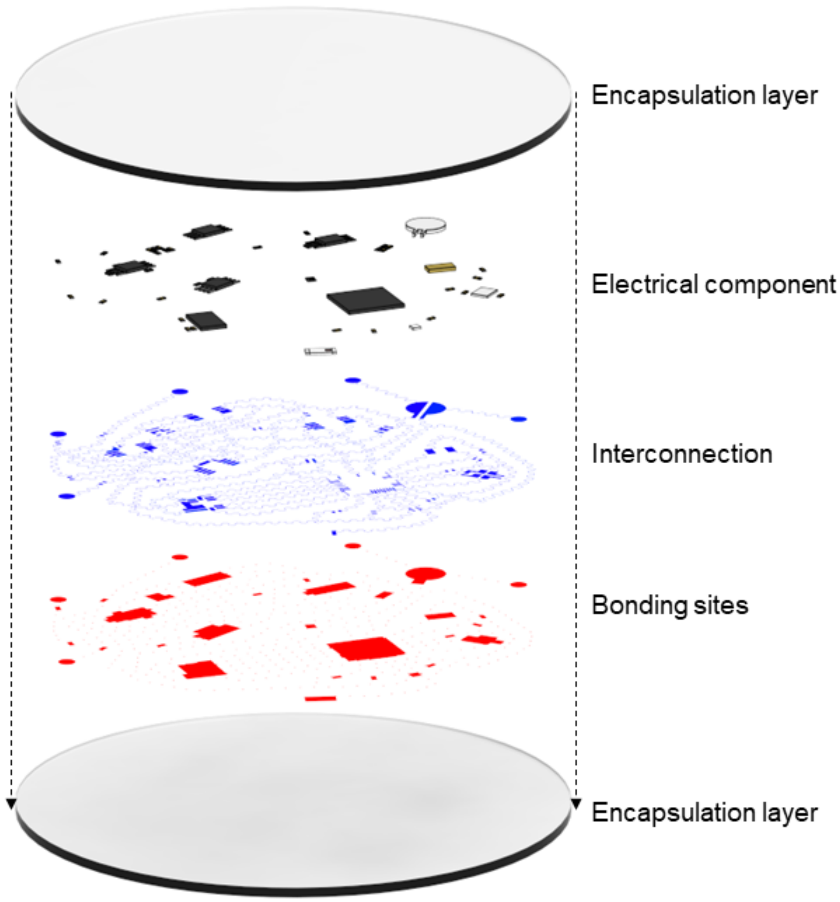


Figure 4.16. Schematics of material integration for 3D coil based circuit.

As depicted in Figure 4.19&4.20, the device functions as a soft, skin mounted technology with important capabilities in monitoring of well-known parameters relevant to physiological health status. Wireless delivery of power to a receiver antenna charges a supercapacitor which then supplies regulated power to the entire system. Sensors allow quantitative measurements of motion, via accelerometry, and electrophysiology, via skin-interfaced electrodes. Raw data pass through a collection of analogue filters and amplifiers

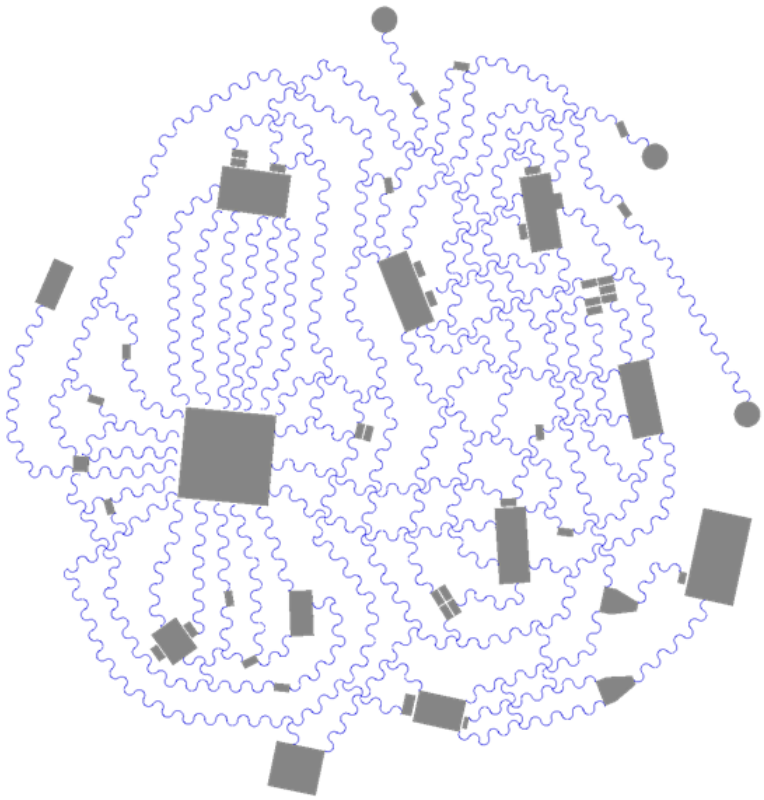

Figure 4.17. Schematic illustration of the 2D precursor for the electronic device system constructed with helical interconnect networks.

prior to wireless transmission using a Bluetooth protocol to a customized app running on a smart phone. Details appear in the Methods section (Section 4.3).

### 4.2.3. Soft encapsulation strategy for enhanced mechanics

Practical applications demand encapsulating layers to protect the active and passive components and the interconnects. As compared with liquid encapsulation [**208**], the solid encapsulation approach adopted in this paper avoids the potential for leakage or evaporation. As in previously reported systems that use 2D serpentines, ultra-low modulus elastomers are attractive due to the minimal mechanical constraints that they impose

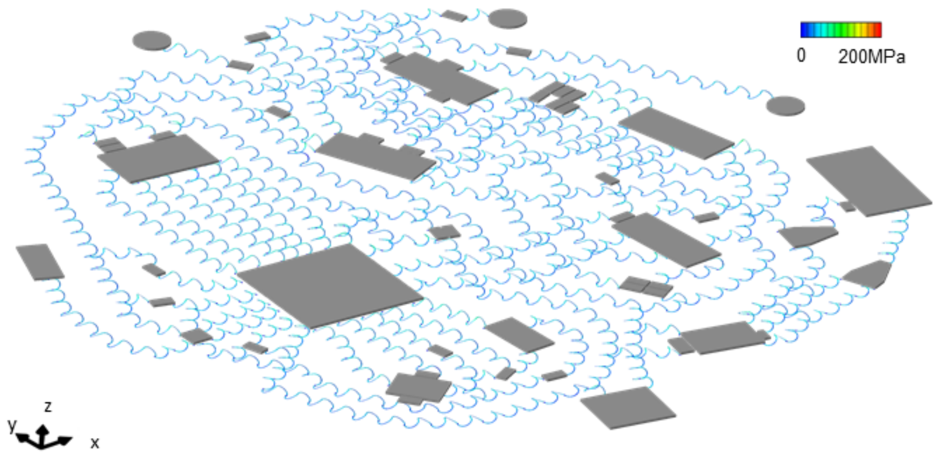


Figure 4.18. FEA prediction on the 3D configuration of the electronic device system constructed with 3D helical interconnect networks. The 3D perspective is the same as the optical image in Figure 4.15. The color represents the magnitude of Misesstress in the metal layer.

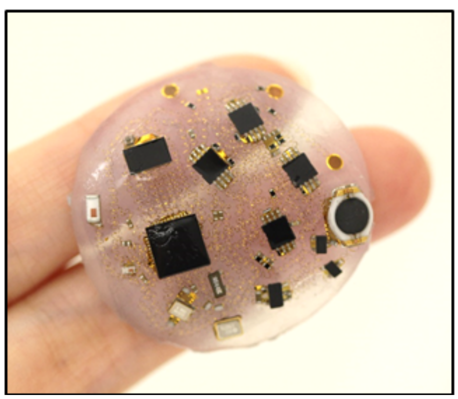

Figure 4.19. Optical image of a device supported by two fingers.

on the motions of the components and interconnect networks. Typically, introduction of this encapsulation material occurs as a final step in the fabrication. An alternative, improved strategy that naturally follows from the 3D assembly process outlined in Figure 4.1 involves applying this material as a liquid precursor at a state of partial release of

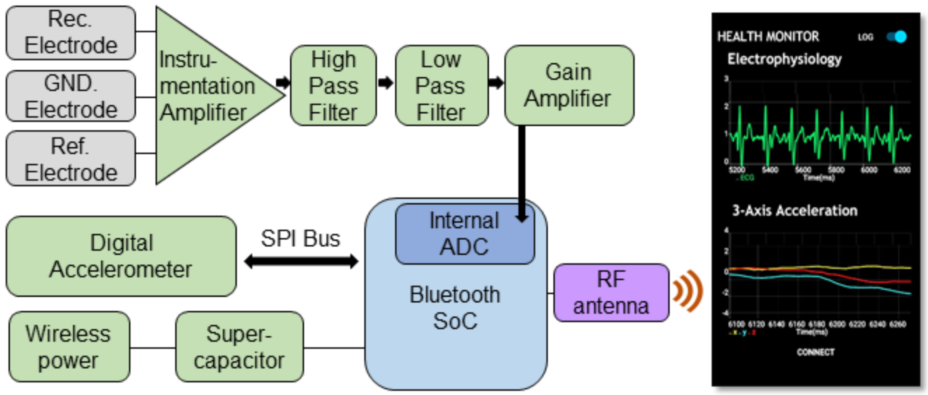


Figure 4.20. Block diagram of the functional components for a set of electrophysiological (EP) sensors with an analogue signal processing unit that includes filters and amplifiers, a three-axial digital accelerometer, a Bluetooth system on a chip (SoC) for signal acquisition and wireless communication, and a wireless power transfer system for battery-free operation. The signal acquisition involves sampling of the EP sensor output through an internal analogue-to-digital converter (ADC) and data acquisition of the accelerometer output via a serial peripheral interface (SPI). When operated using a custom graphical user interface on a smart phone, this system can capture and transmit a range of information related to physiological health.

the substrate prestrain, $\varepsilon_{encap}$, crosslinking it into a solid form and then completing the release (i.e., 2-stage encapsulation strategy, as proposed in Chapter 3), as shown in Figure 4.21. This last step deforms the cured material in a manner that softly embeds the 3D helical interconnects via mechanical interactions during final release. As illustrated by experimental results (Figure 4.22), the 3D buckled structures in the system maintain their original forms during the encapsulation process because their equivalent moduli are sufficiently high that they are not deformed by shear forces associated with the viscosity of the uncured elastomer or liquid.

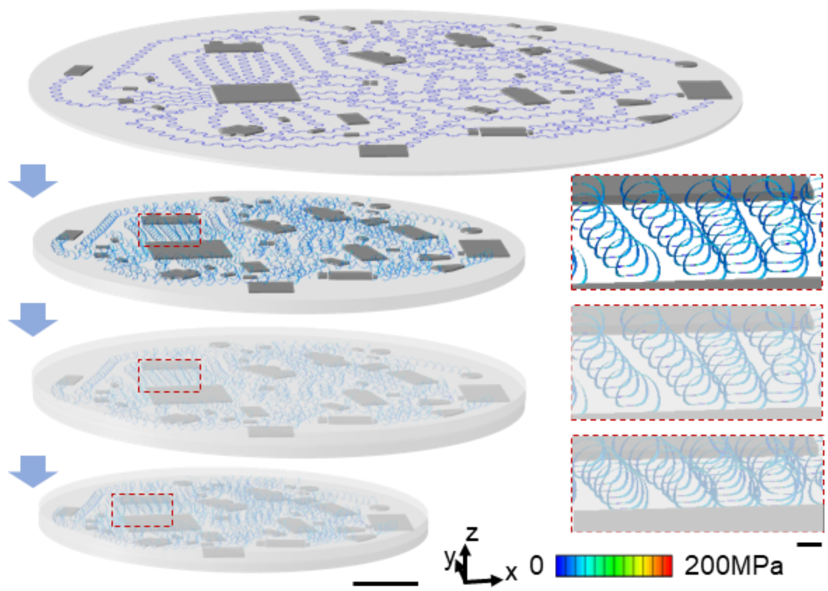


Figure 4.21. Process for soft encapsulation illustrated with FEA results: first, a collection of electronic components joined by an interconnect network in a 2D serpentine design bond at selective sites to a bi-axially prestrained soft elastomeric substrate (Ecoflex 00-50A/B, Smooth-on, USA; E=20 kPa). Partial release of the prestrain mechanically transforms the 2D serpentines into 3D helices. Coating the entire structure with a thin, low-modulus silicone elastomer (Silbione 4717A/B, Bluestar Silicones, France; E=3 kPa) defines the encapsulation layer. Finally, releasing the remaining prestrain enhances the 3D geometry of the helices and completes the process. The insets correspond to magnified views of a local region. Scale bar: 1 cm. The scale bar of the inset is 1 mm.

Quantitative mechanics modeling reveals significant associated improvements in the elastic stretchability (Figure 4.23 and 4.24), compared to the usual case of encapsulation at the final stage of fabrication and assembly. Specifically, the enhancement corresponds to a factor of ~2.2 and 2.8 times for uniaxial and radial stretching, respectively, when $\varepsilon_{encap}$=30% and $\varepsilon_{pre}$=150% for the device in Figure 4.15 ($E_{substrate}$=20 kPa and $E_{encapsulation}$=3 kPa). Modeling is critical for the practical implementation of this concept, simply because the use of $\varepsilon_{encap}$ above a certain threshold (>39% for the case

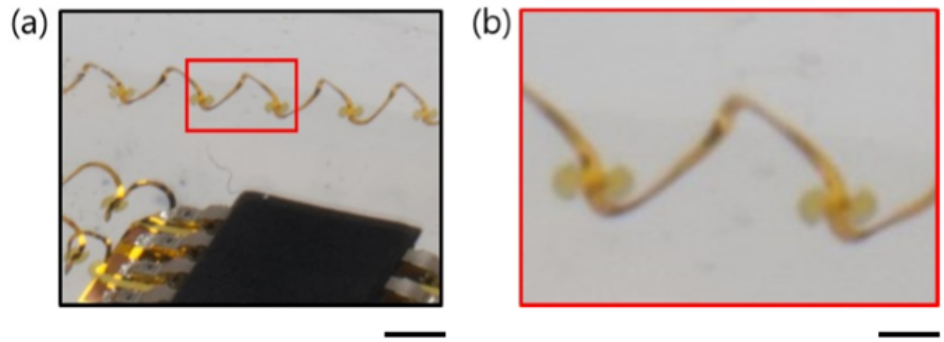


Figure 4.22. Optical images of 3D coil after encapsulation with ultra-soft elastomeric materials (Silbione 4717 A/B, Bluestar Silicones). The 3D structure keeps their original structures well. Scale bars of (a) and (b) are 1mm and 100um, respectively.

examined here) can lead to plastic yielding of the interconnects before full release (Figure 4.21). Near this limit, the elastic stretchability of the encapsulated 3D circuit system approaches that of the unencapsulated counterpart, particularly for uniaxial stretching (for example, 120% versus 144% for X axis and 123% versus 146% for Y axis). By comparison, encapsulation at $\varepsilon_{encap}$=0 (that is, encapsulation after complete assembly, i.e., 1-stage process as mentioned in Chapter 3) retains only limited levels of stretchability (for example, ~50% for X axis, 51% for Y axis, and 25% for radial stretching, respectively), as shown in Figure 4.25a. The deformation mode in Figure 4.25b is, in fact, close to that of an ideal, unencapsulated system (Figure 4.26). In this construction, a radial strain of 70% induces maximum Mises stress of only ~199 MPa (corresponding to its yield strain, ~0.3%) in the active materials (Au of the interconnects), consistent with reversible, elastic behaviors. Furthermore, the stress distribution is uniform across most of the circuit (Figure 4.25c), as additional evidence of the efficient mechanics.

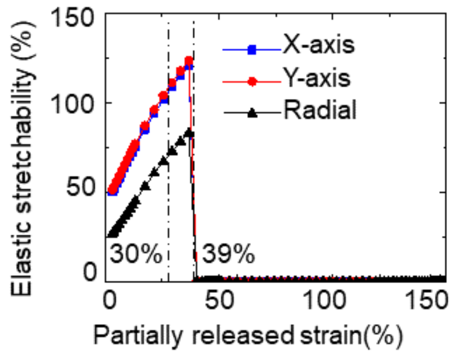


Figure 4.23. Elastic stretchability of a 3D circuit system encapsulated at different states of partially released strain in this two-stage encapsulating process (blue for uniaxial stretching along X axis; red for uniaxial stretching along Y axis; black for radial stretching).

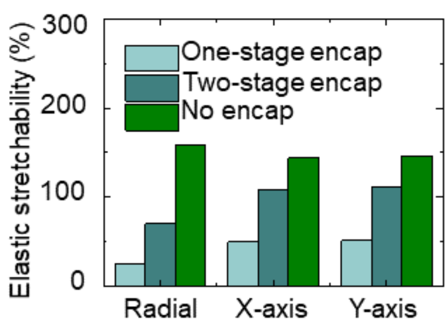


Figure 4.24. Bar graph of the elastic stretchability for a 3D circuit system formed by using a one-stage encapsulating process, two-stage encapsulating process and no encapsulation.

The modulus of the top encapsulation has a significant effect on the stretchability of the 3D helical interconnects (presented in Chapter 2 Figure 2.6a). A low-modulus elastomer (Silbione) reduces mechanical constraints on the deformations of helical interconnects, thereby achieving a much higher stretchability than possible with elastomers with higher modulus values (for example, Ecoflex). The circuit can be designed with improved density

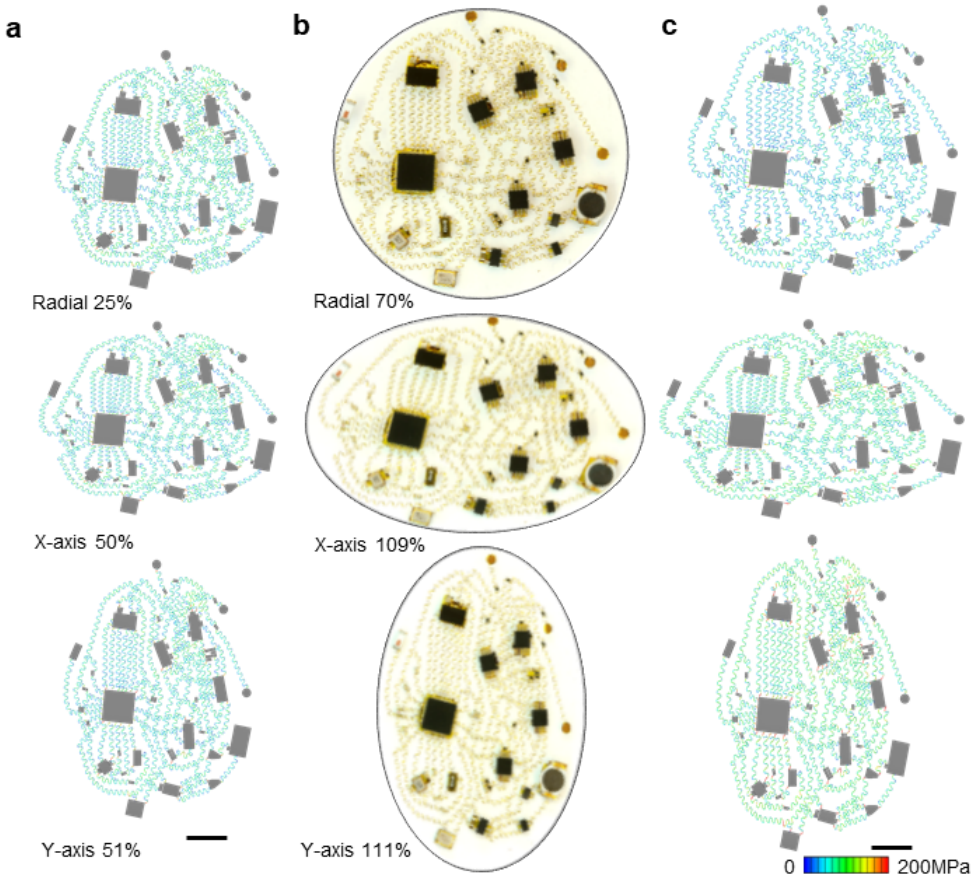


Figure 4.25. System-level deformation and distribution of stresses determined by FEA with encapsulation introduced after (a) full (i.e., 1-stage encapsulation process) and (c) partial (i.e., 2-stage encapsulation process) release of the prestrain. In all of the FEA images, the color represents the magnitude of Mises stress in the metal layer. (b) Optical images of a device deformed in similar ways. Scale bar: 1 cm.

via the use of increased prestrain during the 3D assembly process. By increasing the prestrain from 150% to 200%, the area of entire circuit can be reduced to ∼70% of the original area. The elastic stretchability undergoes a relatively small corresponding reduction, as in Figure 4.27.

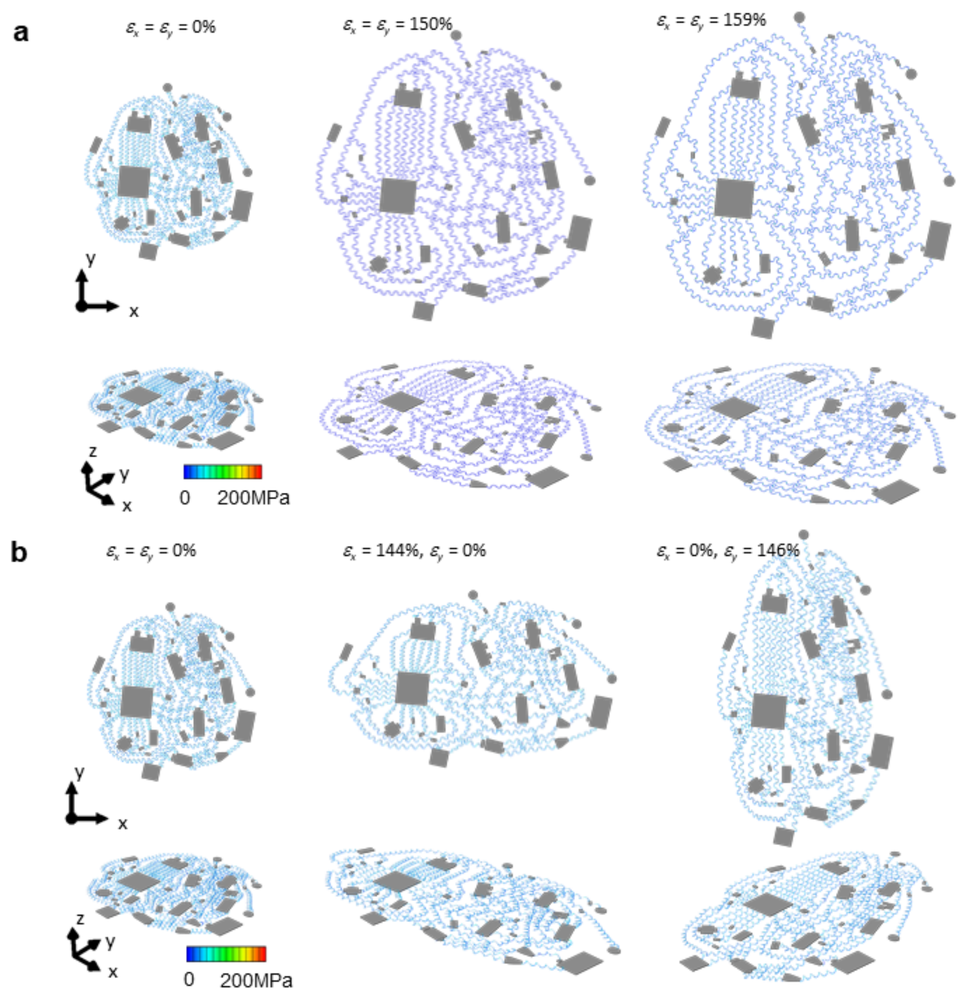


Figure 4.26. Computational studies of the mechanics in an unencapsulated electronic device system with 3D helical interconnect networks. (a) System-level FEA results for the undeformed and deformed configurations of the elctronic device under equal biaxial stretching. Two levels (150% and 159%) of applied strain are adopted, corresponding to the prestrain used in the 3D assembly and the elastic stretchability of device system. (b) System-level FEA results for the undeformed and deformed configurations of the electronic device when uniaxially stretched to the elastic limit (144% for X-axis and 146% for Y-axis). Images with two different view perspectives are shown. The color represents the magnitude of Mises stress in the metal layer.

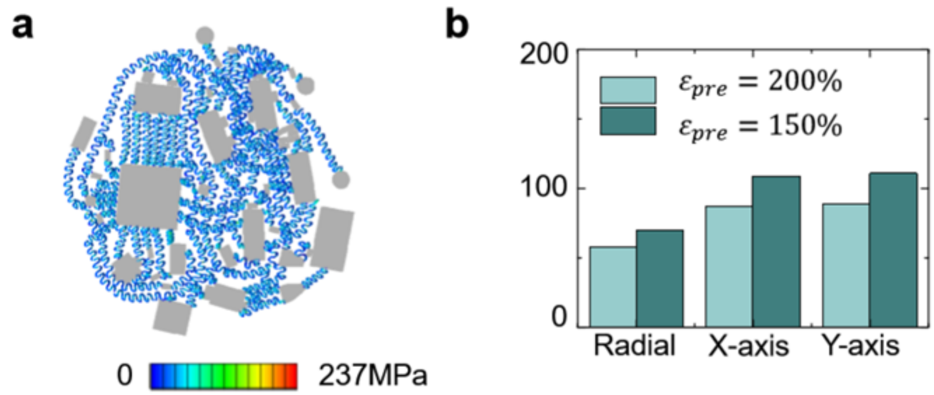


Figure 4.27. Design of circuit system to increase the areal density. (a) FEA result for the deformed configuration of a system with prestrain $\varepsilon_{pre}(200\%)$. (b) Uniaxial and radial elastic stretchability for two prestrains (150% and 200%), and the same encapsulation strain (30%). The color in (a) denotes the Mises stress.

The devices might encounter compression along the thickness direction during practical use, associated with physical contact or normal impact. Quantitative modeling of the encapsulated helical interconnects provides insights into the mechanics associated with such situations. For a variety of prestrains (50%–300%) used in the assembly process, compressive forces (for example, ∼10 kPa) sufficiently large to reduce the out-of-plane dimensions of the interconnects to 30% of the original values (that is, a compression ratio of 0.3) lead to maximum principal strains in the metal layer that are below 1.3%, which is much smaller than the fracture strain (>5%) of gold or copper. This result indicates that the 3D helical interconnects can survive such compression ratios (0.3) and pressures >10kPa. Experimental demonstrations of robust performance of 3D coil interconnect networks, involve simple test structures a LED to allow visual observation of operation. Each LED interconnect takes the form of a 3D helical coil (width 50 $\mu$m, thickness 1 $\mu$m), selectively bonded to an elastomeric substrate (Ecoflex 00–30, Smooth-on, USA; E=$\sim$30 kPa) using interface chemistries described previously and encapsulation with an ultra-soft elastomer (Silbione 4717A/B, Bluestar Silicones, USA; E=$\sim$3 kPa) as outlined above. The computational results and experimental results are in Figure 4.28 and 4.29. The experiments show that an LED system constructed with networks of helical interconnects can survive different types of compressive loadings that might occur in practical use, consistent with modeling results.

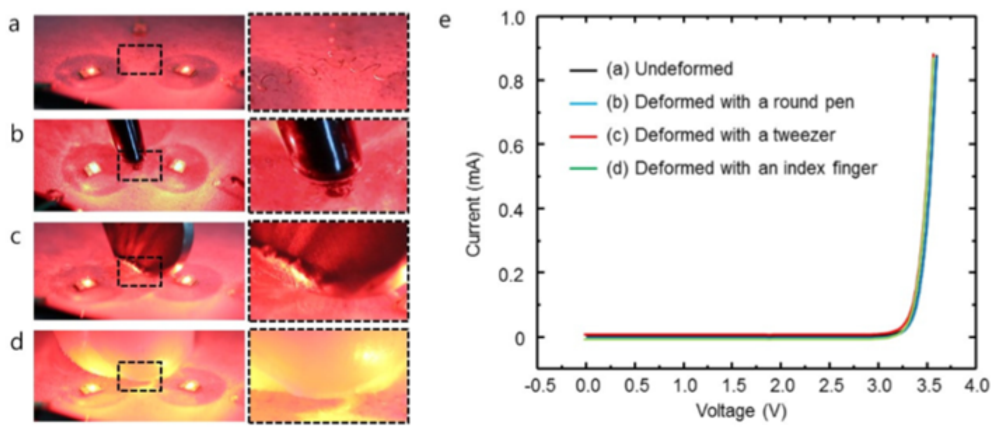


Figure 4.28. A stretchable test structure consisting of a pair of LEDs electrically connected by a 3D helical coil encapsulated in and supported by an elastomer. (a) Compressive loads applied with the tip of a pen (b), the end of a pair of tweezers (c) and an index finger (d). The I-V curves under different conditions are in (e).

Experimental measurements of the mechanical responses also show good agreement with modelling, even at the full system level of $\sim$250 helical interconnects and $\sim$50 chips (Figure 4.25). Overlays of optical images with FEA results (Figure 4.30) facilitate comparisons. Local regions can be examined quantitatively by using the index of structural

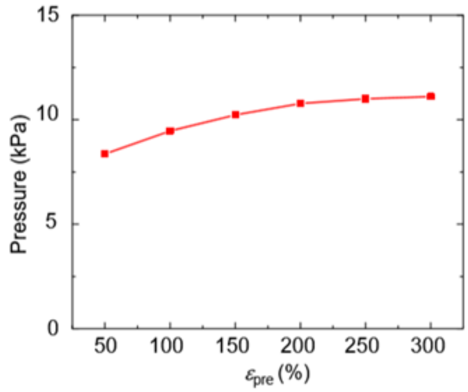


Figure 4.29. FEA results of the pressure needed to compress the 3D helical interconnects such that the out-of-plane dimensions reach 30% of the original values as a function of prestrain used to form the coils.

similarity (SSIM) [**142**]. The results reveal SSIM indices of ~0.81, 0.75 and 0.77, respectively, for the cases of radial, X axis and Y axis stretching shown here (see Figure 4.31 for details). For reference, comparisons of images of local areas to themselves after translation or rotation (Figure 4.32) indicate that an SSIM value of 0.75 corresponds to a 2.3% relative X axis offset, a 2.0% relative Y axis offset or a 3.3° rotation relative to the image center; an SSIM of 0.81 corresponds to a 1.8% X axis offset, a 1.5% Y axis offset or a 2.5° rotation.

### 4.2.4. Demonstration of soft electronics built with 3D helical coil

Figure 4.33, 4.34, 4.35 and 4.36 present optical images of the system in various states of deformation, with an FEA result for the rightmost frame. Functionally, devices with these designs offer reliable operation in all such circumstances (Figure 4.35 and 4.36). Figure 4.37 shows capabilities in three-axis accelerometry for tracking of 3D motion and respiration. As in Figure 4.38, simultaneous monitoring of electrophysiological signals is also

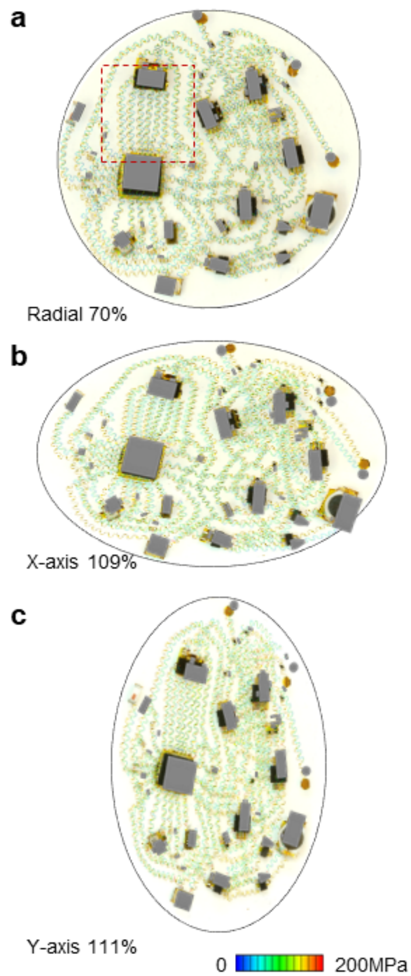


Figure 4.30. Comparison of experiment images and FEA results for the electronic device system with 3D helical interconnect networks under stretching. Optical images overlaid by FEA results for the electronic device system under (a) radial stretching, and uniaxial stretching along (b) X-axis and (c) Y-axis.

possible, including capture of electrocardiogram (ECG), electromyogram (EMG), electrooculogram (EOG) and electroencephalogram (EEG) data for quantitative evaluation of cardiac, muscle, eye and brain activity, respectively. Multimodal operation depicted in Figure 4.39 involves recording of three-axis acceleration and EP signals simultaneously,

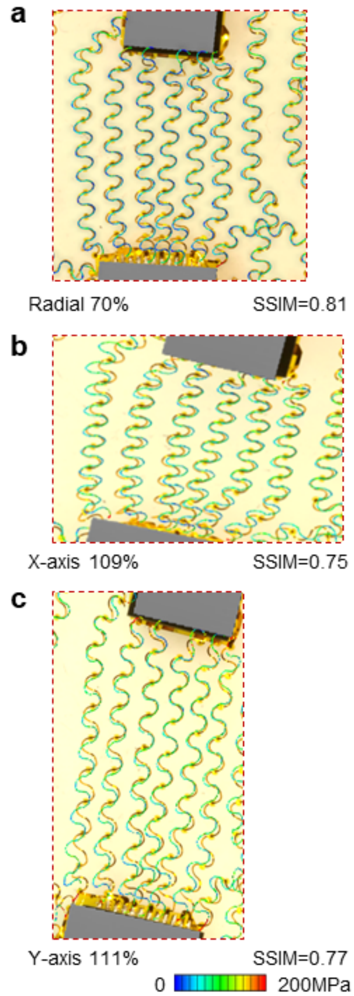


Figure 4.31. Comparison of experiment images and FEA results for a local area of the elctronic device system, with results on Structure Similarity (SSIM). Optical image of a local area of the device (marked by red in Figure 4.30) overlaid by FEA results for the electronic device system under (a) radial stretcing, and uniaxial stretching along (b) X-axis and (c) Y-axis. The SSIM index is calculated using $SSIM(x, y) = (\frac{s_{xy}+C_a}{s_x s_y+C_a})^{\gamma}$, where $S_x$ and $S_y$ are variance of $x$ and $y$, and $s_{xy}$ is the covariance of $x$ and $y$; $C_3 = \frac{1}{2}(k_2 L)^2$ is a variable to stabilize the division with weak denominator, in which $k_2$ is by default taken as 0.03, and $L = 255$ is the dynamic range of the pixel value for the images; $\gamma = 0.5$ is a weight used in the calculation.

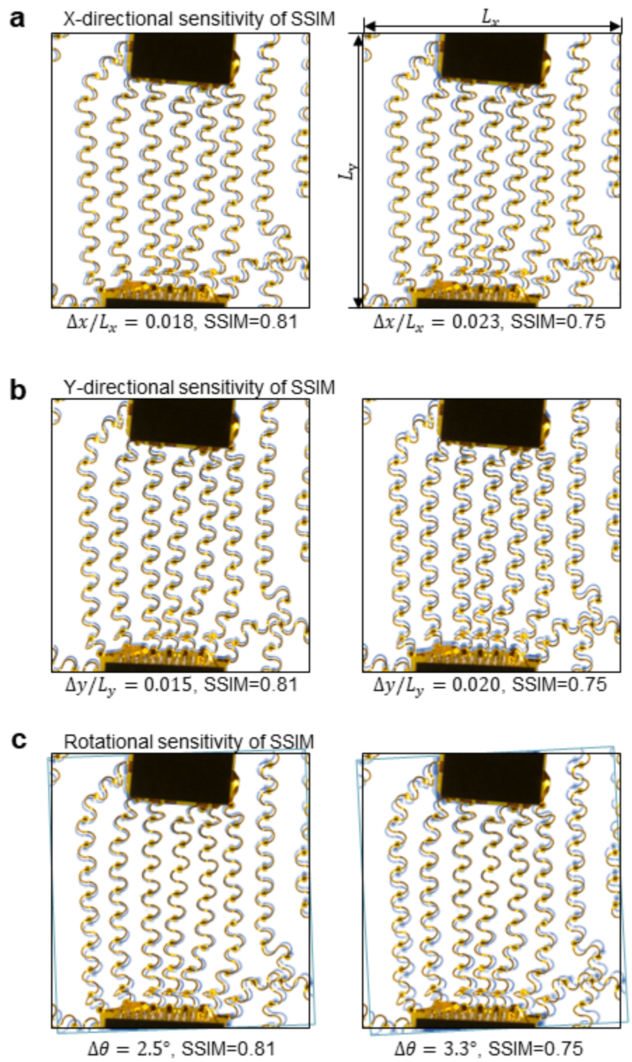


Figure 4.32. Sensitivity of structure similarity (SSIM). (a) Optical image of a local area of the device, overlaid by the same image with two different levels of offset along X-axis to yield SSIM of 0.81 and 0.75. (b) Similar results with two different levels of offset along Y-axis. (c) Similar results with two different levels of rotation with regard to the center.

where the former provides important contextual information on the latter. As shown by Figure 4.40, ECG data collected using a device in an undeformed state are identical to those collected using a device stretched radially to a strain of 50%. This invariance in operation is consistent with electrical resistances of the coils that remain constant under mechanical deformation. The 3D design approaches, the coupled mechanical/electrical considerations in layout and the two-stage encapsulation method, are each critically important in the properties and the operation of such systems.

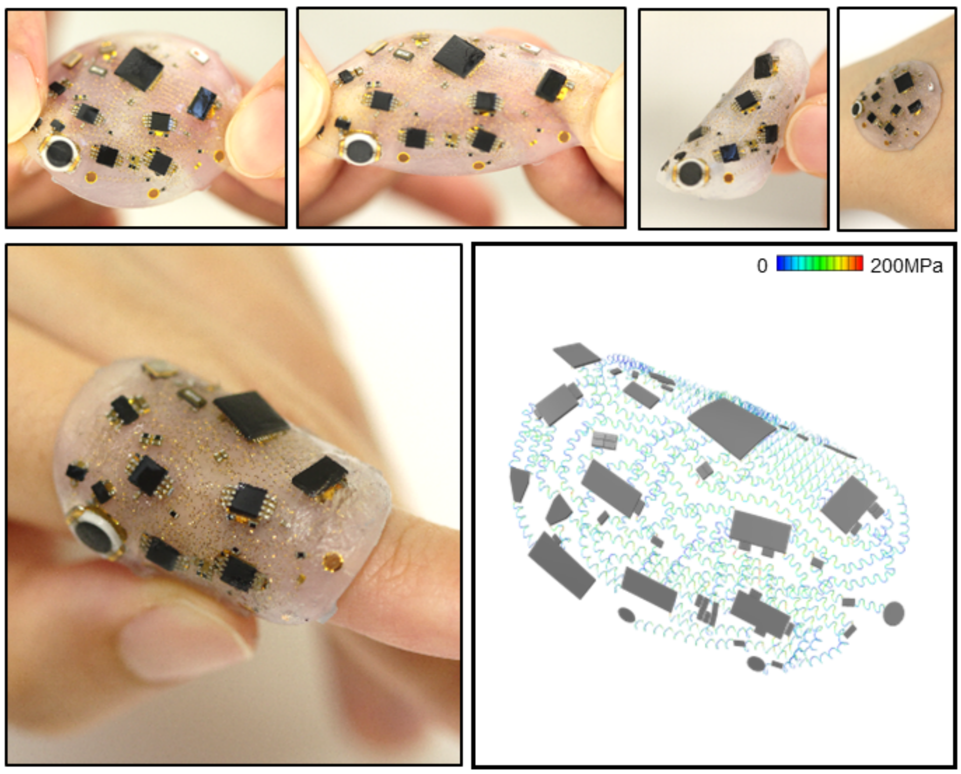


Figure 4.33. Optical images of a device deformed in different ways, with corresponding FEA results in the bottom right box.

## 4.3. Methods

### 4.3.1. Finite element analysis

Three-dimensional FEA techniques allowed prediction of the mechanical deformations and stress distributions of helical interconnects and entire circuit systems, during processes

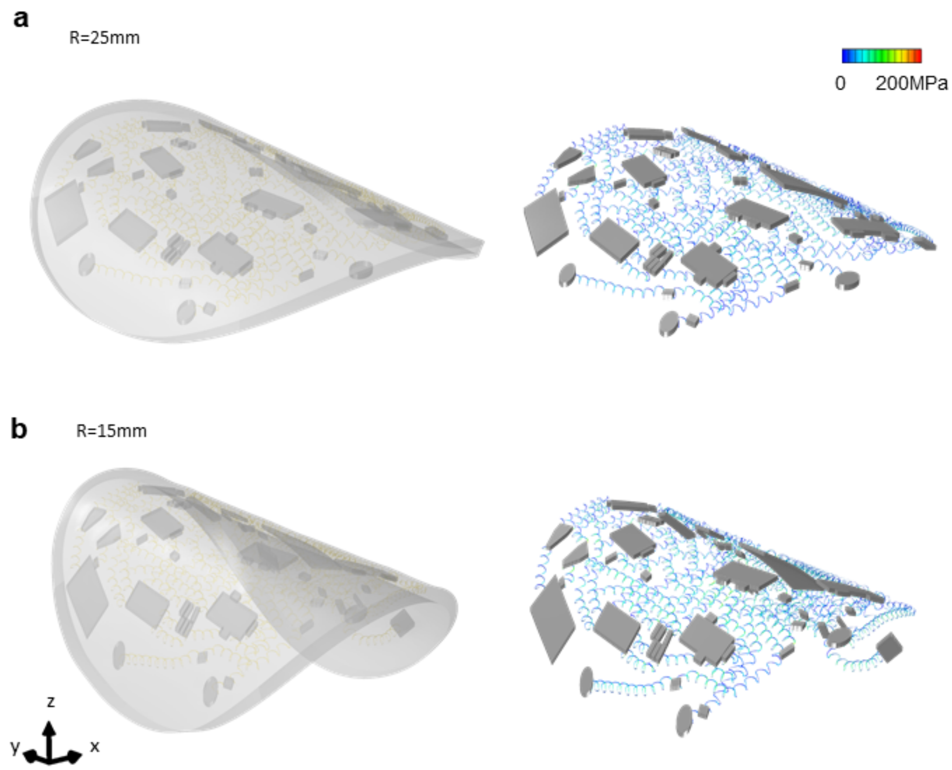


Figure 4.34. Encapsulated electronic device system with 3D helical interconnect networks under bending deformations. (a) System-level FEA result for the deformed configuration of the encapsulated electronic device when wrapped onto a rigid cylinder (radius 25mm). The right image features the distribution of Mises stress in the metal layer. (b) Similar results for the encapsulated electronic device wrapped onto a rigid cylinder (radius 15mm).

of compressive buckling and re-stretching. Four-node shell elements with a three-layer (PI/metal/PI) composite modeled the interconnects, and eight-node solid elements modeled the substrate and encapsulation. Refined meshes ensured computational accuracy using commercial software (Abaqus). The critical buckling strains and corresponding buckling modes determined from linear buckling analyses served as initial imperfections

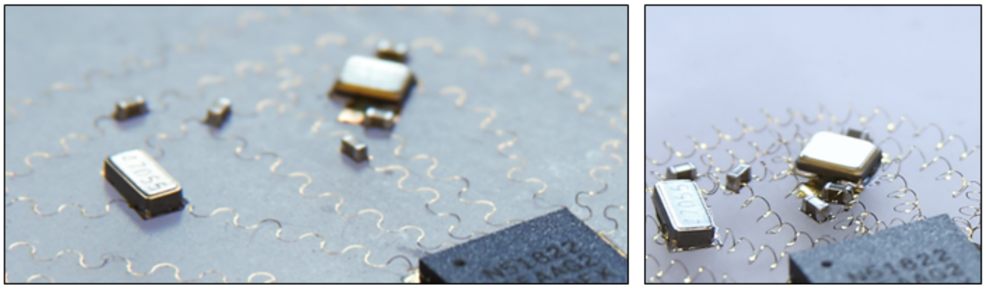

Figure 4.35. Magnified view of the 3D coil based circuit: (a) before and (b) after strain release.

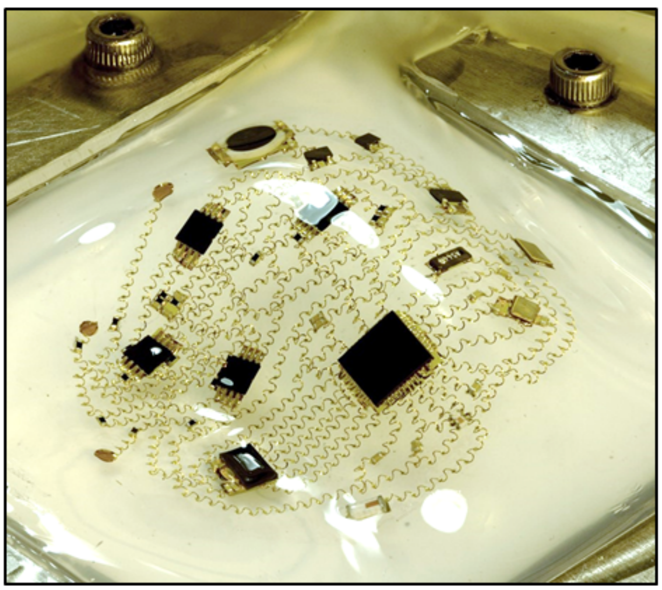

Figure 4.36. Freely deformed 3D coil based circuit.

in the postbuckling analyses to determine the deformed configurations and strain distributions. To evaluate stretchability in the encapsulated condition, 3D helical interconnects determined by postbuckling analyses were embedded in an encapsulation solid that covered the entire area of substrate. The elastic stretchability corresponds to point at which the Mises stresses in the metal layer exceed the yield strength (∼199 MPa for Au and

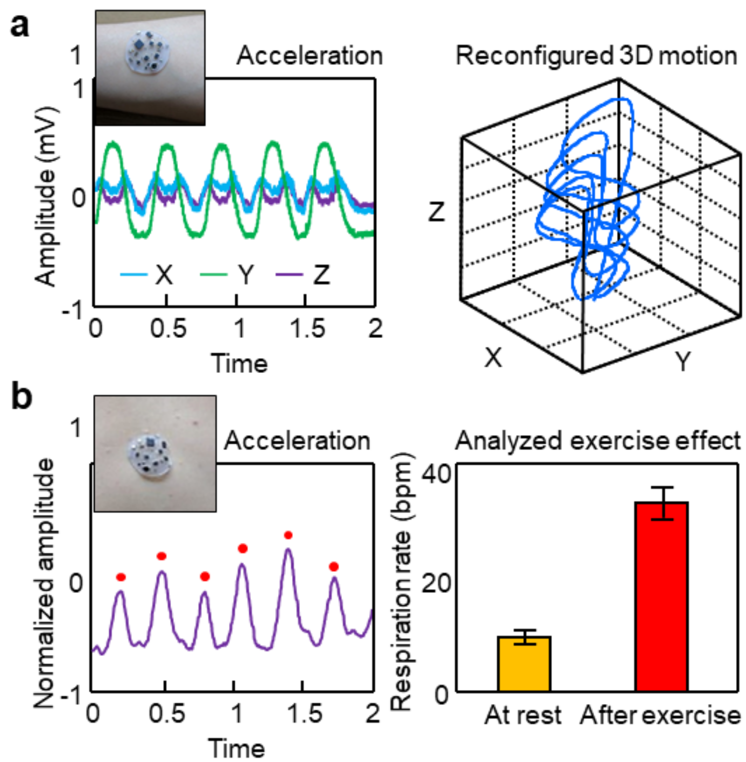


Figure 4.37. (a) Representative recordings of three-axis acceleration from a device on the left forearm and inferred 3D patterns of motion. (b) Results for respiration rate extracted from frequency analysis of accelerometer data from a device placed on the chest, for cases at rest and after physical exercise.

357 MPa for Cu, both corresponding to ~0.3% yield strain) across at least one quarter of the width of any section of the interconnect. Previous experimental studies [**32, 228**] support the use of this type of criterion. A typical hyper-elastic constitutive relation, that is, the Mooney–Rivlin law, captured the properties of the elastomeric substrate (elastic modulus $E_{substrate}$=20 kPa and Poisson's ratio $\nu_{substrate}$=0.49) and encapsulation material ($E_{encapsulation}$=3 kPa and $\nu_{encapsulation}$=0.49). The relevant material parameters are ($C_{10}$=2.68 kPa, $C_{01}$=0.67 kPa, $D_1 = 0.006$ kPa$^{-1}$) for the substrate and ($C_{10} = 0.40$ kPa,

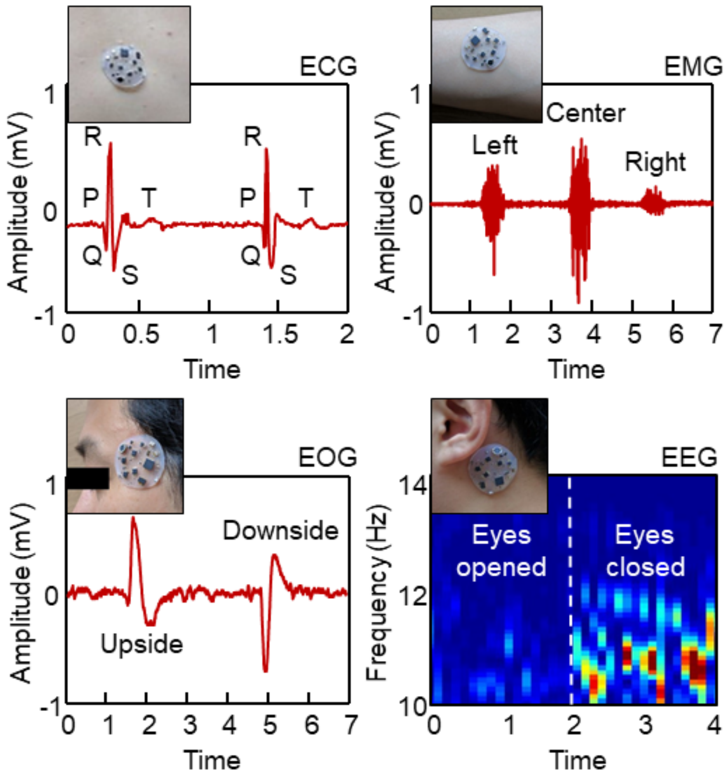


Figure 4.38. Electrophysiological recordings with inset images of the device on the skin: electrocardiogram (ECG), electromyogram (EMG), electrooculogram (EOG) and electroencephalogram (EEG).

$C_{01} = 0.10$ kPa, $D_1 = 0.04$ kPa$^{-1}$) for the encapsulation. The other material parameters are $E_{Au} = 70$ GPa and $\nu_{Au} = 0.44$ for gold; $E_{Ni} = 200$ GPa and $\nu_{Ni} = 0.31$ for nickel; $E_{Cu} = 119$ GPa and $\nu_{Ni} = 0.34$ for copper; and $E_{PI} = 2.5$ GPa and $\nu_{PI} = 0.27$ for PI.

### 4.3.2. Experimental methods

**4.3.2.1. Fabrication of networks of 3D helical coils for fundamental study.** Spin-casting poly(methyl methacrylate) (PMMA; ∼100 nm in thickness, Microchem, USA) formed a thin sacrificial layer on a glass substrate. Spin-casting polyimide (PI;

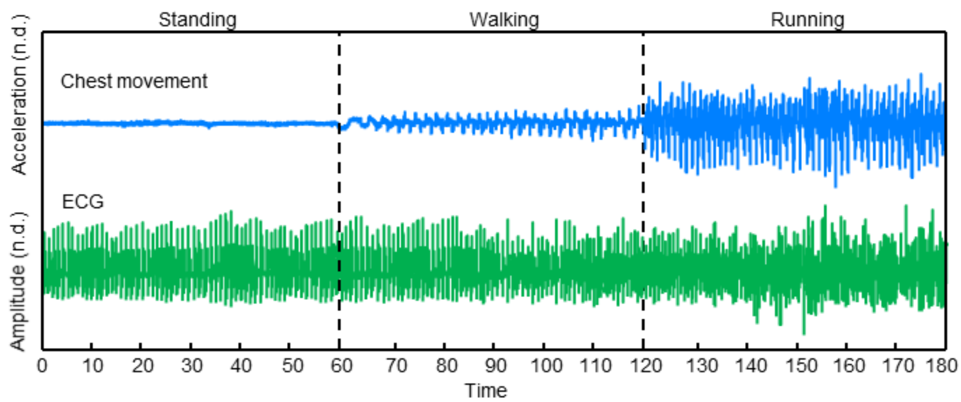


Figure 4.39. Wireless, multimodal monitoring of body activity, through simultaneous measurements of ECG (plotted in green color) and movements of the chest by accelerometry (plotted in blue color) during a time interval that includes standing (0–60s), walking (60–120s) and running (120–180s).

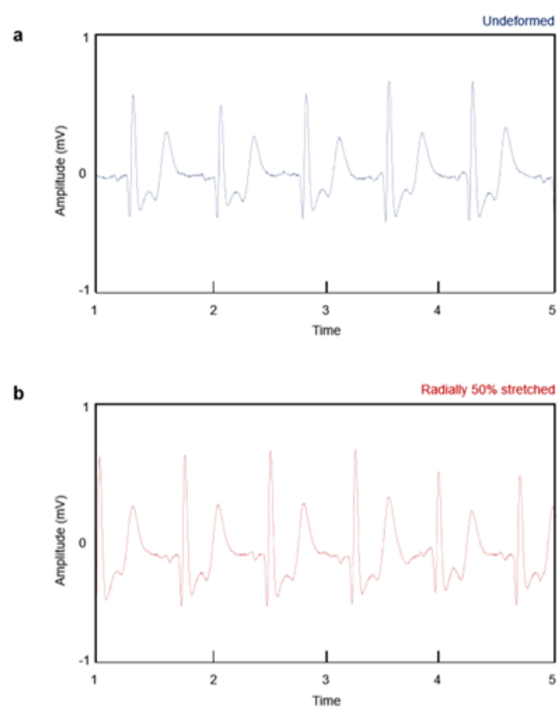


Figure 4.40. Collected ECG signal from the chest: (a) undeformed and (b) radially 50% stretched states.

1∼3 $\mu$m in thickness, Sigma-Aldrich, USA), depositing thin layers of metal by electron beam evaporation (Cr/Au or Cu, thickness 0.1–1 $\mu$m), performing photolithography, wet-etching, spin-casting another layer of polyimide followed by oxygen reactive ion etching defined a network of 2D serpentine structures, referred to here as the 2D precursor. Dissolving the PMMA by immersion in acetone for 10 min allowed retrieval of the 2D precursor onto the surface of a piece of water-soluble tape (Water-Soluble Wave Solder 5414, 3M, USA). Selective deposition of Ti (5 nm)/$SiO_2$(50 nm) by electron beam evaporation through a shadow mask (free-standing patterned sheet of a photodefinable epoxy with thickness of 0.1 mm; SU-8, Microchem, USA) defined sites for strong bonding to a silicone elastomer substrate formed by spin-casting and curing a prepolymer (thickness 1mm; Ecoflex 00-50A/B, Smooth-on, USA) on a glass plate. A custom mechanical stage allowed application of precisely controlled levels of biaxial strain to this elastomer, selected using guidance from computation to achieve the required geometrical transformation from 2D to 3D. Laminating the 2D precursor onto a prestrained substrate and heating (10 min, 70 °C in an oven) the system activated formation of strong siloxane bonds between the patterned SiO2 layer on the 2D precursor and the surface of the silicone substrate. Dissolving the tape by immersion in DI water and releasing the prestrain transformed the 2D precursors into an extended network of 3D helical coils via compressive buckling.

**4.3.2.2. Fabrication process for wireless electronics.** Processes similar to those described in the previous section, but with additional steps in spin-casting, metal deposition, photolithography and reactive ion etching yielded networks with electrically isolated crossing points and contact pads as interfaces to electronic components. A conductive alloy ($In_{97}Ag_3$, Indalloy 290, Indium Corporation, USA) enabled bonding of the contacts associated with the components to the pads in the interconnect network, while still in a 2D geometry on a bi-axially prestretched elastomer substrate. Partially releasing this prestrain followed by casting a uniform layer of an ultra-low-modulus elastomer (Silbione 4717A/B, Bluestar Silicones, France; $E =\sim 3$ kPa) encapsulated the entire system while preserving freedom of motion of the helical coils upon application of strain. This layer physically protected the system from the surroundings during handling and use.

### 4.3.3. Circuit design

**4.3.3.1. Circuit design for electrophysiological sensing module.** The electrocardiography (ECG) circuit used an instrumentation amplifier (INA333, Texas Instruments, common-mode rejection ratio=100 dB) as a pre-amplifier for differential signal inputs to suppress common-mode noise. A driven ground with negative feedback allowed further noise reduction, thereby improving the signal-to-noise ratio. A high-pass filter (4.8 Hz) and a low-pass filter (54.1 Hz) in a SallenKey topology, defined the passband of the circuit. A non-inverting amplifier magnified the filtered signal to provide an overall gain of 40 dB. The circuit used single-ended power at 3.3 V. A DC offset of 1.65 V allows capture of signal in the range between 0 and 3.3 V. An 8-bit analogue-to-digital converter integrated into the wireless chip (nRF51822, Nordic Semiconductor) enabled digital acquisition at a sampling rate of 250 Hz. The same circuit measured electrocardiogram (ECG) and electroencephalogram (EEG) data. The circuit also can perform electrooculography (EOG) and electromyography (EMG) with a gain of 80 dB and a passband of 10-500 Hz and 0.5-20 Hz, respectively.

**4.3.3.2. Circuit design for three-axis acceleration sensing module.** A digital accelerometer (ADXL345, Analog Devices) enabled measurements along three orthogonal axes. The configuration setup involved 13-bit resolution over a range of ±16g, clock polarity=1, and clock phase=1 at a SPI clock speed of 2 MHz. The accelerometer operated at 3 V with bypass capacitors of 10 $\mu$F and 0.1 $\mu$F.

**4.3.3.3. Circuit design for wireless powering module.** Resonant inductive coupling using an unshielded wire wound inductor coil (27T103C, Murata Power Solutions Inc.) served as the basis for a wireless power receiver. A parallel capacitor (12–14 pF) defined a resonance at 13.56 MHz, as measured using an RF Impedance Analyzer (4291A, Hewlett Packard). A full-wave rectifier based on Schottky diodes and a smoothing capacitor rectified the received power. A low-dropout regulator (MIC5205, Microchip Technology) regulated the power at 3.3 V, to charge a supercapacitor (CPH3225A, Seiko Instruments) that operated the embedded system. The transmitter consisted of a circular wire wound coil with a radius of 3 mm, matched at 13.56 MHz, powered with an amplifier module (ID ISC.LR(M)2500, Feig Electronics) capable of delivering between 2 W and 12 W. With this system, 60 mW can be transmitted at 2 W and a 1 cm distance, capable of operating the system, which had a peak power consumption of 30-40 mW.

### 4.3.4. Others

**4.3.4.1. Programming the wireless embedded system.** Commercial packages including Keil $\mu$Vision5 (ARM), Bluetooth Low Energy (BLE) at 2.4 GHz, S110 SoftDevice by Nordic Semiconductor served as tools for building software for the overall system. Wireless transmission of outputs from the ECG circuit and the accelerometer occurred in data packets with sizes of 6 bytes each. A custom Android-based application receives and processes signals from the transmitter. AChartEngine v1.1.0 (The4ViewSoftCompany) defined a graphical user interface with data logging function for further signal processing.

### 4.4. Conclusion

The results presented here establish concepts, as well as routes for practical implementation, for 3D microstructure designs in soft electronics. Specific findings include quantitative advantages of ideal, spring-like mechanics in 3D helical coils compared to traditional 2D layouts; scalable approaches for forming 3D helical frameworks as interconnect networks between advanced microsystem components; combined electrical/mechanical techniques for optimizing system design; encapsulation materials and methods for ideal, 3D mechanics; and multimodal, wireless, skin-mounted demonstration devices for health monitoring. These ideas in 3D design have relevance not only to interconnect networks but also to other sub-systems, such as the antennas, the sensor structures and certain of the active and passive device components as well. Compatibility of the 3D assembly approaches with the most advanced methods in 2D micro/nanofabrication provides alignment both with state-of-the-art microsystems technologies and unusual classes of materials and devices. A combination of established and developing elements in overall architectures that leverage both 2D and 3D layout features affords powerful opportunities not only in bio-integrated electronics but also in many other areas of emerging interest, from soft robotics to systems for virtual reality to hardware for autonomous navigation.

# CHAPTER 5

# Application of 3D Helical Coil on Thermoelectric Generator: Compliant and Stretchable Thermoelectric Coils for Energy Harvesting in Miniature Flexible Devices

With accelerating trends in miniaturization of semiconductor devices, techniques for energy harvesting become increasingly important, especially in wearable technologies and sensors for the Internet-of-things. Although thermoelectric systems have many attractive attributes in this context, maintaining large temperature differences across the device terminals and achieving low thermal impedance interfaces to the surrounding environment become increasingly difficult to achieve as the characteristic dimensions decrease. Here, we propose and demonstrate an architectural solution to this problem, where thin film active materials integrate into compliant, open three dimensional (3D) forms. This approach not only enables efficient thermal impedance matching, but it also multiplies the heat flow through the harvester, thereby increasing the efficiencies for power conversion. Interconnected arrays of 3D thermoelectric coils built using microscale ribbons of monocrystalline silicon as the active material demonstrate these concepts. Quantitative measurements and simulations establish the basic operating principles and the key design features. The results suggest a scalable strategy for deploying hard thermoelectric thin film materials in harvesters that can integrate effectively with soft materials systems, including those of the human body.

## 5.1. Introduction

Thermal gradients are ubiquitous; thermoelectric devices provide means for exploiting these gradients in the generation of electrical power. Here, differences in temperature between the surrounding environment and the human body or an inanimate object/device [**88, 6, 10**] could provide small-scale amounts of power for operation of wearable sensors or "Internet of Things" devices. Continued advances in electronic components and circuit designs enable aggressive down-scaling of power requirements for such systems; the consequences enhance the practical prospects for thermoelectric and other strategies for energy harvesting [**134, 28, 132**]. As examples, integrated processors [**106**] and radio transmitters [**120**] that operate with power in the sub-nW range can be driven using energy harvested from ambient light [**106**] and the endocochlear potential [**121**], respectively. Pairing such platforms with sensors that have similar power budgets could enable distributed, continuous and remote environmental or biochemical monitoring [**125**].

A key challenge in the development of miniaturized thermoelectric harvesters is in matching the thermal impedance of heat exchange with the active material in the natural direction of heat flow, typically oriented out-of-the-plane, through the device. Thin films have minimal thermal impedance in this direction due to their small thicknesses, such that the temperature drop across this direction is, in practical terms of thermoelectric energy harvesting, negligible. As a result, most reported thermoelectric devices based on thin film materials use thermal gradients that form in the plane [**184, 23, 140**]. In geometries of practical significance, the impedance is rarely matched.

The use of thick films (tens to hundreds of microns) deposited by electroplating [**156**] or printing [**88, 156**] can help match the out-of-plane thermal impedance, but this approach typically results in harvesters that are rather bulky [**89**]. In addition, the heat exchange capabilities from natural air convection in such devices is limited by their planar surface areas. The result could be diminishing output voltage over time as the device reaches a steady state temperature distribution. Strategies that exploit thin film materials rolled into cylinders yield multilayer stacks aligned with thermal gradients in the in-plane direction of the films [**197**] can enhance impedance matching. Parasitic flow of heat through the substrate, which is also aligned with the thermal gradient, represents a design challenge inherent in this approach.

Mechanical compliance is an additional consideration for integrating harvesters with the curved surfaces of the human body or with non-planar substrates that can be common in Internet-of-things applications. Combining thin polymer substrates or metal foils with inorganic thermoelectric films, wires or ribbons [**88, 23, 156, 170**] represents a well-developed route to flexible systems. Alternative approaches use organic thermoelectric materials or composites [**190, 143, 117, 21, 5, 116, 14**]. In both cases, however, the resulting planar and thin device designs suffer from the challenges in thermal design mentioned above.

Here we propose and demonstrate an architectural solution to this challenge, in which two dimensional (2D) device structures formed using planar transfer, deposition and patterning techniques serve as precursors in the assembly of interconnected arrays of functional, three dimensional (3D) helical coils. In this way, the in-plane direction of thin film active materials rotates to align towards the out-of-plane direction of the device. This design strategy has the advantage that it is compatible with the most advanced materials and techniques in planar microsystem technologies. Additionally, the naturally compliant nature of the coils allows these systems to conform to complex curvilinear surfaces, even those that are time-dynamic, thereby ensuring excellent thermal contact with the heat source. Above all, the 3D nature of the system provides a multi-fold increase of the surface area, resulting in higher overall heat exchange capability and thus higher maximum power.

## 5.2. Results and Discussion

### 5.2.1. Design and assembly approaches

Our demonstration of this thermoelectric helical coil architecture uses monocrystalline silicon as the active material, as shown in the schematic illustration of Figure 5.1. Here, mechanically guided assembly [**206, 210, 65, 230, 38**] generates 3D helical structures from 2D serpentines via compressive buckling induced by relaxing a previously stretched elastomer substrate to which the serpentines bond at selected locations; strong chemical bonds follow from condensation reactions between surface hydroxyl groups on the surface of the elastomer and patterns of silicon oxide (fabrication procedure in Figure 5.2) formed on the serpentines. The serpentines incorporate silicon ribbons with p- and n-type segments, termed p- and n- “legs”, connected in a series arrangement by lithographically patterned traces of metal (Figure 5.3). Polymer coatings formed on the top and bottom sides encapsulate the system (Figure 5.4) in a manner that also locates the silicon at the neutral mechanical plane to enhance fabrication yields during the bending and twisting deformations associated with transformation from 2D to 3D, and during deployment and use. In the final configuration, the legs serve as the pathways for thermal transport between the substrate and the environment. Specifically, as the substrate equilibrates with the thermal source, heat passes into the coils at the bonding locations. The encapsulation layers have widths larger than those of the silicon ribbons to increase the surface area as the cold-side heat exchanger and to provide mechanical support and protection.

As mentioned previously, the 3D coils also provide remarkable levels of mechanical compliance and robustness during handling and bending (Figure 5.5), even though they incorporate heavily-doped silicon (fracture strain $\approx$0.1% [**186**]). The assembly process can naturally scale to large arrays without deviating from the geometry predicted by finite element analysis (Figure 5.6). Such characteristics render these systems well suited for forming intimate thermal interfaces to the human body, such as the wrist or ankle (Figure 5.7), as well as other objects with curvilinear shapes. Although the examples presented here utilize a particular set of materials, fabrication schemes and device geometries, and the overall concepts have broad applicability.

### 5.2.2. Finite element analysis (FEA) for geometry optimization

The mechanical and thermal properties of 3D coils can be accurately predicted by finite element analysis, such that a full-scale, thermo-mechanically coupled model can provide critical guidance on selection of materials and geometrical configurations. An optimized layout based on using silicon (thickness = 0.2 $\mu$m) and polyimide (PI; total thickness = 8 $\mu$m) as active and encapsulating materials, respectively, incorporates a tapered serpentine geometry. The unit leg length is 1.57 mm with a constant curvature, and the PI widths at the top and bottom of the leg are 0.3 mm and 0.17 mm, respectively (i.e.

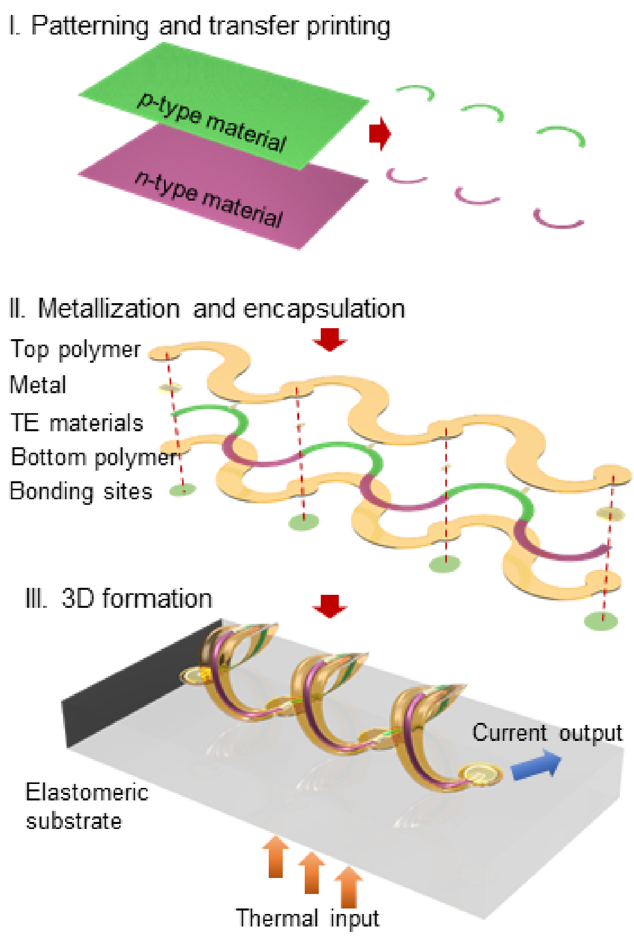


Figure 5.1. Schematic illustration of the process for fabrication and 3D assembly. Thin film p- and n-type materials patterned into two dimensional (2D) serpentine shapes and transferred onto a layer of polyimide define the active materials. Metal junctions and a top coating of polyimide patterned by photolithography and etching, complete the formation of 2D precursor structures. Chemically bonding such systems to a 60% uniaxially pre-stretched silicone substrate at selective locations (hot-side junctions), followed by release of the pre-stretch initiates a process of geometrical transformation that yields the final 3D architectures. See Methods for details.

ratio is 2). The following sections summarize the thermal and mechanical aspects of this computationally guided optimization process.

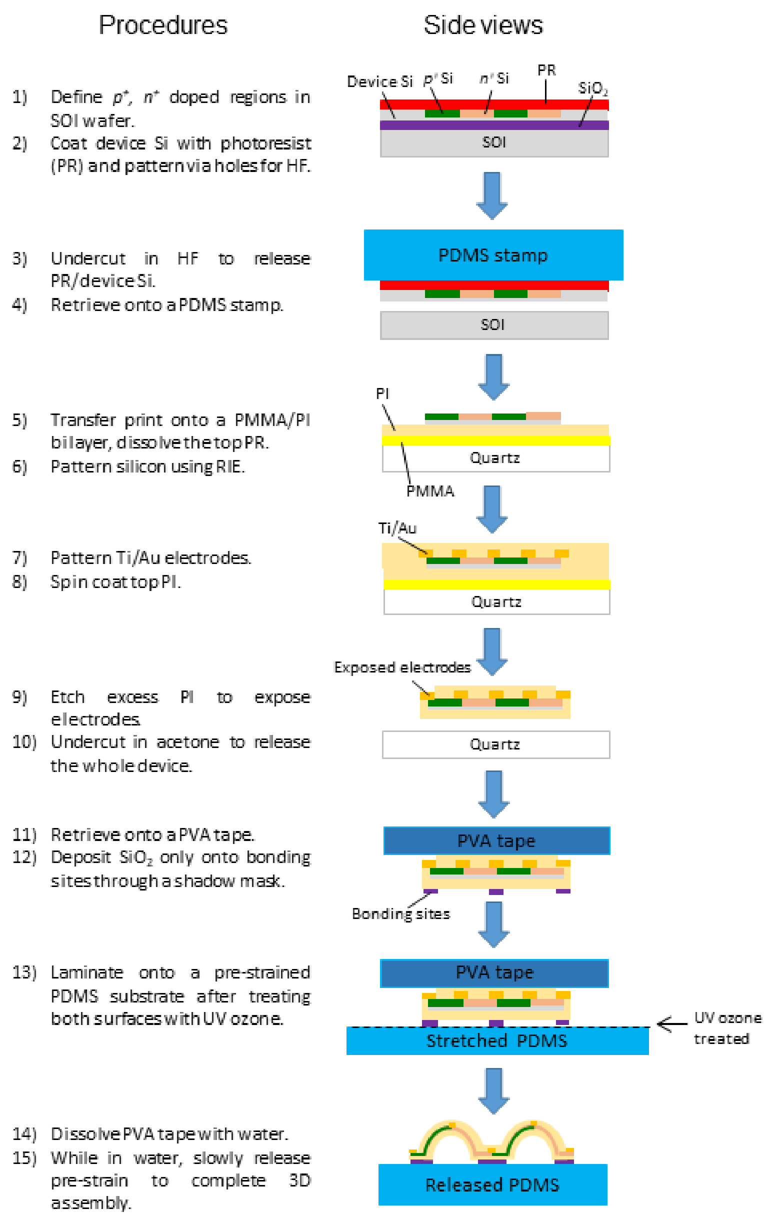


Figure 5.2. Schematic step-by-step fabrication procedures for 3D compliant, stretchable thermoelectric coils.

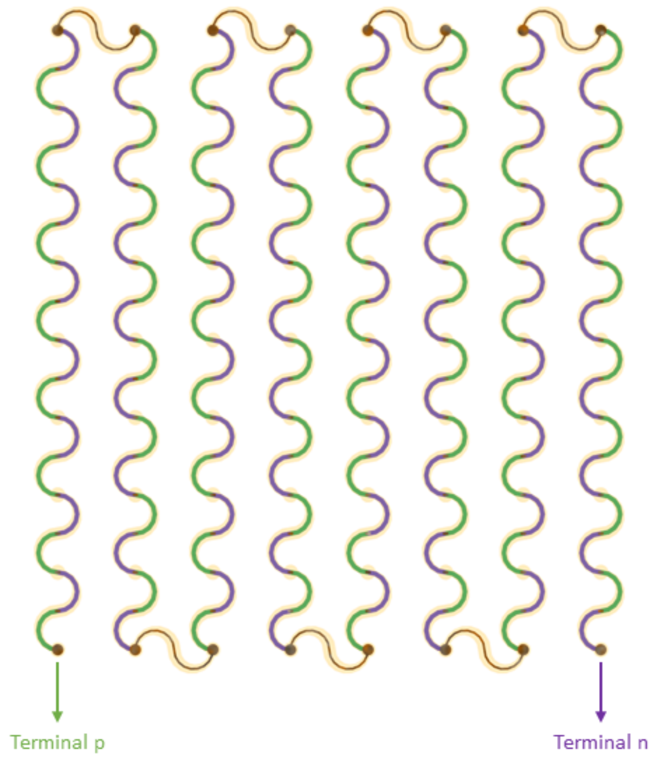


Figure 5.3. Design of 2D precursor for 8×8 array. The colors in silicon represent p type (green) and n type (purple) respectively.

### 5.2.3. Thermal design principles: heat exchange and impedance matching

The advantages of the 3D architecture follow from a set of thermal aspects that are favorable for effective harvesting. For a total heat flow $\dot{Q}$ [W] through a device, the harvested power can be written as $P = \eta \cdot \dot{Q}$ where $\eta$ is the conversion efficiency. Here, only $\dot{Q}$ through the thermoelectric legs $\dot{Q}_{TE}$, i.e. through silicon in our case, can be converted; any heat bypassing the legs does not contribute to $\dot{Q}_{TE}$ and is referred to as "parasitic." The value of $\eta$ is proportional to the difference in temperature across the thermoelectric leg $\Delta T_{TE}$, as $\eta \approx \eta_0 \Delta T_{TE}/T_H$, in a harvesting environment that involves small thermal

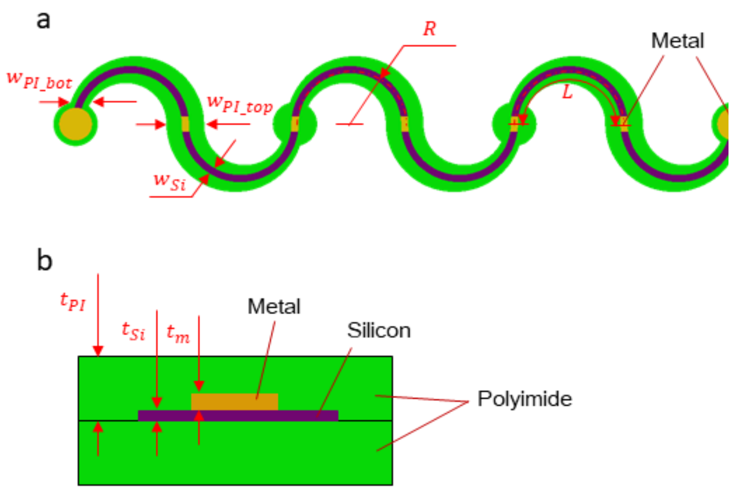


Figure 5.4. Illustration of geometric parameters. (a) Definition of geometric parameters for 2D precursor of spring coil: width of polyimide (PI) $w_{PI,top}$=0.34 mm, $w_{PI,bottom}$=0.17 mm (a tapering width ratio of 2), width of silicon $w_{Si}$=65 $\mu$m, radius of leg $r$=0.5 mm and length of leg $L$=1.57 mm. (b) Schematic illustration of PI encapsulated composite layer (PI/metal/silicon/PI) with optimized thickness $t_{PI}$=4 $\mu$m, $t_{metal}$=0.2 $\mu$m, $t_{Si}$=0.2 $\mu$m.

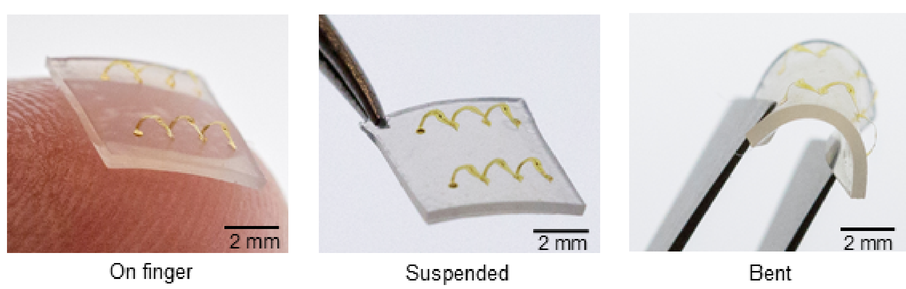


Figure 5.5. Optical images of the resulting 3D thermoelectric coils. The geometry of the structure and the elastomer substrate combine to provide mechanical robustness against handling and mechanical deformation.

gradients and a given hot side temperature $T_H$. Here, $\eta_0$ depends on the thermoelectric figure-or-merit $(zT)$ but not on the device design. According to $P = \frac{\eta_0(zT)}{T_H} \cdot \Delta T_{TE} \cdot \dot{Q}_{TE}$,

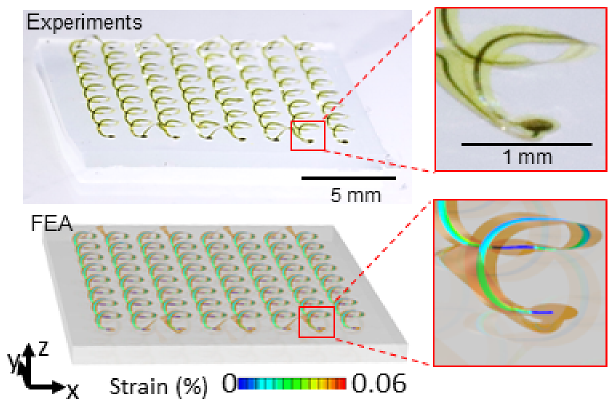


Figure 5.6. Image of an array with 8×8 coils. The magnified view shows that the 3D structure has a geometry consistent with that predicted by finite element analysis. The colored profile represents strain in the silicon leg.

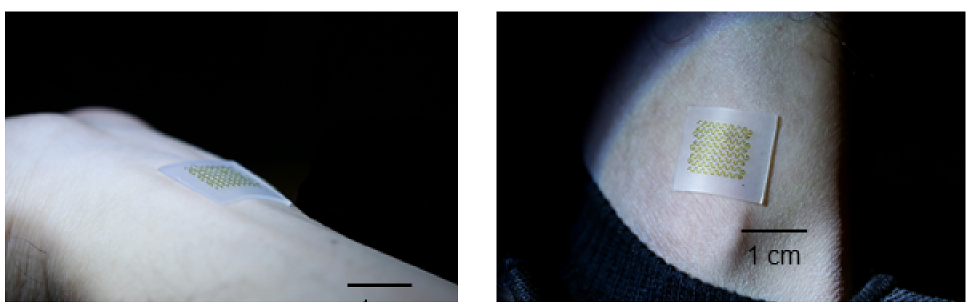


Figure 5.7. Optical images of 3D thermoelectric coils placed on wrist.

the device design goal with a given thermoelectric material and hot side temperature is to maximize the product $\Delta T_{TE} \cdot \dot{Q}_{TE}$.

Because changes in many geometric parameters of the device (e.g. leg length) change $\dot{Q}_{TE}$ and $\Delta T_{TE}$ in opposite directions, the most fundamental limiting factor - the heat exchange capability - should be optimized at the first step of design. The heat exchange capability describes how well the device can receive and dissipate heat from the hot and cold sources, represented by the inverse of the total thermal impedance for heat exchange

$1/\Theta_{ex}$; it determines the upper limit of $\dot{Q}_{TE}$ because $\dot{Q}_{TE} < \Delta T_{Environment}/\Theta_{ex}$, where $\Delta T_{Environment}$ is the temperature difference between the heat source and the surrounding environment. Once the design features that give a minimal $\Theta_{ex}$ are identified, the next step for optimization is to find specific geometric parameters that could produce the maximum $\dot{Q}_{TE}\Delta T_{TE}$. In traditional device geometries, the optimum point occurs when $\Theta_{ex}$ is similar to the impedance of the leg $\Theta_{TE}$ because $\Theta_{TE}$ increases $\Delta T_{TE}$ but decreases $\dot{Q}_{TE}$, analogous to load impedance matching in electronics. This condition is the thermal impedance matching condition.

Following this optimization strategy, we first find the design feature that maximizes the heat exchange capability (minimizes $\Theta_{ex}$). We take advantage of the 3D design space that allows for a large surface area; in harvesters that rely on passive cooling from air convection, the surface area on the cold side determines the total heat flow. In the 3D helical coil system of Figure 5.6, all surfaces except those in contact with the substrate serve as cooling interfaces, with total areas that are much larger than the bonding area. We highlight the role of the leg encapsulation layer, which not only provides mechanical support, but also strongly enhances the heat exchange from an enlarged surface area. Analogous to conventional cooling fins, the optimal geometry for cooling is a diverging profile toward the cold side (i.e. top side). We thus employ a tapering geometry that increases in width towards the top (Figure 5.8). This top-side wide geometry, however, will inevitably increase the load applied to the leg, compromising mechanical stability. Therefore, the thermally favorable design should be limited to within the mechanical stability range.

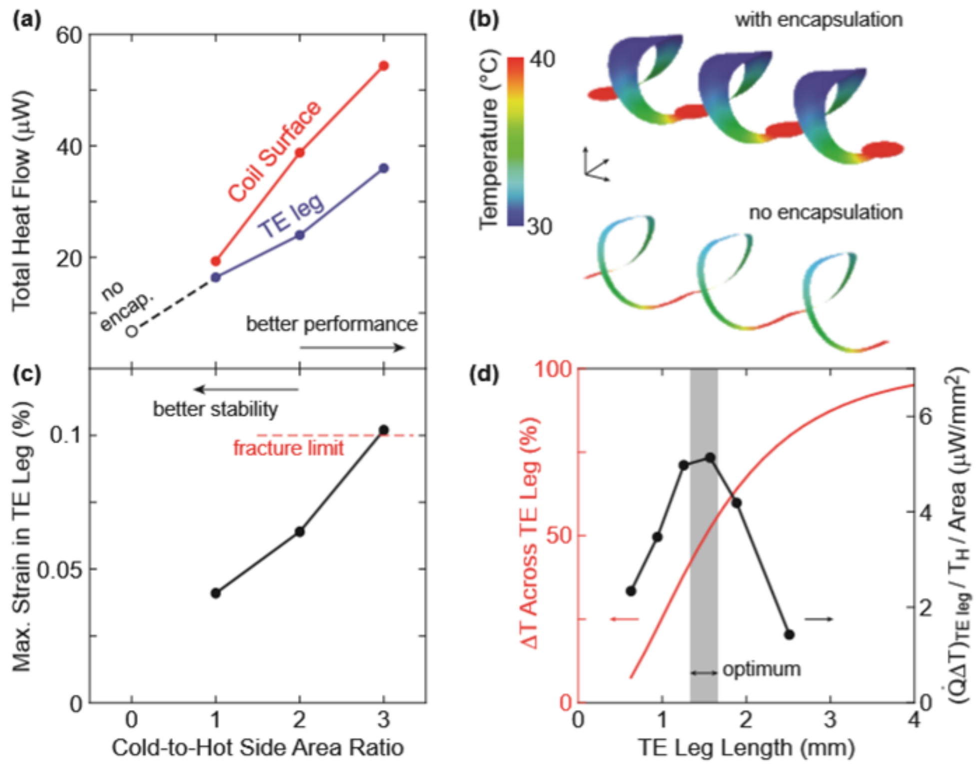


Figure 5.8. Considerations in thermal engineering to optimize choices of design parameters. (a) The total heat flow across the silicon thermoelectric leg (blue) increases as the width of the cold side encapsulated polymer layer is increased. The overall heat dissipation through surface convection (red) increases the heat flow. (b) Simulated temperature profiles by FEA that compare the encapsulated case (the ratio of the area of the cold to the hot side of the leg. (c) The maximum strain in the thermoelectric leg as a function of the ratio of the area of the cold to the hot side. Increasing the area of the cold side, while desirable for improved performance, compromises the mechanical stability. An area ratio of two balanced heat exchange capability and mechanical stability. (d) With an area ratio of two, the leg length is selected to maximize $\Delta T_{TE}\dot{Q}_{TE}$ (right axis, normalized to $T_H$ and area) which is the impedance matching condition. The corresponding fractional temperature drop across the leg is shown on the left axis. All findings presented here are results of modeling of 3×1 coil structures (three leg pairs) with a hot-side thermal bath of 40 °C and the entire surface subject to convective heat dissipation due to ambient air at 20 °C.

To find the optimal tapered geometry, we simulated the dependence of the thermal and mechanical response on the encapsulation layer geometry using FEA. As indicated in Figure 5.8a, simply adding a nontapered encapsulation layer to the bare silicon increases $\dot{Q}_{TE}$ by three-fold (6.2 to 19.3 $\mu$W). Tapering the encapsulation to a higher cold-to-hot side area ratio further increases $\dot{Q}_{TE}$, as expected. The increased heat flow also results in a lower cold side temperature (Figure 5.8b). The maximum strain in the silicon leg also increases with tapering, reaching the silicon fracture limit at a tapered ratio of three (Figure 5.8c and 5.9). In addition, the fabrication yield associated with 3D assembly decreases with tapering because buckling in the downward direction (competing with the upward direction) becomes an increasingly favorable mode (Figure 5.10). To remain in the mechanically stable regime, we selected a cold-to-hot side area ratio of two. We note that this design strategy - to increase the cold side heat exchange with an encapsulation layer - is unique for 3D thermoelectric harvesters. In an in-plane harvester where the surface area is fixed, substrates and encapsulation layers only increase parasitic heat flow, but not $\dot{Q}_{TE}$.

The next focus is on conditions for thermal impedance matching. High heat flow is only beneficial if thermal impedance matching is possible. This condition can be easily achieved in the 3D coil structure because the leg length can be adjusted up to hundreds or thousands of microns; the thermal resistance of the leg is proportional to its length. Simulation results show that the impedance matching condition can be achieved with a leg length ≈1.5 mm (Figure 5.8d), at which a maximum in $\Delta T_{TE}\dot{Q}_{TE}$ (normalized by area and $T_H$) is found. We emphasize that the $\Delta T_{TE}\dot{Q}_{TE}$ calculated here includes only the heat input into the silicon, excluding any parasitic heat. The ability to adjust $\Delta T_{TE}$ across

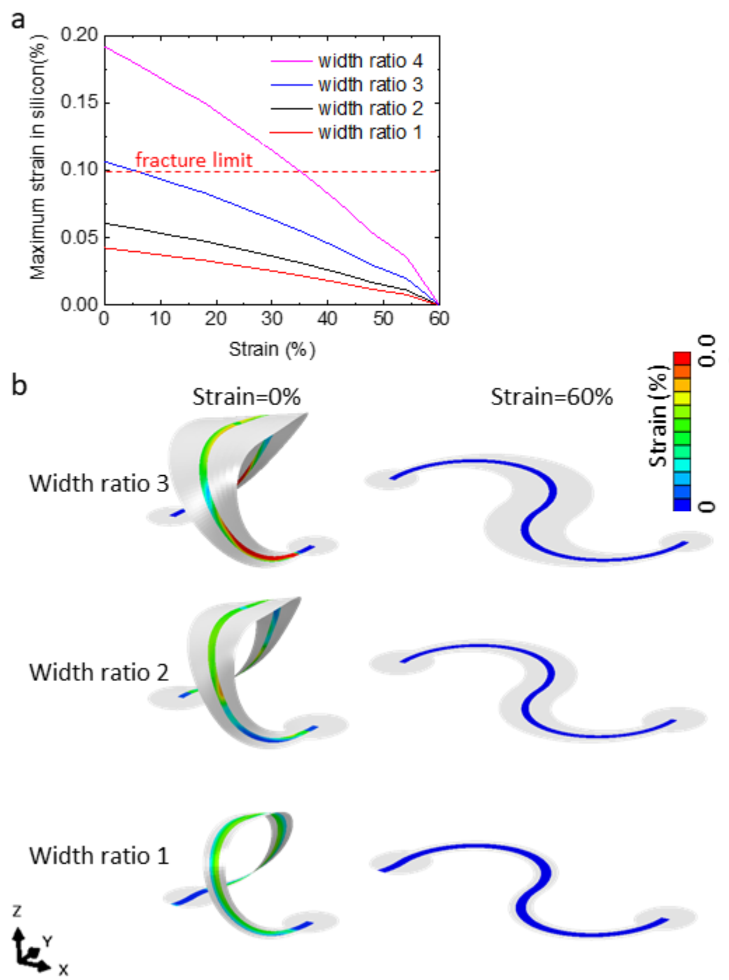


Figure 5.9. Mechanics of in-plane stretching process for 3D spring coil. (a) Maximum strain in silicon layer versus the in-plane stretching strain of 3D spring coil for various designs with different PI width. (b) Deformed configuration with strain distribution in silicon layer for different designs.

such a wide range (and thus obtain the impedance matching condition) in our design is a key differentiating feature relative to conventional film-based harvesters, where only an extremely small $\Delta T_{TE}$ is possible in the out-of-plane direction.

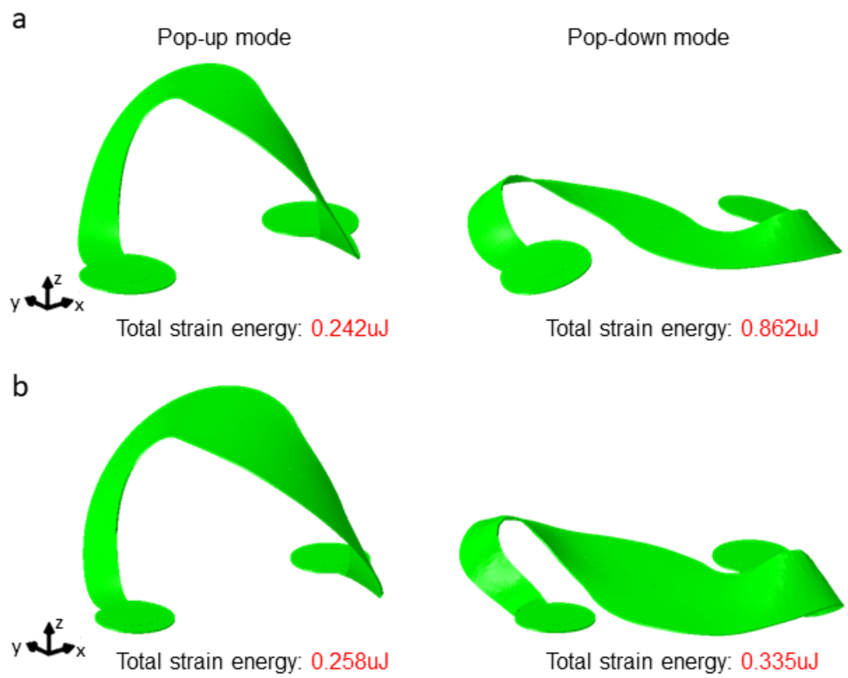


Figure 5.10. Polyimide width effect on yield of buckle-up process. Deformed configuration of pop-up mode and pop-down mode with total strain energy for cold-hot area (a) width ratio 2 and (b) width ratio 3, which indicates that the design with width ratio 3 will have lower yield for buckle-up process.

We note that our design scheme is optimized for harvesting in miniature devices. Because of the priority on minimal occupied space and weight, cooling is made to rely on natural convection. This cooling process dominates the thermal impedance of the harvester, making other design factors like substrate-to-leg conductance much less significant. Instead, increasing the total surface cooling capacity is of utmost priority, exemplified by the fact that the leg encapsulation layer actually enhances the heat flow through the leg (Figure 5.8a; 9.7 nW increase in silicon heat flow by adding a non-tapered encapsulation) despite it introducing parasitic heat flow (2.9 nW) . In other words, the benefit of increased cooling capability greatly outweighs any losses from parasitic heat flow, a regime which might be counterintuitive from the aspect of bulk generators.

### 5.2.4. Mechanical compliance

One of the key advantages of our device is the mechanical compliance to endure substantial amount of bending, in-plane stretching and out-of-plane compression, as opposed to previously reported out-of-plane harvesters [**88**] with limited flexibility or stretchability. Our designed 3D structures can be stretched in the in-plane direction by up to 60% for hundreds of cycles (Figure 5.11, 5.12 and 5.13) and can be vertically compressed up to 30% with only minimal degradation in the electric properties (Figure 5.14 and 5.15). This exceptional level of mechanical compliance in a structure that incorporates silicon follows from a design principle that places silicon in the neutral mechanical plane with respect to deformation, as also predicted by FEA. This design also ensures that the strains in the encapsulation and metal layers are well below the threshold for plastic yielding (Figure 5.16). Stretching in the plane reduces the material strains, as it returns the structure to its original, undeformed 2D geometry. Uniaxial stretching over 200 cycles does not lead to signs of electrical or mechanical failure (Figure 5.12 and 5.13). Comparable results were also found on the 8×8 array (Figure 5.6), where 200 cycles of 60% biaxial stretching resulted in a 22% increase in resistance from 335.4 to 409.7 kΩ.

For vertical compression, measurements indicate the onset of changes in resistance at ≈30% before fracture of the silicon causes an open circuit (Figure 5.15 and 5.17, also consistent with FEA in Figure 5.14 and 5.18. The overall resilience of the 3D coil

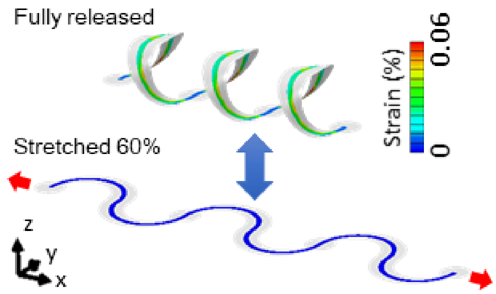


Figure 5.11. Simulated distributions of strain in the silicon thermoelectric leg before and after uniaxial stretching in the plane by 60%. The results indicate reductions in strain upon stretching, as expected based on the compressive buckling process used to form the 3D structures.

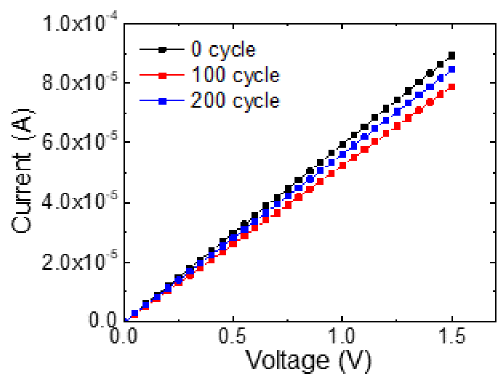


Figure 5.12. Results of experimental durability tests that involve multiple cycles of 60% uniaxial stretch and release on a 3×1 coil structure (strain rate ≈0.01 $s^{-1}$). The data indicate only a small increase in the electrical resistance.

suggests the potential to interface with various miniature device schemes. For example, suitable designs allow for system-level properties that are mechanically and geometrically compatible with those of the soft tissues of the human body.

As most inorganic thermoelectric materials, such as $Bi_2Te_3$-$Sb_2Te_3$ alloys [**87**], $Zn_4Sb_3$ [**183**], and $Cu_2Se$ [**182**], have fracture strains similar to silicon, the measurements and FEA results described above suggest that they could be deployed in similar 3D structures

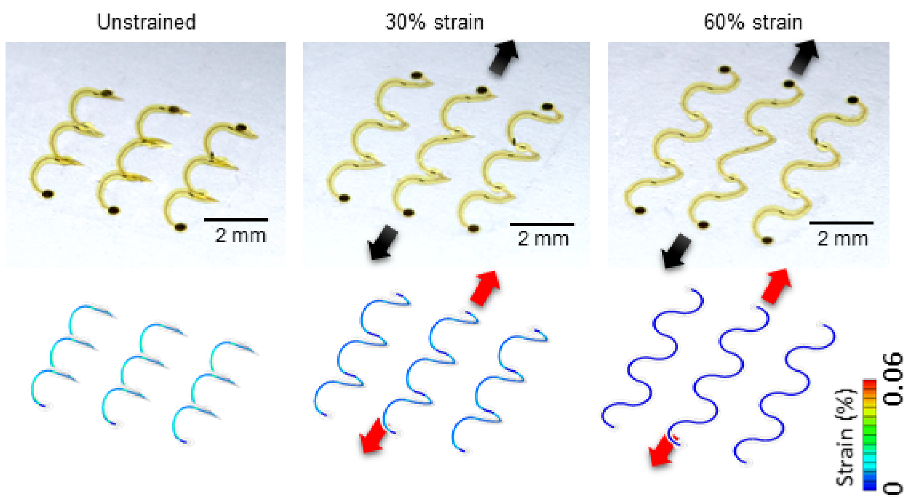


Figure 5.13. Optical images (top row) and simulated structures (bottom row) upon in-plane stretching.

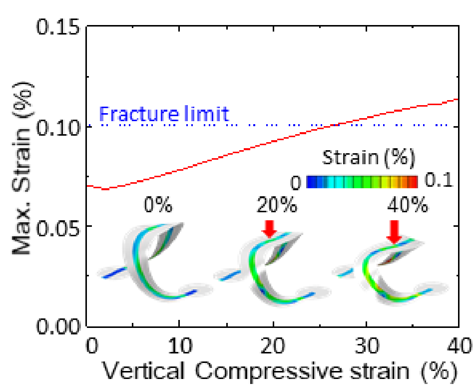


Figure 5.14. Simulated values of the maximum local strain in the thermoelectric leg induced by vertical compression. A maximum compression of 26% is possible before reaching the fracture strain of the silicon, the limiting factor for this system. The inset shows the deformed structure upon compression, including a strain distribution map of the silicon leg. The maximum strain occurs near the hot side, indicated as the fracture point (also see Figure 5.18).

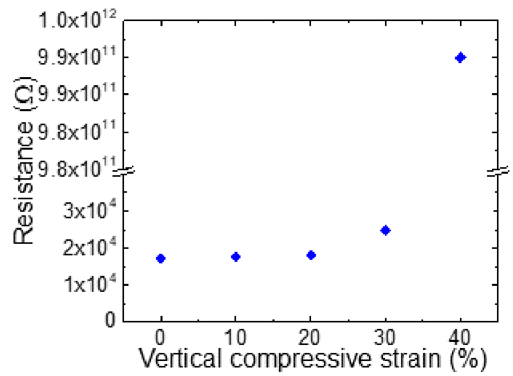


Figure 5.15. Experimental measurements of the device resistance upon vertical compression. The onset of an increase in resistance occurs near the limit predicted by simulation. At a compression of 40%, the device shows open-circuit behavior, due to fracture of the silicon.

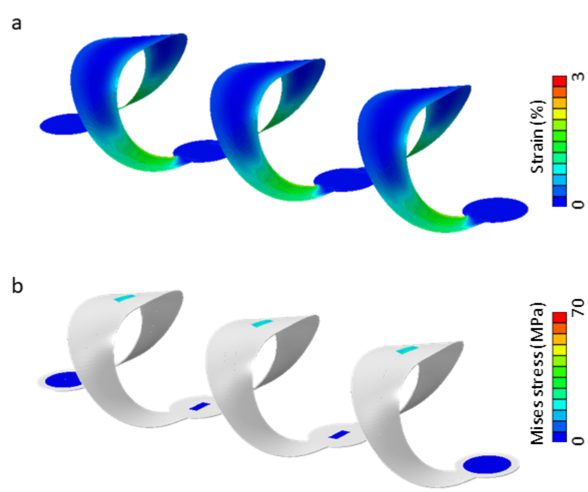


Figure 5.16. Simulated strain/stress distribution in the encapsulation and metal layers. (a) Strain distribution in encapsulation (PI) layer. (b) Mises stress distribution in metal (Ti/Au) layer. Both are well below the yielding limits of the corresponding materials.

with comparable mechanical properties. Use of thermoelectric materials based on organic polymers could further enhance the mechanics and also the heat flow properties.

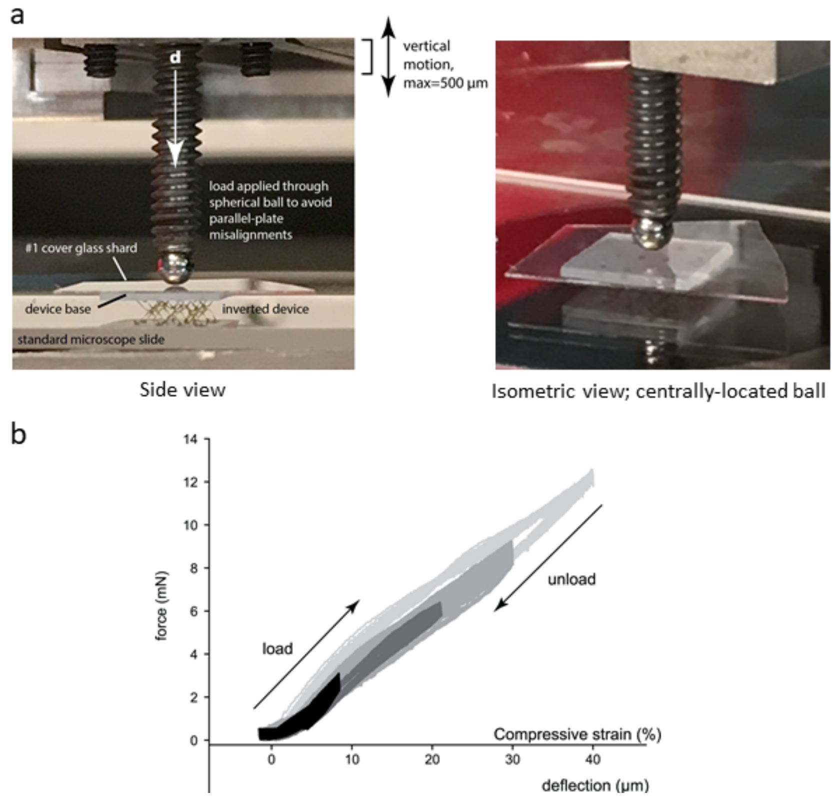


Figure 5.17. Mechanical compression test. (a) side and isometric views of the test setup. (b) the out-of-plane force-displacement response corresponding to 10%, 20%, 30% and 40% compressive strains respectively.

### 5.2.5. Power output and projections

The output characteristics of the harvester (Figure 5.19a-b) that consists of an 8×8 array of coils (Figure 5.19c) are consistent with the design expectations outlined in previous sections. Using measurement procedures outlined in the Methods and Figure 5.20, the open circuit voltage is 51.3 mV at $\Delta T_{Environment}$ = 19 K, yielding an estimated temperature drop of 6.2 K across each individual leg based on an average thermopower of 65 $\mu$V/K measured from the pre-patterned silicon; see Table 5.1. This value is consistent with measurements from a 3×1 array (6.9 K, Figure 5.21), and somewhat smaller than the

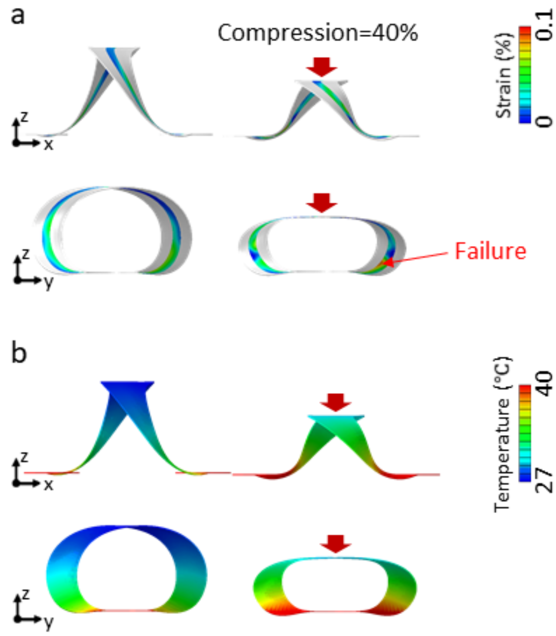


Figure 5.18. Mechanics of vertical compressing process for 3D spring coil. Deformed configuration under 0% and 40% vertical compressive strain for 3D spring coil, with (a) strain distribution in silicon layer and (b) temperature distribution.

design estimation of 9.5 K (Figure 5.8d). The discrepancy follows, at least partly, from uncertainties in the thermal transport parameters used for simulation. In comparison to most literature reports [**88**] where even bulk material harvesters are operated significantly far from thermal impedance matching conditions, these results demonstrate the promise of our matching strategy. The open circuit voltage does not diminish over time in our measurements, indicating that the thermal profile in our device is at steady-state. The maximum power output, i.e. ≈2 nW, is modest, mainly because of the low $zT$ of silicon. Some state-of-art miniature devices including transmitters or bio-sensors [**106, 120, 121**] can be powered at this level, but for current mainstream applications an improvement in power is required.

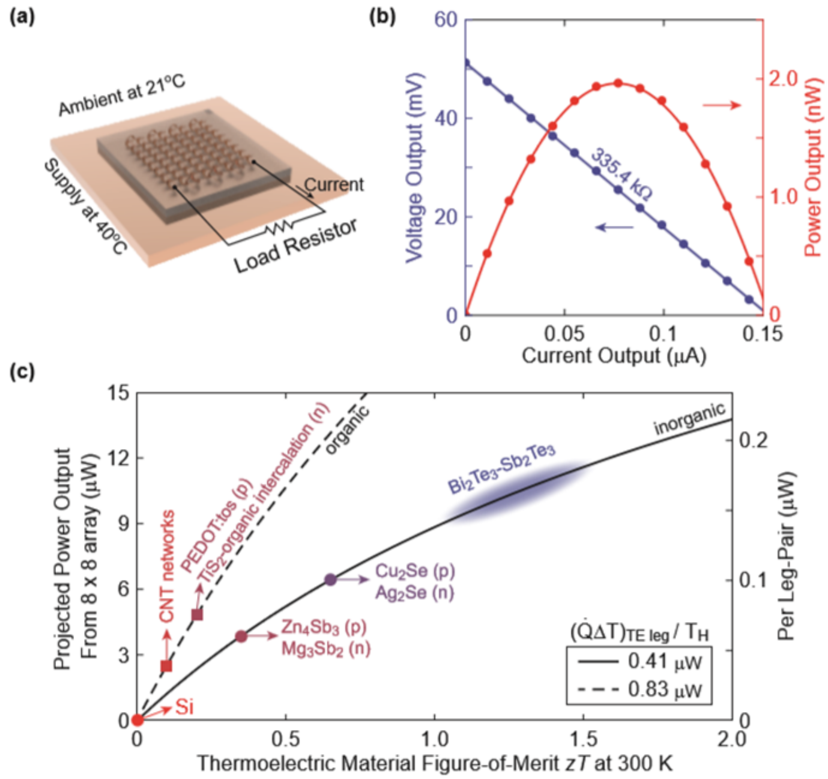


Figure 5.19. Energy harvesting with thermoelectric coils and a road map for power enhancement. (a) Schematic illustration of the measurement conditions for evaluating the performance of the harvesting devices. An 8×8 array was exposed to an environmental temperature difference of 19 °C. (b) Measured power output characteristics of the 8×8 coil array, showing a maximum power of 2 nW. (c) Projected power output achievable by using known thermoelectric materials with thermoelectric figure-of-merit $zT$ higher than that of Si (left axis is for a 8×8 array; right axis shows values on a per coil basis). These powers correspond to $\dot{Q}\Delta T/T_H$ per leg values as indicated in the legend and ideal conversion efficiencies. The dashed and solid lines represent the values from structures obtainable with organic and inorganic materials, respectively (see Figure 5.22). The zT values used here correspond to averages of p- and n-type materials reported in the literature: CNT networks [**116**]; PEDOT-Tos [**14**]; TiS2-organic intercalation [**190**]; $Zn_4Sb_3$ [**16**]; $Mg_3Sb_2$ [**76**]; $Cu_2Se$; $Ag_2Se$; $Bi_2Te_3$-$Sb_2Te_3$.

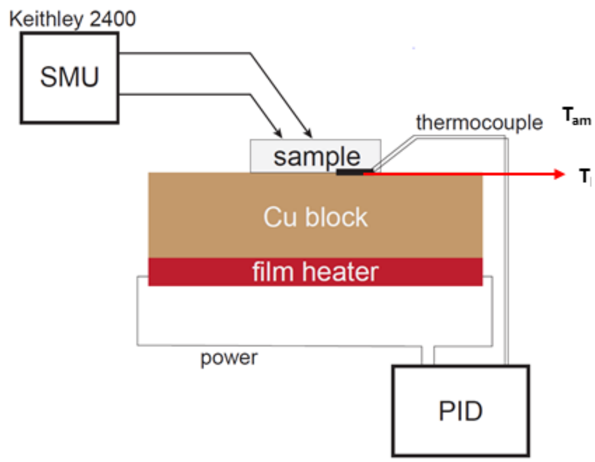


Figure 5.20. Schematic illustrations of the testing setup for measuring the thermoelectric responses of the device.

Table 5.1. Thermoelectric properties for heavily doped n-type and p-type silicon thin films measured in the silicon-on-insulator wafer form before patterning.

| | n-type | p-type |
|---|---|---|
| Resistivity [ $\mathrm{m}\Omega \cdot \mathrm{cm}$] | 0.64 | 0.86 |
| $n_{Hall}$[ /cm$^3$] | 1.9$e$20 | 2.1$e$20 |
| Hall mobility [ cm$^2$/Vs] | 35 | 50 |
| Seebeck [ $\mu$V/K] | -67 | 62 |

The good agreement between modeling and experiment allows use of simulation results to estimate power outputs for harvesters built with other materials, specifically those with better figure-of-merit $zT > 0.1$ than silicon ($zT > 10^{-3}$ at 300 K). Recall that $P = \eta_0(zT) \cdot \frac{\Delta T_{TE}}{T_H}\dot{Q}_{TE}$. For $T_H = 313$ K, we simulate $\Delta T_{TE}\dot{Q}_{TE}$ for designs relevant for two different groups of materials, inorganic and organic, while keeping the occupied area of the coil the

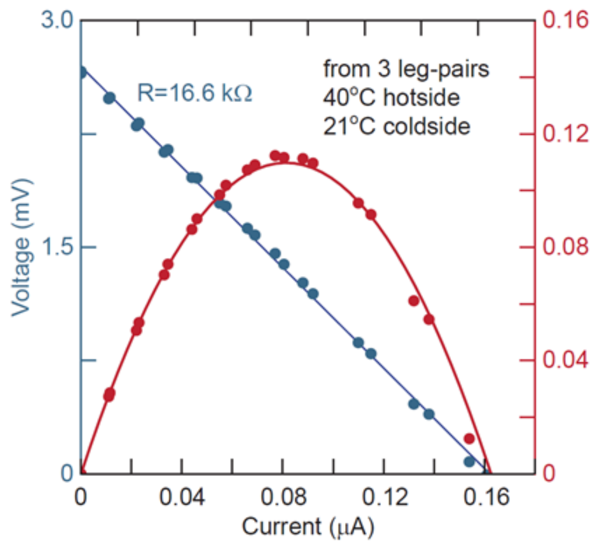


Figure 5.21. Output characteristics of the 3×1 harvester shown in Figure 5.5. The open circuit voltages are 2.66 mV at $\Delta T_{Environment} = 19$ K, which gives an estimated temperature drop of 6.9 K across each individual leg using the Seebeck coefficient measured in Table 5.1.

same as that of the encapsulated silicon design. For organic-based materials (dashed line, Figure 5.19c), we find $\Delta T_{TE}\dot{Q}_{TE}/T_H = 0.83$ $\mu$W (similar to the 0.73 $\mu$W of encapsulated silicon) based on a design that simply replaces the silicon and encapsulation entirely with the organic thermoelectric material (Figure 5.22). For inorganic materials (solid line, Figure 5.19c), the encapsulation again defines the surface area profile and maintains mechanical stability, but the reduced thermal conductivity compared with silicon results in $\Delta T_{TE}\dot{Q}_{TE}/T_H = 0.41$ $\mu$W (Figure 5.22 based on $Bi_2Te_3$-$Sb_2Te_3$). Nevertheless, power output is generally higher by virtue of the higher $zT$ yielding a higher conversion efficiency. Overall, by integrating known thermoelectric materials, power output at the level of a few $\mu$W appears to be possible. Such an improvement to 0.15 $\mu$W per coil would allow

$\approx$100 $\mu$W of power from an area of a typical wrist watch ($\approx$10 cm$^2$) when a similar $\Delta T_{Environment}$ is given. Room for further improvement up to an order of magnitude in total exists from packing coils more efficiently, using designs better optimized for the low-thermal conductivity thermoelectric material, and stacking the coils in 3D with repeated transfer printing (See Figure 5.23 for example design). Our fabrication scheme is generally compatible with other materials, especially the organic variants in Figure 5.19c which allow minimal use of encapsulation layers.

Additional opportunities for improvement in harvesters that use inorganic materials is in the development of thick (or wide) films to reduce the effects of parasitic heat flow through the encapsulation layers, while maintaining mechanically stable designs. For organic or composite materials, additional research on methods for deposition, doping and patterning could yield progress. For all classes of thermoelectric materials, the mechanical properties become more important to understand in the context of the sorts of 3D configurations reported here. A related challenge is to identify materials and compatible metals that do not suffer from electrical resistance increases during the 2D-to-3D mechanical transformation. In the current case of silicon, typically a three-fold increase in resistance is observed during the transformation, possibly due to electrode contact degradation and plastic deformation in some parts of the leg. These various areas represent promising directions for future research.

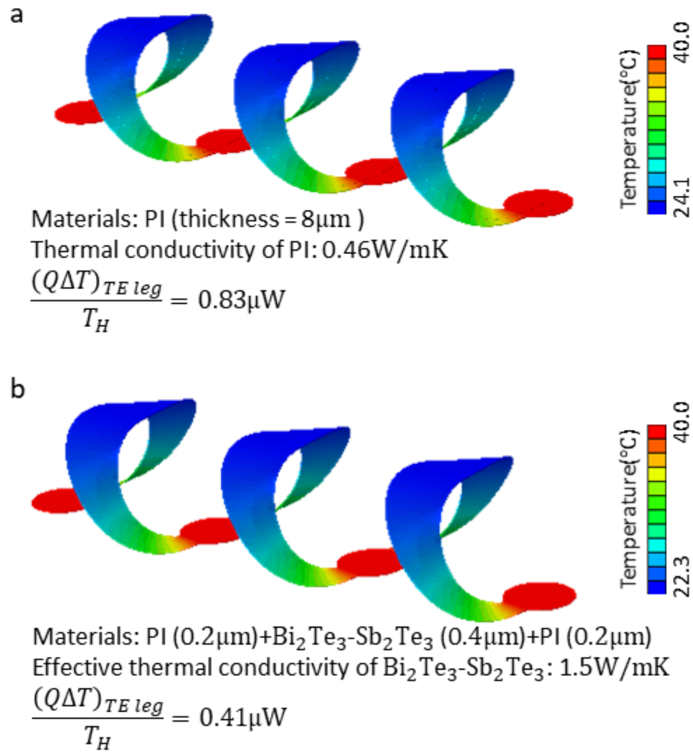


Figure 5.22. Preliminary thermal modeling by replacing silicon with other thermoelectric materials. (a) In the case of organic thermoelectric materials, they are simply modeled as additional PI layers since they typically have similar mechanical properties and thermal conductivity (0.46 W/mK is used in this simulation). (b) In the case of inorganic thermoelectric materials, $Bi_2Te_3$-$Sb_2Te_3$ is used as a reference for properties. The thermal conductivity is set to an effective value of 1.5 W/mK to account for Peltier heat transfer, which is non-negligible in high zT materials.

## 5.3. Materials and Methods

### 5.3.1. Patterning and transfer printing of p- and n- doped single-crystalline silicon

Single-crystalline films of silicon with thickness of 200 nm (silicon-on-insulator, SOI, Soitec) served as the thermoelectric material. A layer of $SiO_2$ (500 nm) formed on the top

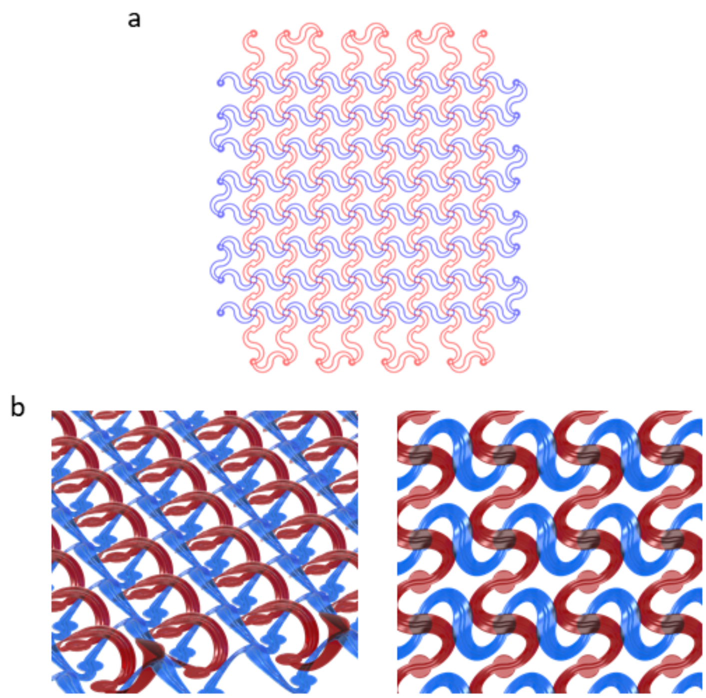


Figure 5.23. The design that uses multilayer stacking to improve the power density. (a) Layout of the 2D precursor that stacks two 8 by 8 designs rotated by 90 ° with respect to each other (see Figure 5.3 for the original 2D precursor). (b) Isometric and top views of the design shown in (a) after 3D assembly.

silicon by plasma-enhanced chemical vapor deposition served as masks for doping. Patterning relied on photolithography and a combination of reactive ion etching ($CF_4$+$O_2$) and wet etching (buffered oxide etchant) to define openings in the $SiO_2$ for solid-state diffusion doping. The p- and n-type regions resulted from doping with boron (1000 °C, 14.5 min) and phosphorus (1000 °C, 5.5 min), respectively. Each dopant type required its own $SiO_2$ mask. A photolithographically patterned layer of photoresist (S1805, MicroChem) defined regions of via holes (3 $\mu$m diameter, 50 $\mu$m pitch), formed through silicon by reactive ion etching ($SF_6$). These holes also enabled etching of the buried oxide layer by immersing the wafer in 49% hydrofluoric acid for 30 min. Thoroughly rinsing the sample with deionized water prepared it for transfer printing. A flat slab of polydimethylsiloxane (Sylgard 184, 1:4) enabled retrieval of the photoresist/Si film and delivery onto a bilayer of polyamic acid (precursor to form polyimide 4 $\mu$m, PI 2545, HD MicroSystems) and poly(methylmethacrylate) (200 nm, PMMA, MicroChem) spin coated sequentially on a silicon handling wafer. Immersion in acetone dissolved the photoresist. Baking in a vacuum oven completed the curing of the polyimide (PI). Finally, photolithography and reactive ion etching ($SF_6$) patterned the silicon into isolated p- and n-type serpentine-like layouts.

### 5.3.2. Fabrication of the 2D thermoelectric precursor and the 3D spring structure

Bilayers of Ti (60 nm) / Au (60 nm) deposited by electron beam evaporation and patterned by photolithography and wet etching served as electrical interconnects between the p- and n-type silicon. This process also defined electrode pads for probing. Spin coating another layer of PI (4 $\mu$m) and patterning it by exposure to an oxygen plasma through a mask of photoresist (10 $\mu$m, AZ 4620, MicroChem) encapsulated the system and completed the fabrication of the 2D thermoelectric precursor. Dissolving the residual photoresist and the underlying PMMA in acetone allowed the precursor to be retrieved onto a piece of water-soluble tape (Aquasol). A pattern of SiOx (50 nm) formed by electron beam evaporation through a shadow mask defined bonding sides on the back side of the precursor. An elastomer substrate (Dragon Skin 10, 1:1, Smooth-On Inc.) stretched to the desired level using a stage served as a substrate for 3D assembly. Exposing the elastomer and the 2D precursor (still on water-soluble tape) to ultraviolet induced ozone (Jelight UVO-Cleaner, 144AX) and then laminating to the two together and baking them in a convection oven at 70 °C formed strong adhesion via condensation reactions at the bonding site interface. Dissolving in warm water removed the tape. Slowly releasing the strain in the elastomer substrate while immersed in water completed the 3D assembly.

### 5.3.3. Finite element analysis

Three-dimensional finite element analysis for the thermo-mechanically coupled system yielded predictions of the mechanical deformations, strain distributions, heat flux and temperature profiles of the individual 3D coil structures as well as the arrays (8×8 and 3×1) during the processes of compressive buckling, re-stretching and vertically compressing. Coupled temperature-displacement four-node shell elements with a four-layer (PI/metal/silicon/PI) composite modeled the 3D coil spring. Refined meshes ensured computational accuracy using a commercial software (Abaqus). Parametric designs led to the mechanically and thermally optimized geometric parameters using a commercial software (Isight) coupled with Abaqus. The heat transfer coefficient at the PI surface was set to 5 $W/(m^2 \cdot K)$. The material parameters used were as follows: $E_{PI} = 2.5$ GPa, $\nu_{PI} = 0.27$ and $\kappa_{PI} = 0.46$ $W/(m \cdot K)$; $E_{Si} = 130$ GPa, $\nu_{Si} = 0.27$ and $\kappa_{Si} =80$ $W/(m \cdot K)$; $E_{metal} =79$ GPa, $\nu_{metal} =0.34$ and $\kappa_{metal} =401$ $W/(m \cdot K)$. Here, $E$ is elastic modulus, $\nu$ is Poisson's ratio, and $\kappa$ is thermal conductivity.

### 5.3.4. Thermoelectric characterization

Transport properties of the doped silicon films were characterized at room temperature. Electrical conductivity and Hall measurements used the van der Pauw method with Mo probes. A 2 T electromagnet generated the magnetic field. Measurements of electrical conductivity used an in-line four point Os probe setup, to yield results consistent with those from the van der Pauw method. The in-plane Seebeck coefficient of the doped silicon film was measured using a scanning probe setup with a maximum temperature difference of ≈8 K. The thermoelectric response of the coil harvester was measured by placing the device on a Cu block that was heated using a film heater attached on the bottom side of the block. A type K thermocouple was attached to the bottom of the harvester substrate, and the film heater was PID controlled to maintain the harvester bottom temperature at 40 °C. Room temperature was measured using another type K thermocouple placed in air near the harvester. The entire setup was built inside a probe station enclosed in a dark box. Electrodes were probed using W needles. The output voltage and current were measured at varied load resistances. To achieve the equivalent effect of switching the load resistance, a source measurement unit (Keithley 2400) was used under current-scanning mode. Also see Figure 5.20.

### 5.3.5. Mechanical characterization

The cyclic stretching tests involved loading the harvester device onto a stretching stage, then uniaxially stretching and releasing between 0 and 60% at a strain rate of 0.013 /s. The vertical compression tests involved compression up to 40% applied by carefully sandwiching the device between two stiff plates and displacing the top plate using a piezoelectric stage (PI-USA, Waltham MA). The total compression was estimated based on the initial nominal coil diameter of 660 $\mu$m. Applying force through a steel spherical probe to the cover glass base (see Figure 5.17) ensured that the sandwiching plates remained in a parallel configuration. In addition, force measurements and side-view monitoring confirmed the uniform loading on multiple coils. Force was measured through the displacement of a 4-bar flexure monitored by capacitive sensors (Lion Precision, Oakdale MN). The transducer stiffness was $\approx$1020 N/m, much stiffer than the out-of-plane stiffness of the devices themselves; the flexure displacement was added on to the prescribed displacement for vertical compression to reach targeted values.

## 5.4. Conclusion

By applying previously proposed 3D coil structure on thermoelectric (TE) materials, we designed and fabricated a novel flexible and stretchable thermoelectric energy harvesting device. Advances in developing flexible and/or wearable TE devices have been impeded largely due to the non-flexibility of state-of-art TE materials and the lack of fabrication methods that are scalable, cost-effective, and compatible with the current Si processing. Although the power output results are still in the nanoWatt range, which indicates future improvements necessary, such as material optimization and minimizing the heat losses through substrate and so forth, this work successfully demonstrates the new flexible device fabrication methods as the proof of concept with reasonable electrical and thermal design optimization. Coupled mechanical and thermal analysis enables this design and optimization process. This concept of 3D flexible thermoelectric energy harvester is applicable to many other thin film materials thus will be of interest in many in the TE society.

## 5.5. Contributions

KN, SDK, and KL contributed equally to this work. KN developed the fabrication process and produced the device. SDK oversaw the thermal and thermoelectric analyses, measured the thermoelectric properties, and modeled the thermal and power characteristics. KL designed the 3D coil structure, optimized the geometric parameters based on coupled thermal and mechanical finite element analysis, and drew the masks. ACD did the mechanical characterization. KJY, JW, and CZ assisted the fabrication process. FZ, ZX, and HW assisted the finite element analysis and optimization. MTA assisted thermoelectric characterization. HL helped designing the mask. SDK, KN, and KL wrote the manuscript. YZ, YH, GJS, and JAR supervised the project. All authors reviewed or edited the manuscript.

CHAPTER 6

# Exploration of a Novel 3D Assembly Approach: Mechanically Guided 3D Self-Assembled Mesostructures on Kirigami Elastomer Substrate

## 6.1. Introduction

Increasing attention on 3D mesostructures results from their wide-range applications in the technologies of micro- and nanosystems, such as microelectronic circuits [**12, 201, 33, 2, 56, 47**], plasmonic and photonic nanosystems [**4, 103, 168, 225, 226**], energy storage and generation devices [**224, 133, 175, 128**], optical/mechanical metamaterials and biomedical tools [**178, 101, 220**]. Many methods have been developed to form interesting classes of 3D micro-/nanostructures including microcontact printing [**61, 138**], self-acuating materials driven formation [**90, 85, 51, 196**], bending/folding of thin films induced by residual stresses or capillary forces [**154, 55, 101, 8, 146, 48, 135**], and addictive manufacturing [**175, 2, 209, 96, 43, 158**]. Recently reported approaches to form 3D archetectures by compressive buckling of the 2D precursor structures, that selectively bonded onto a prestretched elastomer substrate on designed bonding sites, with the relaxation of the prestrain of substrate [**206, 229, 212, 1, 111**]. Such methods are intrinsically compatable with a broad range of advanced materials that exist naturally in 2D forms, thus activates the advantages like high speed, parallel operation, and applicability for extensive length scales from nanometers to centimeters. Analytical and numerical modeling of this process presented quantitatively good agreement with experiment observation, that can serve as a rigorous design tool to define the 2D precursors and predict the spacial configurations of the 3D structures. Despite these advances, there exists an important limitation for these methods that only translational displacement are induced on the bonding sites during the 2D to 3D transformation process when the prestretched elastomer substrate relaxes, that severely limits the variation of the classes of 3D structures. Recently reported approach that replace the uniform elastomer substrates with engineered elastomer substrates of controlled variations in thicknesses provided a extensive class of 3D architectures [**206, 65, 229, 212, 1, 111**], but the bonding sites of these structures are still in translational displacement. Here, we introduce a novel strategy that enables the bonding sites with controllable rotation besides translational displacement, thus excessively extends the complexity of this class of 3D mesostructures. An important uniqueness of this process is the 2-stage releasing of the underlying Kirigami substrate that offers direct transformation of 3D mesostructures by adding rotation to bonding sites in the 2nd stage, and this process is compatible with the recently reported mechanically guided loading-path strategy to further increase the complexity [**38**]. Finite element modeling predicted the assembly of the 3D mesostructures in this presented procedure, and the results are validated by experiments. As simply mentioned, the compatibility of this apprach with a broad range of advanced materials, that from device-grade semiconductors and metals to photo-patterned polymers and commercially available thin films across a broad range of length scales, provides a promising foreseen.

## 6.2. Results and Discussion

Figure 6.1a presents a schematic illustration of the key fabrication steps of forming 3D structures on kirigami substrates via finite element analysis (FEA). The scheme begins with creating through-cuts in a stretchable elastomer (Dragon Skin, Smooth-On) by laser cutting. An axamplary cutting pattern divides the elastomer into connected square units with unit size $D$, cutting width $w$, and spacing between orthogonal cuts $\delta$ (Figure 6.2a). Biaxially stretching the elastomer to 100% strain deforms these individual units in the elastomer, which serves as the assembly substrate for 3D structures. During the stretching process, the units first rotate with their adjacent units rotating in the opposite direction, whilst the strain is smaller than 40%. With strain >40%, the rotation angle, that at the center of a square unit, saturates to the maximum value, such that only stretching occurs in the substrate without rotation (Figure 6.2b and 6.3).

Laminating a patterned 2D precursor on this prestretched elastomer with predefined bonding locations aligned to the pre-selected deformed units registers the bonding locations with programmed deformation during the subsequent assembly process. Initial release of the prestrain (from 100% to 40% strain) of the substarte causes releasing of the unit stretching, leading to the compressive buckling of the 2D precursor into a 3D shape (indicated by the magenta arroes in step 2 in Figure 6.1a). Further release of the prestrain (from 40% to 0% strain) releases the rotation of individual units, resulting in rotation of the bonding sites (indicated by the red and blue arrows in step 3 in Figure 6.1a). This rotation transforms the initial 3D structure formed in the initial step into a distinctly different geometry, because the bonding sites rotates with the rotation of individual kirigami

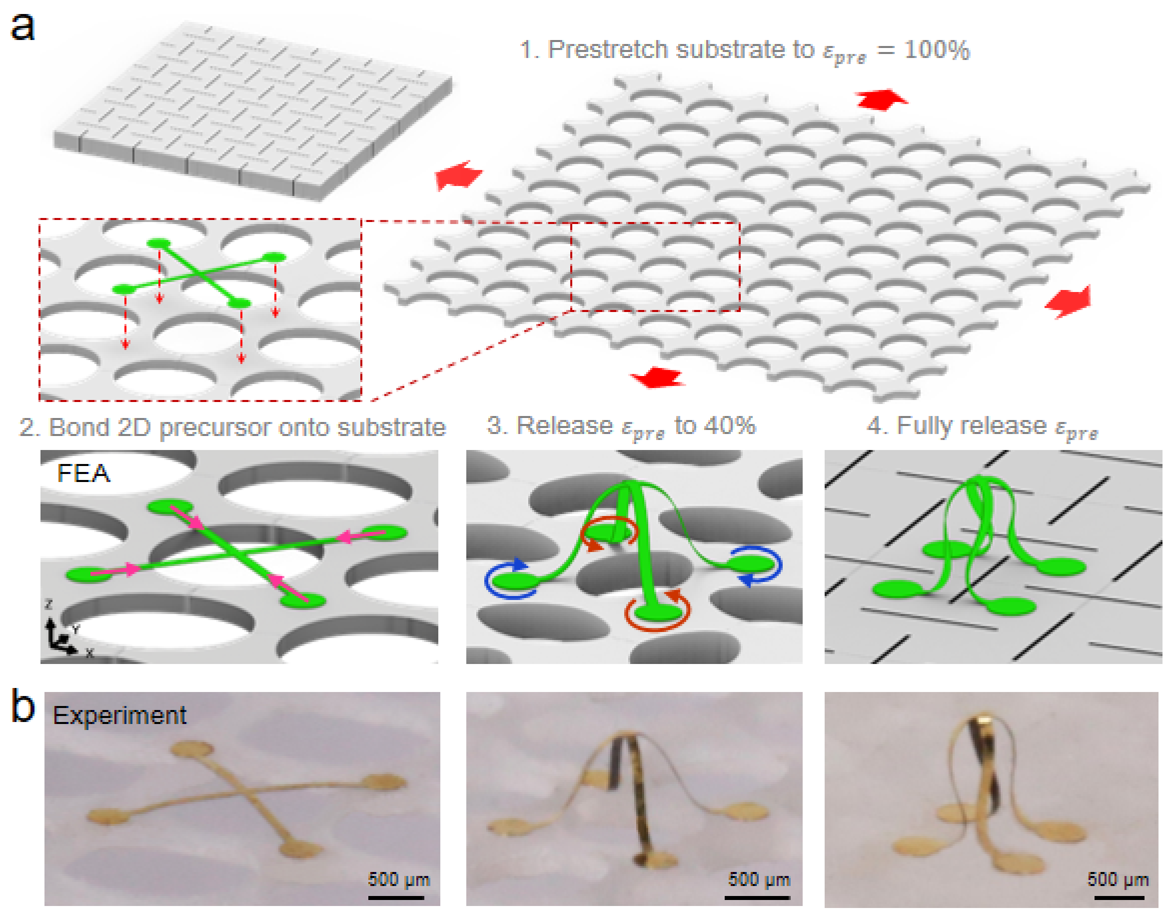


Figure 6.1. Schematic diagram of the (a) 3D assembly approach on kirigami substrate, with (b) optical images of experimental verification.

substrate units. This transformation of 3D architecture is uniquely enabled by the underlying kirigami substrate, thus significantly extends the library of 3D assembled structures induced by compressive buckling that developed recently [**206, 65, 229, 212, 1, 111**].

Figure 6.1b shows the optical images of a 3D structure made of polyimide (PI; 9 $\mu$m in thickness) coated with metal layers (Cr/Au, 10 nm/100 nm in thickness) in the key steps of the assembly process corresponding to the FEA in Figure 6.1. The good agreement between the FEA predictions and experimental results demonstrates the high level

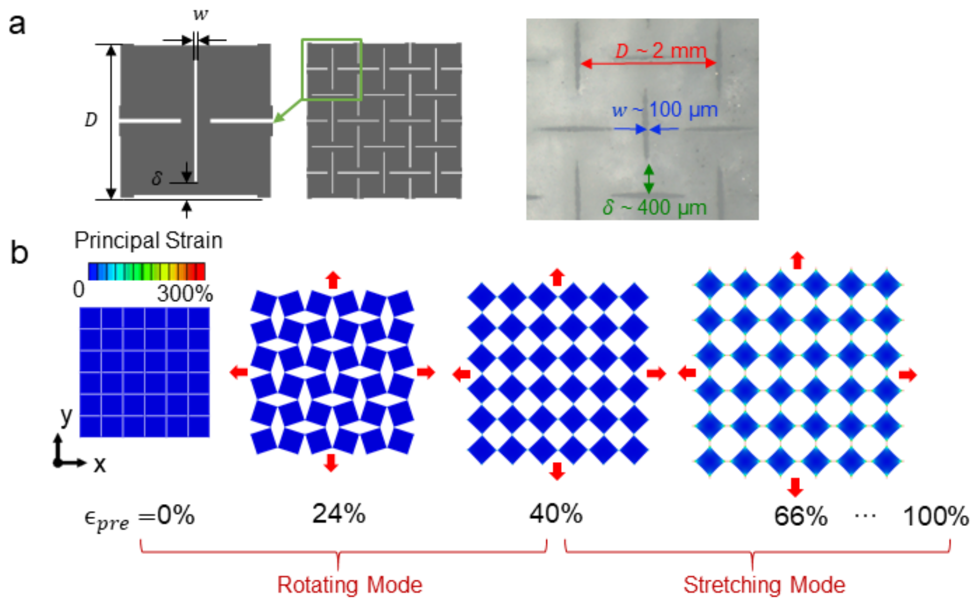


Figure 6.2. (a) Illustration of geometric parameters of square kirigami cut pattern. (b) FEA results presenting the stretched kirigami substrate with different levels of applied strains.

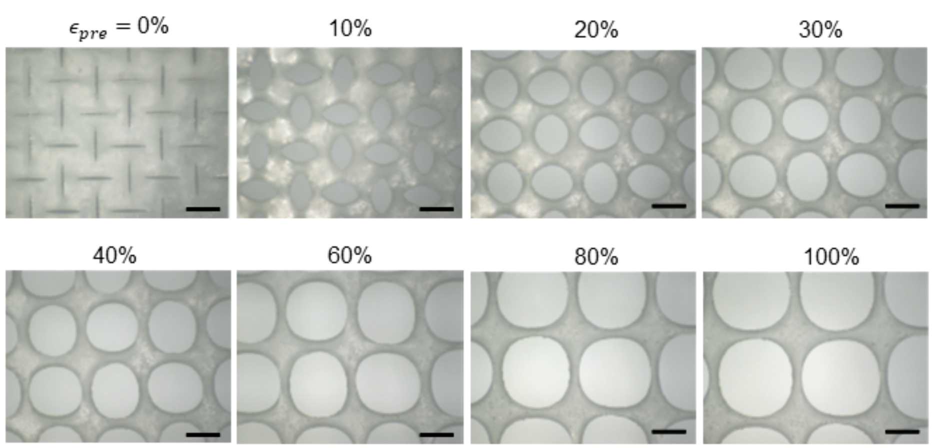


Figure 6.3. Optical images of experimental results for stretched kirigami substrate.

of control of the assembly process. The fabrication process begins with a set of microfabrication steps (spin coating, photolithography, wet/dry etching) to pattern a 2D precursor structure on a flat substrate. Transferring the 2D precursor onto a prestretched kirigami elastomer at predefined bonding locations aligned with the units of substrate completes the registration (see detailed fabrication process in Methods section 6.3).

Figure 6.4 further illustrates the effect of the kirigami cuts on the shape transformation of the 3D structures. The process of release of substrate prestrain from 100% to 40% refers to the “stretching mode”, imparting only compressive forces to the bonding sites of the structure, and this process is identical to the previous reported compressive buckling approach on conventional uniform substrate. Further releasing the substrate prestrain activates the “rotating mode”, whereby shear stress induced by the rotating units leads to the local twisting of the structure. The maximum rotation angles and principal strain of the units depend on the geometric parameters of the cuts (Figure 6.10, 6.11, 6.12, 6.13, 6.14). Typical parameters chosen in experiments ($D = 2$ mm, $w = 100$ $\mu$m, $\delta = 400$ $\mu$m) ensure a maximum rotation anble close 45° within limits of the fracture of the elastomer and the laser cutting resolution.

In addition to simple ribbon structures, more complex architectures and shape transformations could be realized via this assembly process. Figure 6.10 showcases a 3D morphing architecture with two distinct shapes formed after stretching mode (40% strain) and after the rotating mode (0% strain). The design comprises two levels of arrow-like structures of which the “bases” are bonded onto the preselected unites of the kirigami substrate and rotates in opposite directions during the rotating mode, that enables ”folding” of the arrows to a more upward arrangement of the structures from shape I to shape II.

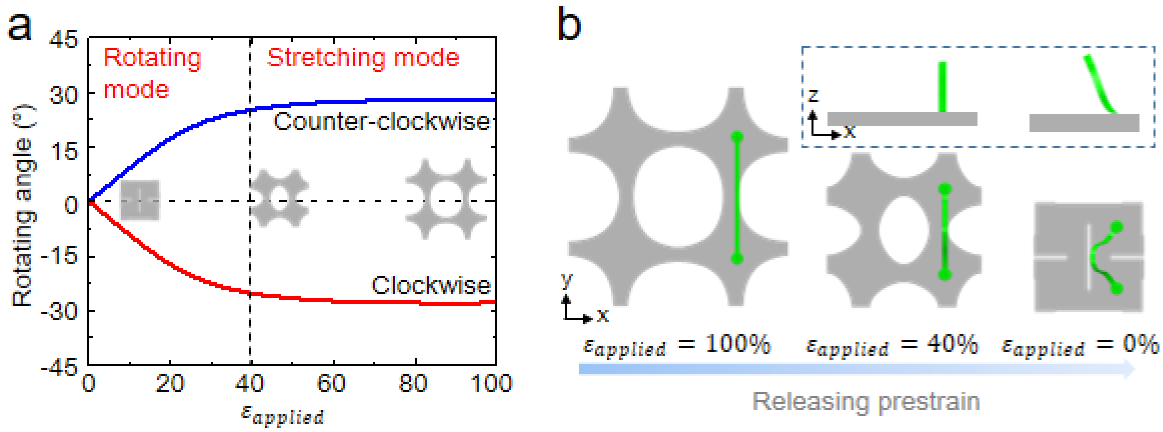


Figure 6.4. Scheme of rotation of kirigami substrate and the induced twisting of 3D structure.

The shape transformations from 2D to the two 3D shapes are continuous and reversible, and can be realized simply by mechanically stretching/releasing the elastomer substrate.

Figure 6.11 presents a broad set of 3D morphable structures formed on kirigami substrates, including several ribbon structures, kirigami membrane structures and origami membrane structures, with FEA results and correlated optical images of experiment. It is noteworthy that this assembly approach can be scaled down to a few hundreds of micrometers, that proved by the SEM images of experiment shown in Figure 6.12. Figure 6.13 presents that multi- structures can be fabricated parallelly on a single piece of kirigami substrate, that indicates the possibility of high fabrication efficiency. Figure 6.14 demonstrates the capability of this process applying various materials such as copper and silicon.

Recently, Fu et al [**38**] reported a novel assembly approach by releasing prestrain via different "loading paths" to form 3D geometries that can morph into multiple states. Our proposed assembly process on kirigami substrate is perfectly compatible to this "loading

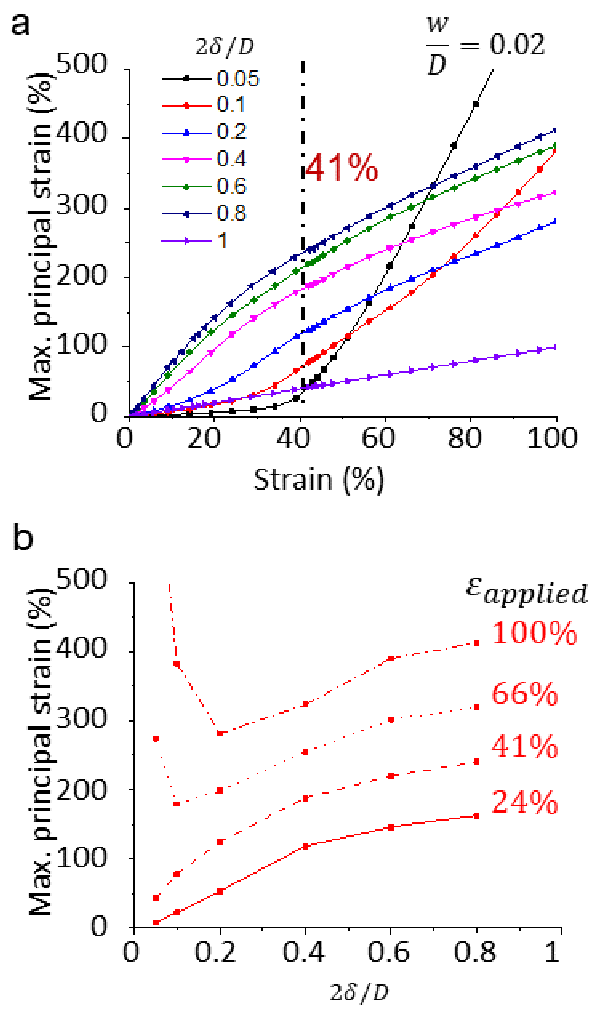


Figure 6.5. Maximum principal strain in substrate (a) versus applied strain for different $\delta/D$ ratio, and (b) versus $\delta/D$ ratio for different applied strain.

path" approach, as presented in Figure 6.15 and 6.16. Figure 6.15a shows the scheme of the stretching process of kirigami substrate with two different loading paths. Note that a rectangular kirigami pattern (aspect ratio = 2.5) is employed in this "loading path" approach, in order to avoid the wrinkling problem in square patterned (aspect ratio = 1.0) substrate under uniaxial stretching (Figure 6.17, 6.18). In loading path

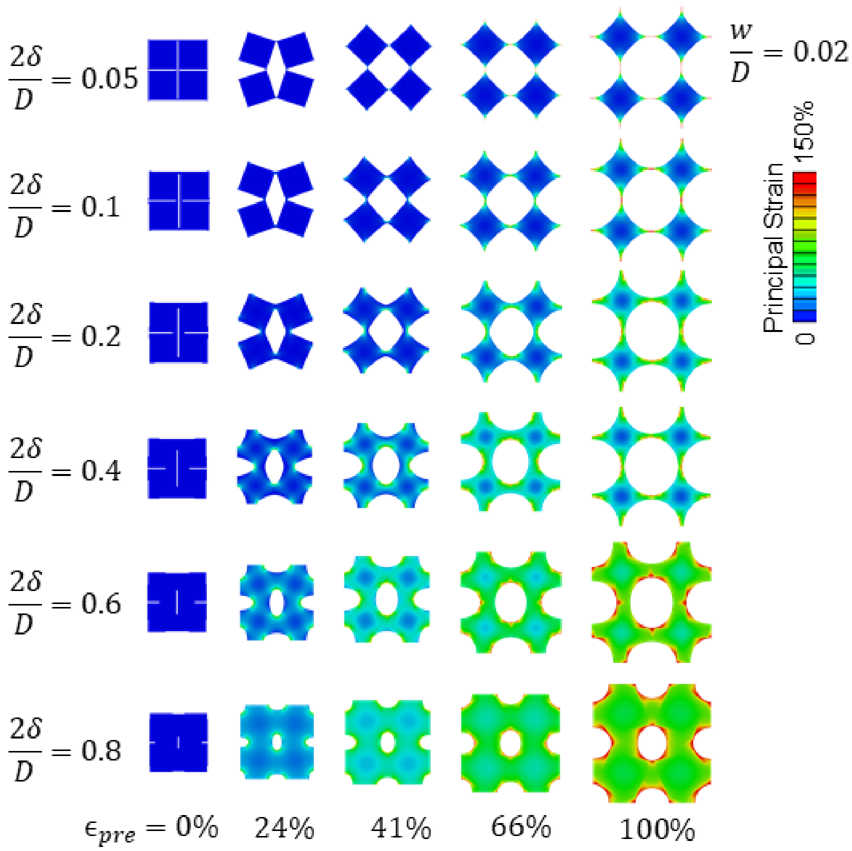


Figure 6.6. FEA results for deformed configuration and maximum strain contour of kirigami substrate with different $\delta/D$ ratio.

I, the kirigami substrate is initially stretched from fully released state (state ①) to an intermediate stretched state (state ③) via rotating mode, then fully stretched to final state (state ④) via stretching mode. However, in loading path II follows from an opposite order that the substrate is initially stretched to another intermediate state (state ②) via a stretching mode and then reaches state ④ via a rotating mode. The release of the prestrain of the kirigami substrate in state ④ via these 2 different loading paths will

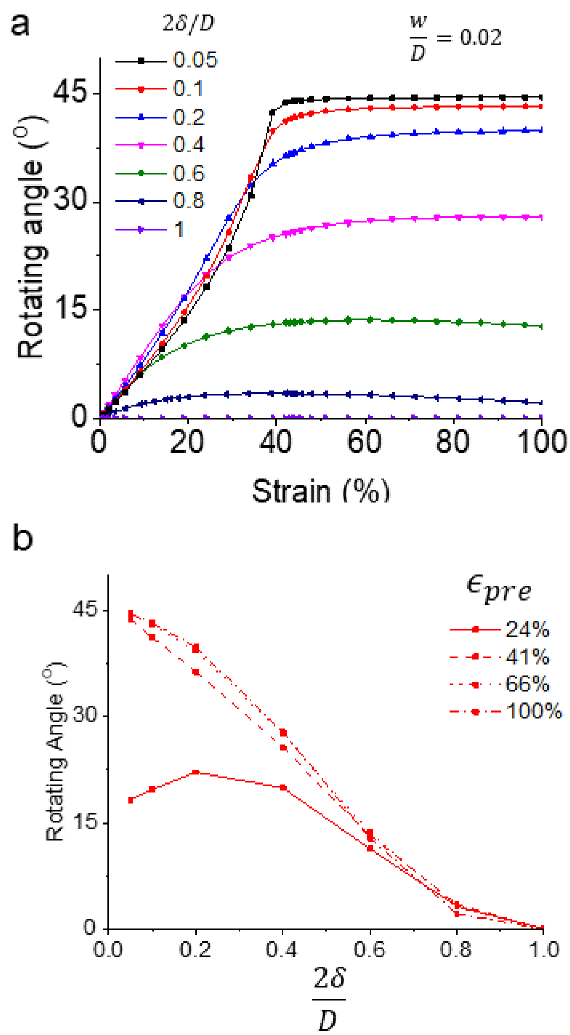


Figure 6.7. Rotating angle (a) versus applied strain for different $\delta/D$ ratio, and (b) versus $\delta/D$ ratio for different applied strain.

lead to 4 different reversely morphable 3D structures (Figure 6.16) for each designed 2D precursor.

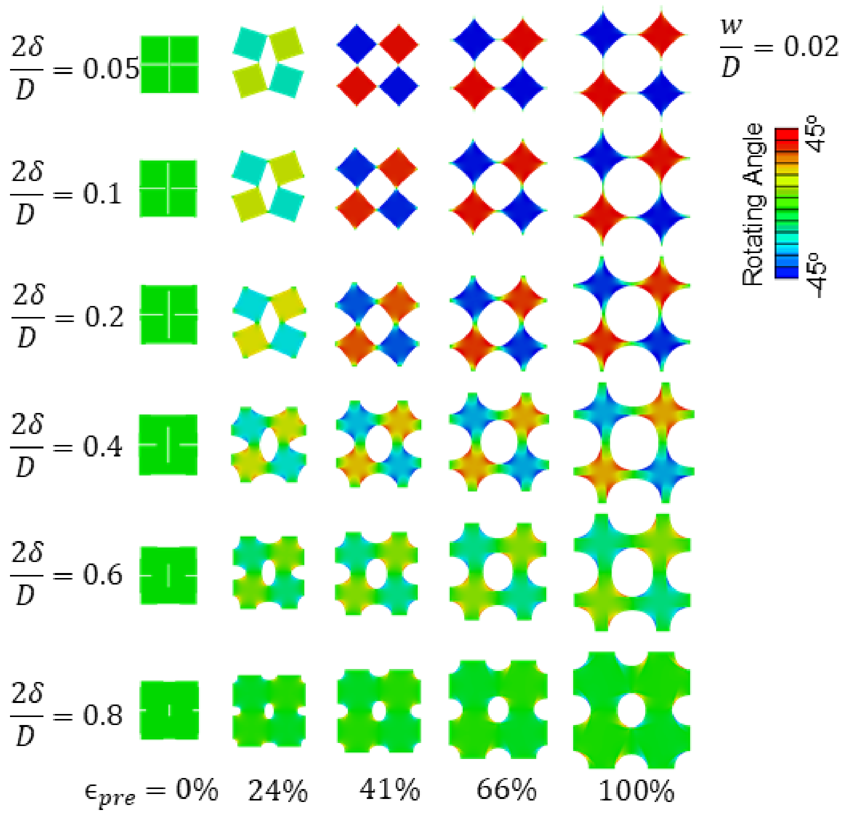


Figure 6.8. FEA results for deformed configuration and rotating angle contour of kirigami substrate with different $\delta/D$ ratio.

## 6.3. Methods

### 6.3.1. Experimental methods

**6.3.1.1. Fabrication of 3D mesostructures on kirigami substrates.** Preparation of 2D precursors began with spin coating (3000 rpm for 30 s) and curing (180 °C for 2 min) a thin poly (methyl methacrylate) (PMMA) layer onto a clean glass slide, followed by spin coating and fully curing (260 °C for 1 hr) a polyimide (PI-2545, HD MicroSytems) layer. The spin speed and times determined the polyimide layer thickness (2-9 $\mu$m depending

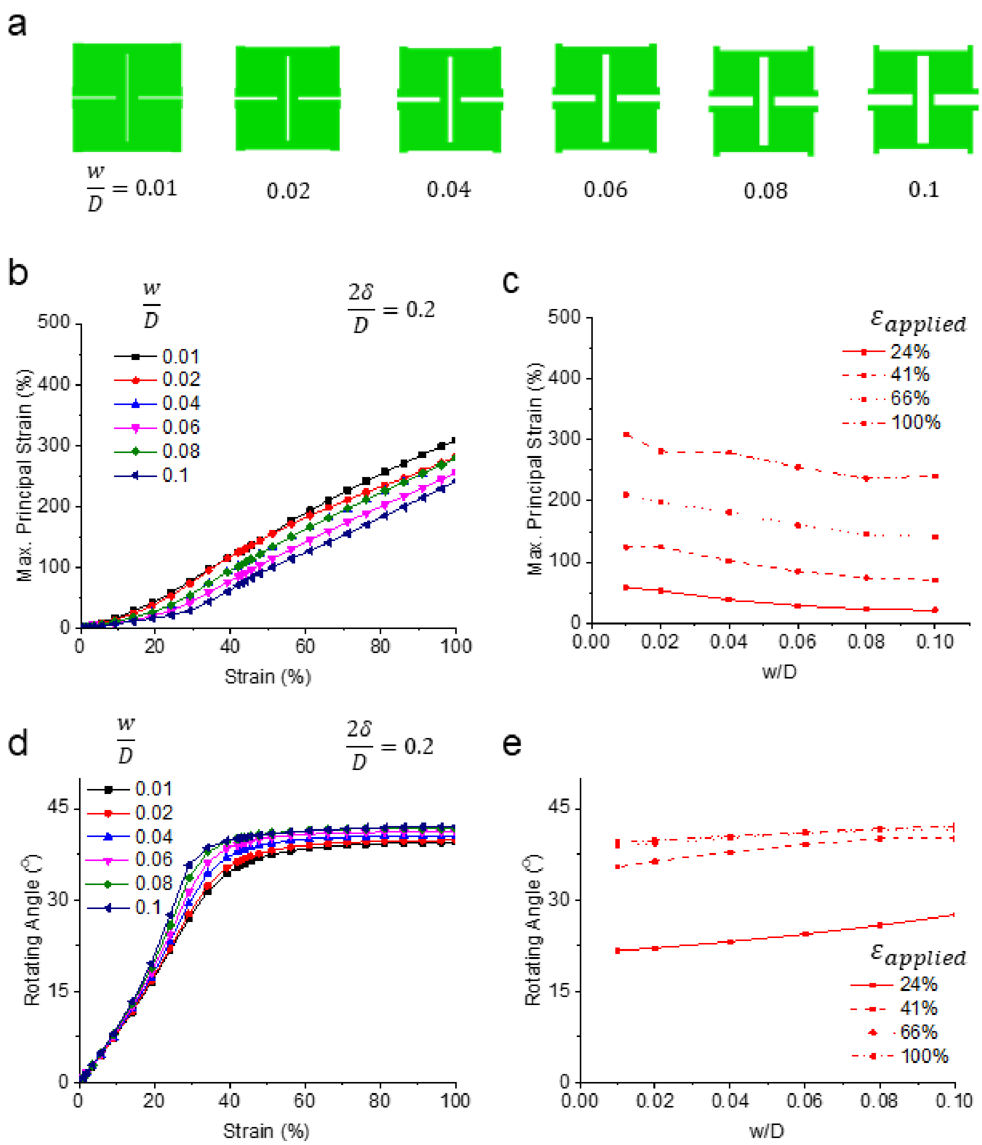


Figure 6.9. Effect of $w/D$ on maximum principal strain and rotating angle of kirigami substrate

on pattern size). A thin layer of chromium (Cr, 10 nm) and gold (Au, 100 nm) deposited on the PI layer by electron beam evaporation and patterned by photolithography and wet etching served as a hard mask for oxygen plasma etching of the PI. Immersion in

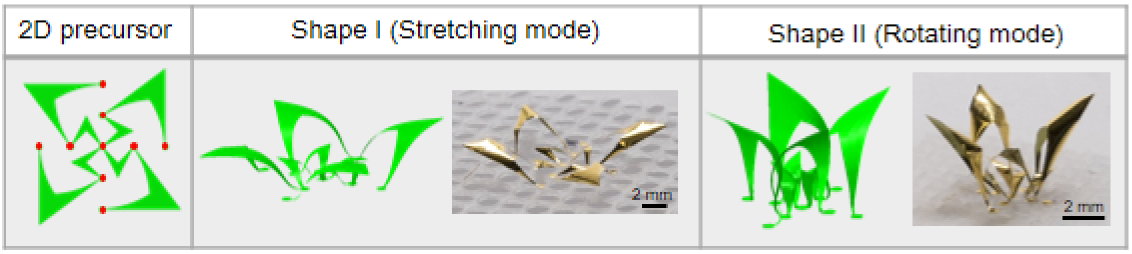


Figure 6.10. A sample of “flower” structure on kirigami substrate.

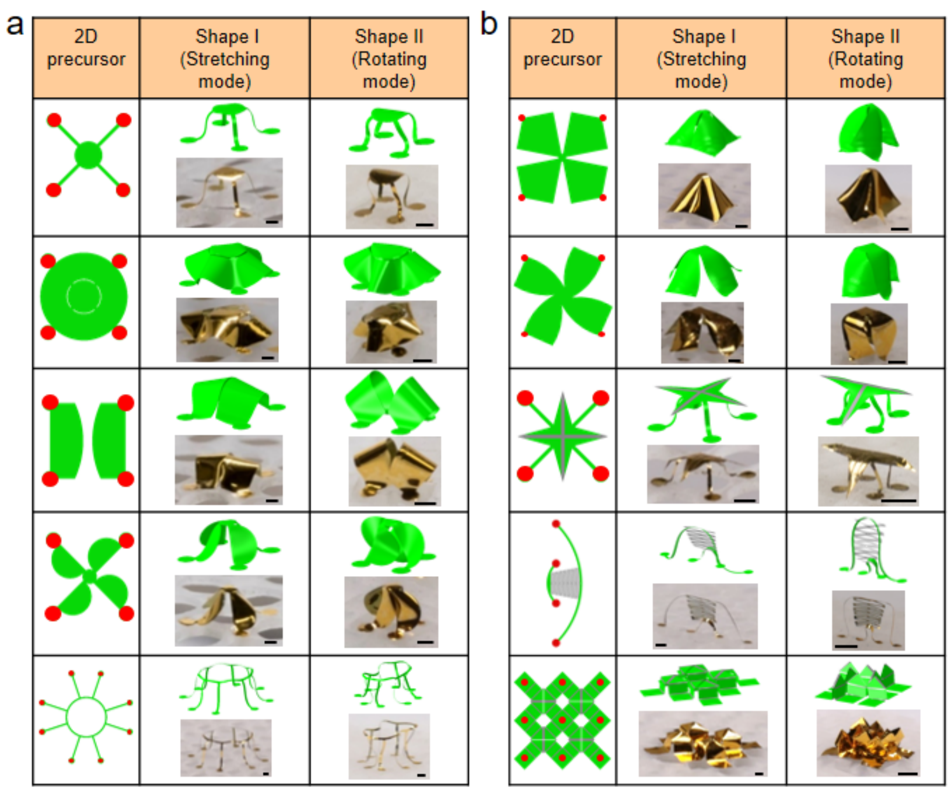


Figure 6.11. A set of 3D structures formed on kirigami substrate.

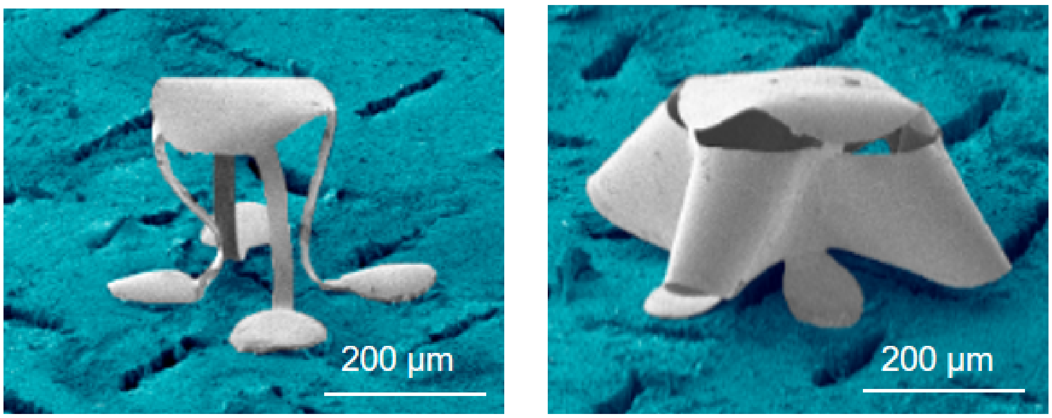


Figure 6.12. SEM images of micro- scale fabrication.


Figure 6.13. Demonstration of parallel fabrication.

acetone overnight dissolved the underlying PMMA layer, thereby allowing the structures to be retrieved from the glass slide and transferred to a water soluble tape (polyvinyl alcohol, PVA). Deposition of Ti/SiO2 (10 nm/50 nm in thickness) via electron beam evaporation through a shadow mask onto the back sides of the structures defined the

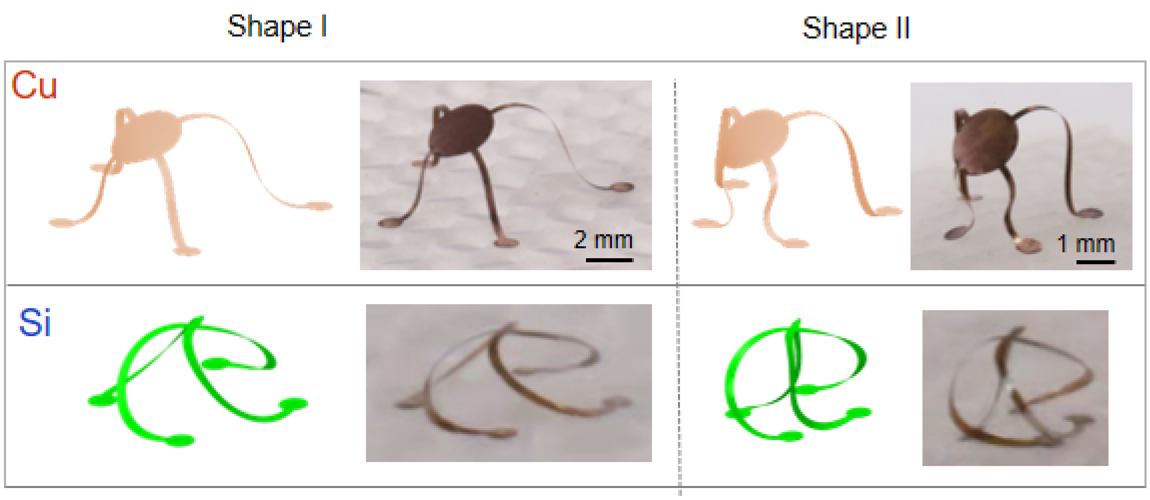


Figure 6.14. Fabrication with various materials.

bonding sites. A thin (~0.7 mm) sheet of silicone elastomer (Dragon Skin, Smooth-On) with cuts created by laser cutter (VLS3.50, Universal Laser Systems) served as the kirigami assembly platform, using 40% power, 30% speed, and 1000 pulses per inch. Exposing the 2D precursors and the elastomer surface to ultraviolet (UV)-ozone generated surface hydroxyl groups to facilitate subsequently bonding. Pre-stretching the elastomer with 100% biaxial strain and laminating the 2D precursors/PVA tape onto the stretched elastomer with subsequent heating (70 °C for 10 min) registered the bonding sites of structures on the rotating units in the elastomer. Dissolving the PVA tape with water and releasing the prestrain transformed the 2D precursors into 3D mesostructures. The scheme of this process appears in Figure 6.19.

**6.3.1.2. Fabrication of 3D origami mesostructures.** The process began by spin coating and curing PMMA (same procedure as described above) and PI (1500 rpm for 60 s, 3 $\mu$m in thickness) on a glass slide, followed by the deposition of titanium (Ti,

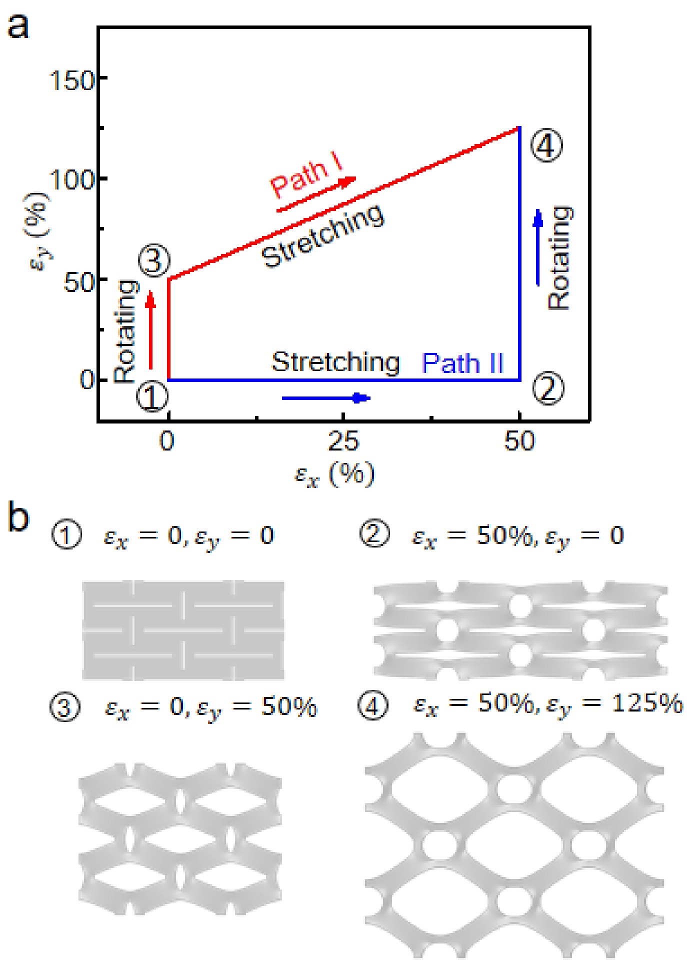


Figure 6.15. Scheme of loading path approach on kirigami substrate.

10 nm) and copper (Cu, 1 $\mu$m) by electron beam evaporation. Photolithography and wetting etching defined the Cu pattern. Deposition of a layer of Cr/Au (10 nm/100 nm in thickness) followed by photolithography and wet etching served as a hard mask for oxygen plasma etching of the PI layer. The remaining steps followed the procedures described above. The scheme of this process appears in Figure 6.20.

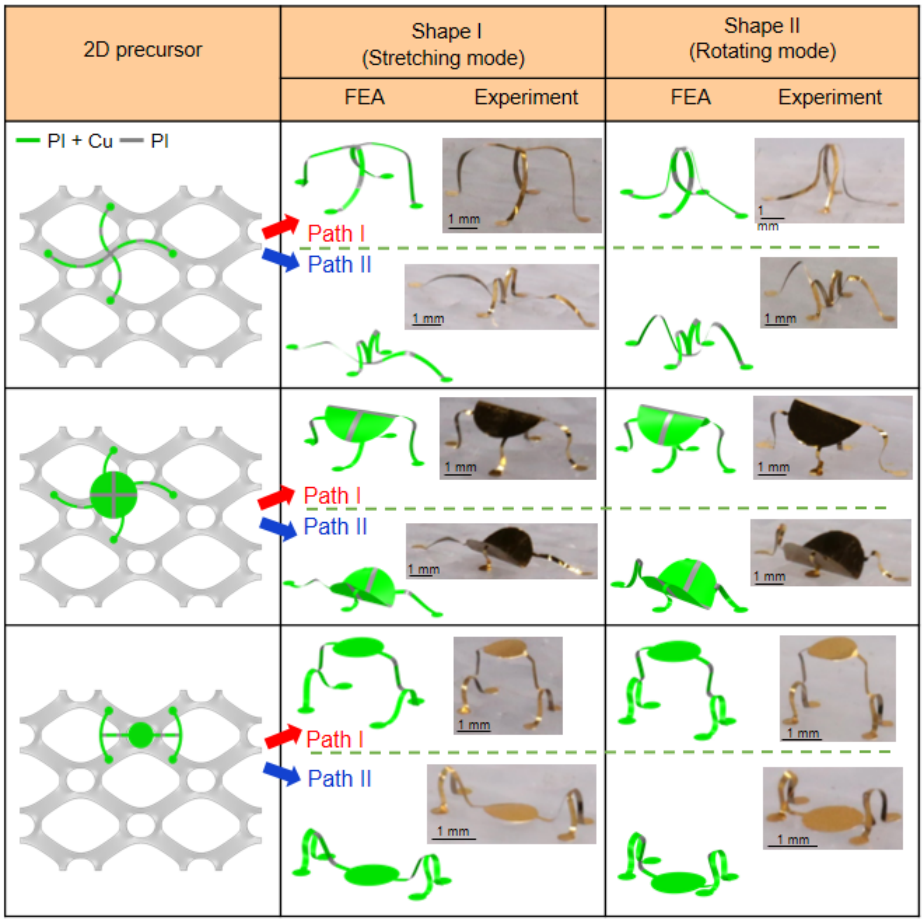


Figure 6.16. A set of 3D structures fabricated by different loading paths on kirigami substrate.

**6.3.1.3. Fabrication of 3D freestanding mesostructures.** Preparation of the 2D precursors began with the spin coating of a thin layer of water soluble polymer (poly(4-styrenesulfonic acid), Sigma-Aldrich) onto a glass slide, followed by spin coating (3000 rpm for 60 s) a mixture of epoxy monomer E44 (molecular weight ∼450 g/mol, China Petrochemical Corporation) and curing agent poly (propylene glycol) bis (2-aminopropyl) ether (Jeffamin D230, Sigma-Aldrich) with a weight ratio of 44:23. After baking the

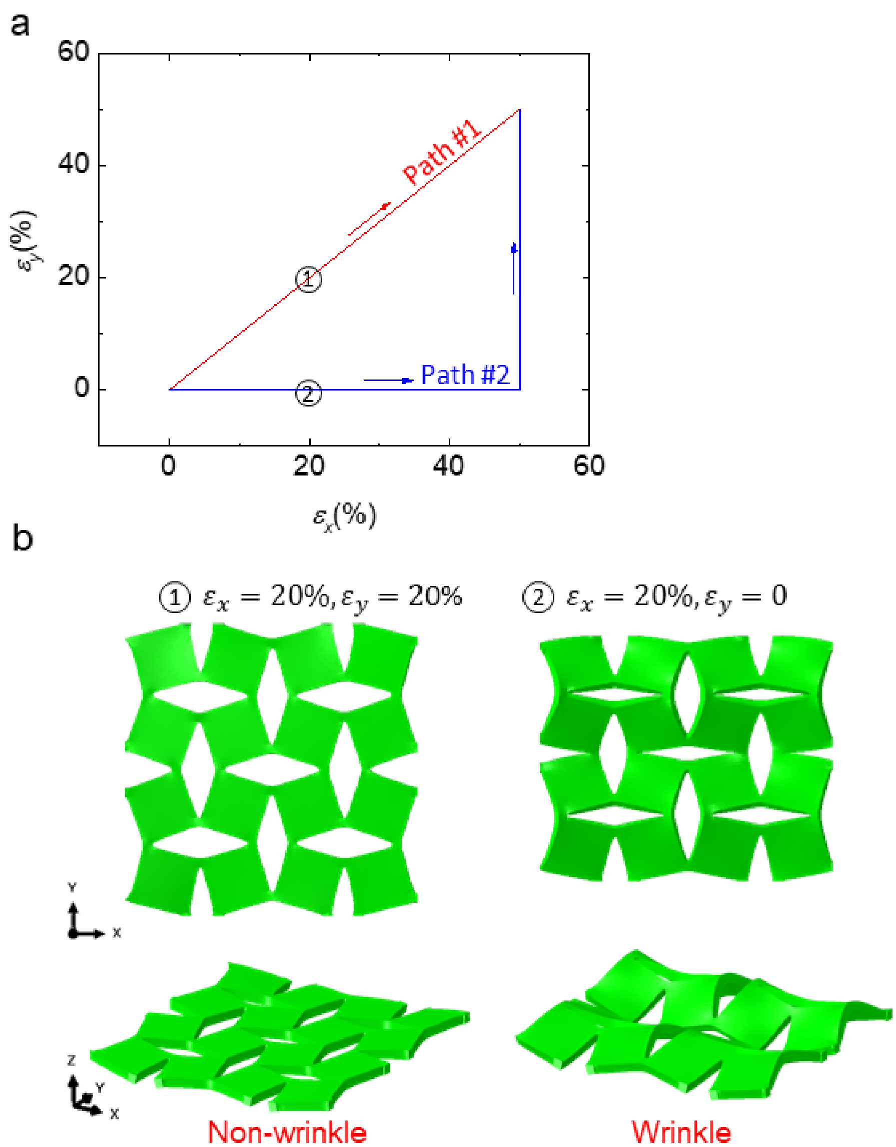


Figure 6.17. Illustration of the wrinkling problem encountered in square patterned kirigami substrate under uniaxial stretching.

mixture (110 °C for 1 hr) in an oven, deposition of a thin layer of Cr/Au (10 nm/100 nm) deposited on the SMP by electron beam evaporation and patterned by photolithography and wet etching served as a hard mask for oxygen plasma etching of the SMP. Immersion

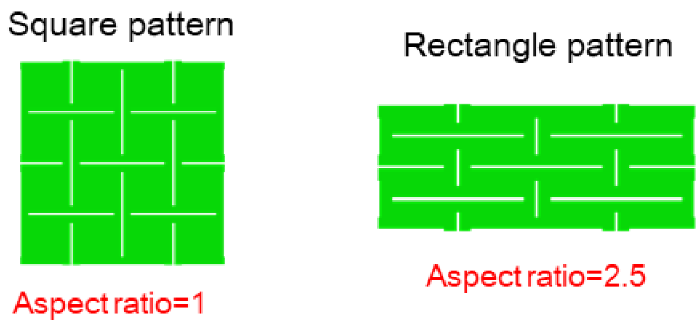


Figure 6.18. Illustration of the aspect ratio.

in water for 48 hrs dissolved the underlying water soluble polymer sacrificial layer and enabled the transfer of the 2D precursors to a PVA tape. Deposition of Ti/Au/Ti/$SiO_2$ (5 nm/100 nm/5 nm/50 nm in thickness) via electron beam evaporation through a shadow mask defined the bonding sites. The buckling steps followed the procedures described above. Thermal treatment (70 °C for 5 min) in an oven fixed the shapes of the buckled 3D SMP structures and immersion of the 3D structures on stretched elastomer in Au etchant for ~5 hr released the structures from the elastomer substrate and etched off the Au mask layer.

**6.3.1.4. Fabrication of 3D silicon mesostructures.** Preparation of the 2D precursors began with patterning the top silicon layer (1.5 $\mu$m in thickness) on a silicon-on-insulator (SOI) wafer using photolithography and dry etching of silicon, followed by partially undercutting the $SiO_2$ layer in hydrofluoric acid (HF, 49%) for 90 sec. Spin coating (3000 rpm for 40 sec) and lithographically patterning a photodefinable epoxy (SU8, Microchem) created a supporting layer for silicon. Another photolithography step on top of the SU8 layer defined the bonding sites, followed by fully undercutting the $SiO_2$ underlayer in HF

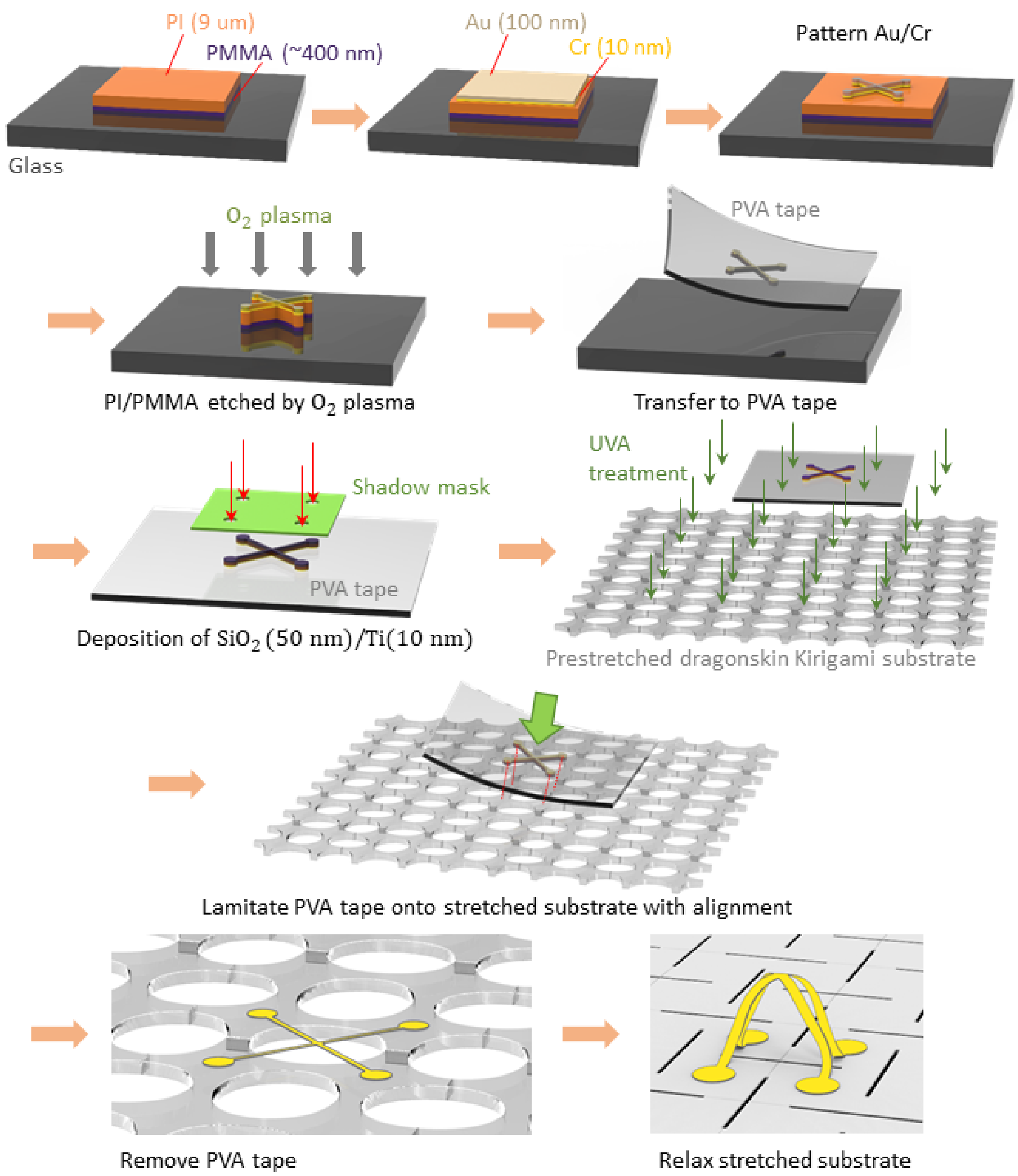


Figure 6.19. Fabrication of 3D mesostructures on kirigami substrate.

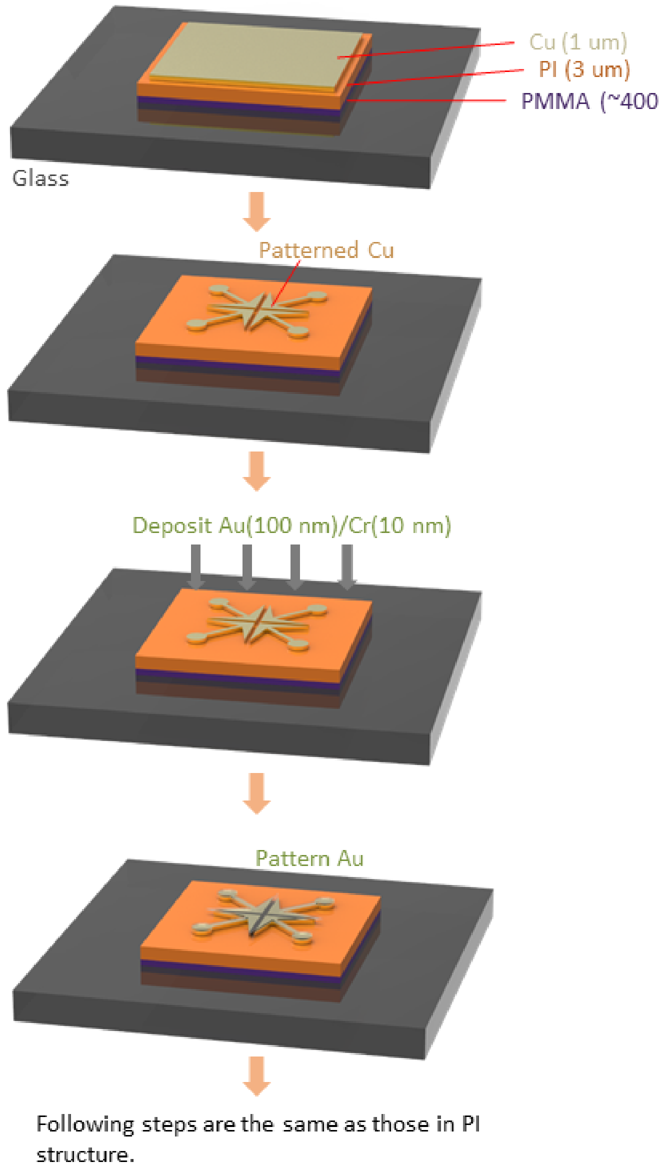


Figure 6.20. Fabrication of 3D origami mesostructures.

(49%) for 4 hrs and subsequent deposition of Ti/$SiO_2$ (10 nm/50 nm in thickness) via electron beam evaporation. The remaining steps (transfer printing, buckling) followed the procedures described above. The scheme of this process appears in Figure 6.21.

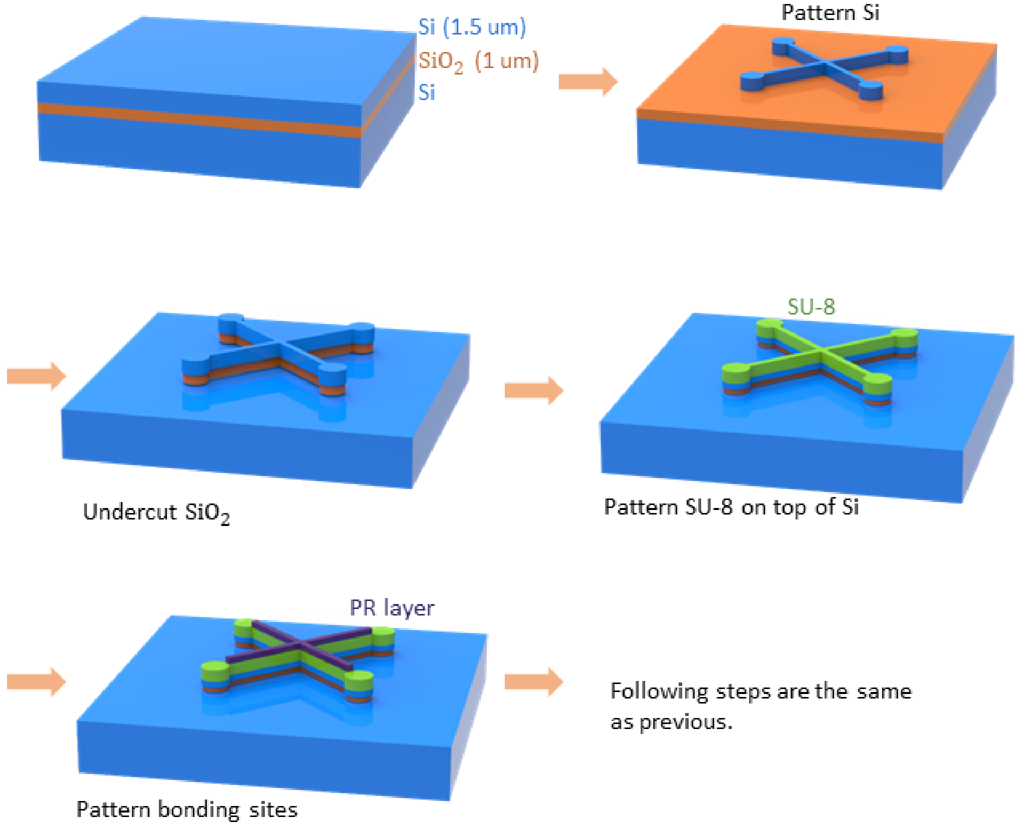


Figure 6.21. Fabrication of 3D silicon mesostructures.

**6.3.1.5. Fabrication of multi-layered 3D mesostructures.** Preparation of the 2D precursors followed the procedures described above. Transfer printing of the 2D precursors from the glass slide to the PVA tape started with the top layer, followed by the transfer printing of the middle and bottom layers onto the PVA tape laminated with the top layer, subsequently. The remaining steps followed the procedures described above.

### 6.3.2. Finite element analysis

Three-dimensional finite element analysis yielded predictions of the mechanical deformations and strain distributions of the 3D structures during the assembly process. Four-node shell elements are employed to model the structures. Refined meshes ensured computational accuracy using a commercial software (Abaqus). The material parameters used were as follows: $E_{PI} = 2.5$ GPa, $\nu_{PI} = 0.27$; $E_{Si} = 130$ GPa, $\nu_{Si} = 0.27$; $E_{Au}$ =79 GPa, $\nu_{Au}$ =0.34. Here, $E$ is elastic modulus and $\nu$ is Poisson's ratio.

## 6.4. Conclusion

We developed a novel 3D assembly approach based on the compressive buckling approach by releasing the prestrain of underlying elastomer substrate with kirigami cut. Previous reported approaches on conventional uniform elastomer substrates provide only translational motion to the bonding sites, which damps the variation of the 3D structures. By adding cut patterns to the elastomer substrate, rotating motions are induced to the bonding sites because of the rotation of individual units of the substrates. Consequently, the top 3D structures can be twisted and the library of the compressively buckled 3D structures is significantly extended. Further exploration applying loading path approach to this novel process on kirigami substrate demonstrates next-level morphability of the 3D structures.

CHAPTER 7

# Application of Freestanding 3D Microstructures: Three-dimensional Microflyer for Air Pollution Detection

## 7.1. Introduction

Growing interests of 3D microstructures have significantly stimulated the development of assembly methods for mesostructures, such as bending/folding of thin films induced by residual stresses of capillary forces [**154, 55, 101, 8, 146, 48, 135**], self-acuating materials driven formation [**90, 85, 51, 196**], microcontact printing [**61, 138**], and addictive manufacturing [**175, 2, 209, 96, 43, 158**]. These 3D mesostructures have broad-range applications in the technologies of micro- and nanosystems, for example, plasmonic and photonic nanosystems [**4, 103, 168, 225, 226**], microelectronic circuits [**12, 201, 33, 2, 56, 47**], optical/mechanical metamaterials and biomedical tools [**178, 101, 220**], and energy storage and generation devices [**224, 133, 175, 128**]. Here we explored a new application of 3D mesostructures, microflyer, that comprises 3D mesostructures, microelectronic systems and micro-aircraft and have potential application such as high altitude air pollution detection.

A broad set of plants spread their inhabitation place by using oncoming wind to fly their seeds away from the parent plant to a suitable place [**15, 17, 46, 122**]. There are two types of wind dispersal seed, one of which is pappose seeds (parachute type) such as dandelions, and the other one is winged seeds such as maple seeds. The pappose seeds utilize drag force acting on the pappi while falling stably at a constant speed in quiescent conditions [**45, 3, 122, 171**], whereas the winged seeds mainly use lift force acting on their wings. The winged seeds can be further classified into two classes, one is glider type which has no rotational motions during falling, and the other one is the rotating type which shows auto-rotation phenomenon during their fall. This phenomenon slows down the descent of the seed to make long-distance flight away from the parent tree by wind [**17, 35, 122**]. In the present study, we proposed several 3D microflyers based on the rotational falling phenomenon with inspiration from several natural seeds. Coupled structure-fluid simulation was employed to characterize the falling behaviors of the microflyer, which are also predicted by analytical model and verified by experiment results.

## 7.2. Results and Discussion

### 7.2.1. Design of 3D microflyers

Figure 7.1 presents a representative set of 3D microflyer structures inspired by several natural seeds such as those of tragopogon dubius, alsomitra macrocarpa, banksia media and diptocarpus, as well as a commercial propeller, as demonstrations for "parachute", "glider" and "rotational falling" types of seeds, respectively. These 3D bio-inspired structures are formed by the compressive buckling 3D assembly approach by releasing the prestrain underlying elastomer substrates [**206, 229, 212, 1, 111**], showing good compatibility of this previously developed process with the application of microflyer structures. Above these single-layer 3D structures, we also explored the capability to form more complex multi-layer structures inspired by see creatures, as presented in Figure 7.2.

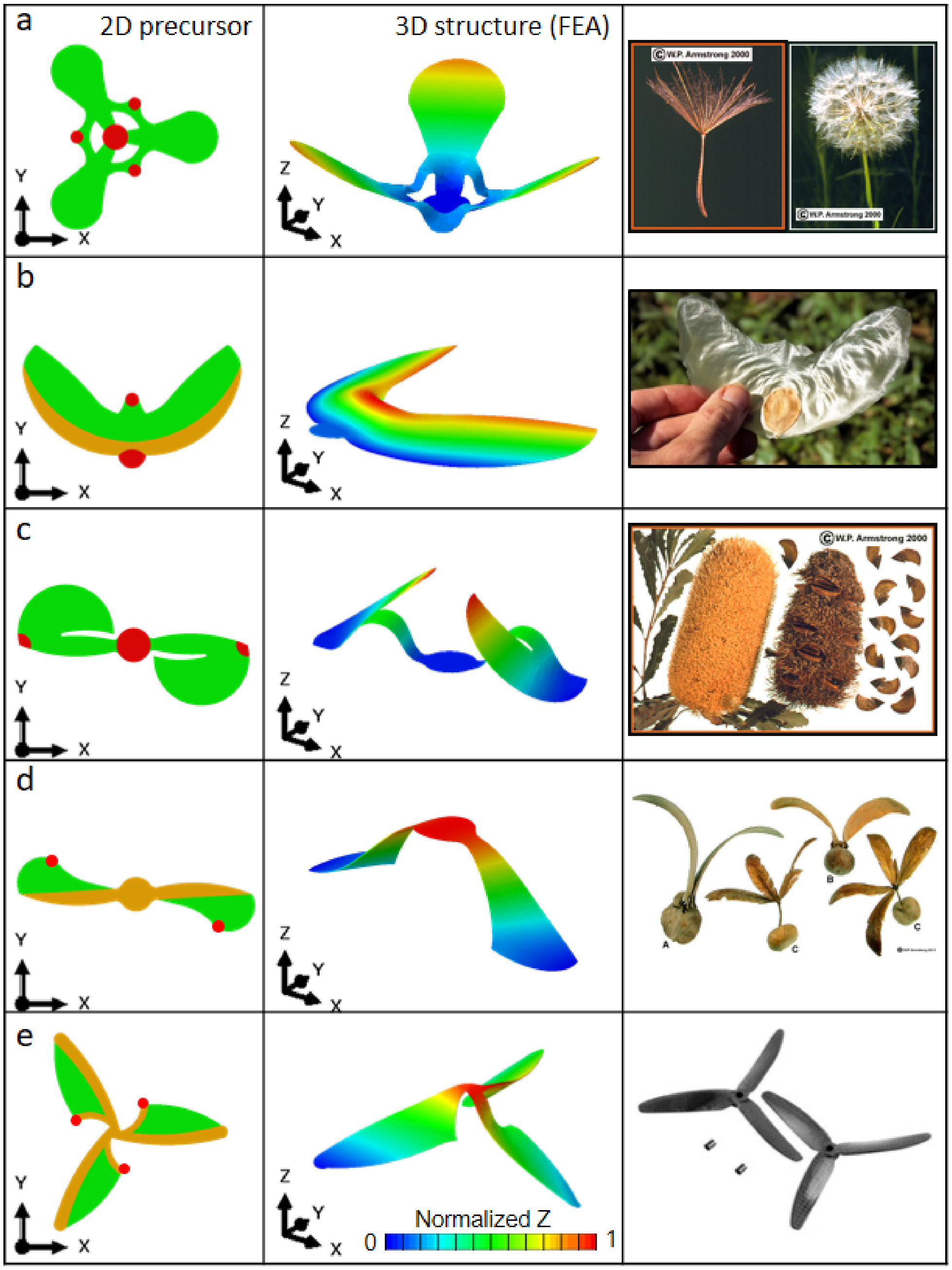


Figure 7.1. Bio-inspired single-layer 3D microflyer structures.

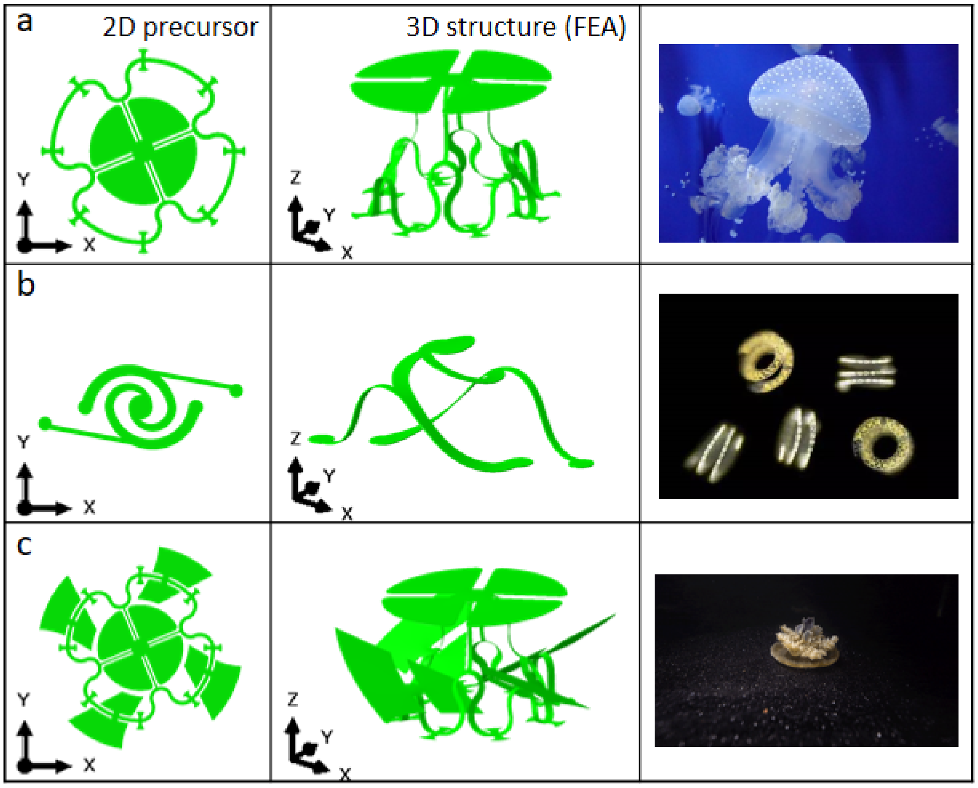


Figure 7.2. Multi-layer microflyer structures inspired by see creatures.

The autorotating seeds draw more interests because of their much higher wing loading [**100**] compared with the other kinds of seeds such as gliders and parachutes, also the stable flying state and the slow terminal falling velocity. With these said, we designed some compressively buckled 3D microflyer prototypes with expected autorotating falling behavior, as shown in Figure 7.3. Most of these structures are designed with tilted airfoils (wings) along rotational direction to enable the rotating motion during falling, except the design D5 which can be regarded as a "parachute" design with no rotational motion.

The falling behavior of these structures are modeled by coupled structure-aerodynamic simulations, as illustrated in Figure 7.4 and the detailed process can be found in the Methods section 7.3. The microflyer is falling stably in the air with a terminal falling velocity $v_T$ and a rotating speed $\omega$, while following the coordinate of microflyer the airflow inlet velocity equals to the terminal falling velocity. The simulation results are presented in Figure 7.5, showing the weight versus terminal falling velocity relations and rotating speed versus terminal falling velocity relations for these 3D microflyer designs. Note that the diameter of these designs are $D$ ~2 mm, ans the Reynolds number for them are $Re$ ~40. The results show large differences of falling behaviors, i.e. terminal falling velocity and rotating speed for a certain weight, among different structures, and the key geometric parameters that affect the falling behavior will be summarized in details in the later section of analytic model. Experiment results of falling tests for these structures done by Bong Hoon Kim et al. show good agreement with the simulation prediction (Figure 7.6) and thus provide verification.

It is noteworthy that these 3D mocroflyer structures show advantage to some conventional structures, such as parachute structure, spherical shell and solid sphere, if compared with the terminal falling velocity free falling in the air. Figure 7.7 and 7.8 present the comparison between the microflyer design D4 with the other 3 conventional structures with the same weight (Figure 7.7) and same size (Figure 7.8), respectively. Same materials (SMP; $\rho$=1.33 g/ml) are used in all structures and same thickness (6 $\mu$m) was used for all shell structures for fair comparison, and the microflyer design D4 still advances with the slowest terminal falling velocity.

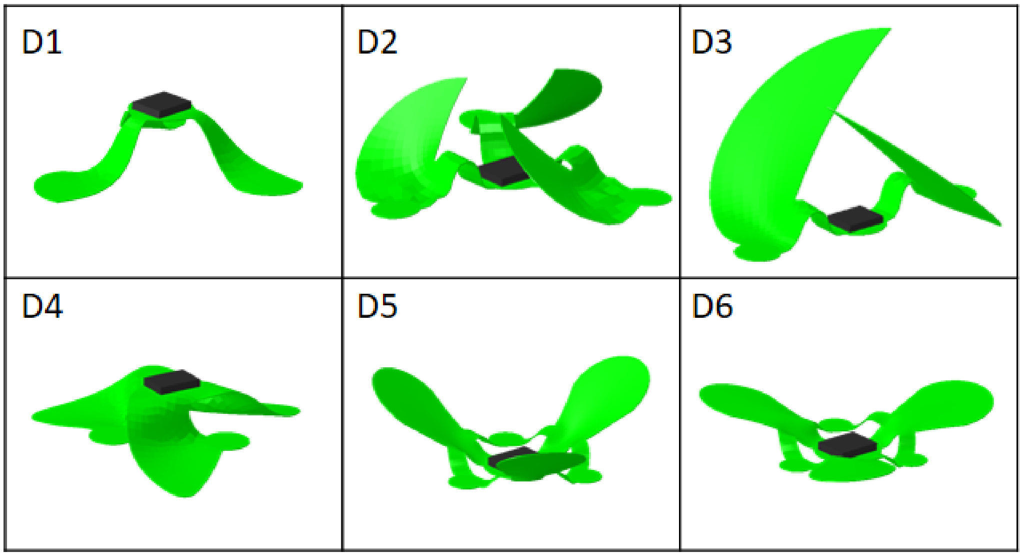


Figure 7.3. A set of 3D microflyer designs.

The 3D microflyers lose their advantages in terminal falling velocity comparing with their 2D precursors which are in planar configuration (Figure 7.9). Ideally speaking, the 2D precursors have smaller terminal falling velocity comparing with their 3D structures, if the 2D precursors can fall in the steady state with its surface normal vector parallel to the falling velocity, which is almost impossible in reality, because the 2D structures will fall fluttering or tumbling [**9**] in condition of different shapes (Figure 7.10). It remains to be a challenge to simulate the fluttering or tumbling behavior for the 2D structures, and as a result, it's hard to determine the terminal falling velocity of 2D precursor in such complex falling states despite it can be smaller than that of 3D structures.

However the 3D structures with rotating motion during falling show advantages in predictable falling path and controllable falling state, while it is difficult to achieve for

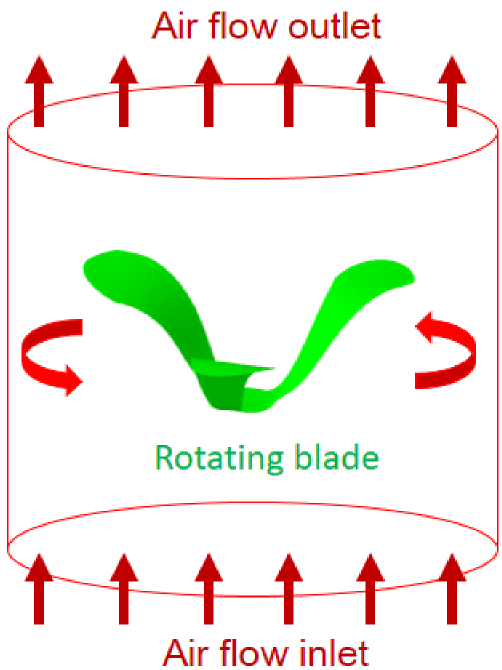


Figure 7.4. Illustration of aerodynamic simulation.

2D precursors because of the fluttering or tumbling problem. Even under the influence of horizontal wind, that have constant wind velocity with negligible turbulence such as in stratosphere [**148**], the 3D microflyer will robustly keep the rotating-falling steady state while the 2D precursor will easily flutter or tumble. The steady state falling velocity of 3D microflyer in horizontal wind can be easily determined. The X-directional velocity is equal to the wind velocity, and the Y-directional velocity is equal to the falling velocity without any wind (that of free falling). Thus, the falling path of the 3D microflyer can be predicted, as illustrated by Figure 7.11. Note that in steady state the Y-directional velocity is not influenced by horizontal wind. Evan under the horizontal wind, the relationship of "falling

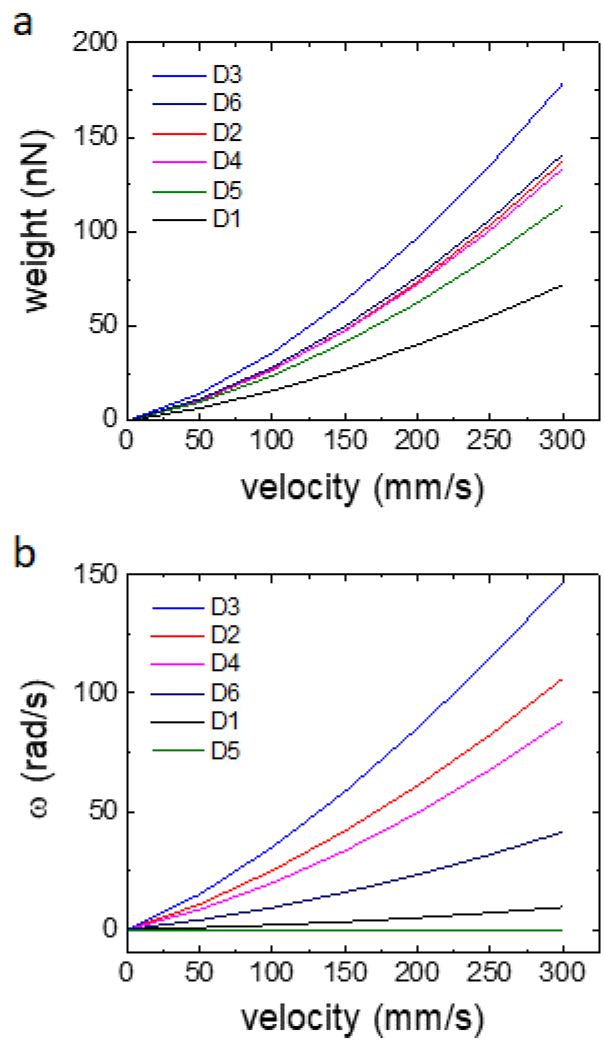


Figure 7.5. Aerodynamic simulation results for a set of microflyer designs shown in Figure 7.3.

hight" and "falling time" of 3D microflyer is nearly the same as the circumstance without any wind.

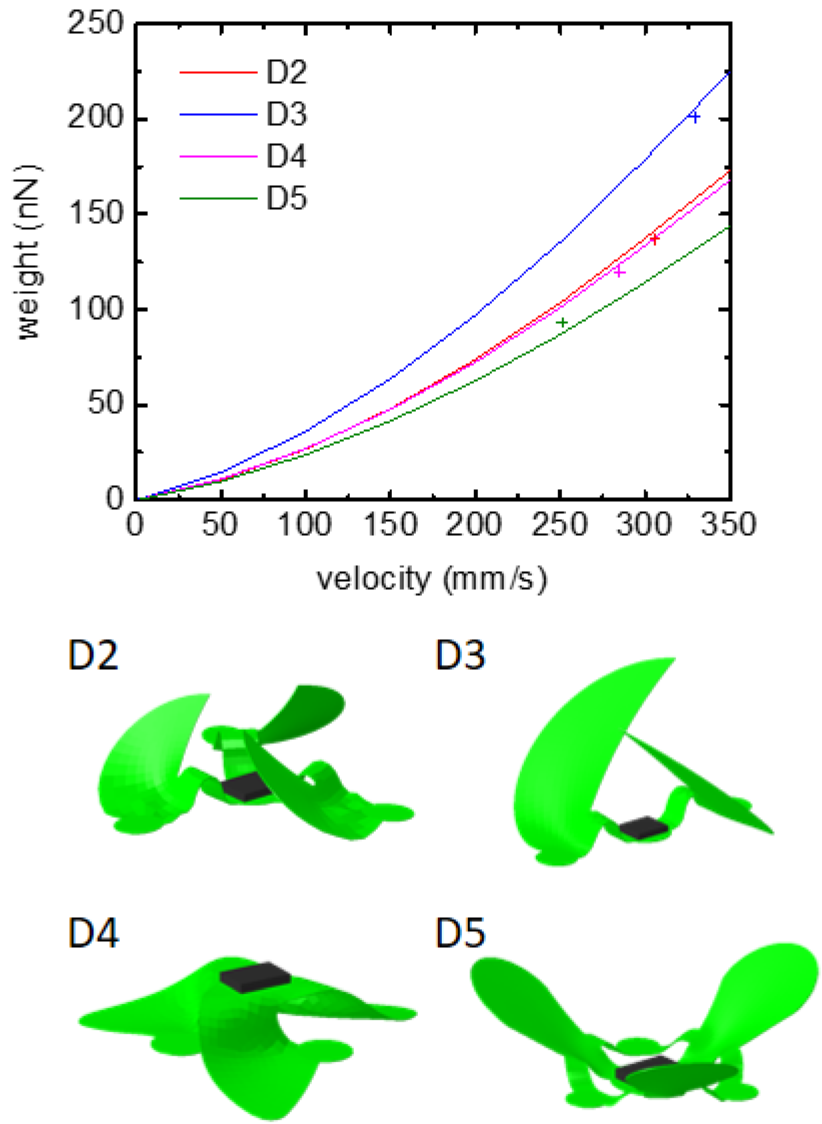


Figure 7.6. Experiment verification by falling test.

### 7.2.2. Analytic model of a falling microflyer

We developed an analytic model to further characterize the falling behavior of the microflyer, based on a highly simplified microflyer model, as shown in Figure 7.12. Neglecting

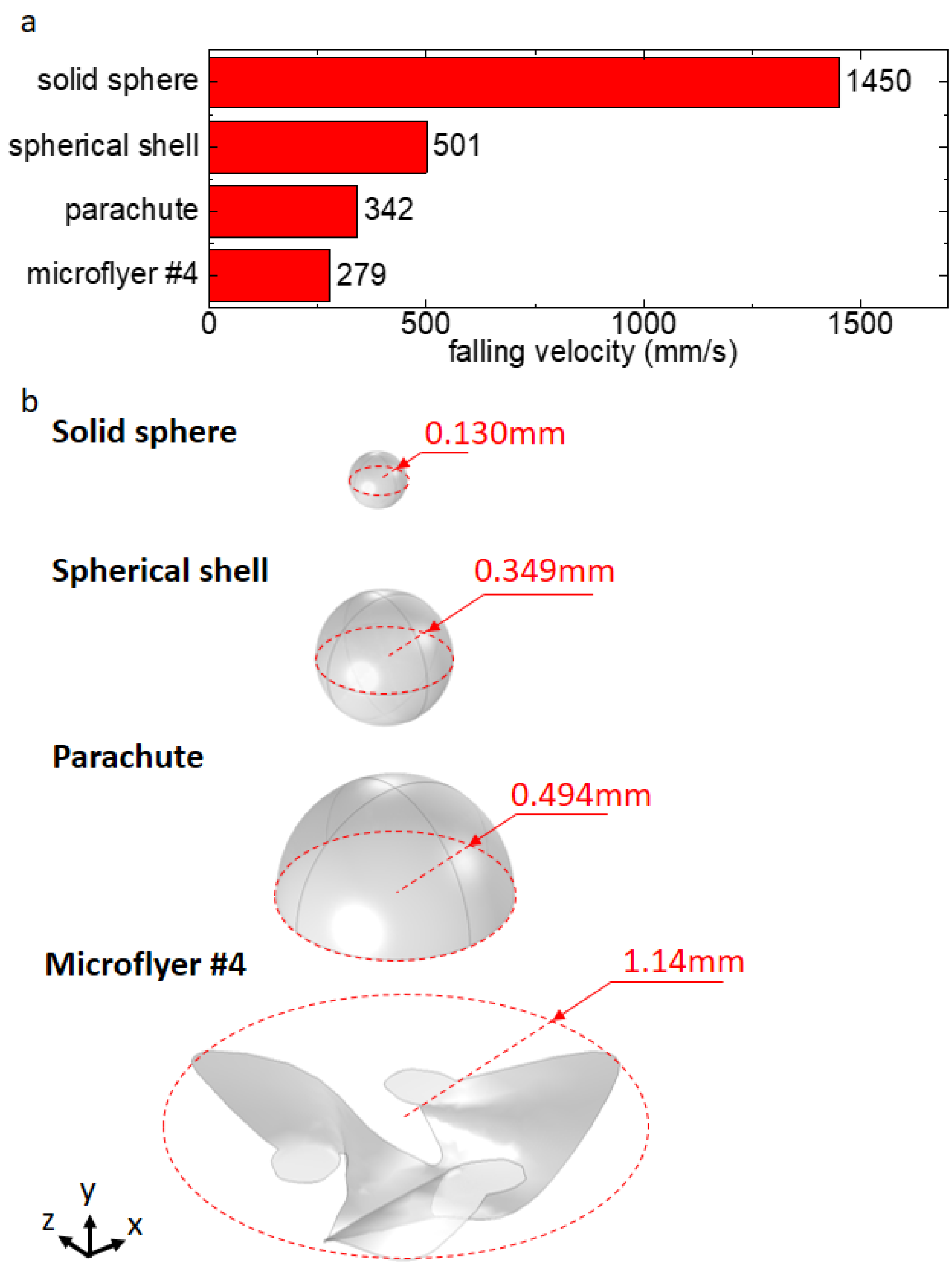


Figure 7.7. Comparison among microflyer and 3 conventional structures in same weight.

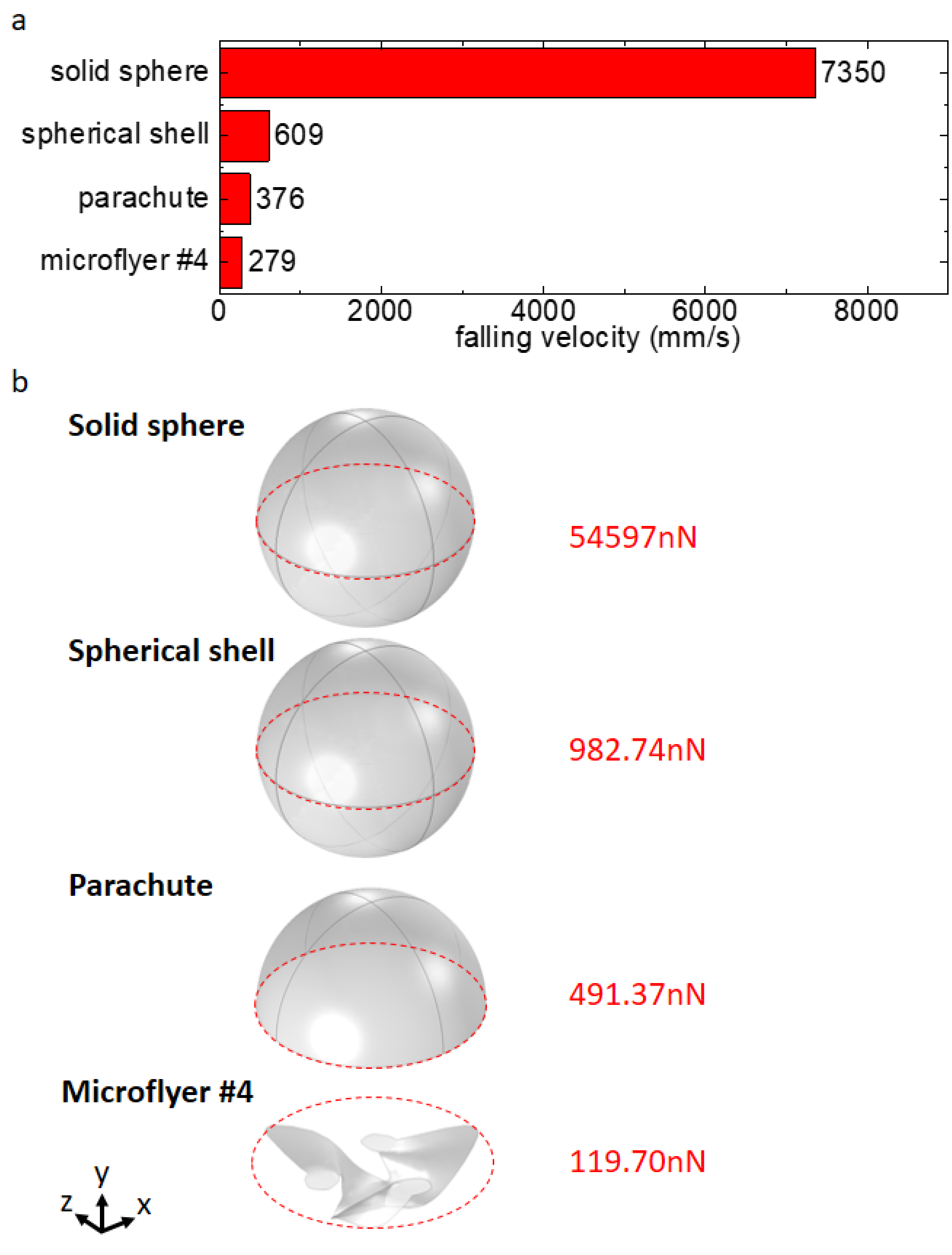


Figure 7.8. Comparison among microflyer and 3 conventional structures in same size.

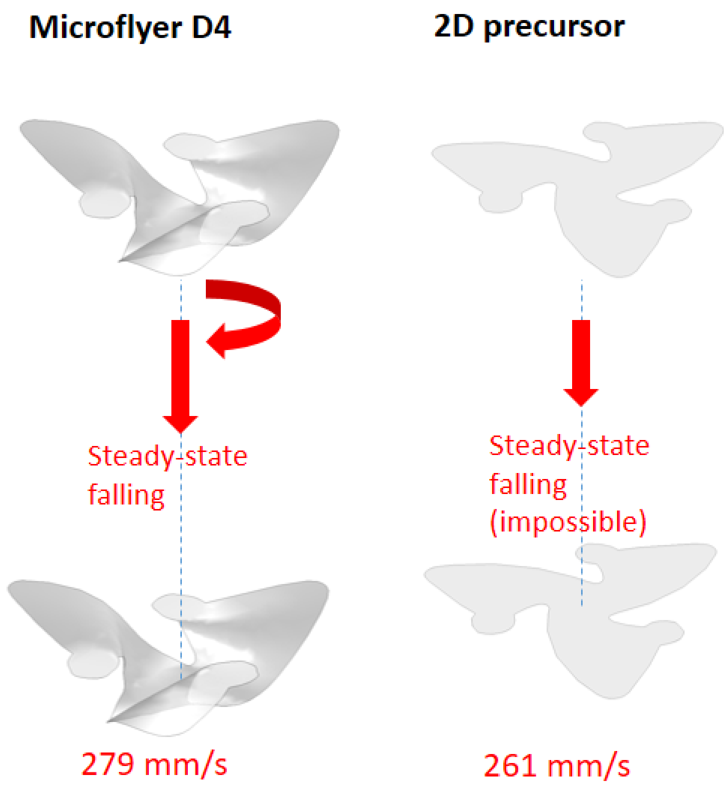


Figure 7.9. Comparison between 3D microflyer and 2D precursor.

the tumble problem, we assume that the microflyer is steadily falling in the air, with terminal falling velocity $v$ and rotating speed $\omega$. This simplified microflyer model consists of several (N, N=8) small blades (width $b$ ($b \ll r$), chord length $c$) locating at radius ($r$), and have the same tilt angle ($\beta$). Take one of the blades into consideration, the lift force ($L$) and drag force ($D$) can be expressed as:

$$L = \frac{1}{2}\rho U_a^2 \cdot bc \cdot C_L$$

$$D = \frac{1}{2}\rho U_a^2 \cdot bc \cdot C_D$$

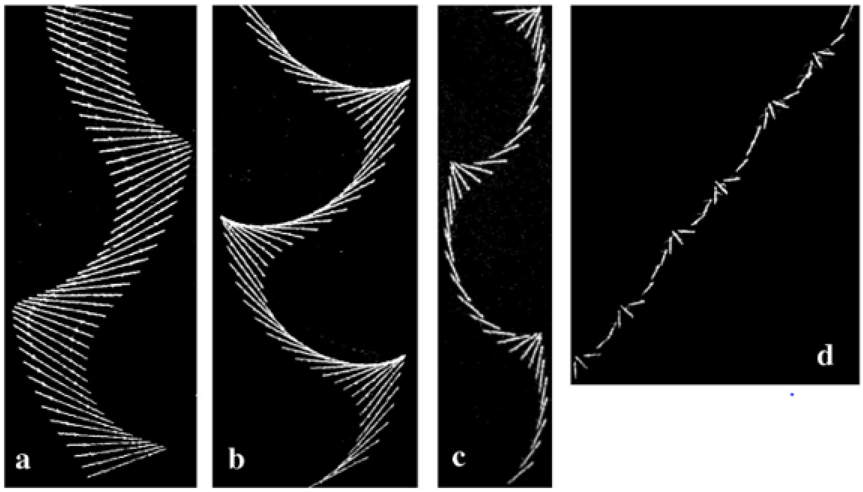


Figure 7.10. Illustration of flutter and tumble falling of 2D precursor.

$C_L$ is the lift coefficient and $C_D$ is the drag coefficient of a single blade. $\rho$ is the density of air, and $U_a$ is the flow velocity "seen" at the coordinate of blade, that

$$U_a = \sqrt{(v^2 + (\omega r)^2}$$

Considering the force equilibrium in rotational and vertical directions,

$$L_\theta = D_\theta$$

$$L_z + D_z = \frac{W}{N}$$

, where W is the weight of microflyer. From the rotational direction force equilibrium, the rotating speed expression is

$$L \cdot \frac{v}{U_a} = D \cdot \frac{\omega r}{U_a}$$

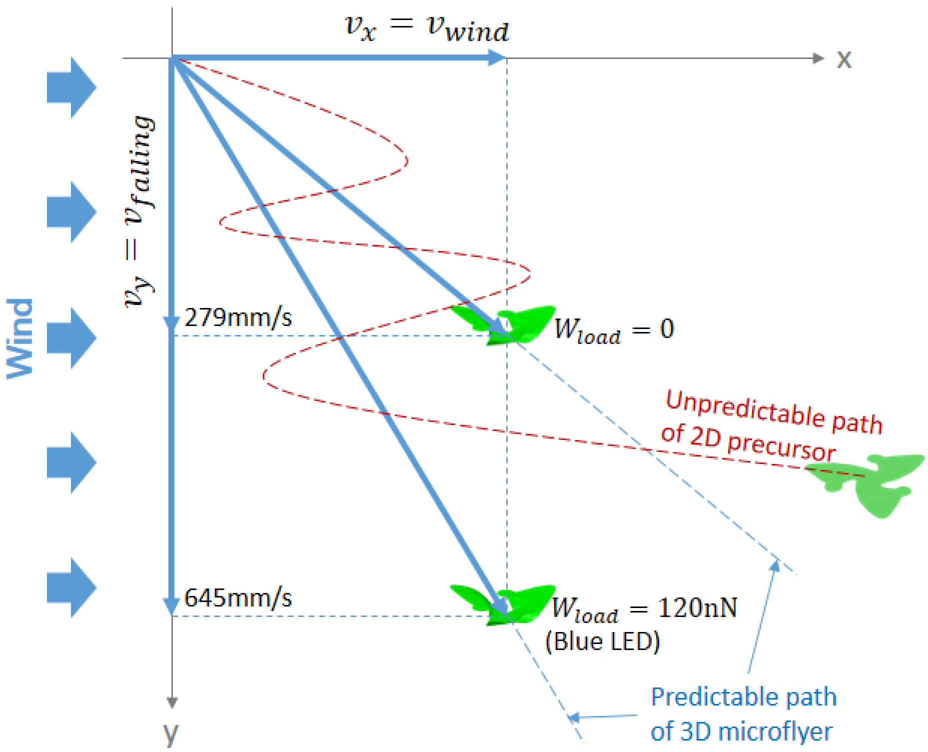


Figure 7.11. Scheme of the falling path for 3D microflyer and 2D precursor under the influence of horizontal wind.

$$\omega = (\frac{L}{D})(\frac{1}{r})v$$

, where $\frac{L}{D}$ is the lift-drag ratio of a blade. The lift-drag ratio $\frac{L}{D}$ is for an blade (airfoil) is determined by the attack angle $\alpha$ for a certain Reynolds number, i.e., $\alpha = 90° - \beta - arctan\frac{\omega r}{v}$. Thus, analytically the rotating angular velocity can be solved with given tilt angle $\beta$ by solving the implicit equation

$$\frac{\omega r}{v} = \frac{L}{D}(\alpha) = \frac{L}{D}(90° - \beta - arctan\frac{\omega r}{v})$$

From the vertical direction ($z$ direction) force equilibrium, the relation between weight and velocity can be derived

$$L \cdot \frac{\omega r}{U_a} + D \cdot \frac{v}{U_a} = \frac{W}{N}$$

$$W = \frac{1}{2}\rho v^2 \cdot [N \cdot b \cdot c] \cdot [1 + (\frac{L}{D})^2]^{\frac{3}{2}} \cdot C_D$$

Comparing with that in form of the drag coefficient of the microflyer,

$$W = \frac{1}{2}\rho v^2 \cdot [N \cdot b \cdot c] \cdot C_{D(m)}$$

a straight-forward conclusion is that the drag coefficient of the microflyer is affected by both the drag coefficient ($C_D$) and the lift-drag ratio ($\frac{L}{D}$) of the blades.

$$C_{D(m)} = C_D \cdot [1 + (\frac{L}{D})^2]^{\frac{3}{2}}$$

Figure 7.13 presents the simulation results showing the drag coefficient and lift-drag ratio for a flat airfoil at different Reynolds numbers. The drag coefficient ($C_D$) of the airfoil increases when Reynolds number decreases or the attack angle ($\alpha$) increases. It is noteworthy that $C_D$ saturates for large $Re$, but for small $Re$, $[Re \cdot C_D]$ is nearly constant (Figure 7.14). This different principle results in the different falling behaviors for microflyer at small $Re$ and large $Re$. For large $Re$ where $C_D$ is a constant, the weight and terminal falling velocity relation is

$$\begin{aligned} W &= \frac{1}{2}\rho v^2 \cdot [N \cdot b \cdot c] \cdot [1 + (\frac{L}{D})^2]^{\frac{3}{2}} \cdot C_D \\ &= \frac{1}{2}\rho v^2 \cdot A \cdot C_{D(m)} \end{aligned} \tag{7.1}$$

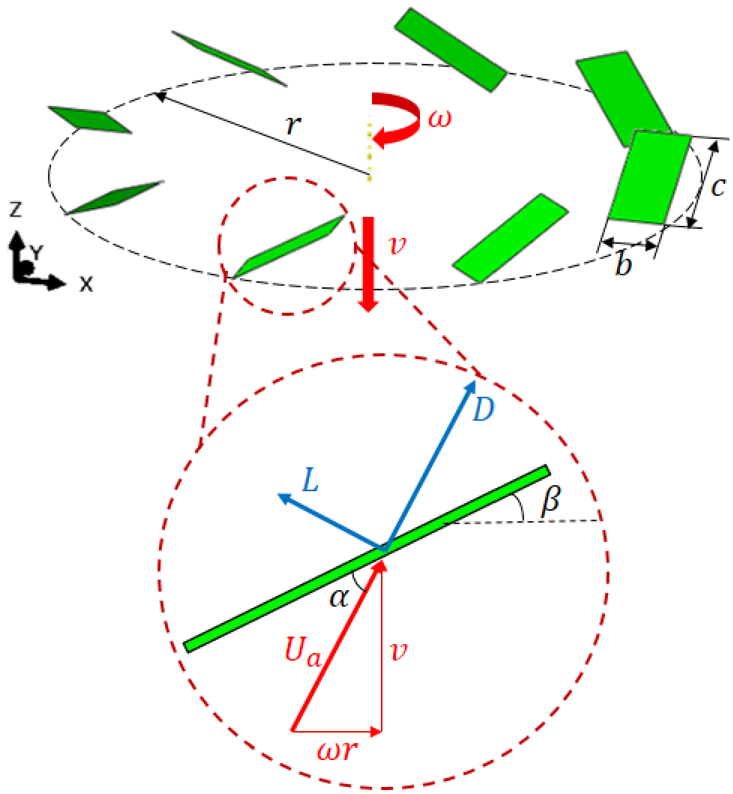


Figure 7.12. Scheme of simplified microflyer model.

However for small $Re$ where $C_D \cdot Re$ is a constant, the weight and terminal falling velocity relation is

$$
\begin{aligned}
W &= \frac{1}{2}\rho v^2 \cdot \frac{1}{Re} \cdot [N \cdot b \cdot c] \cdot [1 + (\frac{L}{D})^2]^{\frac{3}{2}} \cdot C_D \cdot Re \\
&= \frac{1}{2}\mu v \cdot \frac{A}{2r} \cdot [N \cdot b \cdot c] \cdot [1 + (\frac{L}{D})^2]^{\frac{3}{2}} \cdot C_D \cdot Re
\end{aligned}
\tag{7.2}
$$

, which indicates that the microflyer weight is linear to the terminal falling velocity at small $Re$, similar to "Stokes Law". The Lift-drag ratio is also small at small $Re$, but increases rapidly at large $Re$ especially at small attack angles (i.e. $\alpha \approx 5 \sim 10°$) (Figure 7.13b). Therefore for small $Re \ll 1$ where $\frac{L}{D} \ll 1$,

$$C_{D(m)} \approx C_D$$

, which indicates that the lift-drag ratio of the airfoil has very small effect on the microflyer falling behavior, but the drag coefficient dominates. In other words, the lift-drag ratio contributes only at large $Re$.

At small Re number, these analytical results are verified by 3D simulation results of the simplified microflyer model, without any fitting parameters (Figure 7.15). It is clear that at small $Re$ the relation between weight and terminal falling velocity is linear. Figure 7.16 presents the results for a larger microflyer (Diameter ∼40mm) which has a much larger $Re$ ($\sim$ 1300), which shows that the weight of microflyer (mass) is linear to the square of the terminal falling velocity in large $Re$, fitting $C_{D(m)} = 2.0$ for this complex 3D microflyer design.

Further simplify the weight and terminal falling velocity relation by defining the area fill factor $\eta = \frac{A}{\pi r^2}$, we have

$$W = \frac{\pi}{2}\rho r^2 \eta \cdot C_{D(m)} \cdot v^2$$

for large $Re$. For small $Re$, the relation is

$$W = \frac{\pi}{4}\mu r \eta \cdot C_{D(m)} Re \cdot v$$

These relations are derived with condition that the size of the blades are much smaller than the microflyer size, i.e., $\eta \ll 1$. Figure 7.17 presents the simulation results for a

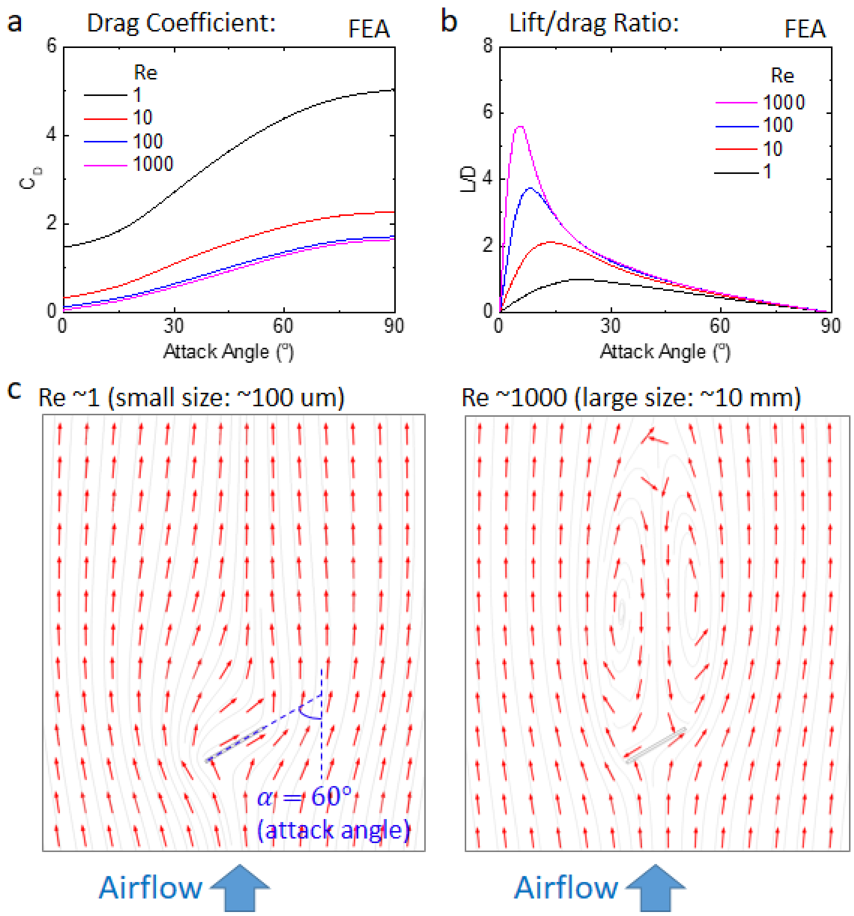


Figure 7.13. Aerodynamic properties of a flat airfoil. (a) Drag coefficient and (b) lift-drag ratio for a flat airfoil at different Reynolds numbers. (c) Velocity field of the flow around the flat airfoil at small and large Reynolds numbers ($Re = 1, Re = 1000$ for left and right, respectively).

large range of fill factor $\eta$ at a small $Re$, showing that for small $\eta$ the $W/v$ is linear to $\eta$ which agrees with the derived equation above. However for large $\eta$, the $W/v$ ratio scales approximately with $\sqrt{\eta}$, thus the amended equations are

$$W = \frac{\pi}{4}\mu r\sqrt{\eta} \cdot G_S \cdot v$$

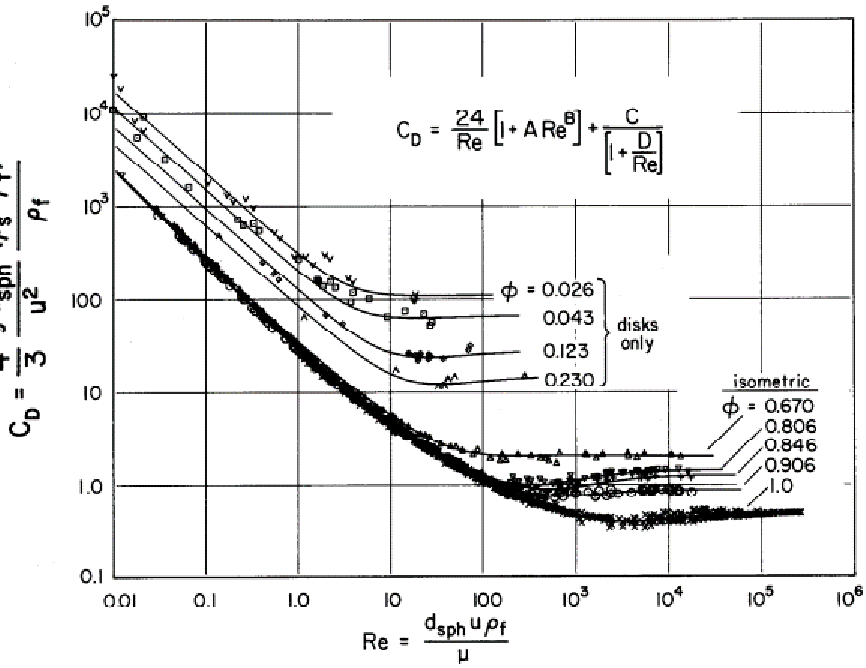


**Fig. 1. Reported drag coefficients for spherical particles (408 data points) and nonspherical particles (506 data points).**

Figure 7.14. Reported drag coefficients for some particles at different Reynolds numbers [**49**].

for small $Re$, and

$$W = \frac{\pi}{2}\rho r^2 \sqrt{\eta} \cdot G_L \cdot v^2$$

for large $Re$. $G_S$ and $G_L$ are the fitting parameters for the relation of small and large $Re$s, respectively.

There are two main factors of air properties, density $\rho$ and dynamic viscosity $\mu$, that affects the falling behavior of microflyers. It is interesting to mention that for small microflyers with small $Re$, the dynamic viscosity plays an important role but the density has no effect, whereas for large microflyers with large $Re$ the air density counts rather than the dynamic viscosity (Figure 7.18). Consequently, changing the temperature of the

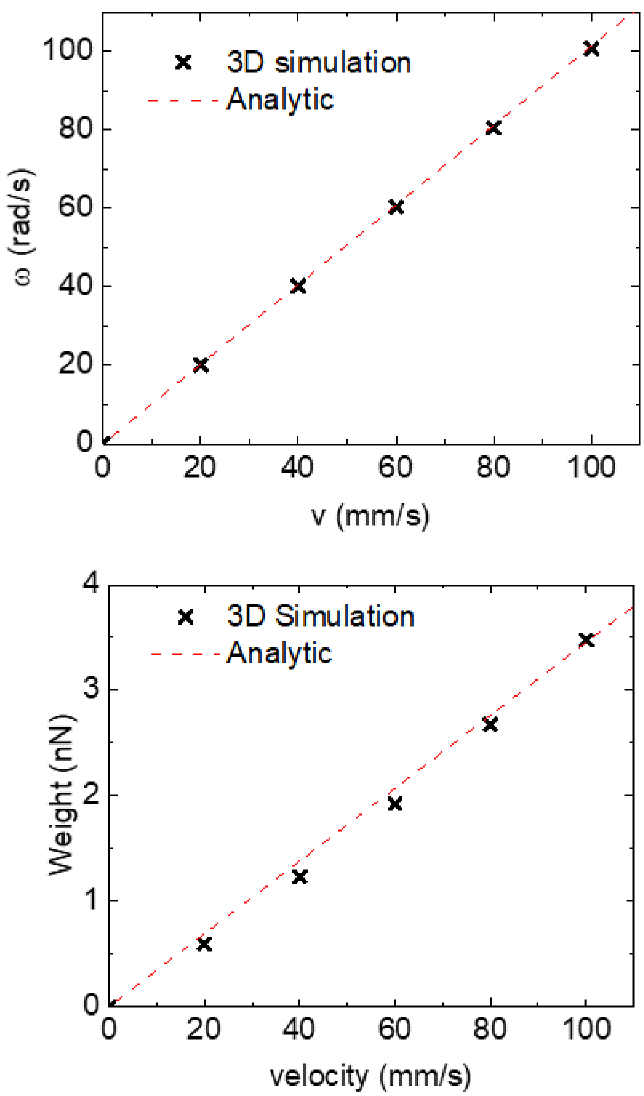


Figure 7.15. 3D aerodynamic simulation results and analytic results for the falling behaviors of a simplified microflyer model at small Re.

air will change the falling behavior of large and small microflyers in opposite ways, i.e. the terminal falling velocity for large microflyer will increase with temperature increasing but will decrease for small microflyer (Figure 7.19). Similar effect can be found if different

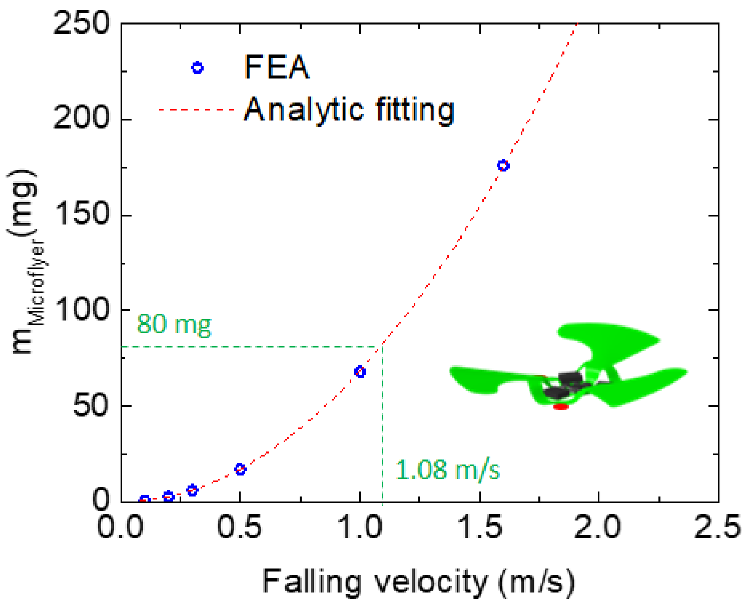


Figure 7.16. Weight versus terminal falling velocity for a 3D microflyer design at large Reynolds number.

gas environments are considered, as shown in Figure 7.20, because of the difference in density and dynamic viscosity for different gases. Also, if we release the microflyers in high altitude, the terminal falling velocity for small microflyers will not change much among different heights because the dynamic viscosity change is small, meanwhile the large microflyers will fall much faster at higher altitudes because of the dramatic decrease of the air density.

### 7.2.3. Structural effect on microflyer falling behavior

We studied the effect of different microflyer structures, in order to further improve the falling behavior of the 3D microflyers, i.e., decreasing the terminal falling velocity. Former

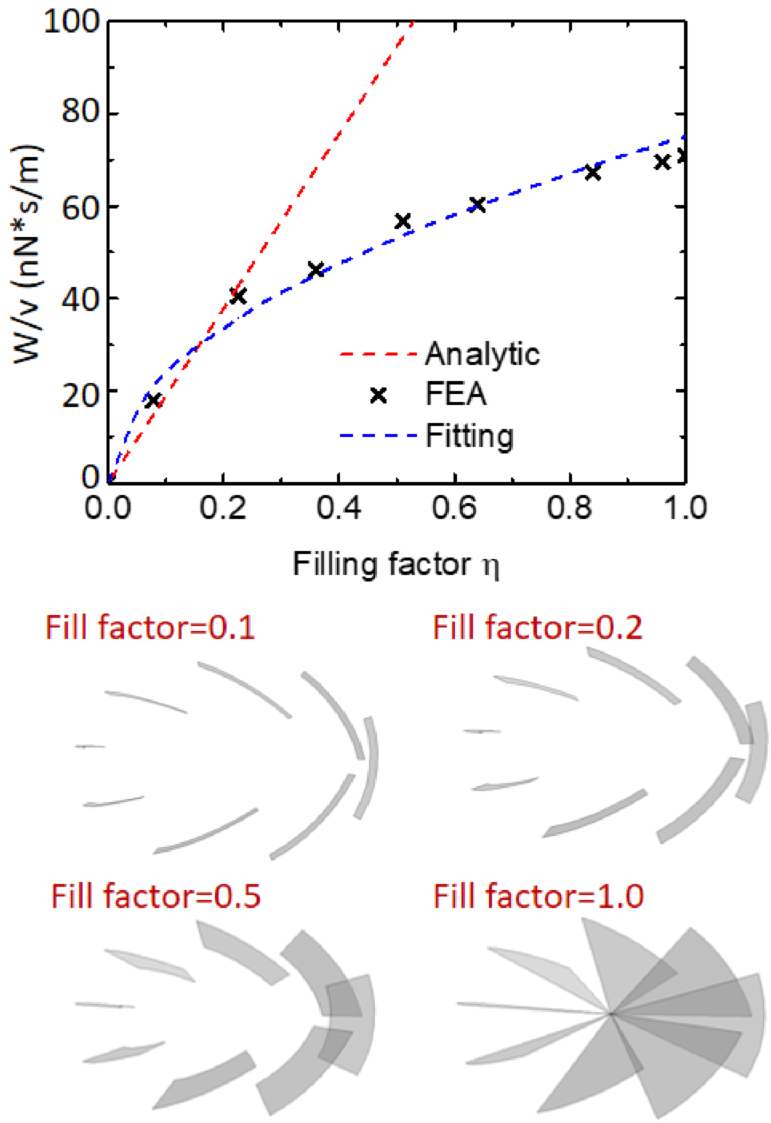


Figure 7.17. Effect of fil factor. (a) $W/v$ versus fill factor for a broad range ($0 \sim 1$). (b) Scheme of simplilfied microflyer model with various fill factors.

small microflyer designs ($R \sim 40$) present different terminal falling velocity with their distinct 3D structures. In spite of the huge differences, the key parameter that affects the terminal falling velocity is the fill factor ($\eta$), as shown in Figure 7.21. Taking in to

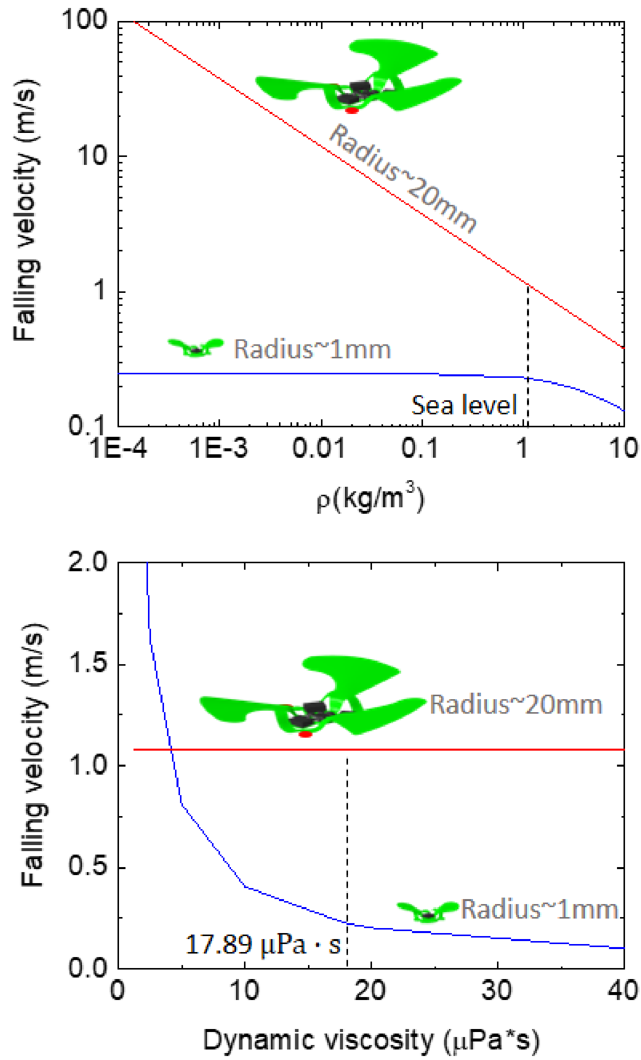


Figure 7.18. Effect of (a) air density and (b) dynamic viscosity on small and large microflyers.

account that the weight of microflyer is

$$W = \rho_m t_m g \cdot \pi r^2 \cdot \eta$$

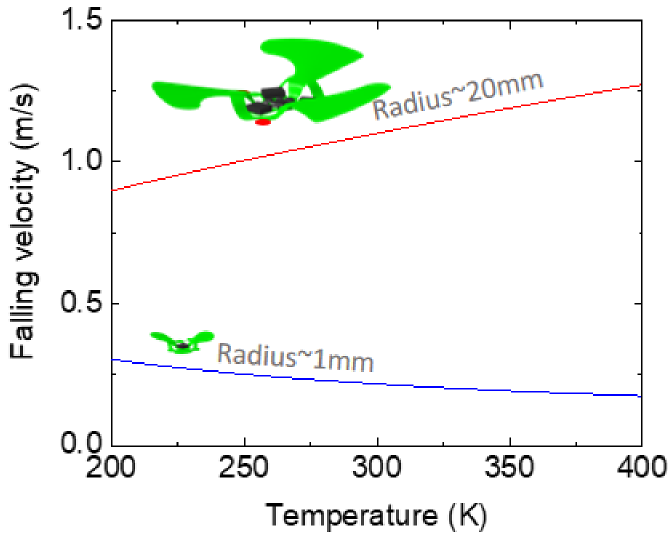


Figure 7.19. Effect of air temperature on small and large microflyers under same pressure.

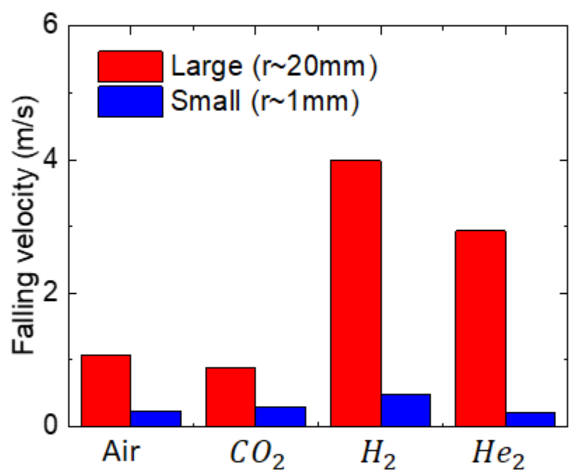


Figure 7.20. Terminal falling velocity of a microflyer demo in different gases.

if there's no payload on microflyer and only the microflyer material contributes to its weight, where $\rho_m = 1.33$ g/mL and $t_m = 6$ $\mu$m are the density and thickness of the microflyer material, and $g = 9.8$ m/s$^2$ is the gravity constant. Applying the weight-velocity relation for small microflyers ($r \sim 1$ mm), the terminal falling velocity as a function of fill factor can be expressed as

$$v = \frac{4\rho_m t_m g \cdot r}{\mu G_S} \cdot \sqrt{\eta}$$

, $G_S = 40$ is the fitting parameter. The results evidence that the different microflyer designs fall on the same curve for the same material, thickness and size. Without any payload, a smaller fill factor design will have slower terminal falling velocity. However this conclusion is not true for structures with payload, as shown in Figure 7.22. For microflyer with payload, the falling velocity is

$$v = \frac{4}{\pi\mu G_S} \cdot (\pi g \rho_m t_m \cdot r\sqrt{\eta} + \frac{W_{load}}{r\sqrt{\eta}})$$

The optimized fill factor $\eta$, which gives the smallest terminal falling velocity is obtained analytically:

$$\eta = \frac{W_{load}}{\pi g \rho_m t_m r^2}$$

Consequently, not the lowest fill factor gives the smallest falling velocity anymore. For example, for a micro- blue LED as the load ($W_{load} \approx 120$ nN), the microflyer design #2 yields the slowest falling velocity among the 4 designs.

The materials and thickness are important factors that affects the terminal falling velocity of microflyer, but they are usually limited by experiment conditions. Thus there's not much space to improve by using lighter materials (lower density) or reducing the thickness. Two methods are studied to further decrease the terminal falling velocity via structural design for small size microflyers and large size microflyers, respectively.

**7.2.3.1. Porosity method for small scale microflyer.** The "porosity" method for small scale microflyers is inspired by some natural solutions illustrated in Figure 7.23. Lotus root can float on the water because of the porosity of its cross section, by reducing the weight or overall density. Also, the feathers usually consist of micro fibers between which there are void spaces, but the aerodynamic property of the feathers is still very good even these void spaces exist. Thus we can add voids on the microflyers, which can largely reduce the weight but have negligible effect on aerodynamic property.

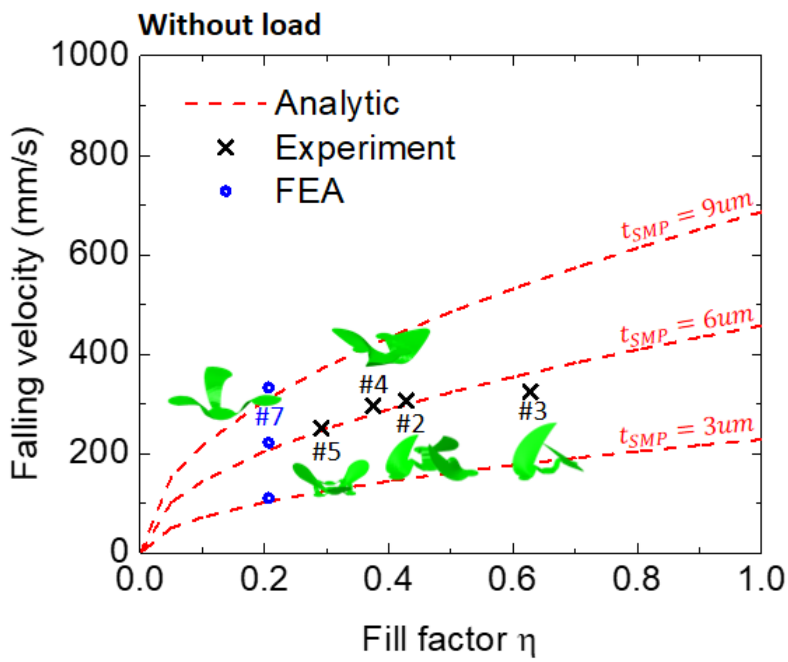


Figure 7.21. Effect of fill factor on microflyer falling velocity without payload.

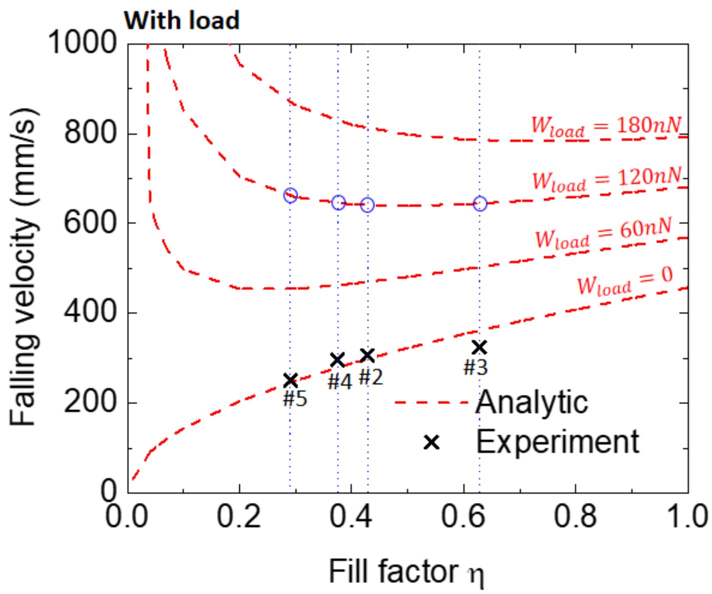


Figure 7.22. Effect of fill factor on microflyer falling velocity with micro LED payload.

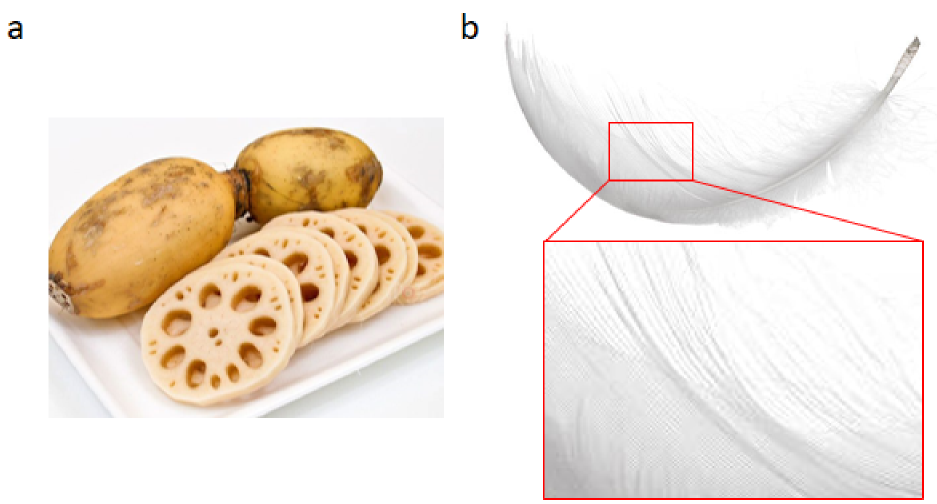


Figure 7.23. Nature inspirations for porosity design.

The "porosity" is defined as the fraction of the void volume over the total volume of microflyer. For a small Reynolds number, the effect of porosity on the drag coefficient is small, which decreases only by a factor of 1.4 as the porosity increases up to 0.9 (Figure 7.24). This is because a low Reynolds number is also equivalent to high viscosity (for fixed density, size of the wing and remote flow velocity). At high viscosity the boundary layers remain unchanged as the porosity increases, as shown in Figure 7.25, which show that the flow around the wing barely changes although voids are added onto the airfoil. As the porosity increases, the rapid decrease of the weight but not drag coefficient at a low Reynolds number suggest that this method can be applied to microscale for the microflyer to decrease the terminal falling velocity.

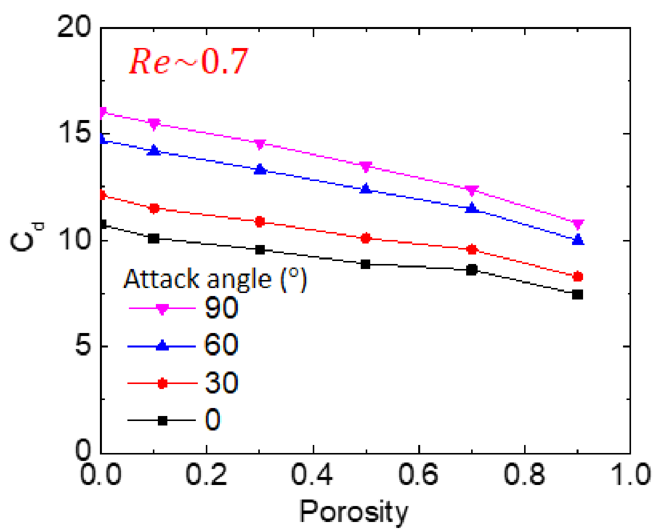


Figure 7.24. Porosity effect on drag coefficient of a flat airfoil at small *Re*.

However this method does not work for large Reynolds numbers. For large Reynolds numbers, the (magnitude of the) velocity increases with the porosity (Figure 7.27), and

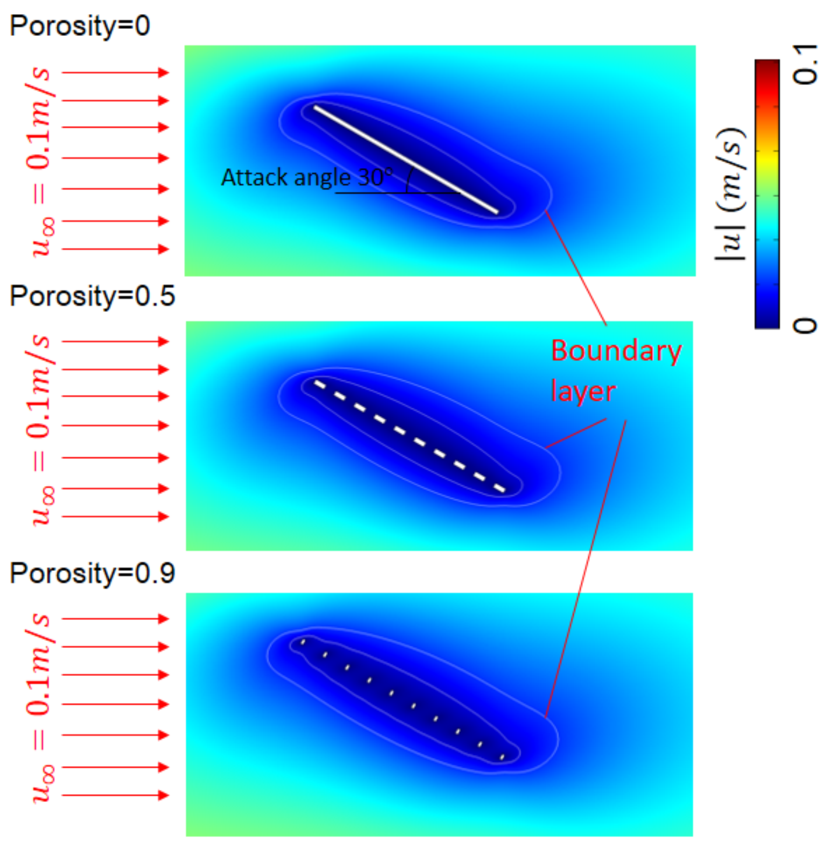


Figure 7.25. Porosity effect on velocity field around a flat airfoil at small $Re$.

the drag coefficient decreases rapidly as the porosity increases. For a high attack angle such as 90°, the drag coefficient decreases by a factor of 4.8 as the porosity increases from 0 to 0.9 (Figure 7.26). As the porosity increases, the simultaneous decrease of the weight and drag coefficient suggests that this method of adding voids on to airfoil does not help much to reduce the falling velocity on the macroscale.

Figure 7.28 and 7.29 shows the porosity method applied on a small microflyer. The terminal falling velocity is reduced by a factor of ~1.3 of the original design (porosity 0) for porosity 0.26, and reduced by a factor of ~1.5 for porosity 0.41. In Figure refc6f28, the

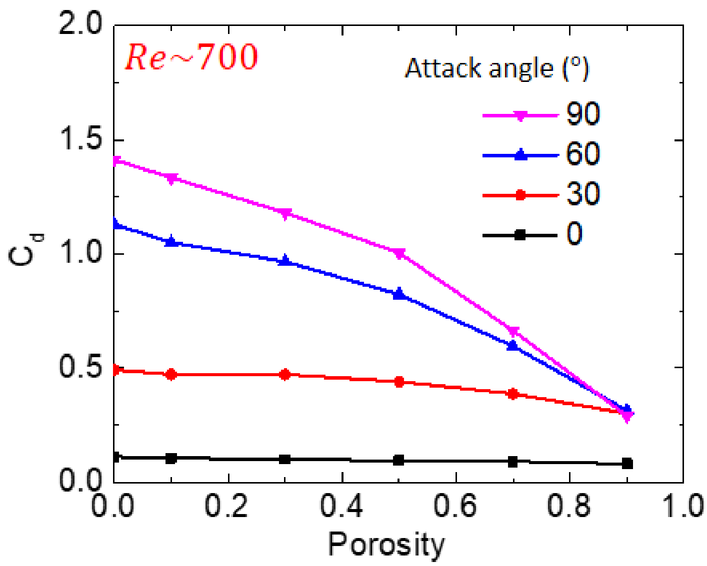


Figure 7.26. Porosity effect on drag coefficient of a flat airfoil at large $Re$.

3D simulation results agrees very well with the prediction from drag coefficient change of 2D airfoil. Figure 7.29 presents some 3D microflyer structure designs with different porosity.

**7.2.3.2. Tilt angle effect on microflyer terminal falling velocity.** The rotating motion of the microflyer as well as the natural seeds are known to be beneficial for the slow terminal falling velocity. This rotating motion is studied for different tilt angles for small and large Reynolds numbers, respectively, and the simplified models of different tilt angles are illustrated in Figure 7.30. For small microflyer (Re$\sim$ 1), the relation of rotating speed and different airfoil tilt angle, as shown in Figure 7.31a, indicates that the maximum rotating speed occurs when $\beta \approx 40°$. The normalized factor $G_S$ characterizing the weight versus terminal falling velocity relation for small scale microflyer is shown in Figure 7.31b, showing that $G_S$ decreases monotonously with the increasing tilt angle. As

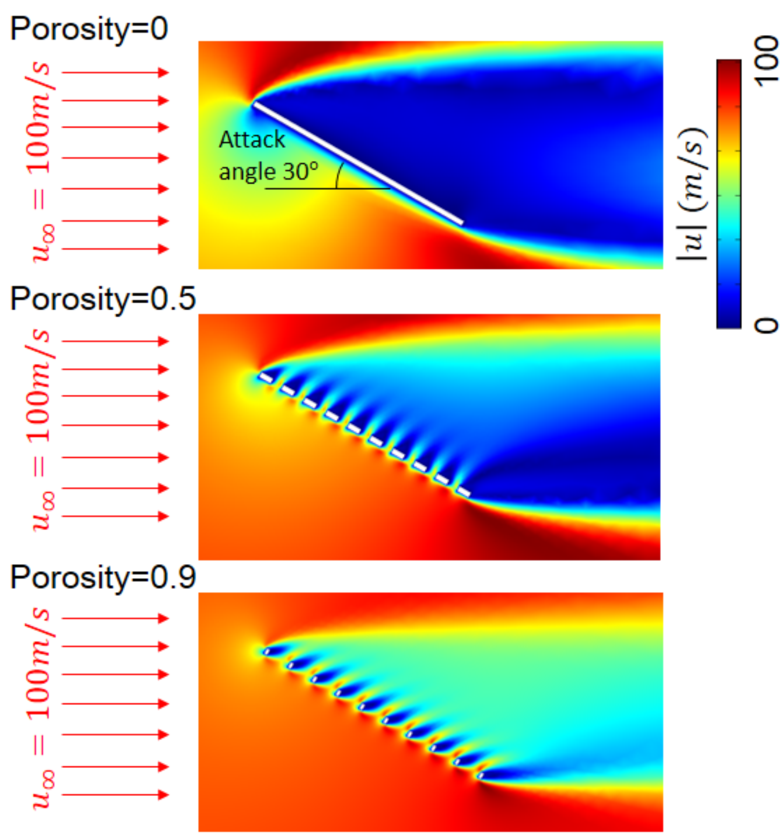


Figure 7.27. Porosity effect on velocity field around a flat airfoil at large $Re$.

a conclusion, for small microflyer, the tilt of airfoils doesn't help to decrease the terminal falling velocity.

For large microflyer ($Re \sim 1000$), the relation of rotating speed and different airfoil tilt angle, as shown in Figure 7.32a, indicates that the maximum rotating speed occurs when $\beta \approx 4^\circ$, which is significantly smaller than the small microflyer. The normalized factor $G_L$, which is a key parameter that characterize the terminal falling velocity relation with microflyer weight, firstly increases with $\beta$ to an optimum value, which is $\sim 23\%$ higher than the case without tilting, then decreases sharply as $\beta$ keeps increasing. This indicates

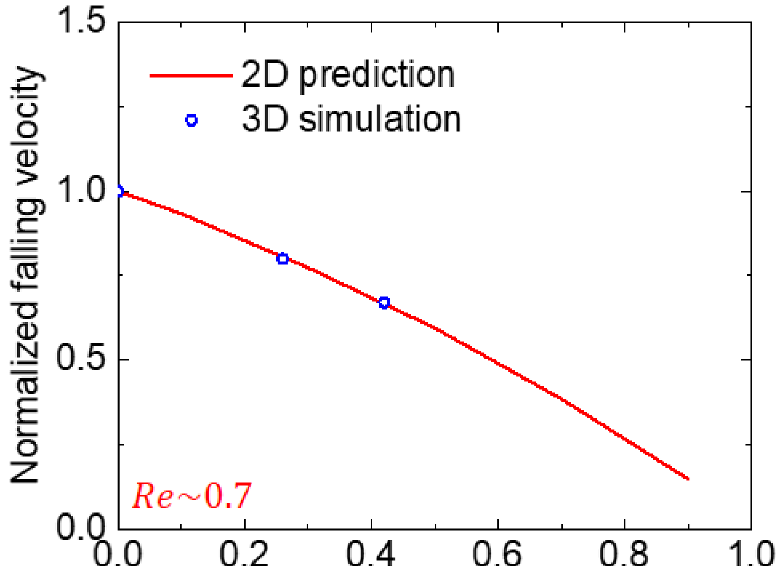


Figure 7.28. Porosity effect on normalized falling velocity. The normalized velocity is normalized by the terminal falling velocity of microflyer with no porosity.

that for microflyer with flat airfoils, the falling velocity can decrease by $\sim 10\%$ by slightly tilting the airfoils.

## 7.3. Methods

### 7.3.1. Finite Element Analysis

Three-dimensional FEA techniques allowed prediction of the mechanical deformations of the 3D structures of the microflyers, during processes of compressive buckling. Four-node shell elements modeled the membrane. Refined meshes ensured computational accuracy using commercial software (Abaqus). The material parameters are $E_{Cu} = 119$ GPa and $\nu_{Ni} = 0.34$ for copper; and $E_{SMP} = 2.5$ GPa and $\nu_{SMP} = 0.27$ for the shape memory polymer.

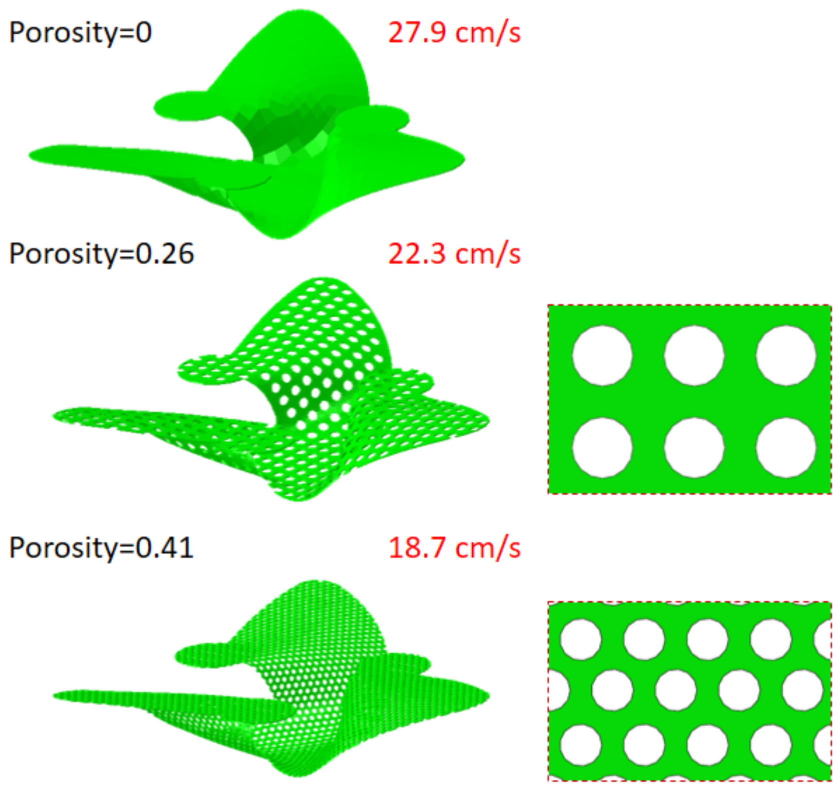


Figure 7.29. Scheme of the porosity structure on 3D microflyer.

### 7.3.2. Computational Fluid Dynamics

The turbulence fluid (rotating machine) model of COMSOL was employed for the three-dimensional aerodynamic simulation of the microflyer falling in the air. The income flow from bottom was set as the terminal falling velocity, while the reaction force integrated on the microflyer was used as the correlated weight of microflyer for the steady state falling. Rotating speed was swept and chosen to make sure the torque on the microflyer

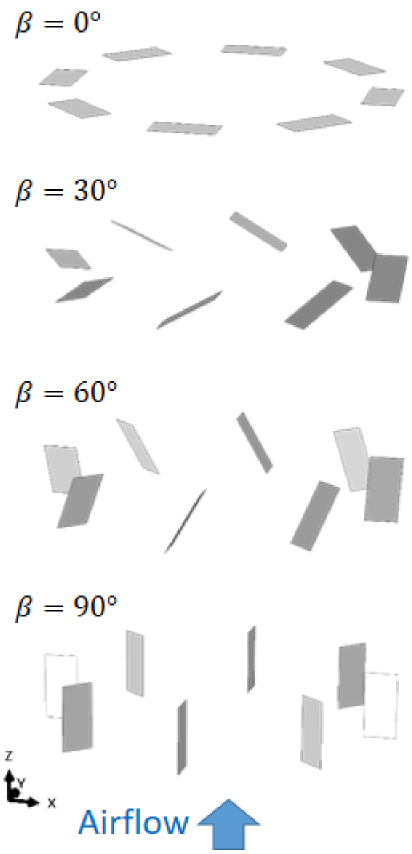


Figure 7.30. Scheme of simplified microflyer model with different tilt angles.

is 0, thus to determine the rotating speed of a given terminal falling velocity. Two-dimensional aerodynamic simulation was used to simulate the aerodynamic properties of the 2D airfoils.

### 7.4. Conclusion

We designed several bio-inspired 3D microflyer designs that will rotating during falling in the air. This kind of 3D microflyers have controllable falling state and predictable

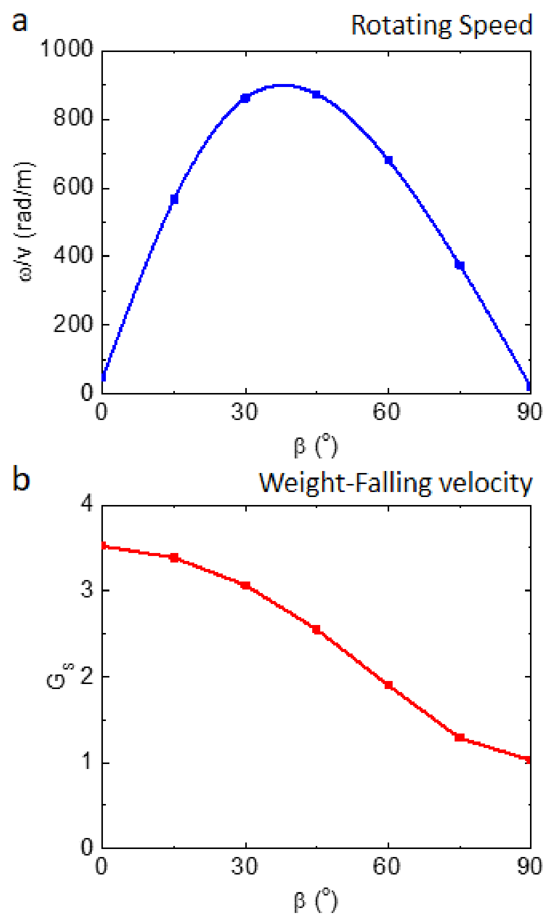


Figure 7.31. Effect of tilt angle on rotating speed and terminal falling velocity for small scale microflyer (small $Re$). Effect of tilt angle on (a) rotating speed and (b) fitting parameter $G_S$.

falling trace in the air, and have reasonably slow terminal falling velocity. 3D simulation was used to study the aerodynamic properties of the microflyers, and an analytic model was developed for the characterization and optimization of the aerodynamic behaviors. Further more, "porosity" method and tilt angle effect are studied to decrease the terminal falling velocity for small microflyer and large microflyer, respectively. These 3D microflyers have potential applications such as high altitude air pollution detection.

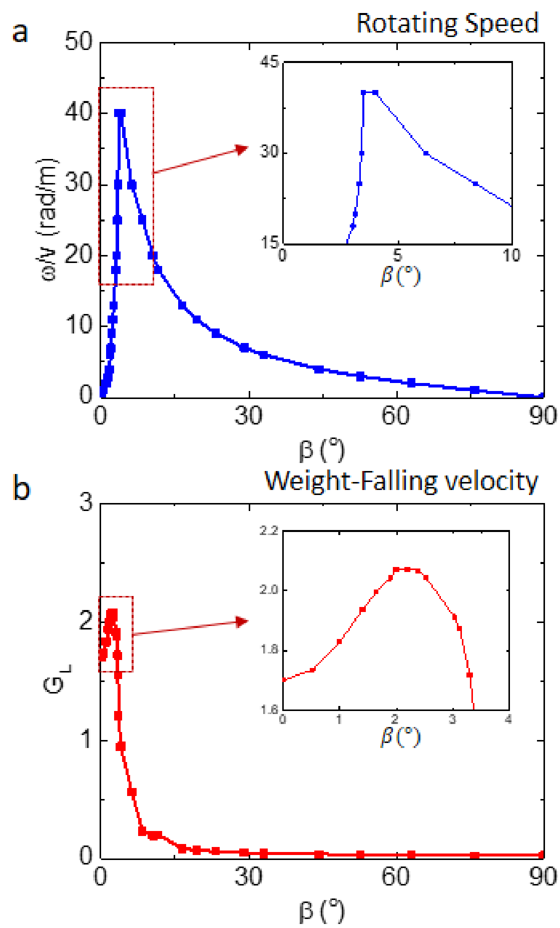


Figure 7.32. Effect of tilt angle on rotating speed and terminal falling velocity for large scale microflyer (large $Re$). Effect of tilt angle on (a) rotating speed and (b) fitting parameter $G_L$.

CHAPTER 8

# Conclusions and Future Work

## 8.1. Conclusions

In this dissertation, we advanced the field of micro-scale 3D asembly and flexible or stretchable electronics by a series of interesting works. We studied the mechanical properties of a novel 3D helical coil structure for stretchable electronics, which provides the possibility of fabricating a new type of highly stretchable electronic device. A generic soft encapsulation for stretchable electronics are proposed, that breaks the stretchability barrier for elastomer encapsulated stretchable devices meanwhile provides robust protection to underlying components. We combined the mechanically guided assembly with micro-structured 3D helical coil components to enable a fully wearable sensing system consisting of integrated circuit (IC) chips. Inspired by this 3D helical coil, we designed and optimized a compliant and stretchable thermoelectric energy harvester, to offer power to miniature flexible devices.

We further explored a novel approach for mechanically guided 3D self-assembled mesostructures by patterning the underlying elastomer substrate with kirigami cuts. The library of the 3D structures are significantly extended by adding rotating motion onto the "bonding sites" of the structures. Also, an important application of a set of 3D microstructures was introduced, microflyer, that can slowly fall in the air with controllable flying state and predictable path and terminal falling velocity.

## 8.2. Future work

The field of 3D assembly and flexible electronics have already drawn a lot of attentions. There's still challenge and promising directions that will significantly advance this area.

Employing novel flexible materials can be a interesting area–for example, novel organic materials, inkject printed electronics with conductive inks or semiconducting materials, graphene and graphene-like 2D materials–that the stretchability barrier will be broken with mechanical and structural design. Current work about organic flexible electronics (or so-called organic plastic electronics) utilize the stretchability of the organic materials with minimal structural design, thus this direction can be closely developed because of the huge advantages of the organic materials on bio-compatibility and compliance, and this is similar to inkject printed electronics (e.g. flexible electronics on paper) and that with graphene materials.

I expect a further application of flexible electronics on the applications of human-machine interfaces such as neuro-interfaces. This area requires further exploration and understanding of the complex mechanisms of the electronic-bio interfaces. Applications such as muscle-neuro interface, brain interface, artificial cochlear and artificial retina are hot areas but still drawing more attentions.

# References

[1] Abdullah, A. M., Nan, K., Rogers, J. A., and Hsia, K. J. Mismatch strain programmed shape transformation of curved bilayer-flexible support assembly. *Extreme Mechanics Letters 7* (2016), 34–41.

[2] Ahn, B. Y., Duoss, E. B., Motala, M. J., Guo, X., Park, S.-I., Xiong, Y., Yoon, J., Nuzzo, R. G., Rogers, J. A., and Lewis, J. A. Omnidirectional printing of flexible, stretchable, and spanning silver microelectrodes. *Science 323*, 5921 (2009), 1590–1593.

[3] Andersen, M. C. Diaspore morphology and seed dispersal in several wind-dispersed asteraceae. *American Journal of Botany 80*, 5 (1993), 487–492.

[4] Arpin, K. A., Mihi, A., Johnson, H. T., Baca, A. J., Rogers, J. A., Lewis, J. A., and Braun, P. V. Multidimensional architectures for functional optical devices. *Advanced Materials 22*, 10 (2010), 1084–1101.

[5] Avery, A. D., Zhou, B. H., Lee, J., Lee, E.-S., Miller, E. M., Ihly, R., Wesenberg, D., Mistry, K. S., Guillot, S. L., Zink, B. L., et al. Tailored semiconducting carbon nanotube networks with enhanced thermoelectric properties. *Nature Energy 1*, 4 (2016), 16033.

[6] Bahk, J.-H., Fang, H., Yazawa, K., and Shakouri, A. Flexible thermoelectric materials and device optimization for wearable energy harvesting. *Journal of Materials Chemistry C 3*, 40 (2015), 10362–10374.

[7] Bariya, M., Nyein, H. Y. Y., and Javey, A. Wearable sweat sensors. *Nature Electronics 1*, 3 (2018), 160.

[8] Bassik, N., Stern, G. M., and Gracias, D. H. Microassembly based on hands free origami with bidirectional curvature. *Applied physics letters 95*, 9 (2009), 091901.

[9] Belmonte, A., Eisenberg, H., and Moses, E. From flutter to tumble: inertial drag and froude similarity in falling paper. *Physical Review Letters 81*, 2 (1998), 345.

[10] Beretta, D., Perego, A., Lanzani, G., and Caironi, M. Organic flexible thermoelectric generators: from modeling, a roadmap towards applications. *Sustainable Energy & Fuels 1*, 1 (2017), 174–190.

[11] Bian, J., Ding, Y., Duan, Y., Wan, X., and Huang, Y. Buckling-driven self-assembly of self-similar inspired micro/nanofibers for ultra-stretchable electronics. *Soft matter 13*, 40 (2017), 7244–7254.

[12] Bishop, D., Pardo, F., Bolle, C., Giles, R., and Aksyuk, V. Silicon micromachines for fun and profit. *Journal of Low Temperature Physics 169*, 5-6 (2012), 386–399.

[13] Bossuyt, F., Vervust, T., and Vanfleteren, J. Stretchable electronics technology for large area applications: fabrication and mechanical characterization. *IEEE Transactions on components, packaging and manufacturing technology 3*, 2 (2013), 229–235.

[14] Bubnova, O., Khan, Z. U., Malti, A., Braun, S., Fahlman, M., Berggren, M., and Crispin, X. Optimization of the thermoelectric figure of merit in the conducting polymer poly (3, 4-ethylenedioxythiophene). *Nature materials 10*, 6 (2011), 429.

[15] Bullock, J. M., Kenward, R. E., and Hails, R. S. *Dispersal ecology: 42nd symposium of the British ecological society*, vol. 42. Cambridge University Press, 2002.

[16] Caillat, T., Fleurial, J.-P., and Borshchevsky, A. Preparation and thermoelectric properties of semiconducting zn4sb3. *Journal of Physics and Chemistry of Solids 58*, 7 (1997), 1119–1125.

[17] Cain, M. L., Milligan, B. G., and Strand, A. E. Long-distance seed dispersal in plant populations. *American journal of botany 87*, 9 (2000), 1217–1227.

[18] Cesarano, I., and Segalman, R. Robocasting provides moldless fabrication from slurry deposition. *Ceramic Industry 148*, 4 (1998), 94–100.

[19] Chang, T., Tanabe, Y., Wojcik, C. C., Barksdale, A. C., Doshay, S., Dong, Z., Liu, H., Zhang, M., Chen, Y., and Su, Y. A general strategy for

stretchable microwave antenna systems using serpentine mesh layouts. *Advanced Functional Materials 27*, 46 (2017), 1703059.

[20] Chen, P. N., Xu, Y. F., He, S. S., Sun, X. M., Pan, S. W., Deng, J., Chen, D. Y., and Peng, H. S. Hierarchically arranged helical fibre actuators driven by solvents and vapours. *Nature Nanotechnology 10*, 12 (2015), 1077–1083.

[21] Cho, C., Wallace, K. L., Tzeng, P., Hsu, J.-H., Yu, C., and Grunlan, J. C. Outstanding low temperature thermoelectric power factor from completely organic thin films enabled by multidimensional conjugated nanomaterials. *Advanced Energy Materials 6*, 7 (2016), 1502168.

[22] Choi, C., Choi, M. K., Liu, S., Kim, M. S., Park, O. K., Im, C., Kim, J., Qin, X., Lee, G. J., and Cho, K. W. Human eye-inspired soft optoelectronic device using high-density mos 2-graphene curved image sensor array. *Nature communications 8*, 1 (2017), 1664.

[23] Choi, J., Cho, K., and Kim, S. Flexible thermoelectric generators composed of n-and p-type silicon nanowires fabricated by top-down method. *Advanced Energy Materials 7*, 7 (2017), 1602138.

[24] Choi, M. K., Yang, J., Kang, K., Kim, D. C., Choi, C., Park, C., Kim, S. J., Chae, S. I., Kim, T. H., Kim, J. H., Hyeon, T., and Kim, D. H. Wearable red-green-blue quantum dot light-emitting diode array using high-resolution intaglio transfer printing. *Nature Communications 6* (2015).

[25] Choi, W. M., Song, J., Khang, D.-Y., Jiang, H., Huang, Y. Y., and Rogers, J. A. Biaxially stretchable "wavy" silicon nanomembranes. *Nano Letters 7*, 6 (2007), 1655–1663.

[26] Cotton, D. P. J., Graz, I. M., and Lacour, S. P. A multifunctional capacitive sensor for stretchable electronic skins. *IEEE Sensors Journal 9*, 12 (2009), 2008–2009.

[27] Cumpston, B. H., Ananthavel, S. P., Barlow, S., Dyer, D. L., Ehrlich, J. E., Erskine, L. L., Heikal, A. A., Kuebler, S. M., Lee, I.-Y. S., McCord-Maughon, D., et al. Two-photon polymerization initiators for three-dimensional optical data storage and microfabrication. *Nature 398*, 6722 (1999), 51.

[28] Dagdeviren, C., Li, Z., and Wang, Z. L. Energy harvesting from the animal/human body for self-powered electronics. *Annual review of biomedical engineering 19* (2017), 85–108.

[29] Derby, B. Printing and prototyping of tissues and scaffolds. *Science 338*, 6109 (2012), 921–926.

[30] Deubel, M., Von Freymann, G., Wegener, M., Pereira, S., Busch, K., and Soukoulis, C. M. Direct laser writing of three-dimensional photonic-crystal templates for telecommunications. *Nature materials 3*, 7 (2004), 444.

[31] Emaminejad, S., Gao, W., Wu, E., Davies, Z. A., Nyein, H. Y. Y., Challa, S., Ryan, S. P., Fahad, H. M., Chen, K., and Shahpar, Z. Autonomous sweat extraction and analysis applied to cystic fibrosis and glucose monitoring using a fully integrated wearable platform. *Proceedings of the National Academy of Sciences 114*, 18 (2017), 4625–4630.

[32] Fan, J. A., Yeo, W.-H., Su, Y., Hattori, Y., Lee, W., Jung, S.-Y., Zhang, Y., Liu, Z., Cheng, H., and Falgout, L. Fractal design concepts for stretchable electronics. *Nature communications 5* (2014), 3266.

[33] Fan, Z., Razavi, H., Do, J.-w., Moriwaki, A., Ergen, O., Chueh, Y.-L., Leu, P. W., Ho, J. C., Takahashi, T., Reichertz, L. A., et al. Three-dimensional nanopillar-array photovoltaics on low-cost and flexible substrates. *Nature materials 8*, 8 (2009), 648.

[34] Felton, S., Tolley, M., Demaine, E., Rus, D., and Wood, R. A method for building self-folding machines. *Science 345*, 6197 (2014), 644–646.

[35] Fenner, M. *Seed ecology*. Springer Science & Business Media, 2012.

[36] Filipov, E. T., Tachi, T., and Paulino, G. H. Origami tubes assembled into stiff, yet reconfigurable structures and metamaterials. *Proceedings of the National Academy of Sciences 112*, 40 (2015), 12321–12326.

[37] Foroughi, J., Spinks, G. M., Wallace, G. G., Oh, J., Kozlov, M. E., Fang, S. L., Mirfakhrai, T., Madden, J. D. W., Shin, M. K., Kim, S. J., and Baughman, R. H. Torsional carbon nanotube artificial muscles. *Science 334*, 6055 (2011), 494–497.

[38] Fu, H., Nan, K., Bai, W., Huang, W., Bai, K., Lu, L., Zhou, C., Liu, Y., Liu, F., and Wang, J. Morphable 3d mesostructures and microelectronic devices by multistable buckling mechanics. *Nature materials 17*, 3 (2018), 268.

[39] Gao, W., Emaminejad, S., Nyein, H. Y. Y., Challa, S., Chen, K., Peck, A., Fahad, H. M., Ota, H., Shiraki, H., and Kiriya, D. Fully integrated

wearable sensor arrays for multiplexed in situ perspiration analysis. *Nature 529*, 7587 (2016), 509.

[40] Gao, Y., Zhang, Y., Wang, X., Sim, K., Liu, J., Chen, J., Feng, X., Xu, H., and Yu, C. Moisture-triggered physically transient electronics. *Science advances 3*, 9 (2017), e1701222.

[41] Ge, Q., Dunn, C. K., Qi, H. J., and Dunn, M. L. Active origami by 4d printing. *Smart Materials and Structures 23*, 9 (2014), 094007.

[42] Ge, Q., Qi, H. J., and Dunn, M. L. Active materials by four-dimension printing. *Applied Physics Letters 103*, 13 (2013), 131901.

[43] Gladman, A. S., Matsumoto, E. A., Nuzzo, R. G., Mahadevan, L., and Lewis, J. A. Biomimetic 4d printing. *Nature materials 15*, 4 (2016), 413.

[44] Gonzalez, M., Axisa, F., Bulcke, M. V., Brosteaux, D., Vandevelde, B., and Vanfleteren, J. Design of metal interconnects for stretchable electronic circuits. *Microelectronics Reliability 48*, 6 (2008), 825–832.

[45] Greene, D., and Johnson, E. The aerodynamics of plumed seeds. *Functional Ecology* (1990), 117–125.

[46] Greene, D., and Johnson, E. Seed mass and dispersal capacity in wind-dispersed diaspores. *Oikos* (1993), 69–74.

[47] Grimm, D., Bof Bufon, C. C., Deneke, C., Atkinson, P., Thurmer, D. J., Schaffel, F., Gorantla, S., Bachmatiuk, A., and Schmidt, O. G. Rolled-up nanomembranes as compact 3d architectures for field effect transistors and fluidic sensing applications. *Nano letters 13*, 1 (2012), 213–218.

[48] Guo, X., Li, H., Ahn, B. Y., Duoss, E. B., Hsia, K. J., Lewis, J. A., and Nuzzo, R. G. Two-and three-dimensional folding of thin film single-crystalline silicon for photovoltaic power applications. *Proceedings of the National Academy of Sciences 106*, 48 (2009), 20149–20154.

[49] Haider, A., and Levenspiel, O. Drag coefficient and terminal velocity of spherical and nonspherical particles. *Powder technology 58*, 1 (1989), 63–70.

[50] Haines, C. S., Lima, M. D., Li, N., Spinks, G. M., Foroughi, J., Madden, J. D. W., Kim, S. H., Fang, S. L., de Andrade, M. J., Goktepe, F., Goktepe, O., Mirvakili, S. M., Naficy, S., Lepro, X., Oh, J. Y., Kozlov, M. E., Kim, S. J., Xu, X. R., Swedlove, B. J., Wallace, G. G., and

Baughman, R. H. Artificial muscles from fishing line and sewing thread. *Science 343*, 6173 (2014), 868–872.

[51] Hawkes, E., An, B., Benbernou, N. M., Tanaka, H., Kim, S., Demaine, E., Rus, D., and Wood, R. J. Programmable matter by folding. *Proceedings of the National Academy of Sciences 107*, 28 (2010), 12441–12445.

[52] Hsu, Y.-Y., Gonzalez, M., Bossuyt, F., Axisa, F., Vanfleteren, J., and De Wolf, I. In situ observations on deformation behavior and stretching-induced failure of fine pitch stretchable interconnect. *Journal of Materials research 24*, 12 (2009), 3573–3582.

[53] Hsu, Y.-Y., Gonzalez, M., Bossuyt, F., Axisa, F., Vanfleteren, J., and De Wolf, I. The effect of pitch on deformation behavior and the stretching-induced failure of a polymer-encapsulated stretchable circuit. *Journal of Micromechanics and Microengineering 20*, 7 (2010), 075036.

[54] Hsu, Y.-Y., Gonzalez, M., Bossuyt, F., Axisa, F., Vanfleteren, J., and De Wolf, I. The effects of encapsulation on deformation behavior and failure mechanisms of stretchable interconnects. *Thin Solid Films 519*, 7 (2011), 2225–2234.

[55] Huang, M., Cavallo, F., Liu, F., and Lagally, M. G. Nanomechanical architecture of semiconductor nanomembranes. *Nanoscale 3*, 1 (2011), 96–120.

[56] Huang, W., Yu, X., Froeter, P., Xu, R., Ferreira, P., and Li, X. On-chip inductors with self-rolled-up sin x nanomembrane tubes: A novel design platform for extreme miniaturization. *Nano letters 12*, 12 (2012), 6283–6288.

[57] Huang, X., Liu, Y., Cheng, H., Shin, W.-J., Fan, J. A., Liu, Z., Lu, C.-J., Kong, G.-W., Chen, K., and Patnaik, D. Materials and designs for wireless epidermal sensors of hydration and strain. *Advanced Functional Materials 24*, 25 (2014), 3846–3854.

[58] Huang, Y., Ding, Y., Bian, J., Su, Y., Zhou, J., Duan, Y., and Yin, Z. Hyper-stretchable self-powered sensors based on electrohydrodynamically printed, self-similar piezoelectric nano/microfibers. *Nano Energy 40* (2017), 432–439.

[59] Huang, Y. A., Wang, Y. Z., Xiao, L., Liu, H. M., Dong, W. T., and Yin, Z. P. Microfluidic serpentine antennas with designed mechanical tunability. *Lab on a Chip 14* (2014), 4205–4212.

[60] Hull, C., Feygin, M., Baron, Y., Sanders, R., Sachs, E., Lightman, A., and Wohlers, T. Rapid prototyping: current technology and future potential. *Rapid Prototyping Journal 1*, 1 (1995), 11–19.

[61] Jackman, R. J., Wilbur, J. L., and Whitesides, G. M. Fabrication of submicrometer features on curved substrates by microcontact printing. *Science 269*, 5224 (1995), 664–666.

[62] Jamal, M., Zarafshar, A. M., and Gracias, D. H. Differentially photo-crosslinked polymers enable self-assembling microfluidics. *Nature communications 2* (2011), 527.

[63] Jang, K.-I., Chung, H. U., Xu, S., Lee, C. H., Luan, H., Jeong, J., Cheng, H., Kim, G.-T., Han, S. Y., and Lee, J. W. Soft network composite materials with deterministic and bio-inspired designs. *Nature communications 6* (2015), 6566.

[64] Jang, K. I., Han, S. Y., Xu, S., Mathewson, K. E., Zhang, Y. H., Jeong, J. W., Kim, G. T., Webb, C., Lee, J. W., Dawidczyk, T. J., Kim, R. H., Song, Y. M., Yeo, W. H., Kim, S., Cheng, H. Y., Il Rhee, S., Chung, J., Kim, B., Chung, H. U., Lee, D. J., Yang, Y. Y., Cho, M., Gaspar, J. G., Carbonari, R., Fabiani, M., Gratton, G., Huang, Y. G., and Rogers, J. A. Rugged and breathable forms of stretchable electronics with adherent composite substrates for transcutaneous monitoring. *Nature Communications 5* (2014), 4779.

[65] Jang, K.-I., Li, K., Chung, H. U., Xu, S., Jung, H. N., Yang, Y., Kwak, J. W., Jung, H. H., Song, J., and Yang, C. Self-assembled three dimensional network designs for soft electronics. *Nature Communications 8* (2017), 15894.

[66] Janusziewicz, R., Tumbleston, J. R., Quintanilla, A. L., Mecham, S. J., and DeSimone, J. M. Layerless fabrication with continuous liquid interface production. *Proceedings of the National Academy of Sciences 113*, 42 (2016), 11703–11708.

[67] Jeong, J. W., McCall, J. G., Shin, G., Zhang, Y. H., Al-Hasani, R., Kim, M., Li, S., Sim, J. Y., Jang, K. I., Shi, Y., Hong, D. Y., Liu, Y. H., Schmitz, G. P., Xia, L., He, Z. B., Gamble, P., Ray, W. Z., Huang, Y. G., Bruchas, M. R., and Rogers, J. A. Wireless optofluidic systems for programmable in vivo pharmacology and optogenetics. *Cell 162*, 3 (2015), 662–674.

[68] Jia, Z., Tucker, M. B., and Li, T. Failure mechanics of organic-inorganic multilayer permeation barriers in flexible electronics. *Composites Science and Technology 71*, 3 (2011), 365–372.

[69] Jiang, H., Khang, D.-Y., Song, J., Sun, Y., Huang, Y., and Rogers, J. A. Finite deformation mechanics in buckled thin films on compliant supports. *Proceedings of the National Academy of Sciences 104*, 40 (2007), 15607–15612.

[70] Jinno, H., Fukuda, K., Xu, X., Park, S., Suzuki, Y., Koizumi, M., Yokota, T., Osaka, I., Takimiya, K., and Someya, T. Stretchable and waterproof elastomer-coated organic photovoltaics for washable electronic textile applications. *Nature Energy 2*, 10 (2017), 780.

[71] Jung, S., Kim, J. H., Kim, J., Choi, S., Lee, J., Park, I., Hyeon, T., and Kim, D. H. Reverse-micelle-induced porous pressure-sensitive rubber for wearable human-machine interfaces. *Advanced Materials 26*, 28 (2014), 4825–+.

[72] Jung, Y. H., Chang, T.-H., Zhang, H., Yao, C., Zheng, Q., Yang, V. W., Mi, H., Kim, M., Cho, S. J., and Park, D.-W. High-performance green flexible electronics based on biodegradable cellulose nanofibril paper. *Nature communications 6* (2015), 7170.

[73] Jung, Y. H., Zhang, H., Cho, S. J., and Ma, Z. Flexible and stretchable microwave microelectronic devices and circuits. *IEEE Transactions on Electron Devices 64*, 5 (2017), 1881–1893.

[74] Kabiri Ameri, S., Ho, R., Jang, H., Tao, L., Wang, Y., Wang, L., Schnyer, D. M., Akinwande, D., and Lu, N. Graphene electronic tattoo sensors. *ACS nano 11*, 8 (2017), 7634–7641.

[75] Kaltenbrunner, M., Sekitani, T., Reeder, J., Yokota, T., Kuribara, K., Tokuhara, T., Drack, M., Schwediauer, R., Graz, I., and Bauer-Gogonea, S. An ultra-lightweight design for imperceptible plastic electronics. *Nature 499*, 7459 (2013), 458.

[76] Kanno, T., Tamaki, H., Sato, H. K., Kang, S. D., Ohno, S., Imasato, K., Kuo, J. J., Snyder, G. J., and Miyazaki, Y. Enhancement of average thermoelectric figure of merit by increasing the grain-size of mg3. 2sb1. 5bi0. 49te0. 01. *Applied Physics Letters 112*, 3 (2018), 033903.

[77] Keplinger, C., Sun, J.-Y., Foo, C. C., Rothemund, P., Whitesides, G. M., and Suo, Z. Stretchable, transparent, ionic conductors. *Science 341*, 6149 (2013), 984–987.

[78] KHANG, D.-Y., JIANG, H., HUANG, Y., AND ROGERS, J. A. A stretchable form of single-crystal silicon for high-performance electronics on rubber substrates. *Science 311*, 5758 (2006), 208–212.

[79] KIM, B. H., LEE, J., WON, S. M., XIE, Z., CHANG, J.-K., YU, Y., CHO, Y. K., JANG, H., JEONG, J. Y., AND LEE, Y. Three-dimensional silicon electronic systems fabricated by compressive buckling process. *ACS nano 12*, 5 (2018), 4164–4171.

[80] KIM, D. H., GHAFFARI, R., LU, N. S., WANG, S. D., LEE, S. P., KEUM, H., D'ANGELO, R., KLINKER, L., SU, Y. W., LU, C. F., KIM, Y. S., AMEEN, A., LI, Y. H., ZHANG, Y. H., DE GRAFF, B., HSU, Y. Y., LIU, Z. J., RUSKIN, J., XU, L. Z., LU, C., OMENETTO, F. G., HUANG, Y. G., MANSOUR, M., SLEPIAN, M. J., AND ROGERS, J. A. Electronic sensor and actuator webs for large-area complex geometry cardiac mapping and therapy. *Proceedings of the National Academy of Sciences of the United States of America 109*, 49 (2012), 19910–19915.

[81] KIM, D. H., LIU, Z. J., KIM, Y. S., WU, J., SONG, J. Z., KIM, H. S., HUANG, Y. G., HWANG, K. C., ZHANG, Y. W., AND ROGERS, J. A. Optimized structural designs for stretchable silicon integrated circuits. *Small 5*, 24 (2009), 2841–2847.

[82] KIM, D.-H., LU, N., MA, R., KIM, Y.-S., KIM, R.-H., WANG, S., WU, J., WON, S. M., TAO, H., AND ISLAM, A. Epidermal electronics. *science 333*, 6044 (2011), 838–843.

[83] KIM, D. H., LU, N. S., HUANG, Y. G., AND ROGERS, J. A. Materials for stretchable electronics in bioinspired and biointegrated devices. *Mrs Bulletin 37*, 3 (2012), 226–235.

[84] KIM, D.-H., SONG, J., CHOI, W. M., KIM, H.-S., KIM, R.-H., LIU, Z., HUANG, Y. Y., HWANG, K.-C., ZHANG, Y.-W., AND ROGERS, J. A. Materials and noncoplanar mesh designs for integrated circuits with linear elastic responses to extreme mechanical deformations. *Proceedings of the National Academy of Sciences* (2008), pnas. 0807476105.

[85] KIM, J., HANNA, J. A., BYUN, M., SANTANGELO, C. D., AND HAYWARD, R. C. Designing responsive buckled surfaces by halftone gel lithography. *Science 335*, 6073 (2012), 1201–1205.

[86] KIM, J., LEE, M., SHIM, H. J., GHAFFARI, R., CHO, H. R., SON, D., JUNG, Y. H., SOH, M., CHOI, C., JUNG, S., CHU, K., JEON, D., LEE, S. T., KIM,

J. H., Choi, S. H., Hyeon, T., and Kim, D. H. Stretchable silicon nanoribbon electronics for skin prosthesis. *Nature Communications 5* (2014), 5747.

[87] Kim, S., Yamamoto, S., and Aizawa, T. Thermoelectric properties of anisotropy-controlled p-type bi–te–sb system via bulk mechanical alloying and shear extrusion. *Journal of alloys and compounds 375*, 1-2 (2004), 107–113.

[88] Kim, S. J., We, J. H., and Cho, B. J. A wearable thermoelectric generator fabricated on a glass fabric. *Energy & Environmental Science 7*, 6 (2014), 1959–1965.

[89] Kishi, M., Nemoto, H., Hamao, T., Yamamoto, M., Sudou, S., Mandai, M., and Yamamoto, S. Micro thermoelectric modules and their application to wristwatches as an energy source. In *Thermoelectrics, 1999. Eighteenth International Conference on* (1999), IEEE, pp. 301–307.

[90] Klein, Y., Efrati, E., and Sharon, E. Shaping of elastic sheets by prescription of non-euclidean metrics. *Science 315*, 5815 (2007), 1116–1120.

[91] Ko, H. C., Stoykovich, M. P., Song, J. Z., Malyarchuk, V., Choi, W. M., Yu, C. J., Geddes, J. B., Xiao, J. L., Wang, S. D., Huang, Y. G., and Rogers, J. A. A hemispherical electronic eye camera based on compressible silicon optoelectronics. *Nature 454*, 7205 (2008), 748–753.

[92] Koh, A., Kang, D., Xue, Y., Lee, S., Pielak, R. M., Kim, J., Hwang, T., Min, S., Banks, A., Bastien, P., Manco, M. C., Wang, L., Ammann, K. R., Jang, K. I., Won, P., Han, S., Ghaffari, R., Paik, U., Slepian, M. J., Balooch, G., Huang, Y. G., and Rogers, J. A. A soft, wearable microfluidic device for the capture, storage, and colorimetric sensing of sweat. *Science Translational Medicine 8*, 366 (2016), 366ra165.

[93] Kumar, S. Selective laser sintering: a qualitative and objective approach. *Jom 55*, 10 (2003), 43–47.

[94] Lacour, S. P., Courtine, G., and Guck, J. Materials and technologies for soft implantable neuroprostheses. *Nature Reviews Materials 1*, 10 (2016), 16063.

[95] Lacour, S. P., Jones, J., Wagner, S., Li, T., and Suo, Z. Stretchable interconnects for elastic electronic surfaces. *Proceedings of the IEEE 93*, 8 (2005), 1459–1467.

[96] Lebel, L. L., Aissa, B., Khakani, M. A. E., and Therriault, D. Ultraviolet-assisted direct-write fabrication of carbon nanotube/polymer nanocomposite microcoils. *Advanced Materials 22*, 5 (2010), 592–596.

[97] Lee, H., Choi, T. K., Lee, Y. B., Cho, H. R., Ghaffari, R., Wang, L., Choi, H. J., Chung, T. D., Lu, N., and Hyeon, T. A graphene-based electrochemical device with thermoresponsive microneedles for diabetes monitoring and therapy. *Nature nanotechnology 11*, 6 (2016), 566.

[98] Lee, H., Lee, Y., Song, C., Cho, H. R., Ghaffari, R., Choi, T. K., Kim, K. H., Lee, Y. B., Ling, D., Lee, H., Yu, S. J., Choi, S. H., Hyeon, T., and Kim, D. H. An endoscope with integrated transparent bioelectronics and theranostic nanoparticles for colon cancer treatment. *Nature Communications 6* (2015).

[99] Lee, S., Reuveny, A., Reeder, J., Lee, S., Jin, H., Liu, Q., Yokota, T., Sekitani, T., Isoyama, T., and Abe, Y. A transparent bending-insensitive pressure sensor. *Nature nanotechnology 11*, 5 (2016), 472.

[100] Lentink, D., Dickson, W. B., Van Leeuwen, J. L., and Dickinson, M. H. Leading-edge vortices elevate lift of autorotating plant seeds. *Science 324*, 5933 (2009), 1438–1440.

[101] Leong, T. G., Randall, C. L., Benson, B. R., Bassik, N., Stern, G. M., and Gracias, D. H. Tetherless thermobiochemically actuated microgrippers. *Proceedings of the National Academy of Sciences* (2009), pnas–0807698106.

[102] Lewis, J. A., and Gratson, G. M. Direct writing in three dimensions. *Materials today 7*, 7-8 (2004), 32–39.

[103] Li, J., Liang, G., Zhu, X., and Yang, S. Exploiting nanoroughness on holographically patterned three-dimensional photonic crystals. *Advanced Functional Materials 22*, 14 (2012), 2980–2986.

[104] Li, T., Suo, Z., Lacour, S. P., and Wagner, S. Compliant thin film patterns of stiff materials as platforms for stretchable electronics. *Journal of materials research 20*, 12 (2005), 3274–3277.

[105] Li, Y., Zhang, J., Xing, Y., and Song, J. Thermomechanical analysis of epidermal electronic devices integrated with human skin. *Journal of Applied Mechanics 84*, 11 (2017), 111004.

[106] Lim, W., Lee, I., Sylvester, D., and Blaauw, D. 8.2 batteryless sub-nw cortex-m0+ processor with dynamic leakage-suppression logic. In *Solid-State Circuits Conference-(ISSCC), 2015 IEEE International* (2015), IEEE, pp. 1–3.

[107] Lin, S. T., Yuk, H., Zhang, T., Parada, G. A., Koo, H., Yu, C. J., and Zhao, X. H. Stretchable hydrogel electronics and devices. *Advanced Materials* (2015), In Press (DOI: 10.1002/adma.201504152).

[108] Lipomi, D. J., Vosgueritchian, M., Tee, B. C., Hellstrom, S. L., Lee, J. A., Fox, C. H., and Bao, Z. Skin-like pressure and strain sensors based on transparent elastic films of carbon nanotubes. *Nature nanotechnology 6*, 12 (2011), 788.

[109] Liu, K., Wu, J., Paulino, G. H., and Qi, H. J. Programmable deployment of tensegrity structures by stimulus-responsive polymers. *Scientific reports 7*, 1 (2017), 3511.

[110] Liu, Y., Boyles, J. K., Genzer, J., and Dickey, M. D. Self-folding of polymer sheets using local light absorption. *Soft Matter 8*, 6 (2012), 1764–1769.

[111] Liu, Y., Yan, Z., Lin, Q., Guo, X., Han, M., Nan, K., Hwang, K.-C., Huang, Y., Zhang, Y., and Rogers, J. A. Guided formation of 3d helical mesostructures by mechanical buckling: Analytical modeling and experimental validation. *Advanced functional materials 26*, 17 (2016), 2909–2918.

[112] Liu, Z., Qi, D., Leow, W. R., Yu, J., Xiloyannnis, M., Cappello, L., Liu, Y., Zhu, B., Jiang, Y., and Chen, G. 3d-structured stretchable strain sensors for out-of-plane force detection. *Advanced Materials* (2018), 1707285.

[113] Lu, N. S., Wang, X., Suo, Z. G., and Vlassak, J. Metal films on polymer substrates stretched beyond 50*Applied Physics Letters 91*, 22 (2007), 221909.

[114] Lu, N. S., and Yang, S. X. Mechanics for stretchable sensors. *Current Opinion in Solid State & Materials Science 19*, 3 (2015), 149–159.

[115] Ma, Y., Pharr, M., Wang, L., Kim, J., Liu, Y., Xue, Y., Ning, R., Wang, X., Chung, H. U., and Feng, X. Soft elastomers with ionic liquid-filled cavities as strain isolating substrates for wearable electronics. *small 13*, 9 (2017), 1602954.

[116] MacLeod, B. A., Stanton, N. J., Gould, I. E., Wesenberg, D., Ihly, R., Owczarczyk, Z. R., Hurst, K. E., Fewox, C. S., Folmar, C. N., Hughes,

K. H., et al. Large n-and p-type thermoelectric power factors from doped semiconducting single-walled carbon nanotube thin films. *Energy & Environmental Science 10*, 10 (2017), 2168–2179.

[117] Mai, C.-K., Russ, B., Fronk, S. L., Hu, N., Chan-Park, M. B., Urban, J. J., Segalman, R. A., Chabinyc, M. L., and Bazan, G. C. Varying the ionic functionalities of conjugated polyelectrolytes leads to both p-and n-type carbon nanotube composites for flexible thermoelectrics. *Energy & Environmental Science 8*, 8 (2015), 2341–2346.

[118] Maruo, S., and Kawata, S. Two-photon-absorbed near-infrared photopolymerization for three-dimensional microfabrication. *Journal of microelectromechanical systems 7*, 4 (1998), 411–415.

[119] Maruo, S., Nakamura, O., and Kawata, S. Three-dimensional microfabrication with two-photon-absorbed photopolymerization. *Optics letters 22*, 2 (1997), 132–134.

[120] Mercier, P. P., Bandyopadhyay, S., Lysaght, A. C., Stankovic, K. M., and Chandrakasan, A. P. A sub-nw 2.4 ghz transmitter for low data-rate sensing applications. *IEEE journal of solid-state circuits 49*, 7 (2014), 1463–1474.

[121] Mercier, P. P., Lysaght, A. C., Bandyopadhyay, S., Chandrakasan, A. P., and Stankovic, K. M. Energy extraction from the biologic battery in the inner ear. *Nature biotechnology 30*, 12 (2012), 1240.

[122] Minami, S., and Azuma, A. Various flying modes of wind-dispersal seeds. *Journal of Theoretical Biology 225*, 1 (2003), 1–14.

[123] Minev, I. R., Musienko, P., Hirsch, A., Barraud, Q., Wenger, N., Moraud, E. M., Gandar, J., Capogrosso, M., Milekovic, T., and Asboth, L. Electronic dura mater for long-term multimodal neural interfaces. *Science 347*, 6218 (2015), 159–163.

[124] Murphy, S. V., and Atala, A. 3d bioprinting of tissues and organs. *Nature biotechnology 32*, 8 (2014), 773.

[125] Nadeau, P., Mimee, M., Carim, S., Lu, T. K., and Chandrakasan, A. P. 21.1 nanowatt circuit interface to whole-cell bacterial sensors. In *Solid-State Circuits Conference (ISSCC), 2017 IEEE International* (2017), IEEE, pp. 352–353.

[126] Oh, J. Y., Rondeau-Gagne, S., Chiu, Y.-C., Chortos, A., Lissel, F., Wang, G.-J. N., Schroeder, B. C., Kurosawa, T., Lopez, J., and Katsumata, T. Intrinsically stretchable and healable semiconducting polymer for organic transistors. *Nature 539*, 7629 (2016), 411.

[127] Ota, H., Chen, K., Lin, Y., Kiriya, D., Shiraki, H., Yu, Z., Ha, T.-J., and Javey, A. Highly deformable liquid-state heterojunction sensors. *Nature communications 5* (2014), 5032.

[128] Pan, L., Yu, G., Zhai, D., Lee, H. R., Zhao, W., Liu, N., Wang, H., Tee, B. C.-K., Shi, Y., Cui, Y., et al. Hierarchical nanostructured conducting polymer hydrogel with high electrochemical activity. *Proceedings of the National Academy of Sciences 109*, 24 (2012), 9287–9292.

[129] Park, D.-W., Ness, J. P., Brodnick, S. K., Esquibel, C., Novello, J., Atry, F., Baek, D.-H., Kim, H., Bong, J., and Swanson, K. I. Electrical neural stimulation and simultaneous in vivo monitoring with transparent graphene electrode arrays implanted in gcamp6f mice. *ACS nano 12*, 1 (2018), 148–157.

[130] Park, J., Choi, S., Janardhan, A. H., Lee, S. Y., Raut, S., Soares, J., Shin, K., Yang, S. X., Lee, C., Kang, K. W., Cho, H. R., Kim, S. J., Seo, P., Hyun, W., Jung, S., Lee, H. J., Lee, N., Choi, S. H., Sacks, M., Lu, N. S., Josephson, M. E., Hyeon, T., Kim, D. H., and Hwang, H. J. Electromechanical cardioplasty using a wrapped elasto-conductive epicardial mesh. *Science Translational Medicine 8*, 344 (2016).

[131] Pendry, J. B., Holden, A. J., Robbins, D. J., and Stewart, W. Magnetism from conductors and enhanced nonlinear phenomena. *IEEE transactions on microwave theory and techniques 47*, 11 (1999), 2075–2084.

[132] Peng, J., Kang, S. D., and Snyder, G. J. Optimization principles and the figure of merit for triboelectric generators. *Science advances 3*, 12 (2017), eaap8576.

[133] Pikul, J. H., Zhang, H. G., Cho, J., Braun, P. V., and King, W. P. High-power lithium ion microbatteries from interdigitated three-dimensional bicontinuous nanoporous electrodes. *Nature communications 4* (2013), 1732.

[134] Priya, S., and Inman, D. J. *Energy harvesting technologies*, vol. 21. Springer, 2009.

[135] Py, C., Reverdy, P., Doppler, L., Bico, J., Roman, B., and Baroud, C. N. Capillary origami: spontaneous wrapping of a droplet with an elastic sheet. *Physical review letters 98*, 15 (2007), 156103.

[136] Raviv, D., Zhao, W., McKnelly, C., Papadopoulou, A., Kadambi, A., Shi, B., Hirsch, S., Dikovsky, D., Zyracki, M., Olguin, C., et al. Active printed materials for complex self-evolving deformations. *Scientific reports 4* (2014), 7422.

[137] Rogers, J. A. Electronics for the human body. *Jama 313*, 6 (2015), 561–562.

[138] Rogers, J. A., Jackman, R. J., and Whitesides, G. M. Constructing single- and multiple-helical microcoils and characterizing their performance as components of microinductors and microelectromagnets. *Journal of microelectromechanical systems 6*, 3 (1997), 184–192.

[139] Rogers, J. A., Someya, T., and Huang, Y. Materials and mechanics for stretchable electronics. *science 327*, 5973 (2010), 1603–1607.

[140] Rojas, J. P., Conchouso, D., Arevalo, A., Singh, D., Foulds, I. G., and Hussain, M. M. based origami flexible and foldable thermoelectric nanogenerator. *Nano Energy 31* (2017), 296–301.

[141] Rossi, F., Castellani, B., and Nicolini, A. Benefits and challenges of mechanical spring systems for energy storage applications. *70th Conference of the Italian Thermal Machines Engineering Association, Ati2015 82* (2015), 805–810.

[142] Rouse, D. M., and Hemami, S. S. Analyzing the role of visual structure in the recognition of natural image content with multi-scale ssim. *Proceedings of the SPIE 6806* (2008), 680615.

[143] Russ, B., Glaudell, A., Urban, J. J., Chabinyc, M. L., and Segalman, R. A. Organic thermoelectric materials for energy harvesting and temperature control. *Nature Reviews Materials 1*, 10 (2016), 16050.

[144] Ryu, J., D'Amato, M., Cui, X., Long, K. N., Jerry Qi, H., and Dunn, M. L. Photo-origami-bending and folding polymers with light. *Applied Physics Letters 100*, 16 (2012), 161908.

[145] Scarpello, M. L., Kurup, D., Rogier, H., Ginste, D. V., Axisa, F., Vanfleteren, J., Joseph, W., Martens, L., and Vermeeren, G. Design of an implantable slot dipole conformal flexible antenna for biomedical applications. *IEEE transactions on antennas and propagation 59*, 10 (2011), 3556–3564.

[146] Schmidt, O. G., and Eberl, K. Nanotechnology: Thin solid films roll up into nanotubes. *Nature 410*, 6825 (2001), 168.

[147] Seerden, K. A., Reis, N., Evans, J. R., Grant, P. S., Halloran, J. W., and Derby, B. Ink-jet printing of wax-based alumina suspensions. *Journal of the American Ceramic Society 84*, 11 (2001), 2514–2520.

[148] Seinfeld, J. H., and Pandis, S. N. *Atmospheric chemistry and physics: from air pollution to climate change*. John Wiley & Sons, 2012.

[149] Sekitani, T., Nakajima, H., Maeda, H., Fukushima, T., Aida, T., Hata, K., and Someya, T. Stretchable active-matrix organic light-emitting diode display using printable elastic conductors. *Nature materials 8*, 6 (2009), 494.

[150] Sekitani, T., Noguchi, Y., Hata, K., Fukushima, T., Aida, T., and Someya, T. A rubberlike stretchable active matrix using elastic conductors. *Science 321*, 5895 (2008), 1468–1472.

[151] Seo, J.-H., Zhang, K., Kim, M., Zhao, D., Yang, H., Zhou, W., and Ma, Z. Flexible phototransistors based on single-crystalline silicon nanomembranes. *Advanced Optical Materials 4*, 1 (2016), 120–125.

[152] Shang, Y. Y., Li, Y. B., He, X. D., Zhang, L. H., Li, Z., Li, P. X., Shi, E. Z., Wu, S. T., and Cao, A. Y. Elastic carbon nanotube straight yarns embedded with helical loops. *Nanoscale 5*, 6 (2013), 2403–2410.

[153] Shelby, R. A., Smith, D. R., and Schultz, S. Experimental verification of a negative index of refraction. *science 292*, 5514 (2001), 77–79.

[154] Shenoy, V. B., and Gracias, D. H. Self-folding thin-film materials: From nanopolyhedra to graphene origami. *Mrs Bulletin 37*, 9 (2012), 847–854.

[155] Shi, Y., and Hearst, J. E. The kirchhoff elastic rod, the nonlinear schrodinger equation, and dna supercoiling. *Journal of Chemical Physics 101* (1994), 5186–5200.

[156] Shin, S., Kumar, R., Roh, J. W., Ko, D.-S., Kim, H.-S., Kim, S. I., Yin, L., Schlossberg, S. M., Cui, S., You, J.-M., et al. High-performance screen-printed thermoelectric films on fabrics. *Scientific reports 7*, 1 (2017), 7317.

[157] Shyu, T. C., Damasceno, P. F., Dodd, P. M., Lamoureux, A., Xu, L., Shlian, M., Shtein, M., Glotzer, S. C., and Kotov, N. A. A kirigami approach to engineering elasticity in nanocomposites through patterned defects. *Nature materials 14*, 8 (2015), 785–9.

[158] Skylar-Scott, M. A., Gunasekaran, S., and Lewis, J. A. Laser-assisted direct ink writing of planar and 3d metal architectures. *Proceedings of the National Academy of Sciences 113*, 22 (2016), 6137–6142.

[159] Someya, T., Bao, Z., and Malliaras, G. G. The rise of plastic bioelectronics. *Nature 540*, 7633 (2016), 379.

[160] Son, D., Lee, J., Qiao, S., Ghaffari, R., Kim, J., Lee, J. E., Song, C., Kim, S. J., Lee, D. J., and Jun, S. W. Multifunctional wearable devices for diagnosis and therapy of movement disorders. *Nature nanotechnology 9*, 5 (2014), 397.

[161] Song, J., Feng, X., and Huang, Y. Mechanics and thermal management of stretchable inorganic electronics. *National science review 3*, 1 (2015), 128–143.

[162] Song, J., Huang, Y., Xiao, J., Wang, S., Hwang, K. C., Ko, H. C., Kim, D. H., Stoykovich, M. P., and Rogers, J. A. Mechanics of noncoplanar mesh design for stretchable electronic circuits. *Journal of Applied Physics 105*, 12 (2009), 123516.

[163] Song, J. H., Edirisinghe, M. J., and Evans, J. R. Formulation and multilayer jet printing of ceramic inks. *Journal of the American Ceramic Society 82*, 12 (1999), 3374–3380.

[164] Song, L., Myers, A. C., Adams, J. J., and Zhu, Y. Stretchable and reversibly deformable radio frequency antennas based on silver nanowires. *ACS applied materials & interfaces 6*, 6 (2014), 4248–4253.

[165] Song, Z., Ma, T., Tang, R., Cheng, Q., Wang, X., Krishnaraju, D., Panat, R., Chan, C. K., Yu, H., and Jiang, H. Origami lithium-ion batteries. *Nature communications 5* (2014), 3140.

[166] Song, Z., Wang, X., Lv, C., An, Y., Liang, M., Ma, T., He, D., Zheng, Y.-J., Huang, S.-Q., and Yu, H. Kirigami-based stretchable lithium-ion batteries. *Scientific reports 5* (2015), 10988.

[167] Sorgini, F., Mazzoni, A., Massari, L., Calio, R., Galassi, C., Kukreja, S. L., Sinibaldi, E., Carrozza, M. C., and Oddo, C. M. Encapsulation of piezoelectric transducers for sensory augmentation and substitution with wearable haptic devices. *Micromachines 8*, 9 (2017), 270.

[168] Soukoulis, C. M., and Wegener, M. Past achievements and future challenges in the development of three-dimensional photonic metamaterials. *nature photonics 5*, 9 (2011), 523.

[169] Su, Y., Ping, X., Yu, K. J., Lee, J. W., Fan, J. A., Wang, B., Li, M., Li, R., Harburg, D. V., and Huang, Y. In-plane deformation mechanics for highly stretchable electronics. *Advanced Materials 29*, 8 (2017), 1604989.

[170] Suarez, F., Parekh, D. P., Ladd, C., Vashaee, D., Dickey, M. D., and Öztürk, M. C. Flexible thermoelectric generator using bulk legs and liquid metal interconnects for wearable electronics. *Applied energy 202* (2017), 736–745.

[171] Sudo, S. Morphological design of dandelion. In *Proc. 2008 SEM XI International Congress and Exposition on Experimental and Applied Mechanics* (2008), pp. 1–8.

[172] Sun, C., Fang, N., Wu, D., and Zhang, X. Projection micro-stereolithography using digital micro-mirror dynamic mask. *Sensors and Actuators A: Physical 121*, 1 (2005), 113–120.

[173] Sun, H.-B., Kawakami, T., Xu, Y., Ye, J.-Y., Matuso, S., Misawa, H., Miwa, M., and Kaneko, R. Real three-dimensional microstructures fabricated by photopolymerization of resins through two-photon absorption. *Optics letters 25*, 15 (2000), 1110–1112.

[174] Sun, J.-Y., Keplinger, C., Whitesides, G. M., and Suo, Z. Ionic skin. *Advanced Materials 26*, 45 (2014), 7608–7614.

[175] Sun, K., Wei, T.-S., Ahn, B. Y., Seo, J. Y., Dillon, S. J., and Lewis, J. A. 3d printing of interdigitated li-ion microbattery architectures. *Advanced Materials 25*, 33 (2013), 4539–4543.

[176] Sun, Y., Choi, W. M., Jiang, H., Huang, Y. Y., and Rogers, J. A. Controlled buckling of semiconductor nanoribbons for stretchable electronics. *Nature nanotechnology 1*, 3 (2006), 201.

[177] Suo, Z. G. Mechanics of stretchable electronics and soft machines. *Mrs Bulletin 37*, 3 (2012), 218–225.

[178] Tian, B., Liu, J., Dvir, T., Jin, L., Tsui, J. H., Qing, Q., Suo, Z., Langer, R., Kohane, D. S., and Lieber, C. M. Macroporous nanowire nanoelectronic scaffolds for synthetic tissues. *Nature materials 11*, 11 (2012), 986.

[179] Tibbits, S. 4d printing: multi-material shape change. *Architectural Design 84*, 1 (2014), 116–121.

[180] Truby, R. L., and Lewis, J. A. Printing soft matter in three dimensions. *Nature 540*, 7633 (2016), 371.

[181] Tumbleston, J. R., Shirvanyants, D., Ermoshkin, N., Janusziewicz, R., Johnson, A. R., Kelly, D., Chen, K., Pinschmidt, R., Rolland, J. P., Ermoshkin, A., et al. Continuous liquid interface production of 3d objects. *Science* (2015), aaa2397.

[182] Tyagi, K., Gahtori, B., Bathula, S., Jayasimhadri, M., Sharma, S., Singh, N. K., Haranath, D., Srivastava, A., and Dhar, A. Crystal structure and mechanical properties of spark plasma sintered cu2se: An efficient photovoltaic and thermoelectric material. *Solid State Communications 207* (2015), 21–25.

[183] Ueno, K., Yamamoto, A., Noguchi, T., Inoue, T., Sodeoka, S., and Obara, H. Optimization of hot-press conditions of zn4sb3 for high thermoelectric performance. ii. mechanical properties. *Journal of alloys and compounds 388*, 1 (2005), 118–121.

[184] Varghese, T., Hollar, C., Richardson, J., Kempf, N., Han, C., Gamarachchi, P., Estrada, D., Mehta, R. J., and Zhang, Y. High-performance and flexible thermoelectric films by screen printing solution-processed nanoplate crystals. *Scientific reports 6* (2016), 33135.

[185] Vashist, S. K., Luppa, P. B., Yeo, L. Y., Ozcan, A., and Luong, J. H. T. Emerging technologies for next-generation point-of-care testing. *Trends in Biotechnology 33*, 11 (2015), 692–705.

[186] Vedde, J., and Gravesen, P. The fracture strength of nitrogen doped silicon wafers. *Materials Science Science and Engineering B-Solid State Materials for Advanced Technology: l996 36*, 1-3 (1996), 246–250.

[187] Viventi, J., Kim, D. H., Moss, J. D., Kim, Y. S., Blanco, J. A., Annetta, N., Hicks, A., Xiao, J. L., Huang, Y. G., Callans, D. J., Rogers, J. A., and Litt, B. A conformal, bio-interfaced class of silicon electronics for mapping cardiac electrophysiology. *Science Translational Medicine 2*, 24 (2010), 24ra22.

[188] Viventi, J., Kim, D.-H., Vigeland, L., Frechette, E. S., Blanco, J. A., Kim, Y.-S., Avrin, A. E., Tiruvadi, V. R., Hwang, S.-W., and Vanleer, A. C. Flexible, foldable, actively multiplexed, high-density electrode array for mapping brain activity in vivo. *Nature neuroscience 14*, 12 (2011), 1599.

[189] Wagner, S., and Bauer, S. Materials for stretchable electronics. *Mrs Bulletin 37*, 3 (2012), 207–217.

[190] Wan, C., Gu, X., Dang, F., Itoh, T., Wang, Y., Sasaki, H., Kondo, M., Koga, K., Yabuki, K., Snyder, G. J., et al. Flexible n-type thermoelectric materials by organic intercalation of layered transition metal dichalcogenide tis 2. *Nature materials 14*, 6 (2015), 622.

[191] Wang, C., Hwang, D., Yu, Z., Takei, K., Park, J., Chen, T., Ma, B., and Javey, A. User-interactive electronic skin for instantaneous pressure visualization. *Nature materials 12*, 10 (2013), 899.

[192] Wang, C., Sim, K., Chen, J., Kim, H., Rao, Z., Li, Y., Chen, W., Song, J., Verduzco, R., and Yu, C. Soft ultrathin electronics innervated adaptive fully soft robots. *Advanced Materials 30*, 13 (2018), 1706695.

[193] Wang, G.-J. N., Gasperini, A., and Bao, Z. Stretchable polymer semiconductors for plastic electronics. *Advanced Electronic Materials 4*, 2 (2018), 1700429.

[194] Wang, J. S., Wang, G., Feng, X. Q., Kitamura, T., Kang, Y. L., Yu, S. W., and Qin, Q. H. Hierarchical chirality transfer in the growth of towel gourd tendrils. *Scientific Reports 3* (2013), 3102.

[195] Wang, T., Yang, H., Qi, D., Liu, Z., Cai, P., Zhang, H., and Chen, X. Mechano-based transductive sensing for wearable healthcare. *Small 14*, 11 (2018), 1702933.

[196] Ware, T. H., McConney, M. E., Wie, J. J., Tondiglia, V. P., and White, T. J. Voxelated liquid crystal elastomers. *Science 347*, 6225 (2015), 982–984.

[197] Weber, J., Potje-Kamloth, K., Haase, F., Detemple, P., Völklein, F., and Doll, T. Coin-size coiled-up polymer foil thermoelectric power generator for wearable electronics. *Sensors and Actuators A: Physical 132*, 1 (2006), 325–330.

[198] White, T. J., and Broer, D. J. Programmable and adaptive mechanics with liquid crystal polymer networks and elastomers. *Nature materials 14*, 11 (2015), 1087.

[199] Widlund, T., Yang, S. X., Hsu, Y. Y., and Lu, N. S. Stretchability and compliance of freestanding serpentine-shaped ribbons. *International Journal of Solids and Structures 51* (2014), 4026–4037.

[200] Wilson, W. C., and Boland, T. Cell and organ printing 1: protein and cell printers. *The Anatomical Record Part A: discoveries in molecular, cellular, and evolutionary biology 272*, 2 (2003), 491–496.

[201] Wood, R. J. The challenge of manufacturing between macro and micro. *American Scientist 102*, 2 (2014), 124.

[202] Wu, J., Yuan, C., Ding, Z., Isakov, M., Mao, Y., Wang, T., Dunn, M. L., and Qi, H. J. Multi-shape active composites by 3d printing of digital shape memory polymers. *Scientific reports 6* (2016), 24224.

[203] Xu, F., Lu, W., and Zhu, Y. Controlled 3d buckling of silicon nanowires for stretchable electronics. *Acs Nano 5*, 1 (2011), 672–678.

[204] Xu, J., Wang, S., Wang, G.-J. N., Zhu, C., Luo, S., Jin, L., Gu, X., Chen, S., Feig, V. R., and To, J. W. Highly stretchable polymer semiconductor films through the nanoconfinement effect. *Science 355*, 6320 (2017), 59–64.

[205] Xu, R., Lee, J. W., Pan, T., Ma, S., Wang, J., Han, J. H., Ma, Y., Rogers, J. A., and Huang, Y. Designing thin, ultrastretchable electronics with stacked circuits and elastomeric encapsulation materials. *Advanced functional materials 27*, 4 (2017), 1604545.

[206] Xu, S., Yan, Z., Jang, K.-I., Huang, W., Fu, H., Kim, J., Wei, Z., Flavin, M., McCracken, J., and Wang, R. Assembly of micro/nanomaterials into complex, three-dimensional architectures by compressive buckling. *Science 347*, 6218 (2015), 154–159.

[207] Xu, S., Zhang, Y., Cho, J., Lee, J., Huang, X., Jia, L., Fan, J. A., Su, Y., Su, J., and Zhang, H. Stretchable batteries with self-similar serpentine interconnects and integrated wireless recharging systems. *Nature communications 4* (2013), 1543.

[208] Xu, S., Zhang, Y., Jia, L., Mathewson, K. E., Jang, K.-I., Kim, J., Fu, H., Huang, X., Chava, P., and Wang, R. Soft microfluidic assemblies of sensors, circuits, and radios for the skin. *Science 344*, 6179 (2014), 70–74.

[209] Yamada, A., Niikura, F., and Ikuta, K. A three-dimensional microfabrication system for biodegradable polymers with high resolution and biocompatibility. *Journal of Micromechanics and Microengineering 18*, 2 (2008), 025035.

[210] Yan, Z., Han, M., Shi, Y., Badea, A., Yang, Y., Kulkarni, A., Hanson, E., Kandel, M. E., Wen, X., Zhang, F., et al. Three-dimensional

mesostructures as high-temperature growth templates, electronic cellular scaffolds, and self-propelled microrobots. *Proceedings of the National Academy of Sciences 114*, 45 (2017), E9455–E9464.

[211] Yan, Z., Zhang, F., Liu, F., Han, M., Ou, D., Liu, Y., Lin, Q., Guo, X., Fu, H., Xie, Z., et al. Mechanical assembly of complex, 3d mesostructures from releasable multilayers of advanced materials. *Science advances 2*, 9 (2016), e1601014.

[212] Yan, Z., Zhang, F., Wang, J., Liu, F., Guo, X., Nan, K., Lin, Q., Gao, M., Xiao, D., Shi, Y., et al. Controlled mechanical buckling for origami-inspired construction of 3d microstructures in advanced materials. *Advanced functional materials 26*, 16 (2016), 2629–2639.

[213] Yang, M., and Kotov, N. A. Nanoscale helices from inorganic materials. *Journal of Materials Chemistry 21*, 19 (2011), 6775–6792.

[214] Yang, S., Chen, Y.-C., Nicolini, L., Pasupathy, P., Sacks, J., Su, B., Yang, R., Sanchez, D., Chang, Y.-F., and Wang, P. "cut-and-paste" manufacture of multiparametric epidermal sensor systems. *Advanced Materials 27*, 41 (2015), 6423–6430.

[215] Yang, S. X., Su, B., Bitar, G., and Lu, N. S. Stretchability of indium tin oxide (ito) serpentine thin films supported by kapton substrates. *International Journal of Fracture 190*, 1-2 (2014), 99–110.

[216] Yao, S., and Zhu, Y. Wearable multifunctional sensors using printed stretchable conductors made of silver nanowires. *Nanoscale 6*, 4 (2014), 2345–2352.

[217] Yao, S. S., and Zhu, Y. Nanomaterial-enabled stretchable conductors: Strategies, materials and devices. *Advanced Materials 27*, 9 (2015), 1480–1511.

[218] Yu, C., Li, X., Ma, T., Rong, J., Zhang, R., Shaffer, J., An, Y., Liu, Q., Wei, B., and Jiang, H. Silicon thin films as anodes for high-performance lithium-ion batteries with effective stress relaxation. *Advanced Energy Materials 2*, 1 (2012), 68–73.

[219] Yu, C. J., Masarapu, C., Rong, J. P., Wei, B. Q., and Jiang, H. Q. Stretchable supercapacitors based on buckled single-walled carbon nanotube macrofilms. *Advanced Materials 21*, 47 (2009), 4793–+.

[220] Yu, M., Huang, Y., Ballweg, J., Shin, H., Huang, M., Savage, D. E., Lagally, M. G., Dent, E. W., Blick, R. H., and Williams, J. C. Semiconductor nanomembrane tubes: three-dimensional confinement for controlled neurite outgrowth. *ACS nano 5*, 4 (2011), 2447–2457.

[221] Yu, Z., Graudejus, O., Tsay, C., Lacour, S. P., Wagner, S., and Morrison, B. Monitoring hippocampus electrical activity in vitro on an elastically deformable microelectrode array. *Journal of Neurotrauma 26*, 7 (2009), 1135–1145.

[222] Zang, J., Ryu, S., Pugno, N., Wang, Q., Tu, Q., Buehler, M. J., and Zhao, X. Multifunctionality and control of the crumpling and unfolding of large-area graphene. *Nature Materials 12*, 4 (2013), 321–325.

[223] Zang, J. F., Cao, C. Y., Feng, Y. Y., Liu, J., and Zhao, X. H. Stretchable and high-performance supercapacitors with crumpled graphene papers. *Scientific Reports 4* (2014).

[224] Zhang, H., Yu, X., and Braun, P. V. Three-dimensional bicontinuous ultrafast-charge and-discharge bulk battery electrodes. *Nature nanotechnology 6*, 5 (2011), 277.

[225] Zhang, W., Ding, F., and Chou, S. Y. Large enhancement of upconversion luminescence of nayf4: Yb3+/er3+ nanocrystal by 3d plasmonic nano-antennas. *Advanced Materials 24*, 35 (2012), OP236–OP241.

[226] Zhang, W., Ding, F., Li, W.-D., Wang, Y., Hu, J., and Chou, S. Y. Giant and uniform fluorescence enhancement over large areas using plasmonic nanodots in 3d resonant cavity nanoantenna by nanoimprinting. *Nanotechnology 23*, 22 (2012), 225301.

[227] Zhang, X., Jiang, X., and Sun, C. Micro-stereolithography of polymeric and ceramic microstructures. *Sensors and Actuators A: Physical 77*, 2 (1999), 149–156.

[228] Zhang, Y., Wang, S., Li, X., Fan, J. A., Xu, S., Song, Y. M., Choi, K.-J., Yeo, W.-H., Lee, W., and Nazaar, S. N. Experimental and theoretical studies of serpentine microstructures bonded to prestrained elastomers for stretchable electronics. *Advanced Functional Materials 24*, 14 (2014), 2028–2037.

[229] Zhang, Y., Yan, Z., Nan, K., Xiao, D., Liu, Y., Luan, H., Fu, H., Wang, X., Yang, Q., and Wang, J. A mechanically driven form of kirigami as a route to 3d mesostructures in micro/nanomembranes. *Proceedings of the National Academy of Sciences 112*, 38 (2015), 11757–11764.

[230] Zhang, Y., Zhang, F., Yan, Z., Ma, Q., Li, X., Huang, Y., and Rogers, J. A. Printing, folding and assembly methods for forming 3d mesostructures in advanced materials. *Nature Reviews Materials 2*, 4 (2017), 17019.

[231] Zhang, Y. H., Fu, H. R., Su, Y. W., Xu, S., Cheng, H. Y., Fan, J. A., Hwang, K. C., Rogers, J. A., and Huang, Y. Mechanics of ultra-stretchable self-similar serpentine interconnects. *Acta Materialia 61*, 20 (2013), 7816–7827.

[232] Zhang, Y. H., Fu, H. R., Xu, S., Fan, J. A., Hwang, K. C., Jiang, J. Q., Rogers, J. A., and Huang, Y. G. A hierarchical computational model for stretchable interconnects with fractal-inspired designs. *Journal of the Mechanics and Physics of Solids 72* (2014), 115–130.

[233] Zhang, Y. H., Huang, Y. G., and Rogers, J. A. Mechanics of stretchable batteries and supercapacitors. *Current Opinion in Solid State and Materials Science 19* (2015), 190–199.

[234] Zhang, Y.-H., Li, Y., Fu, S.-Y., Xin, J. H., Daoud, W. A., and Li, L.-F. Synthesis and cryogenic properties of polyimide-silica hybrid films by sol-gel process. *Polymer 46*, 19 (2005), 8373–8378.

[235] Zhang, Y. H., Xu, S., Fu, H. R., Lee, J., Su, J., Hwang, K. C., Rogers, J. A., and Huang, Y. Buckling in serpentine microstructures and applications in elastomer-supported ultra-stretchable electronics with high areal coverage. *Soft Matter 9* (2013), 8062–8070.

[236] Zheng, X., Deotte, J., Alonso, M. P., Farquar, G. R., Weisgraber, T. H., Gemberling, S., Lee, H., Fang, N., and Spadaccini, C. M. Design and optimization of a light-emitting diode projection micro-stereolithography three-dimensional manufacturing system. *Review of Scientific Instruments 83*, 12 (2012), 125001.

[237] Zheng, X., Lee, H., Weisgraber, T. H., Shusteff, M., DeOtte, J., Duoss, E. B., Kuntz, J. D., Biener, M. M., Ge, Q., Jackson, J. A., et al. Ultralight, ultrastiff mechanical metamaterials. *Science 344*, 6190 (2014), 1373–1377.

[238] Zhu, S. Z., Huang, Y. J., and Li, T. Extremely compliant and highly stretchable patterned graphene. *Applied Physics Letters 104*, 17 (2014).

[239] Zhu, Y., and Xu, F. Buckling of aligned carbon nanotubes as stretchable conductors: A new manufacturing strategy. *Advanced Materials 24*, 8 (2012), 1073–1077.

# Vita

**Education**

PhD candidate in Theoretical and Applied Mechanics in Northwestern University, USA, September 2014 - present.

Bachelor of Science (June 2014) in Engineering Mechanics, Tsinghua University, China.

**Publications**

[1] K. Jang*, **K. Li***, H. Chung*, S. Xu, H. Jung, Y. Yang, J. Kwak, H. Jung, J. Song, C. Yang, A. Wang, Z. Liu, J. Lee, B. Kim, J. Kim, J. Lee, Y. Yu, B. Kim, H. Jang, K. Yu, J. Kim, J. Lee, J. Jeong, Y. Song, Y. Huang, Y. Zhang, J. Rogers, “Self-Assembled, Three Dimensional Network Designs for Soft Elecronics”, *Nature Communications* 8 (2017).

[2] K. Nan*, S. Kang*, **K. Li***, K. Yu, F. Zhu, J. Wang, A. Dunn, C. Zhou, Z. Xie, M. Agne, H. Wang, H. Luan, Y. Zhang, Y. Huang, J. Snyder, J. Rogers, “Compliant and stretchable thermoelectric coils for energy harvesting in miniature flexible devices”, *Science Advances* (2018).

[3] **K. Li***, X. Cheng*, F. Zhu, L. Li, Z. Xie, H. Luan, Z. Wang, Z. Ji, H. Wang, F. Liu, Y. Xue, C. Jiang, X. Feng, L. Li, J. Rogers, Y. Huang and Y. Zhang, “A Generic Soft Encapsulation Strategy for Stretchable Electronics”, submitted.

[4] K. Nan, H. Luan, Z. Yan, X. Ning, Y. Wang, A. Wang, J. Wang, M. Han, M. Chang, **K. Li**, Y. Zhang, W. Huang, Y. Xue, Y. Huang, Y. Zhang, and J.A. Rogers, “Engineered

Elastomer Substrates for Guided Assembly of Complex 3D Mesostructures by Spatially Nonuniform Compressive Buckling", *Advanced Functional Materials* 27, 1604545 (2017).

[5] J. Kim, A. Banks, H. Cheng, Z. Xie, S. Xu, K.-I. Jang, J.W. Lee, Z. Liu, P. Gutruf, X. Huang, P. Wei, F. Liu, **K. Li**, M. Dalal, R. Ghaffari, X. Feng, Y. Huang, S. Gupta, U. Paik and J.A. Rogers, "Epidermal Electronics with Advanced Capabilities in Near-Field Communication", *Small* 11(8), 906-912 (2015).

[6] S. Lee, G. Ha, D. Wright, Y. Ma, E. Sen-Gupta, N. Haubrich, P. Branche, W. Li, G. Huppert, M. Johnson, H. Mutlu, **K. Li**, N. Sheth, J. Wright, Y. Huang, M. Mansour, J.A. Rogers, R. Ghaffari, "Highly Flexible, Wearable, and Disposable Cardiac Biosensors for Remote and Ambulatory Monitoring", *Npj Digital Medicine*, 2 (2018).

[7] S. Han, J. Kim, S. Won, Y. Ma, D. Kang, Z. Xie, K. Lee, H. Chung, A. Banks, S. Min, S. Heo, C. Davies, J. Lee, C. Lee, B. Kim, **K. Li**, Y. Zhou, C. Wei, X. Feng, Y. Huang, J. Rogers, "Battery-free, wireless sensors for fullbody pressure and temperature mapping", *Science Translational Medicine* 10.435 (2018): eaan4950.

[8] B. Kim, F. Liu, Y. Yu, H. Jang, Z. Xie, **K. Li**, J. Lee, J. Jeong, A. Ryu, Y. Lee, N. Oh, J. Kim, J. Kim, S. Jeong, K. Jang, S. Lee, Y. Huang, Y. Zhang and J.A. Rogers, "Mechanically Guided Assembly of 3D Electronic Systems", *Advanced Functional Materials* 10.1002 (2018).

**Presentations at professional meetings**

[1] **K. Li** and Y. Huang, A Smart, "Always-on" Health-Monitoring System, Poster presentation delivered at *Partnerships for Innovations Grantee Conference*, Atlanta, GA, USA, 2017.

[2] **K. Li** and Y. Huang, Self-assembled 3D Network Design for Soft Electronics, Oral presentation delivered at *United States National Conference of Theoretical and Applied Mechanics*, Chicago, IL, USA, 2018.

[3] **K. Li** and Y. Huang, Self-assembled 3D Network Design for Soft Electronics, Poster presentation delivered at *International Conference on Flexible Electronics* (Best Poster Award), Hangzhou, China, 2018.

**Awards**

Chinese Government Award for Outstanding Self-Financed Students Abroad 2017

*Chinese Government*

Walter P. Murphy Fellowship 2014

*Northwestern University*

Qian Xuesen Elite Student Program Outstanding Graduate Thesis Award 2014

*Tsinghua University*

Qian Xuesen Elite Student Fellowship 2011

*Tsinghua University*

Second-class Fellowship Outstanding Merits 2010

*Tsinghua University*

Gold Medal (Final Stage) of Chinese Physics Olympiad (CPhO) 2009

*Chinese Physics Olympiad Committee*